TECHNISCHE UNIVERSITÄT WIEN
Vienna | Austria

DISSERTATION

Computationally Guided Optimization of High-Entropy Sublattice Ceramic Thin Films

carried out for the purpose of obtaining the degree of Doctor technicae (Dr. techn.), submitted at TU Wien, Faculty of Mechanical and Industrial Engineering, by

ANDREAS KRETSCHMER

Mat.Nr. 1126413

under the supervision of

Univ.Prof. Dipl.-Ing. Dr.mont. Paul Heinz Mayrhofer

Institute of Materials Science and Technology, E308

VIENNA, AUGUST 2021

Reviewed by

.....

Jochen Michael Schneider

Lehrstuhl für Werkstoffchemie
RWTH Aachen
Kopernikusstraße 10,
52074 Aachen, Germany

.....

Ulf Jansson
Department of Chemistry –
Ångström laboratory
Uppsala Universitet
Lägerhyddsvägen 1,
751 21 Uppsala, Sweden

This work was supported by the Austrian Competence Center for Tribology (AC^2T) within the framework of the Austrian COMET Program (project K2 InTribology, no. 872176).

I confirm, that going to press of this thesis needs the confirmation of the examination committee.

Affidavit

I declare in lieu of oath, that I wrote this thesis and performed the associated research myself, using only literature cited in this volume. I confirm that this work is original and has not been submitted elsewhere for any examination, nor is it currently under consideration for a thesis elsewhere.

I acknowledge that the submitted work will be checked electronically-technically using suitable and state-of-the-art means (plagiarism detection software). On the one hand, this ensures that the submitted work was prepared according to the high-quality standards within the applicable rules to ensure good scientific practice "Code of Conduct" at the TU Wien. On the other hand, a comparison with other student theses avoids violations of my personal copyright.

Vienna, August 2021 Andreas Kretschmer

Acknowledgements

Three years, two additional children, and one global pandemic. It has been most interesting. I had the pleasure of working with many marvelous companions in my PhD journey, and although I cannot name all here, I want to mention the most significant people who helped me on my path. **Paul**, you invited me into your research group, you gave me guidance when I needed it and otherwise you gave me space to peruse my ideas. Working in your group was a wonderful and stimulating experience and it enriched me in more ways than I can express. I had to learn so many new things, coming from my chemistry background, but the whole research group was always helpful when I was lost. Most noteworthy among my colleague in this regard is **Alexander Kirnbauer**, who mentored me during my early stages in the world of PVD coatings. With high entropy in our coatings and high entropy on our desks and never lacking a splash of humor it was always pleasant learning from you. The fascinating world of DFT was introduced to me by **Nikola Koutná** and **David Holec**, and your guidance and scripts saved me from countless uphill struggles. I am grateful to many more colleagues and scientific collaborators, here I want to express my collective thanks to **you all**.

Many people have contributed to where I am today. I always had a teacher in technical and mathematical aspects in my brother **Jens**, whose watchful eyes spotted many details in my thesis upon proof-reading that I would have overlooked a hundred times over. Next, I want to thank **my parents** who incited my love for books at a very young age and never stopped believing in me. I had difficulties in my first years in school, but your continued support allowed me rise above these trials and develop a deep love and fascination for learning. This fascination is still ablaze in me even today and it is the reason why I pursued this dissertation. Not only did you care for my education, but you are also the most gentle and loving parents one could wish for. Now that I am a father and have experienced the hardships and joys of having kids myself, I can only begin to appreciate everything you did for me. As great as you were as parents during my upbringing, as great are you know as grandparents. Your undying love to your offspring is exemplary and my sweet children are so fortunate to have you. I strive to meet

your compassion and love.

Speaking of passion, my curiosity is matched or even surpassed by my kids, two of which I got during this PhD. **Livia**, **Linnea**, and **Rorik**, you set an example with your livelihood and inquisitiveness in everyday life. I yearn everyday to come home to you, even if you occasionally wreck our place. Know that I strive to rediscover the child in me, so that I can be amazed again about the small things in our world. I cannot wait to go exploring with you.

There is one more person who worked as much towards my thesis as myself. Without **Rita**, my second soul, I could not have accomplished my work. Rita, you are a marvelous mother, logistics officer, common sense, and most of all my safe haven. You scatter my doubts, take care of our wonderful children, and manage our life at home. Only through your continued efforts can I be successful. Through you, I feel tranquility. I therefore want to ask you a special question.

"If you trust in yourself... and believe in your dreams... and follow your star... you'll still get beaten by people who spent their time working hard and learning things and weren't so lazy."

— Terry Pratchett, The Wee Free Men

Abstract

The ever increasing demand for improved performance in protective thin films motivates development of new materials. A recently emerged material class is the family of high-entropy sublattice ceramics, which are defined by a near-equiatomic random solid solution of five or more metals in the metal-sublattice of ceramic compounds like borides, carbides, nitrides, or oxides. Their good mechanical and thermal stability has rendered these materials attractive for development in thin films. The main challenge in this field is the exploration of optimal compositions due to the sheer number of possible element combinations, which cannot be accessed systematically in a reasonable time-frame by experiments alone. Instead, computational screenings of promising compositions can guide experimental research. This two-pronged approach is the foundation of this thesis with Density Functional Theory (DFT) calculations as a tool to screen for and understand material properties, and experimental magnetron sputtering to study real coatings.

An experimental study on (Al, Cr, Nb, Ta, Ti)N thin films shows great potential of Si-alloying to improve the coating performance. The Si incorporation leads to increased hardness and lowered Young's modulus by grain refinement, improves phase stability in vacuum, and increases the oxidation resistance at 850 °C tremendously by densifying the formed oxide layer. This oxide is single-phase rutile-structure despite the presence of Al, and stabilized by the configurational entropy at high temperatures, as calculated by DFT.

The role of the sputtering gas composition was investigated in the (Al, Mo, Ta, V, W)N system. Two nitride coatings with different N-vacancy concentrations and an oxynitride coating were prepared. These coatings exhibit very different microstructures and textures, which also reflects in the hardness. Especially the N-deficient coating shows a high hardness and good thermal stability. The oxynitride coating possesses a high as-deposited hardness, but upon annealing binary oxide phases with high specific volumes are formed that crack the coating open and lead to almost complete oxidation of the coating.

The incorporation of boron into a nitride was explored in (Hf, Ta, Ti, V, Zr)-B-

N. DFT calculations show a strong preference for the NaCl-type phase with good mechanical properties. Reactive sputtering of such boronnitride coatings leads to a mixed-phase coating with amorphous BN and low hardness, but non-reactive sputtering leads to a single-phase face centered cubic coating with up to 46 GPa hardness and thermal stability up to 1200 °C. This highlights the great potential of mixed non-metal sublattices in ceramic high-entropy materials.

The importance of configurational entropy on the phase stability of high-entropy materials is often claimed, but has not yet been quantified. In a high-throughput DFT study the interaction of enthalpic and entropic contributions to the phase stability of 126 combinations of equimolar Al-containing high-entropy sublattice nitrides was investigated. All compositions were found to be metastable with 0.10-0.27 eV/at enthalpy-governed driving force for decomposition, in part caused by the formation of wurtzite-structured AlN. The entropy stabilization at 1073 K amounts to only ≈-0.06 eV/at, not enough to counteract the enthalpy-driven decomposition. Instead, strain energies, caused by large volume differences between the educt and product phases, lead to stabilization of 22 compositions. The predictions show good agreement with X-ray diffraction and atom probe tomography data of four annealed nitride coatings. This study demonstrates that configurational entropy should not be taken for granted as effective stabilizing agent in ceramic high-entropy materials, but strain energies offer an alternative route for material design that has not been considered yet in ceramic high-entropy materials.

Kurzfassung

Die steigenden Ansprüche an die Leistung schützender Dünnschichten motiviert die Entwicklung neuer Materialien. Eine relativ junge Materialklasse stellt die Familie der Hoch-Entropie Keramiken dar, die durch eine nahezu equimolare feste Lösung von fünf oder mehr Metallen auf dem Metalluntergitter in Keramiken wie Boriden, Carbiden, Nitriden, oder Oxiden, charakterisiert sind. Wegen guter mechanischer und thermischer Eigenschaften sind diese Materialien attraktiv für die Entwicklung dünner Schichten. Die größte Herausforderung in diesem Gebiet ist die Entdeckung optimaler Zusammensetzungen, da durch die enorme Anzahl möglicher Elementkombinationen diese durch Experimente nicht in einer annehmbaren Zeit systematisch erforscht werden können. Stattdessen bieten Simulationen eine gute Richtungsweisung für experimentelle Untersuchungen. Dieser zweigleisige Ansatz ist auch die Grundlage dieser Arbeit mit Dichtefunktional-Theorie (DFT) Rechnungen as Werkzeug, um verschiedene Materialeigenschaften zu erforschen und zu verstehen, und Schichtherstellung mit Magnetron-sputtering um reale Schichten zu untersuchen.

Eine experimentelle Studie von (Al, Cr, Nb, Ta, Ti)N-Dünnschichten zeigt großes Potential für Addition von Si, um die Schichten zu verbessern. Der Si-Einbau führt zu höherer Härte und geringerem E-Modul durch Kornverfeinerung, verbessert the Phasenstabilität im Vakuum, und verbessert die Oxidationsbeständigkeit bei 850 °C enorm, indem es die gebildete Oxidschicht verdichtet. Dieses Oxid ist eine einphasige feste Lösung in Rutil-Struktur trotz der Gegenwart von Al, und ist bei hohen Temperaturen stabilisiert durch die Konfigurationsentropie, wie mit DFT berechnet wurde.

Der Einfluss der Sputtergaszusammensetzung auf die Schichteigenschaften wurde im System (Al, Mo, Ta, V, W)N untersucht. Zwei Nitridschichten mit verschiedenen N-Leerstellenkonzentrationen und eine Oxynitridschicht wurden abgeschieden. Dabei zeigen sich sehr verschiedene Mikrostrukturen und Texturen, welche sich auch in der Härte wiederspiegeln. Vor allem die N-arme Schicht zeigt eine hohe Härte und gute Phasenstabilität. Die Oxynitrid-Schicht besitzt auch eine hohe Härte im abgeschiedenen Zustand, aber beim Vakuumglühen reißt die

Schicht auf durch Bildung binärer Oxidphasen mit großen spezifischen Volumina, was zu fast vollständiger Oxidation führt.

Der Einbau von Bor in ein Nitrid wurde in (Hf, Ta, Ti, V, Zr)-B-N untersucht. DFT Rechnungen zeigen eine starke Präferenz für die NaCl-Struktur mit guten mechanischen Eigenschaften. Reaktives Sputtern von solchen Metallbornitrid Schichten führt zu einem Phasengemisch mit amorphem BN und geringer Härte, aber nicht-reaktives Sputtern führt zu einer einphasigen, flächenzentriert kubischen Schicht mit bis zu 46 GPa Härte und thermischer Stabilität bis zu 1200 °C. Das zeigt das große Potential von gemischten Nichtmetall Untergittern in keramischen Hoch-Entropie Materialien.

Die Bedeutung der Konfigurationsentropie auf die Phasenstabilität von Hoch-Entropie Materialien wird oft behauptet, wurde aber noch nie quantifiziert. In einer Hochdurchsatz DFT Studie wurde das Gegenspiel von enthalpischen und entropischen Beiträgen auf die Phasenstabilität von 126 Kombinationen von equimolaren Al-enthaltenden Hoch-Entropie-Untergitter-Nitriden untersucht. Alle Zusammensetzungen sind metastabil mit 0.10-0.27 eV/at Enthalpie-getrieber Triebkraft zur Entmischung, unter anderem verursacht durch Bildung von AlN in Wurtzit-Struktur. Die Entropiestabilisierung bei 1073 K beträgt nur ≈-0.06 eV/at, zu wenig, um die Enthalpie-getriebene Zersetzung aufzuhalten. Stattdessen führt Verzerrungsenergie, verursacht durch die großen Volumenunterschiede zwischen Edukt- und Produktphasen, zur Stabilisierung von 22 Zusammensetzungen. Die Berechnungen zeigen gute Übereinstimmung mit Röntgendiffraktion und Atomsondentomographie von vier geglühten Nitridschichten. Diese Studie zeigt, dass Konfigurationsentropie nicht generell zur Stabilisierung von keramischen Hoch-Entropie-Materialien führt, aber Verzerrungsenergien offenbaren eine alternative Route für Materialdesign, die bisher noch nicht für Hoch-Entropie Materialien verwendet wurde.

Contents

CHAPTER 1

Introduction

The first metal discovered by humankind is believed to be gold, which is the only metal that can be found in pure state in nature and does not corrode under normal conditions. Due to its softness it had no technical purpose until very recently, when applications in microelectronics were found. Instead, it was used for decoration throughout millennia. Its extremely high malleability and corrosion resistance allowed the production of very thin and chemically durable sheets that were used to adorn vases, talismans, burial objects, and many other ceremonial goods. The process of applying coatings is therefore many thousand years old and gold is the first material used by mankind for this purpose. The production and science of thin films has come a long way since then. In the eighteenth and nineteenth century, electrodeposition and sol-gel processes (from liquid solutions), and sputtering and arc deposition processes (from the gas phase) were invented for film growth. The first coatings obtained from the gas phase were usually metal oxide films due to poor vacuum conditions. With the development of better vacuum pumps and analytical tools, the growth conditions could be improved and fundamental understanding of thin films could be attained. [1]

Nowadays, coatings are paramount in enhancing the properties of bulk materials. Every object comes into contact with its surrounding by the surface. Thin films can modify this surface to improve the appearance, or protect from wear, corrosion, and provide diffusion barriers. The advantage of thin films over bulk materials thereby is the small quantity that is required for full functionalisation of the surface. In addition, through the high cooling rates (typically $\sim 10^6\,\mathrm{K/s}$)

during transition from the gas to the solid phase, physical vapor deposition (PVD) allows the kinetically controlled synthesis of meta-stable materials, which are not attainable by conventional metallurgy. The atomic bombardment also introduces many point defects in the crystal lattice that improve the mechanical strength of PVD materials. By adjusting the deposition parameters, the coating properties can be tweaked to the desired purpose. Thin films increase the productivity and decrease material consumption, therefore they improve the economic and ecologic efficiency of many processes. [1, 2]

One important branch of such processes is the cutting tool industry. Cutting tools require a hard edge, need to resist wear and oxidation, and need to hold these properties at high temperatures and loads that arise from the cutting process. Different ceramic hard coatings have been developed to protect the cutting tools and increase their lifetime, a large group of these coatings are formed by so-called transition metal nitrides. The first generation of protective coatings was formed by TiN, which crystallizes in the face centered cubic (fcc) NaCl structure and can be deposited either with PVD or chemical vapor deposition. While the tool-lifetime was improved by such a protective coating, the coating itself soon yielded during machining due to softening and oxidation. The processes behind this failure are defect annihilation at elevated temperatures, and oxidation, since Ti does not form a dense protective oxide scale. These weaknesses were amended by the next generation of nitride coatings, which rely on the incorporation of Al in the fcc lattice and are still dominating the market: $(Al, Ti)N$, or $(Al, Cr)N$. The benefit of Al-incorporation is twofold, on the one hand Al forms a dense oxide, so that the $(Al, Ti)N$ offers in-situ protection against oxidation. On the other hand, the stable crystal structure of AlN is the hexagonal wurtzite structure. With PVD, Al can be meta-stably forced into the cubic lattice up to an Al content of $\sim 60 - 70\,\text{at}\%$ on the metal-sublattice. At high temperatures, where relaxation processes set in, $(Al, Ti)N$ undergoes spinodal decomposition, where at first AlN forms coherent cubic-phased domains. The different lattice parameters from AlN and TiN cause strain fields that increase the hardness, this effect is called age-hardening. Only at a later stage of decomposition is the AlN transformed into its stable wurtzite structure, ultimately leading to deterioration of the mechanical

properties. The demand for increased productivity pushes the research activity to improve the properties of thin films beyond coatings like (Al, Ti)N to allow higher cutting speeds and decrease process downtime. [3–7]

The concept of alloying different elements is paramount to the success of modern materials. For large spans of the past, humankind used pure copper for metalworking. With the advent of the bronze age, alloying was devised, allowing for lighter and sturdier tools. In the same fashion the performance of PVD TiN was improved by Al-alloying. With progressing time and production methods, more refined materials have become available. Nowadays we possess access to a huge variety of materials, but until the very recent history they all shared a commonality: The materials consisted of a main component, like copper for bronze or iron for steel, whose properties can then be tuned by alloying. In all these cases, the characteristic properties of the material are still determined by the main component. [8]

This paradigm was abandoned in 2004, when two independent research groups, lead by Cantor [9] and Yeh [10], individually developed the concept of what will be referred to as "high-entropy" materials in this thesis. By alloying 5 different metals in equiatomic ratios, a new material class was devised, which is characterized by its lack of a main component. Instead, the properties are governed by 4 "core-effects": The high configurational entropy, severe lattice distortion, sluggish diffusion, and the so-called cocktail-effect. [11]

Since high-entropy materials show properties like higher hardness, toughness, thermal stability, and oxidation resistance, compared to conventional alloys, they are prime candidates for development of protective hard coatings. The biggest challenge that the high-entropy community is facing today, is the selection of elements to combine. The number of possible combinations N that can be formed out of C components, where each alloy differs in composition by $x\%$, is $N = (100/x)^{C-1}$. For 40 elements and a difference in composition between alloys of 1 %, $N = 10^{78}$. When we relate this number to the estimated number of atoms in our galaxy, 10^{66}, the magnitude of the problem becomes clear. Experimental research is not capable of dealing with so many possibilities systematically. We therefore need methods to sort this vast phase space beforehand. One of the most

important tools is a chemist's gut feeling, which elements could lead to desired properties and pair up well with other elements. This is of course only a first step. By using computational screening methods, more refined results can be obtained. Density Functional Theory (DFT) calculations allow the prediction of properties on atomistic scale. It is therefore a useful method to investigate the relationships between elements in high-entropy materials. For this reason, DFT was chosen as a computational tool to investigate properties like phase stabilities or mechanical properties of different element combinations. With this guide, interesting compositions where then investigated experimentally. This thesis is therefore focused on a combinatorial methodology of computational and experimental investigations. [8, 11]

CHAPTER 2

High-Entropy Materials

In this chapter, the history and current understanding of fundamental properties of high-entropy materials are reviewed.

2.1 Recent Developments

High-entropy materials have developed into a highly active research topic over the last few years. A Scopus [12] search with the search term "high-entropy AND alloy" shows an exponential-like increase of publications from 2004, when the pioneering work by Yeh et al. [10] and Cantor et al. [9] was published, to 1485 entries in 2020. In the first years after 2004, only a few dozen publications on this topic appeared each year, but after 2012 the pace picked up rapidly with more than 100 yearly publications. Among the works on High-entropy alloys (HEA), the so-called "Cantor-alloy" CrCoFeMnNi takes a very prominent place.

The exploration of ceramic high-entropy materials lags behind the development of metallic alloys in number of publications, but has proven its potential for great properties multiple times. The search term "high-entropy AND ceramic OR nitride OR oxide OR carbide OR boride" yields much fewer entries in Scopus. The first two publications on nitride coatings by Chen et al. [13, 14] followed shortly after the first studies on HEA, but after that, high-entropy sublattice ceramics (HESC) were considered only by few people until very recently. Only for 2018 onwards, does the Scopus search for ceramics turn up more than 100 entries,

in 2020, 406 publications are reported, but many of these are false positives and actually studies on metallic HEA.

The vast majority of works in the field of HESC concerns nitride (HESN) coatings, studying the influence of metal composition, substrate temperature, bias, or N_2 flow rate on the coating properties. Nitrides stand in the focus due to their ease to deposit from metallic targets in the simple fcc NaCl-type structure by reactive PVD techniques, and their usefulness in protective applications as hard coatings, often reaching between 30 and 40 GPa in hardness. Nitrides have also been tested as diffusion barrier from 2008 onward [15], showing promising results due to the proposed sluggish diffusion.

First high-entropy sublattice oxide (HESO) coatings were deposited in 2007 [16] and 2010 [17], but oxides received little attention afterwards. Only in the last few years was the development of new oxides accelerated and HESO were synthesized in many different structures like the NaCl [18], spinel [19], fluorite [20], rutile [21], or perovskite [22] structure. Many studies on HESO are motivated by electric, thermal, or catalytical applications (see [23] for an overview). The highest reported hardness in HESO is 24 GPa in a rutile-structured $(Al, Cr, Nb, Ta, Ti)O_2$ coating [21].

Boron as additive in HEA was already studied by Lee et al. in 2007 [24], but the development of ceramic high-entropy sublattice borides (HESB) took as long as 2016 [25] (in bulk). Two diboride coatings, forming the hexagonal AlB_2-type structure, have been published in the meantime [26, 27], with reported hardness values above 45 GPa. Therefore, HESB still represent a very unexplored terrain.

Carbon was considered as constituent in HEA from 2009 on [28], forming carbide precipitates in similar fashion as in steel. Dedicated High-entropy sublattice carbides were developed in 2012 [29] as biocompatible coatings, but research on this topic picked up the pace as late as 2018 [30–33], among these also a high-throughput study [34]. The hardness of these carbide coatings depends strongly on crystallinity and deposition conditions, so that values between 22 and 48 GPa [35] have been reported so far.

Mixed ceramic classes are still a rarity, only two high-entropy sublattice carbonitride [36, 37], and an oxynitride coating [38] have been reported so far.

Other investigated ceramic classes include silicides [39, 40], selenides [41], and sulfides [42], the exploration of which has barely begun.

Research activity is not only expended on the synthesis of new high-entropy materials, but also on their fundamental principles. This includes research on the actual impact of the core-effects, which will be outlined in Section 2.4, and efficient methodologies to screen for optimal compositions, see Section 5.7 for a detailed overview from computational perspective. Many questions around high-entropy materials are still unsolved and this topic will accompany materials scientists for many years to come.

2.2 Definition

Cantor [9] and Yeh [10] called their findings in 2004 "equiatomic multicomponent alloys" and "high-entropy alloys with multiple principal elements", respectively. Other names like "compositionally complex materials" [43], or "concentrated complex alloys" [44] are also in use. A widely accepted nomenclature for such materials does not exist yet, since the impact of the high-entropy effect in such materials is disputed [44]. A pragmatic naming convention should be clear, concise, unambiguous and easy to pronounce. However, many of the currently disseminated options are imprecise or ambiguous. While Cantor was definitely right to call his $Co_{20}Cr_{20}Fe_{20}Mn_{20}Ni_{20}$ alloy an "equiatomic multicomponent alloy", this name is excluding any composition that deviates from that strict compositional rule. Many studies have shown that the high-entropy effect is also present in near-equiatomic compositions, therefore this name is not useful for a general classification. "Compositionally complex materials" on the other hand is a very broad term and can be understood very differently by different researchers. Anything consisting of several comprising elements, single-phase or multi-phase, ordered or disordered, could be encompassed by such a definition, and the properties of such defined materials can vary significantly. Different requirements like possible multi-phase structures, a lower number of constituting elements compared to high-entropy materials, or concentrations below 35 at% for each component have been formulated [45–48]. These definitions are difficult to

reconcile, but the intention of the researchers is presumably to stake out materials that exhibit much higher degrees of disorder than classical alloys like for example steels, but do not meet the strict requirements of high-entropy materials (see below). "Multi-principal element alloys" is also not a precise term, since in a strict sense even a simple TiN consists of multiple (more than one) principal elements. Therefore, the term "high-entropy" material will be used throughout this thesis where applicable, since it clearly states the aim of reaching a high configurational entropy – necessarily within a single phase – which is directly linked to the properties that we look for in such materials. It is also a short name, both easy to remember and to pronounce.

High-entropy materials can be classified based on their composition or the entropy S. The first composition-based definition by Yeh [10] stated, that a high-entropy alloy needs to consist of 5 or more principal elements with concentrations between 5 and 35 at% each. This definition is however not consistent, as for 5 elements it allowed a maximum configurational entropy of $1.61 \cdot R$, $R = 8.314\,\mathrm{J/Kmol}$ being the gas constant, and a minimum configurational entropy of $1.36 \cdot R$, which can be topped by an equimolar 4-component alloy with $S_{conf} = 1.39 \cdot R$. Additionally, this definition is not restricted to single phase materials, which would reduce the configurational entropy even further. On the other hand, an equiatomic alloy with 25 metals would yield a very high configurational entropy and thus properties expected of a high-entropy material, even though each metal would only amount to 4 at%. So this composition-based definition alone is insufficient.

The issue of defining high-entropy materials can be resolved by taking the entropy directly into account. The first entropy-based definition used the configurational entropy of single-phased, equiatomic two-element and five-element alloys as thresholds, to classify materials into low-entropy ($S_{conf} < 0.69 \cdot R$), medium-entropy ($0.69 \cdot R \leq S_{conf} < 1.61 \cdot R$), and high-entropy materials ($S_{conf} \geq 1.61 \cdot R$) [11]. A more pragmatic solution was devised by combining the two classification methods. As a result, a minimum configurational entropy of $S_{conf} \geq 1.5 \cdot R$ defines a high-entropy, $1 \cdot R \leq S_{conf} < 1.5 \cdot R$ a medium-entropy, and $S_{conf} < 1 \cdot R$ a low-entropy material. This definition is elegant and useful as it

takes into account the single-phase nature of a high-entropy alloy, excludes alloys with less than 5 main components, and tolerates small deviations from equiatomic compositions. For a single-phased material with 5 components, this means that the concentration of each component must be between 10-30 at%. This definition is also convenient in PVD, where exact stoichiometric compositions are very difficult to realize. [26, 44]

Whatever definition is chosen to classify high-entropy materials, one should be wary of dogmatic conventions. Every classification method should only be viewed as a guideline, especially since the limits were chosen arbitrarily (or, presumably, for their round numbers). For example, two similar materials with $S_{conf} = 1.49 \cdot R$ and $S_{conf} = 1.51 \cdot R$, respectively, will behave only slightly different and the relevant properties will likely be found in both. Ultimately, the exploration of interesting materials should stand above all these considerations. [44]

The high-entropy effect in metallic alloys can also be achieved in ceramics like nitrides, oxides, carbides, and borides. In this case, binary ceramics like TiN, Al_2O_3, TaC, or ZrB_2 take the place of metals so that the configurational entropy is stored only in the metal sublattice, while the non-metal sublattice remains usually unchanged. When applying the same definition as for metallic alloys, such a material would not be considered high-entropic, since a large fraction of the atoms are positioned on well defined places. For a high-entropy nitride with 1:1 stoichiometry and with 5 metals on one sublattice and full occupancy of the non-metal sublattice with N, the maximum configurational entropy would be only $\sim 0.8 \cdot R$. However, the very essence of high-entropy materials is the absence of a dominating solvent in a solid solution. The special properties that are summarized in the core-effects (Section 2.4) result from this circumstance, and this relationship also applies to ceramics. In Figure 2.1, two crystal lattices, calculated by DFT, are compared: a binary nitride a), and a high-entropy sublattice nitride b). This simple calculation visualizes the local lattice distortion, where even the N atoms do not have ideal fixed places. Moreover, many studies of such ceramics demonstrate the success of the high-entropy concept in such materials. It is therefore fitting to adjust the definition of high-entropy ceramics by relating the configurational entropy to the binary ceramics instead of elements, therefore

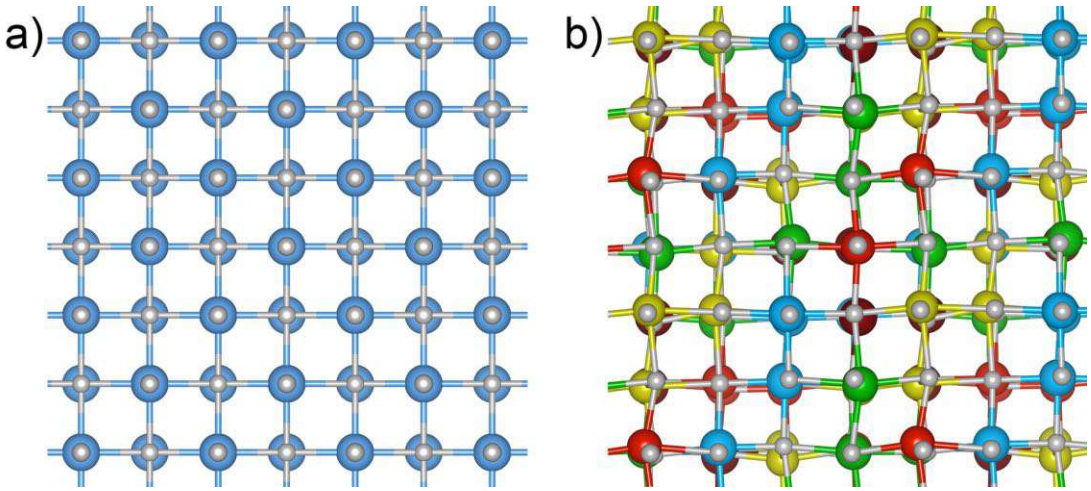

Figure 2.1: Comparison of (0 0 1) crystal lattice planes of a binary nitride a), and a high-entropy sublattice nitride b). The shown structures are fully relaxed cells from DFT calculations.

the entropy has to be defined per formula unit instead of per atom [49]. This method is convenient, since we can use the same numerical value for different stoichiometries in ceramics to classify a high-entropy material. Pursuing the aim of a concise and unambiguous nomenclature, these ceramics will therefore be referred to as "high-entropy sublattice ceramics" throughout the thesis.

2.3 Thermodynamics of High-Entropy Materials

Ludwig Boltzmann defined the entropy of a system by statistical thermodynamics:

$$S = k_B \ln w\,, \tag{2.1}$$

where S denotes the entropy of a closed macroscopic state in thermodynamic equilibrium, $k_B = 1.380\,649 \cdot 10^{-23}\,\mathrm{J/K}$ the Boltzmann constant, and w the number of micro-states that exist for the given macro-state. Look for example at the nitrides in Figure 2.1: In the perfect TiN crystal, there is only one possible microstate, since each atom has its determined place. But in the HESN the same macrostate (the configuration of atoms) can be achieved in multiple possible ways by exchanging certain metal atoms. Statistically, the configuration of such

a mixture of nitrides as HESN is more likely than the formation of separated domains of each individual nitride due to the number of involved microstates. Thus the entropy stabilization can be understood intuitively from statistical thermodynamics. To predict the phase stability of an alloy system against its constituents, the Gibbs free energy of mixing can be calculated as

$$\Delta G_{mix} = \Delta H_{mix} - T\Delta S_{mix}\,, \tag{2.2}$$

where ΔG_{mix} is the Gibbs free energy of mixing, ΔH_{mix} the enthalpy of mixing, T the absolute temperature, and ΔS_{mix} the entropy of mixing, calculated from the configurational entropies of the reactants. To reach the necessary condition for phase stability, $\Delta G_{mix} < 0$, either ΔH_{mix} must be negative, or $T\Delta S_{mix} > \Delta H_{mix}$, if ΔH_{mix} is positive. For a constant ΔH_{mix}, a larger ΔS_{mix} results in a higher stability of the material. When dealing with HESC, the disorder is usually contained only on a sublattice, the configurational entropy is therefore often considered per formula unit instead of per atom. The ideal configurational entropy, S_{conf}, is

$$S_{conf} = -R\sum_i X_i \ln X_i\,, \tag{2.3}$$

where R is the gas constant, and X_i the molar concentration of the ith component. In the case of an equiatomic solid solution of N constituents, the mixing entropy is maximized and Equation 2.3 can be simplified to

$$S_{conf} = R\ln N\,. \tag{2.4}$$

For solid solutions with 1, 2, 3, 4, and 5 components the configurational entropy is 0, 0.69, 1.10, 1.38, and $1.61 \cdot R$, respectively [8, 50]. In the case of a mixed metal- and nonmetal-sublattice, the convention of considering S_{conf} per formula unit instead of per atom is not applicable anymore. S_{conf} then needs to be calculated separately for each sublattice:

$$S_{conf} = -R\left(\sum_{j=1}^{J} a^j \sum_{i=1}^{N} X_i^j \ln X_i^j\right) \Bigg/ \sum_{j=1}^{J} a^j\ , \tag{2.5}$$

where a^j is the number of sites on the jth sublattice and X_i^j is the concentration of the ith element on the jth sublattice. For ceramics, the total number of

sublattices J is usually 2, and their relative weight depends on the stoichiometry. In a HESN with perfect non-metal sublattice, the total S_{conf} needs to be divided by two since only half the atoms contribute to configurational entropy. In a rutile structured oxide with metal:nonmetal ratio of 1:2, the relative frequency of metal and non-metal sites leads to a correction factor of 1/3 and 2/3 for each sublattice, respectively. [44]

The description in Equation 2.3 is idealized, since it presumes chemically different but equal-sized atoms, which are placed on the lattice sites. In reality, different chemical species have different sizes, so that the hereby distorted lattice increases the uncertainty of positions to an important extent. That atom sizes are usually scaled down in displays of crystal structures for better visibility only adds to this confusion. Excess terms for the total molar entropy by different atom sizes, atomic vibrations, magnetic moments, and electronic effects should therefore be considered as well. The configurational entropy in solid solutions is often stated to be dominating the mixing enthalpy [8, 11, 51, 52], but in the so-called "Cantor-alloy", CoCrFeMnNi, electronic, vibrational, and magnetic excitations have been reported to amount to 50 % of the configurational entropy [53]. However, this does not necessarily mean that e. g. vibrational entropy dominates the entropy change of a reaction, since educt and product phases can have very similar vibrational entropies, so that their contributions cancel each other out. Anthony et al. [54] found that the difference in vibrational entropy between the solid solution and ordered phase of Fe_3Al was about $0.1 \cdot R$. In contrast, Swan-Wood et al. [55] reported that the difference of vibrational entropies between unordered and ordered FeCr was of the same magnitude as the difference in configurational entropy. The magnitudes of the excess contributions have not been treated yet on a wider scope, which is aggravated by the complicated procedures to calculate those contributions [44]. In effect, only the ideal configurational entropy, which is accessible from Equation 2.3, is commonly used to predict phase stability in high-entropy materials.

2.4 The Four Core-Effects of High-Entropy Materials

Yeh [11] summarized the special properties that accompany high-entropy materials: (1) high configurational entropy, (2) lattice distortion, (3) sluggish diffusion, and (4) cocktail effects.

2.4.1 High Configurational Entropy

The high configurational entropy promotes single disordered phases that are composed of many elements in a solid solution. This was deduced from Equation 2.4 and by the fact, that the first investigated high-entropy alloys featured single-phase structures. It has been argued that this is counter-intuitive [11], since the Gibbs phase rule for constant pressure,

$$P + F' = C + 1\,, \tag{2.6}$$

states that in a system of C components and F' degrees of freedom (here the pressure is excluded, since its influence on solid phase reactions is usually negligible), P phases can co-exist simultaneously. For five components one can expect a maximum of 6 possible phases in equilibrium at an invariant reaction. However, the Gibbs phase rule states only the maximum number of phases that can co-exist at given parameters, and not the probability that a number of phases co-exist in reality. Observing the maximum number of possible phases is rather uncommon in both low-entropy and high-entropy alloys. Furthermore, the single-phase solid solutions in body centered cubic (bcc) or fcc structure are often reported for as-cast alloys, which can feature non-equilibrium phases as well. The importance of configurational entropy on phase stability in high-entropy alloys is therefore disputed [44, 56].

Likewise, many single phase coatings with good properties have been reported for numerous HESC [21, 23], but especially for PVD coatings, metastable phases need to be considered even more thoroughly. Several research groups claim that configurational entropy stabilizes the high-entropy phase of ceramics and thus

dominates the energy landscape. The argumentation essentially revolves around oxides [52, 57–60], but none of the studies make an effort to quantify the entropic and enthalpic contributions. Since only the metal sublattice, which makes up only 1/3 of the atoms in a MeO_2 stoichiometry, contributes to configurational entropy, this generalized claim is doubtful, given the lack of evidence.

Addressing the relationship between enthalpy and entropy quantitatively is one of the cornerstones of this thesis.

2.4.2 Lattice Distortion

Every atom in a high-entropy solid solution is surrounded by a variety of atoms with different sizes, this causes the lattice to be strained locally. An average crystalline lattice can be seen in X-ray diffraction experiments, but the different atomic sizes, bond strengths, crystal structures and the asymmetrical arrangement of the constituent elements cause the lattice to be severely distorted on atomic scale. This distortion is higher than in conventional alloys where the lattice is determined by the main component and where most atoms are surrounded mainly by their own kind.

The distorted lattice affects the hardness and strength, which are increased due to solution hardening, and also the X-ray diffraction (XRD) intensities. Yeh et al. [61] showed, that by increasing the number of elements in a solid solution from pure metals to seven elements in the system Al-Co-Cr-Cu-Fe-Ni-Si, the XRD peak intensity decreased with each added element. This was explained with the roughening of the diffraction planes caused by differently sized atoms. This distortion can also be seen in Figure 2.1, which shows a binary nitride a) and a high-entropy sublattice nitride b) after full cell relaxation in a DFT calculation. The lattice distortion affects the intensities similar to the temperature effect and can also be modeled in the same fashion.

The theoretical lattice distortion δ has been expressed using atomic radii in metallic alloys [62], or covalent bond lengths in ceramics [25]:

$$\delta = \sqrt{\sum_{i=1}^{N} X_i \left(1 - \frac{r_i}{\overline{r}}\right)^2}, \tag{2.7}$$

with X_i being the mole fraction of the ith component, r_i the size of the ith constituent (for example atomic radii in metals), and $\overline{r}$ the average size of all constituents present.

A general quantitative treatment of experimental lattice distortion is still missing for high-entropy materials, only one study [63] attempted to measure real lattice distortions from high-resolution transmission electron microscopy so far.

2.4.3 Sluggish Diffusion

Closely related to the distorted lattice, diffusion processes are slowed down considerably in high-entropy solid solutions compared to conventional alloys. High-entropy materials can be considered a whole-solute matrix, in which for example a vacancy, responsible for one of the transport mechanisms in crystals, is surrounded by different elements that compete over the vacancy. Tsai et al. [64] proposed, that the large fluctuation of lattice potential energy causes slower diffusion and higher activation energy in high-entropy materials. They found that in the system Co-Cr-Fe-Mn-Ni, the melting point normalized activation energies of diffusion for each constituent, Q/T_m, increased with each additional element that was present in the matrix, reaching the highest value in the high-entropy alloy and the lowest value in the pure metals. This was later put in perspective by Dabrowa et al. [65] who reported that the sluggishness of diffusion depended greatly on whether Mn was present in the alloy. Incidentally, this element was present in almost all diffusion studies of high-entropy alloys hitherto, leading to biased results. This dependence on Mn was explained with the low melting point of Mn, which accordingly lowered the homologous temperature that was used in the diffusion studies. The authors have therefore shown, that simply the number of elements alone does not dictate the diffusion process. These works have shed some light on the processes behind sluggish diffusion in alloys, but we still lack proper understanding of this effect. [27, 66–68]

Theoretical considerations aside, slow diffusion processes have been demonstrated in several applications of high-entropy materials. In metallic alloys, slowed down phase separation and hindered grain growth have been reported, which enable the formation and retention of nano-precipitates that

enhance mechanic properties via the Hall-Petch relationship [10, 69]. The superior high-temperature performance of different ceramic materials have also been attributed to sluggish diffusion processes. This was shown in the hardness retention and slow decomposition reactions of coatings designed for protective applications [27, 66] or for diffusion barriers for metal diffusion [67, 68, 70, 71]. While not yet sufficiently understood, sluggish diffusion therefore plays an important role in the performance of high-entropy materials.

2.4.4 Cocktail Effect

The term "cocktail effect" was coined by Ranganathan [72], and means the formation of unexpected synergies when mixing many elements together. An example of such a behavior is the phase change in $Al_xCoCrCuFeNi$ from fcc to fcc+bcc, and bcc, and the resulting increase in hardness, with increasing Al content (an fcc metal) [10]. This behavior cannot be explained from mixing rules alone and was thus attributed to such a synergistic effect [44].

CHAPTER 3

Coating Synthesis and Characterization

This chapter lays down the theoretical background of coating synthesis by reactive magnetron sputterung, and the analysis of crystal structure, microstructure, chemistry, and mechanical properties of such deposited films.

3.1 Reactive Magnetron Sputtering

Physical Vapor Deposition encompasses techniques that create thin films on a substrate by evaporating metals from a source through energetic bombardement, transporting this vapor to a substrate, and depositing the atoms on the substrate with subsequent film growth. A major advantage of PVD is its compositional versatility. The coatings are formed from atoms or ions in the gas phase, where all substances are fully miscible, which then hit a substrate with a significantly lower temperature than the gas. The very high cooling rate upon collision prevents separation of the atoms into thermodynamically favored phases. This enables the deposition of metastable compositions that are not accessible with other methods like Chemical Vapor Deposition or sintering of pressed powders. A variety of different PVD techniques are available to create hard coatings, such as cathodic arc evaporation, ion plating, or sputter deposition, of which the latter was used to deposit the coatings in this thesis.

The basic principle of sputter deposition is the ejection of atoms or ions from a source ("target") through bombardment with fast ions. The momentum transfer causes the evaporation of target atoms that travel in a linear fashion through the

vacuum until they hit either a surface with subsequent film growth, or residual gas atoms in the chamber. When the sputter or working gas (usually Ar) is mixed with a reactive gas like N_2 or O_2, a compound coating can be formed at the substrate from a metallic target, this process is then called reactive sputtering. The sputtering process is usually also aided by a magnetic field, which traps the electrons in the plasma to reach higher ionization rates for more efficient sputtering, this is then called magnetron sputtering. [2]

3.1.1 The Sputtering Process

A schematic of a reactive magnetron sputtering process can be seen in Figure 3.1. The apparatus consists of an evacuated chamber, where a source (cathode) and a substrate face each other. After pumping down to a base pressure of $\sim 10^{-4}$ Pa to remove contaminants, a noble gas, usually Ar, is introduced at a low pressure in the range of a few Pa. By applying a strong voltage difference between cathode and anode, some electrons can follow the electric field gradient due to their low mass, leaving their comparatively inert nucleus with the rest of its electrons behind. The sputter gas is thus ionized. The freed electrons move towards the anode and the formed cations move towards the cathode. Impact excitation with freed electrons heats the gas and causes it to glow due to atomic excitation and relaxation, hence a visible plasma with a characteristic color (blue for Ar, red-pink for N_2) is formed. This is called a glow discharge. When ions or neutral atoms hit the cathode surface with high velocity, the kinetic energy is imparted onto the cathode material. This causes atoms to be ejected from the cathode, the ejected atoms then travel linearly through the chamber until collision occurs. At the substrate, the sputtered particles condensate and grow a film. The film growth can also be assisted by applying a negative bias potential relative to the chamber walls to the substrates, which increases the kinetic energy of inbound ionized species. [2, 73]

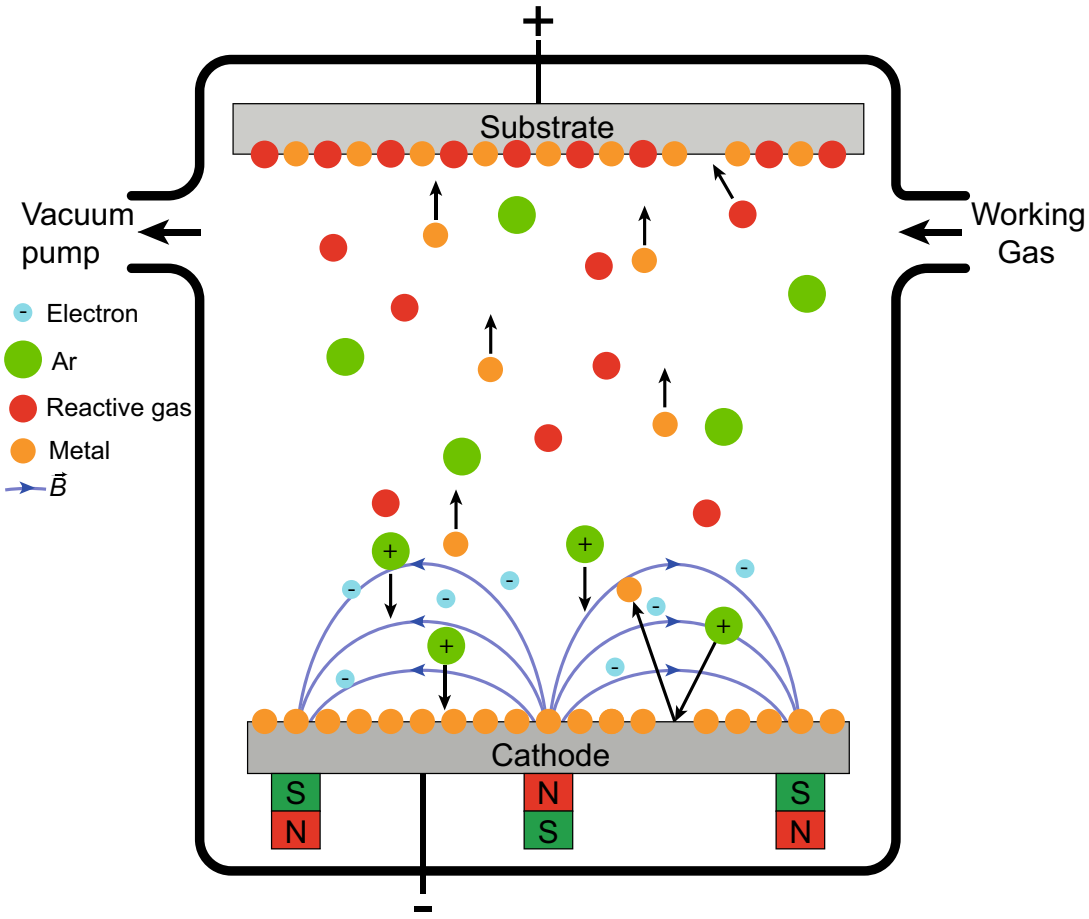

Figure 3.1: Schematic of a reactive magnetron sputtering process. Adapted from [2] and [74].

3.1.2 The Magnetron

In a glow discharge, the electrons needed to sustain the discharge by impact ionization of the working gas move towards and disappear into the anode, where they are lost for the sputtering process. To increase the ion concentration and thus the sputter yield, either the voltage difference, or the pressure needs to be increased. A higher voltage difference leads to an electron flux with higher power density, resulting in significant heating at the substrate. A higher pressure on the other hand would lead to more scattering events of the sputtered particles, reducing at first the kinetic energy (critical for film growth, see Section 3.1.5) and at higher pressures also the flux of the sputtered particles due to bounce-back

events, diminishing the growth rate. Both approaches therefore work only within narrow limits, which restricts the usefulness of pure glow-discharge sputtering. This can be remedied by magnetic fields.

In an electric field the electrons are accelerated towards the anode. By applying an additional magnetic field, the electron trajectories are modified by the Lorentz force,

$$\mathbf{f} = q(\mathbf{e} + \mathbf{v} \times \mathbf{b_m}), \tag{3.1}$$

where $\mathbf{f}$ is the Lorentz force acting on the electron, q the electron's charge, $\mathbf{e}$ the electric field, $\mathbf{b_m}$ the magnetic field, and $\mathbf{v}$ the velocity of the electron. The Lorentz force is perpendicular to $\mathbf{v}$ and $\mathbf{b_m}$, forcing the electrons in a spiraling motion. The most common type of magnetrons are planar magnetrons (see Figure 3.1), where the magnet is positioned behind the cathode. It consists of a central disk magnetic pole and an annular pole surrounding it, resulting in circular field lines. In this setup, the Lorentz force constrains the electrons into the area between the two magnetic poles. This is hence where the discharge plasma (the ionized Ar) is sustained and where the sputtering events are concentrated. This leads to circular erosion tracks on the target, often referred to as "racetracks". With this trapping effect, magnetron sputtering leads to a higher electron density in the discharge, more impact ionization events, and thus a higher ion concentration. The increased ionization efficiency enables a reduced operating pressure at the same erosion rate. Consequently the sputtered atoms suffer fewer collisions and reach the substrate with more energy, allowing for higher deposition rates and denser coatings. [2]

3.1.3 Reactive Sputtering

Depending on the cathode material, several methods of powering the magnetron are possible, the easiest way is using a Direct Current (DC) power supply. When possible, metal cathodes are the preferred choice over ceramic materials since they are conductive (thermally and electrically), easy to process, and insusceptible to shock, whereas ceramic cathodes are often not conductive and break easily. In general, metallic targets can therefore be operated with higher power densities than ceramic targets. In pure Ar, this limits the choice of materials for depositions

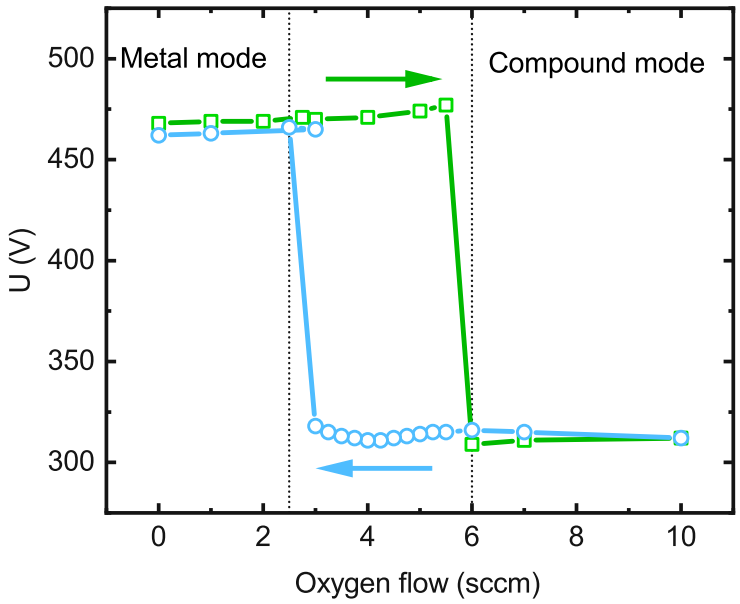

Figure 3.2: Hysteresis of the discharge voltage caused by target poisoning with oxygen. When the O_2 partial pressure is raised above a certain threshold, the target surface is fully oxidized, and the sputter rate collapses. Removing this poisoning requires a much lower O_2 partial pressure than the initial poisoning threshold. In metal mode, high deposition rates are achieved, but coatings may end up understoichiometric. In compound mode, stoichiometric coatings can be deposited, but at low deposition rates. Data provided courtesy of Stefan Kagerer (TU Wien).

to metallic films. By mixing the sputtering gas with a reactive gas like N_2, O_2, or Acetylene, compound thin films like nitrides, oxides, or carbides can be deposited from metallic cathodes. The presence of a reactive gas increases the complexity of the sputtering process. This is most notable in the so-called poisoning effect (Figure 3.2).

When the partial pressure of the reactive gas is increased step-wise, the discharge voltage decreases sharply above a certain threshold value. When decreasing the partial pressure again, the original voltage is reached only at a much lower partial pressure than the threshold pressure from before, thus a hysteresis is formed. With low oxygen flow the deposition rate is high, but the coatings are often not stoichiometric compounds, this region is defined as "metal mode". In the high oxygen flow rate regime the coatings are stoichiometric compounds, but the deposition rate is low, this region is called "compound

mode". The influence of the reactive gas on the formation of the hysteresis has been modeled with chemisorption on the substrate surface [75] and reactive ion implantation at the target [76, 77] to understand this behavior. At low partial pressures, the impact of the reactive gas is low, since it is completely consumed by the deposited metal atoms on the substrate. When the partial pressure increases, the surface region of the target becomes oxidized by chemisorption of the reactive gas. This reduces the sputter yield since the compound has a higher surface binding energy. Therefore less metal is sputtered and more reactive gas is available for target poisoning. This quickly leads to complete coverage of the target and substrate surfaces and the sudden drop in discharge voltage. To free the target surface from the compound material, the partial pressure needs to be reduced well below the critical flow for target poisoning since the sputter yield of the compound is much lower than for the metal. [2]

The coatings presented in this thesis were all deposited with a modified Heraeus Leybold Z400 magnetron sputtering system in DC mode, using powder metallurgically prepared 75 mm-targets with Ar as working gas, often mixed with N_2 for reactive depositions.

3.1.4 Nucleation and Film Growth

Film growth is a competitive process between adsorption and re-evaporation of adsorbed species, especially so in the early stages of deposition, when nuclei are small with large surfaces and thus the boiling points of all species are reduced. For a film to grow, adsorbed species must meet by surface diffusion and form stable nuclei, which are more likely to grow than to dissociate. One critical parameter for this stability is the size of the nucleus. The principle can be exemplified by the homogeneous nucleation of a spherical particle with radius r, for example of ice in water below the melting point at 0 °C. In this regime, the Gibbs free energy per unit of volume, ΔG_V, is lower in the solid phase, so that the formation of a three-dimensional solid volume leads to a decrease in overall free energy. But to form this volume, a two-dimensional surface area has to be created as well, which has a high energy due to unsaturated bonds. The change in free energy of

a spherical cluster in a homogeneous medium is

$$\Delta G = 4\pi r^2\gamma - 4/3\pi r^3 \Delta G_V\,, \tag{3.2}$$

with γ being the interfacial energy per unit area. The first term describes the surface penalty, the second term the energy gain by the volume. By solving $d(\Delta G)/dr = 0$, the critical cluster size r^* and the nucleation activation barrier ΔG^* can be calculated by

$$r^* = -2\gamma/\Delta G_V \tag{3.3}$$

and

$$\Delta G^* = 16\gamma^3\pi/3(\Delta G_V)^2\,. \tag{3.4}$$

When abstracting from the geometry-related factors, the relationships $r^* \propto \gamma/\Delta G_V$ and $\Delta G^* \propto \gamma^3/(\Delta G_V)^2$ become visible. For a growing nucleus the energy penalty from the surface is initially larger due to a large surface/volume ratio, so that small clusters rapidly dissociate again. Only in a larger particle does the energy benefit from the volume compensate the surface energy, since the volume energy is proportional to r^3, whereas the surface grows proportional to r^2. A small nucleus is therefore unstable and can dissociate. Only when the critical radius r^* is exceeded, does further growth of r decrease ΔG, so that further growth is favorable and the nucleus becomes stable. This is demonstrated in Figure 3.3.

From the first and second law of thermodynamics it follows, that $\Delta G_V \propto T_d$, T_d being the deposition temperature, in further consequence $r^* \propto 1/T_d$, so that at higher temperatures stable nuclei are easier formed. Film growth always entails random surface diffusion of species. At high temperatures the mobility of adatoms is higher, so that the free mean path of adatoms is larger, leading to fewer but larger clusters.

Three different models have been formulated for the actual film growth on substrates: The three-dimensional island growth by Volmer-Weber, where clusters develop into islands that subsequently coalesce into a continuous film, is prevalent where bonds between adatoms are stronger than bonds to the substrate (for example metals on SiO_2). The two-dimensional Frank-van der Merwe growth, where each layer is completed before starting the next one, is governed by

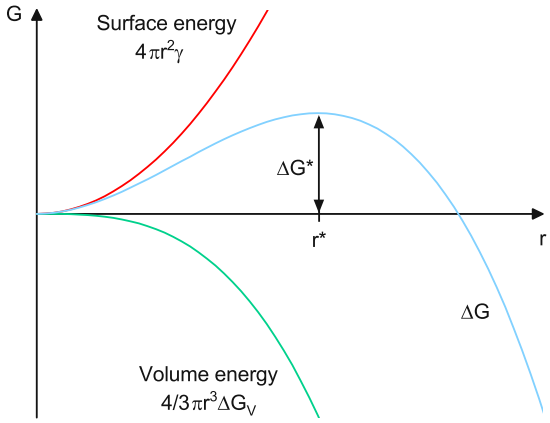

Figure 3.3: Energy cost for formation of a spherical cluster from homogenous nucleation with radius r, r^* is the critical radius. Adapted from [2].

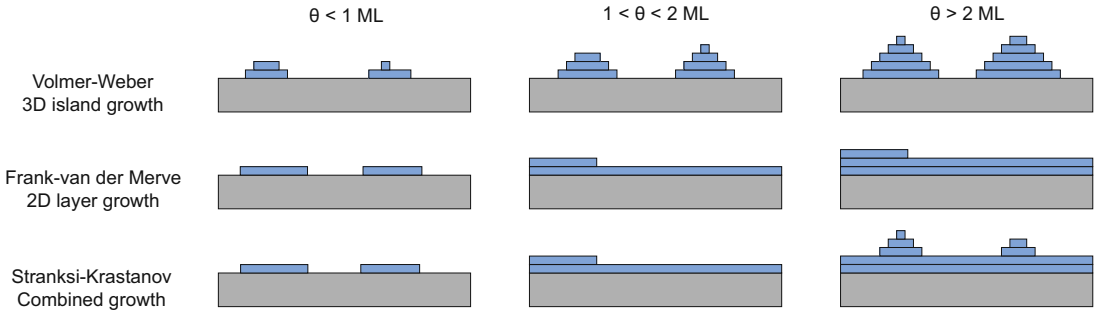

Figure 3.4: The three film growth models for different surface coverage levels θ in monolayers (ML). Adapted from [2].

weaker adatom-adatom bonds than to the substrate. It is the obvious path for homoepitaxial films such as Cu on Cu, but can also be seen in heteroepitaxial films. In heteroepitaxy however, the inevitable lattice mismatch leads to increasing strain energy with growing film thickness, triggering relaxation processes such as misfit dislocations above a certain threshold. Another relaxation process is the third growth mode, developed by Stranksi and Krastanow, where the initial growth of one or two monolayers is superseded by island growth. The transition is caused by the growing strain energy, so that after a few monolayers the surface energy for formation of islands (which have space to relax perpendicular to the growth direction) is smaller than the strain energy penalty of the next continuous layer. This is a common occurrence in PVD films. For a graphical representation of the three models see Figure 3.4. [2, 78]

3.1.5 Structure Zone Model

As shown in the previous paragraphs, nucleation and film growth are influenced by several parameters, giving rise to different evolving microstructures in PVD coatings. Since the microstructure influences the properties of the grown film tremendously, the impact of deposition parameters on the microstructure has been summarized in different structure zone models (SZM). The first SZM by Movchan et al. [79] distinguished three different zones of growth in thermal evaporation processes in dependence of the homologous temperature $T_h = T_d/T_m$, with T_d and T_m as the deposition temperature and melting point, respectively. The homologous temperature is used to simplify comparisons between different species, which have different diffusion speeds that correlate inversely with the melting point (itself a measure for bond strength). The different zones evolve due to qualitatively different adatom mobilities. In zone 1 ($T_h < 0.3$), the adatom mobility is low, which leads to continued nucleation of grains with little transport between them. This leads to fine fibrous crystallites with many defects and voids at the grain boundaries, also due to shadowing effects of growing crystallites. In zone 2 ($0.3 < T_h < 0.5$), surface diffusion leads to uniform columnar grains, the voids between grains can be filled up by mobile adatoms, and at higher temperatures, the grain size increases. In zone 3 ($T_h > 0.5$), bulk diffusion enables recrystallization, leading to dense films with large grains and few defects. Since point defects and grain boundaries improve the strength of PVD coatings considerably, zone 3 coatings are typically less hard.

The SZM was refined by Barna et al. [80], introducing a transition zone T ($0.2 < T_h < 0.4$) between zone 1 and 2. In this region, surface diffusion is possible, but still restricted to grain boundaries. This results in competitive grain growth where some grains overgrow others, leading to V-shaped crystallites. The grain size is very small near the substrate, and increases throughout the film. In this zone, the grains are still small, but compact, which is ideal for mechanical properties.

Deposition pressure was introduced as a further parameter in sputtered coatings by Thornton [81]. At low pressure, sputtered particles suffer no or few collisions on their journey to the substrate, so that they impinge with most of

their initial kinetic energy, usually several eV. This energy is sufficient to promote adatom arrangement. At higher deposition pressures, sputtered particles lose most of their energy due to collisions, so that the kinetic energy on impingement is greatly reduced. As such, the pressure can be understood as a parameter for kinetic effects. This SZM was modified by Messier et al. [82], who replaced the pressure axis with an ion energy axis. However, this parameter does not encompass different ionization ratios or time-inhomogeneous energy distributions (like in pulsed bias depositions), which influence the microstructure significantly.

Anders [83] proposed an extended structure zone diagram that includes plasma and ion effects, to generalize the deposition parameters as much as possible (see Figure 3.5). He extended the homologous temperature to a generalized temperature, $T^* = T_h + T_{pot}$, encompassing also the temperature shift caused by the potential energy of arriving particles. This includes heat of sublimation, cohesive energy, and ionization energy. The linear pressure axis was replaced by a logarithmic axis of normalized energy, E^*, which contains displacement and heating effects by kinetic energy of the impinging particles. The third axis shows the net film thickness t^*, thus visualizing thickness reduction due to densification and resputtering. In this SZM, each zone extends into the previous zone at lower T^* and high E^* due to kinetically enabled adatom mobility. When increasing the temperature, the film thickness decreases from zone 1 up to zone 3 due to increasing densification of the film. This is most pronounced between zone 1 and T, where the majority of pores is filled. With increasing E^*, the film thickness is on one hand reduced due to densification – again most pronounced in zone 1, which transitions into a denser low-T^* zone T at high E^* – but on the other hand also by resputtering of already deposited material. Since ionization yields in magnetron sputtering are typically low, the E^* axis is more important for techniques that ionize a large portion of the sputtered atoms like High-Power Impulse Magnetron Sputtering or Arc Evaporation. Particle bombardment with high kinetic energy causes atomic displacement and defects, which competes with temperature-driven annihilation processes. This can be seen in the low-T^*-high-E^* zone 3, where the columnar structure of zone 2 is recrystallized, but repeated defect generation by particle bombardment prevents grain growth, leading to a

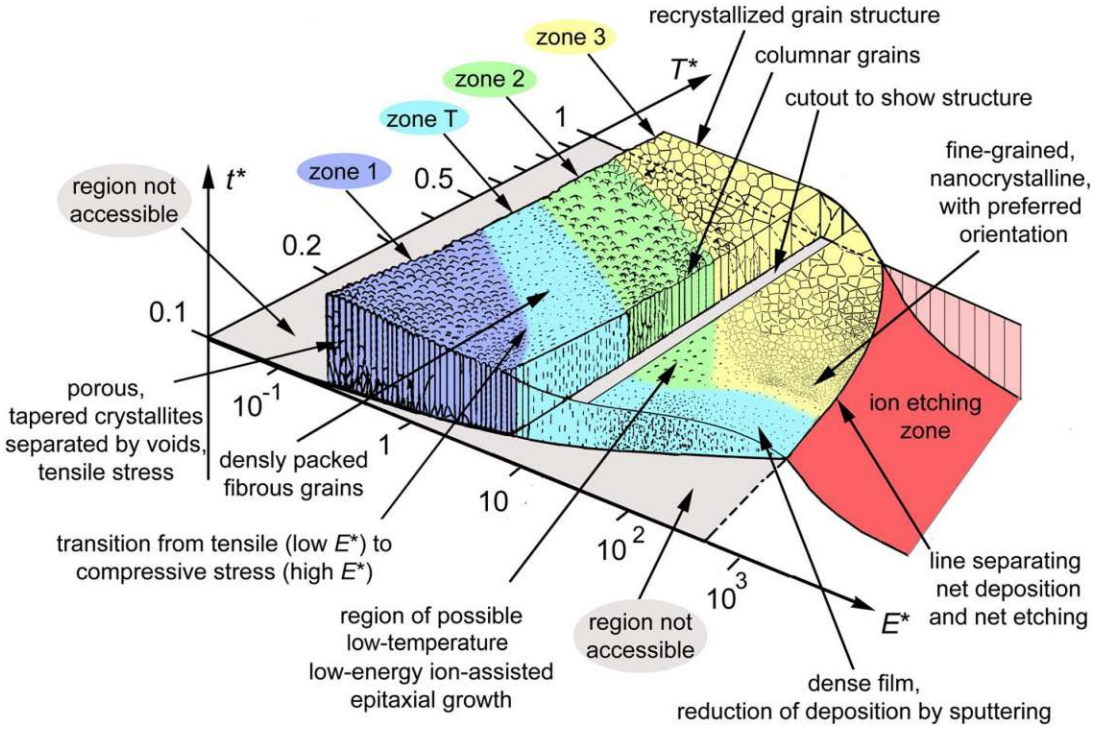

Figure 3.5: Structure zone model showing the influence of generalized temperature T^*, time t^*, and normalized energy E^* on the microstructure. Taken with permission from [83] (© Elsevier).

fine-grained, nanocrystalline structure. Above a certain E^*, the ion etching zone indicates negative film growth, this is used in practice to clean substrates prior to deposition. The grey regions in Figure 3.5 are marked as inaccessible due to kinetic heating of the film (thus a very low-T^*-very high-E^* region cannot exist), and because the sputtered particles cannot be decelerated beyond a certain point when approaching the substrate. [73, 83]

3.2 Analysis of Thin Films

Thin films represent only a tiny fraction of the whole sample volume in comparison to the substrate. For example, a 5 µm thick coating on a 500 µm thick single crystal would make up only 1/100 of the whole volume, and this fraction can also be significantly smaller. All analysis methods therefore need to be surface-sensitive, so that the signal from the region of interest is not drowned by the

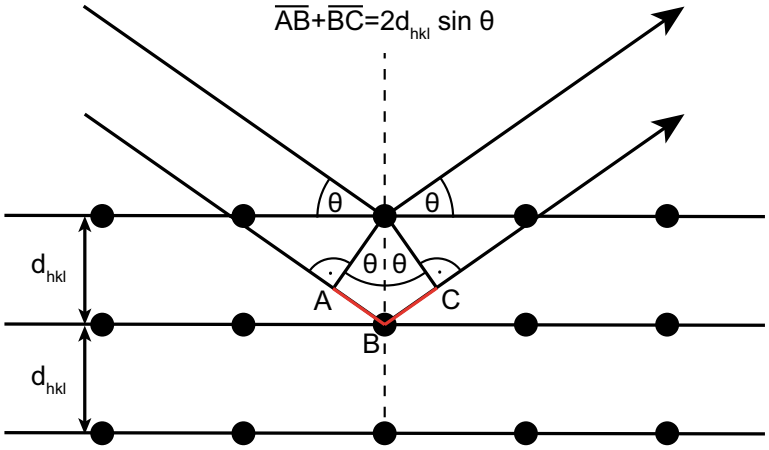

Figure 3.6: Visual interpretation of Bragg's law. The additional path $\overline{ABC}$, traveled by the lower X-ray beam, needs to be a multitude of the wavelength λ to preserve the phase relationship between the two rays. Adapted from [84].

information from the substrate volume.

3.2.1 X-Ray Diffraction

The diffraction of X-rays on periodic crystal planes was first discovered in 1912 and is a valuable tool for structural analysis of materials. The basis of X-ray diffraction is Bragg's law (see Figure 3.6)

$$n\lambda = 2d_{hkl}\sin\theta\,, \tag{3.5}$$

where n is the diffraction order, λ the wavelength, d_{hkl} the spacing between reflecting lattice planes, and θ the diffraction angle. When electromagnetic radiation with a wavelength similar to atomic distances hits a solid, a part of the radiation is scattered on atoms at the surface, while the rest penetrates deeper into the material. When atoms are arranged in a three-dimensional periodic order, they form lattice planes, marked by the Miller-indices hkl. Under certain orientations of the crystal these planes become perpendicular to the surface with a distance of d_{hkl} to each other. Each scattering atom acts as the source of a new spherical wave by Huygens principle, so that by interference of these periodical sources, each plane can be viewed as a semitransparent mirror to the X-rays. Two in-phase X-ray beams that hit the crystal with an angle θ and are "reflected"

on two subsequent lattice planes, will be in phase after reflection only if the Bragg condition is met. This means that when the additional path traveled by the lower penetrating beam $\overline{\mathrm{ABC}} = n\lambda$, the two beams are in phase again after reflection, and interfere constructively. When the Bragg condition is not met, the phase relationship is broken and the two beams will interfere destructively and cancel each other out. Therefore a crystal will show a distinct diffraction pattern with reflexes that depend on lattice parameters and crystal symmetry. The number of reflex positions and their relative positions give information on the number of phases, crystal symmetry and lattice spacings. In a powder sample the individual grains are oriented randomly, so that the intensity of reflexes follows a natural pattern. In thin films, the structure relationship between substrate and coating often leads to texturing, so that some crystallographic orientations are predominant. This becomes apparent by the intensities of the diffracted reflexes. The peak width contains information on grain size and micro-stresses. All reflexes have a natural line width, which is caused by the limited size of all measured crystallites. Since the diffraction pattern is composed of spherical waves, emanating from the atoms, the number of scattering centers determines the shape of this pattern. The more scattering centers participate in this interference, the sharper the diffraction pattern becomes. In nanometer sized crystals, this leads to visibly increased line widths compared to larger crystals. The Scherrer equation describes the relationship between domain size D_{hkl} and line width B^D

$$D_{hkl} = \frac{K\lambda}{B^D \cos\theta}, \tag{3.6}$$

where K is a factor that considers the mosaicity of the crystallites. The line width is also affected by local perturbations of crystal symmetry, which alters the lattice spacing locally, so that the Bragg condition is fulfilled not only for a sharp angle, but for a small range of angles. This can be caused by temperature induced lattice vibrations, giving rise to broader reflexes at high temperatures, or micro-stresses. In high-entropy materials, the distorted lattice also causes broader peaks, this influence has been described as similar to the temperature effect [61]. In HESC coatings, all these effects come into play, since the deposited grains are usually small and contain many defects, which give rise to micro-stresses. The

mixing of differently sized elements within a phase completes this cocktail, so that observed line widths of HESC coatings are usually very broad.

A common measurement setup for polycrystalline samples is the Bragg-Brentano geometry. Here the incident and diffracted X-ray beams enter and leave the sample under the same angle θ. Different diffraction angles are measured by moving the X-ray source and the detector closer to each other along the focusing circle. By this setup only lattice planes perpendicular to the surface can be measured. Samples were analyzed in this geometry using a PANanlytical XPert Pro MPD ($\theta-\theta$ diffractometer) equipped with a Cu–Kα source ($\lambda = 0.154\,08\,\mathrm{nm}$), operated at 45 kV and 40 mA. [84]

3.2.2 Electron Microscopy

The resolution limit of visible-light microscopy is governed by the wavelength of the light. The Rayleigh criterion

$$d = \frac{0.61\lambda}{n \sin \alpha} \tag{3.7}$$

states the smallest distance d, that can be resolved in a visible-light microscope. It depends on the wavelength λ, the refractive index n, and the angle of collection of the magnifying lens α. In a good microscope $d \approx \lambda$, so that visible light can be used to resolve features down to roughly 500 nm in size, which is insufficient to study microstructures in coatings. This limit is circumvented with electron microscopy, the ground-breaking principle behind this technique is the wave-particle duality of matter, described in de Broglie's expression

$$\lambda = h/p\,, \tag{3.8}$$

linking the wavelength λ with the momentum p by Planck's constant $h = 6.626\,070\,15 \cdot 10^{-34}$ Js. In electron microscopy, electrons are accelerated by a high voltage drop, V, to the kinetic energy eV, with $e = 1.602\,176\,634 \cdot 10^{-19}$ C being the elemental charge of the electron. The momentum of the electron can thus be written as

$$p = m_0 v = \sqrt{2 m_0 e V}\,, \tag{3.9}$$

with m_0 being the electrons mass and v its velocity. De Broglies relationship in Equation 3.8 can therefore be written as

$$\lambda = \frac{h}{\sqrt{2m_0 eV}}. \tag{3.10}$$

For electrons, accelerated with dozens or hundreds of kV, λ is therefore only a tiny fraction of a nanometer, allowing resolution of much smaller features.

Two types of electron microscopy are commonly used in materials science, these are Scanning Electron Micsroscopy (SEM), and Transmission Electron Microscopy (TEM). Both techniques use a high-energy electron beam to record magnified images and to apply a variety of analytical methods. SEM is used to analyze "bulk" samples (like several µm thick coatings), whereas TEM requires electron transparent samples with thicknesses typically $< 100\,\text{nm}$. [85]

3.2.2.1 Scanning Electron Microscopy

In SEM, an electron beam is generated with beam energies typically between 1-30 keV, focused by electromagnetic lenses, and scanned across a sample. Two types of electron guns are used: Thermionic and field emission sources. Thermionic sources use a W filament (having a high melting point) or a LaB_6 crystal (having a low work function) that is heated to high temperatures. A fraction of the electrons thereby receives enough energy to overcome the work function of the material, and is emitted. Field emission sources use the fact that the strength of an electric field F is increased at sharp points with small radius r, when a voltage V is applied: $F = V/r$. When a large voltage is applied to such a finely prepared tip, the energy barrier with its associated work function is deformed so that the electrons can tunnel out of the tip (this process is described in more detail in Section 3.2.3.2). Since the electrons are emitted in a wide range of divergent angles, they are focused by the so-called Wehnelt cylinder around the electron source, to which a negative bias potential is applied. This causes the electrons to cross-over, forming a virtual source with a certain diameter, and from there electromagnetic lenses guide the electron beam. Field emission requires better vacuum conditions to operate and is therefore pricier, but it produces the smallest cross-over, the highest brightness (current density per unit solid angle of

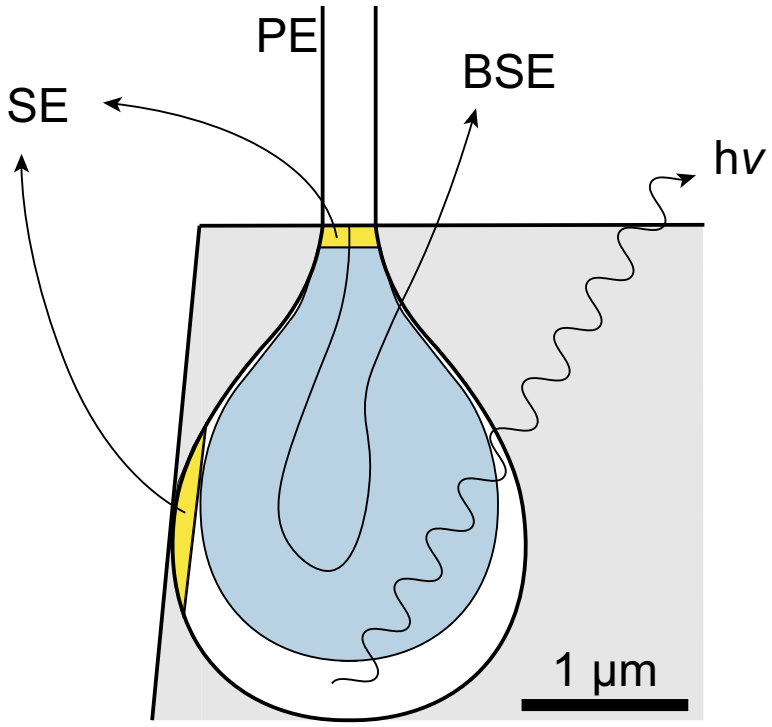

Figure 3.7: Excitation volume of the primary electron beam (PE, drawn with magnified cross-section) near a sharp topographical edge. Secondary electrons (SE) are generated throughout the volume, but can only escape from regions near the surface (yellow). Backscatter electrons (BSE) and X-rays (hν) have higher energy and are contributed from larger volumes (blue and white, respectively).

the source) and the lowest energy spread of the electrons, making it the state of the art for high resolution imaging. After passing through different lenses and apertures, the electrons penetrate the sample material up to $\approx 5\,\mu m$ deep, depending on beam energy and sample composition. This region is called the excitation volume. In this volume the primary electrons cause several events – inelastic scattering, elastic scattering, and ionization – that generate signals to be processed. The scattering effects also broaden the electron beam as it travels into the material, leading to a plume-shaped excitation volume, narrower near the surface, and broader, the deeper it penetrates. This is shown schematically in Figure 3.7.

Upon traveling through the material, beam electrons exchange energy with the atoms. If sufficient energy is transferred, so-called secondary electrons (SE), possessing low energies of a few eV, are generated from loosely bound electrons

in the outer shells of the atoms. These SE suffer the same inelastic scattering and thus quickly lose their energy and are absorbed by the sample again, but if they are released in the vicinity of the surface (where the excitation volume is still narrow), a number of them can escape the sample, be extracted with an electric field and counted by the detector (typically an Everhart-Thornley dector). Since excitation volumes near topographical edges intersect the surface not only at the entrance location of the primary beam, but also deeper within the volume (see Figure 3.7), these excitation volumes have additional surface-near regions, where more SE can escape from the sample into the vacuum. The SE signal therefore yields both high spatial resolution and topographic contrast, making it ideal for topographic images with high detail. Since the SE are extracted with an electrical field to the detector, which is mounted sideways relative to the sample surface, the SE emerging from edges facing the detector are collected with high efficiency, while SE stemming from averted edges are partly re-absorbed by the same edge. This leads to a typical shadowing effect in SE images, which aides the interpretation of topographical features.

The inelastic energy transfer from the primary electrons can also happen to tightly bound electrons from inner shells, if the transferred energy lies in the range of hundreds to thousands of eV. This ionization leaves the atom additionally in an excited state, from which the atom can relax by lowering an electron from an upper shell with lower binding energy into the vacant position. The difference in energies between the two states is then emitted either as X-ray photon with characteristic energy for its element, or via the Auger-process, which requires very sensitive instrumentation and is therefore not used in SEM. Since X-rays have comparatively low absorption coefficients, they can leave the sample from anywhere inside the excitation volume. Thus X-rays can be used to analyze the local chemical composition of the material, but the spatial resolution is much inferior to SE. Two methods of detection are used to discriminate the energy of the X-rays: Wavelength dispersive (WDS) and energy dispersive spectroscopy (EDS). Wavelength dispersive systems separate energies of different X-rays by their wavelength. According to Bragg's law (Equation 3.5), photons with different energies and thus wavelenghts diffract from a crystal under different angles. In the

experimental setup, the X-rays are focused on a single crystal at a fixed position, and a detector collects the different X-rays, now separated by the diffraction angle. This setup is sensitive and has a high energy resolution, but is also costly and slow, since the detector scans the wavelenghts sequentially. EDS on the other hand uses a Si-based semi-conductor with a certain band-gap as detector. All incident X-rays are detected simultaneously by absorption in the semi-conductor, their energies are determined by the number of generated electron-hole pairs. These pairs are collected in an anode where they cause a voltage spike, the magnitude of which corresponds to the photon energy. The sensitivity and energy resolution of EDS is worse compared to WDS, but the technology is comparably cheap and the measurement is very fast. EDS is therefore common for general purpose chemical analysis and was also used in this thesis.

By electrostatic interaction with the atomic nuclei, the primary electrons can also scatter elastically. Thereby only the direction of the primary electrons is changed, usually only a few degrees per scattering event, but sometimes more. By undergoing enough elastic scattering events, some primary electrons are eventually directed towards the surface again, where they leave the sample with energies in a range from almost the full initial energy down to several eV, depending on how much inelastic scattering the electrons suffered. These electrons are called backscattered electrons (BSE), and are also useful for imaging. Since attractive forces with the positively charged nuclei are responsible for elastic scattering, materials with a higher mean order number Z result in more elastic scattering and thus more BSE to collect. The BSE images therefore show a great Z- or elemental contrast. Note, that both SE and BSE show topographic and Z-contrast at the same time, but the topographic contrast is much more pronounced in SE, while the Z-contrast is dominant in BSE. Since most BSE have very high kinetic energies, they can also leave the sample from lower regions of the excitation volume, their lateral resolution is therefore worse compared to SE. BSE are detected with a ring electrode that is positioned above the sample around the primary electron beam. BSE and SE can be separated by their energy, during BSE measurement the low-energy SE can be extracted to the Everhart-Thornley detector with a weak electrostatic field, which does not significantly affect the

trajectory of the high-energy BSE, thus the BSE detector counts only the BSE. SE on the other hand are much more numerous, so that occasional stray BSE do not affect the generation of SE images to a high degree.

SEM can also give information on the local crystal structure and orientation using so-called Electron Backscatter Diffraction (EBSD). The basis of this technique is the formation of Kikuchi lines by multiple scattering of electrons in the sample, first incoherent scattering, followed by Bragg diffraction. Incoherent scattering first strays the trajectories of the electrons by a small random amount, some of these electrons are then scattered on a crystallographic plane of the sample under a certain angle as determined by the Bragg condition in Equation 3.5. For a large ensemble, these twice scattered electrons form a pair of cones (so-called Kossel cones) that are oriented symmetrically around the diffracting plane. The entire cone vertex forms the diffracting angle θ to the diffracting plane. The intersection of such a cone with a planar screen or detector forms a hyperbola, which appears as a straight line, since the detector is far away from the sample. These lines are called Kikuchi lines or bands. The number, relative position, and orienation of these lines is highly dependent on the crystal structure (which governs the diffracting planes), and also orientation. Kikuchi lines are therefore a powerful tool to measure the crystal orientation, when the crystal symmetry is known. In an EBSD measurement, the electron beam is rastered across the sample surface, at each point the corresponding Kikuchi pattern is then recorded, from which the orientation of every recorded grain can be calculated. In a standard EBSD measurement diffracted BSE are used to generate these patterns. The geometrical setup of the EBSD detector requires that the sample is tilted by 70°, so that enough intensity falls on the detector. This limits the spatial resolution, so that only rather coarse micro-structures can be observed in sufficient detail. But the method can be adapted to suit micro-columnar thin films, by measuring the Kikuchi patterns in transmission. This requires a thin sample, which can be prepared like for TEM investigation. The method is then called Transmission Kikuchi Diffraction (TKD). [86–88]

SEM investigations in this thesis were conducted with a FEI Quanta F200 Scanning Electron Microscope, equipped with a Field Emission Gun (FEG). The

SEM was operated at 5 kV for SE images to investigate growth morphology and deposition rates. EDS linescans and BSE images were recorded with 20 kV to measure and image chemical compositions. TKD patterns were recorded with 30 kV acceleration voltage on prepared TEM samples.

3.2.2.2 Transmission Electron Microscopy

Scanning Electron Microscopy is one of the most important analytical techniques in the field of materials science. Its major limitation is the formation of the excitation plume that limits the spatial resolution. This can be overcome by Transmission Electron Microscopy, which uses the same electron sources, but operates on samples thinned to < 100 nm, so that the incident electron beam cannot undergo enough scattering events to broaden the beam significantly. Thereby, the excitation volume is small and the resolution limit is circumvented, allowing images down to atomic resolution to be recorded. The typical operation voltage for a TEM is 200 kV, which also improves the spatial resolution due to the shorter wavelength of the electrons. By interaction with the sample many different secondary signals are generated that are used analytically.

The apparatus consists of several lenses (electromagnets) and apertures that guide and limit the electron beam, see Figure 3.8 for a schematic overview. The sample is usually illuminated by an electron source from the top, where a system of condensor lenses and a condensor aperture align and trim the electron beam parallel to the optical axis. The beam passes through the thin sample, where several interactions take place. The objective lens collects all forward scattered and diffracted rays and focuses them in its back focal plane. The intermediate lens then selects either the objective plane, leading to an image, or the back focal plane of the objective lens, which leads to a diffraction pattern of the sample. This sets the fundamental operation modes in the TEM apart: imaging and diffraction mode. The projector lens underneath the intermediate lens simply magnifies whatever image is passed onto it on a screen, where the final image is formed.

Each point of the back focal plane of the objective lens contains rays from the whole sample, which were diffracted into the same angle. The objective aperture

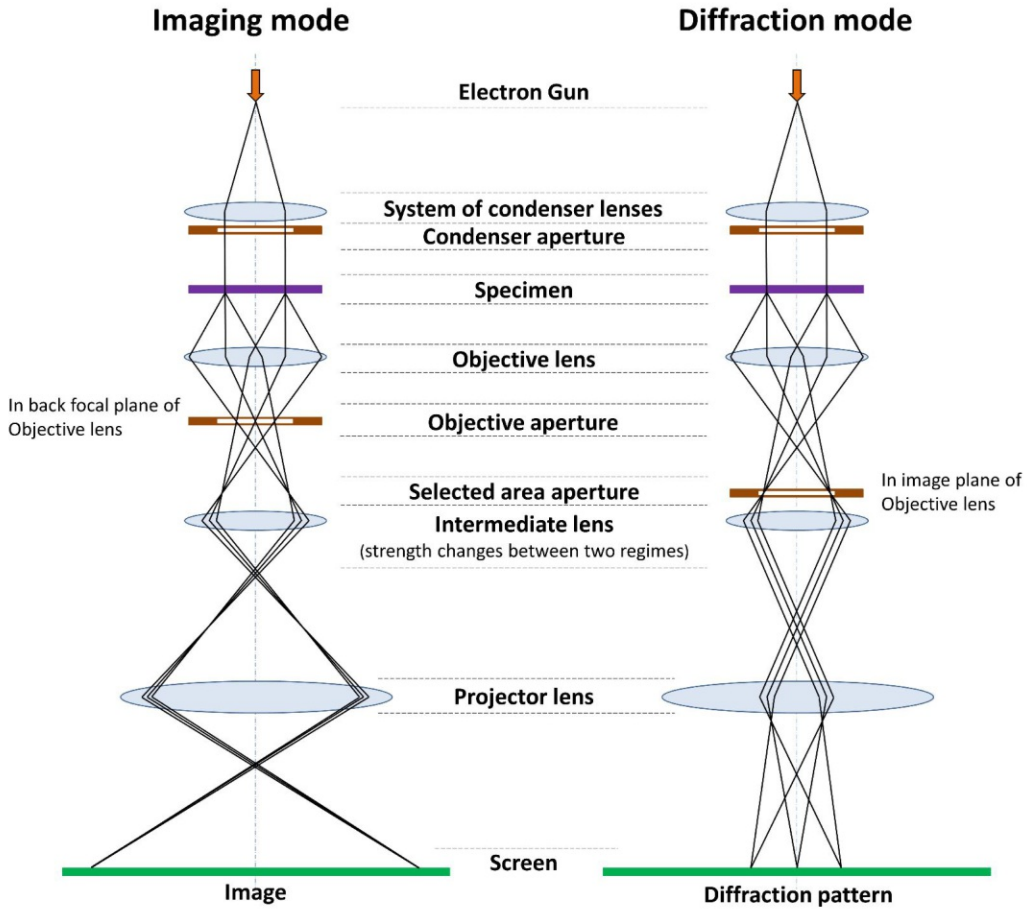

Figure 3.8: Schematic setup of a TEM in imaging (left) and diffraction mode (right). Created by Eric Kvaalen under the CC BY-SA 4.0 license.

can therefore be inserted in this plane to select rays that are diffracted into a certain angle, and form an image with high contrast from these rays. When the aperture selects the direct beam, a so-called bright-field (BF) image is formed, if diffracted rays are collected, a so-called dark-field (DF) image is formed. Without aperture, the contrast of BF and DF would recombine on the screen to a low contrast image. Instrumentally, DF images can be achieved in two ways, either by moving the objective aperture out of the optical axis, so that only diffracted rays at some distance from the optical axis pass through the objective aperture. This is colloquially called "dirty" DF. The electromagnetic lenses are far from ideal, thin

lenses (the introductory chapter of [85] compares the quality of electromagnetic lenses to using the bottom of a bottle as lens in light microscopy) and thus manipulate electrons worse, the more the beam strays from the optical axis. The axial DF mode should therefore be favored, where the primary beam is tilted off-axis, so that the diffracted spot of interest now lies in the optical axis. The difference between BF and DF images lies in their contrast, which is defined as intensity difference between two adjacent regions 1 and 2:

$$C = \frac{I_2 - I_1}{I_1}\,. \tag{3.11}$$

Since most electrons pass the sample without change of direction, the average intensity in BF images is high. Intensity variations due to mass-thickness contrast or diffraction contrast cause relatively little intensity change compared to the base intensity, thus the contrast is lower. BF images therefore appear generally bright with dark regions for example at precipitates with higher mean order number Z, or at grains with certain orientations in a polycrystalline sample. DF images on the other hand contain a smaller average intensity, and thus show higher contrast in such regions. Generally speaking, BF images give more of an overview of the sample, while DF images highlight the contrast-rich regions, while lacking information from other areas of the sample.

The mass-thickness contrast results from incoherent elastic scattering and depends on the atomic number Z (similar to BSE generation in SEM), and the thickness of the specimen. The higher the atomic number or the thicker the sample, the more scattering events occur, leading to dark areas in BF and bright areas in DF mode. Crystalline materials show additional diffraction contrast. When the incident beam meets crystal planes under the Bragg condition (see Equation 3.5), the electrons scatter coherently. In a polycrystalline sample the grains are oriented in a more or less random fashion, so that under a certain beam condition, a fraction of the grains fulfills the Bragg condition, and scatters the electrons coherently. These grains will appear darker in BF and brighter in DF mode, highlighting grains with the same orientation.

The back focal plane of the objective lens contains focused spots from the direct beam and all diffracted beams, which thus form a diffraction pattern. In diffraction mode, the intermediate lens uses this pattern and projects it to the

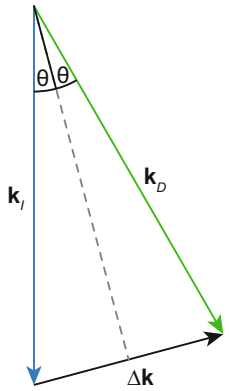

Figure 3.9: The incident wave-vector $\mathbf{k}_I$ and the diffracted wave-vector $\mathbf{k}_D$ fulfill the Bragg-condition only for certain angles θ. $\Delta\mathbf{k}$ is the difference vector. Adapted from [85].

projector lens, which itself magnifies the diffraction pattern. Since diffracted beams necessarily fulfill the Bragg condition for diffracting on the same set of crystal planes, and electrons interact strongly with matter due to Coulomb interaction, electrons are generally diffracted not only once within a sample, but multiple times. A beam that is diffracted twice on a set of crystalline planes is thus oriented like the original beam, but laterally displaced. Among other effects this gives rise to higher order diffraction spots, whose rigorous treatment via dynamical scattering theory far exceeds the scope of this section, but can be understood in a simplified phenomenological way with the Bragg and Laue conditions.

When an electron beam is diffracted (shows constructive interference from several scattering centers), its direction is usually changed. This can be exemplified by the wave-vectors $\mathbf{k}$, which point in the direction of the wave propagation and have the length of $1/\lambda$, with λ being the wavelength of the electrons. In a scattering event, the electron propagation can be separated into an incident wave-vector $\mathbf{k}_I$ and a diffracted wave-vector $\mathbf{k}_D$. The difference vector

$$\Delta\mathbf{k} = \mathbf{k}_D - \mathbf{k}_I\,, \tag{3.12}$$

is the change in direction due to diffraction, while λ is assumed to remain constant, see Figure 3.9. For constructive interference, the Bragg equation (Equation 3.5) must be fulfilled, so that

$$|\Delta\mathbf{k}| = \frac{2\sin\theta}{\lambda}. \tag{3.13}$$

From Equation 3.5 it therefore follows that $|\Delta\mathbf{k}| = n/d$, making $\Delta\mathbf{k}$ a vector with unit nm^{-1}, so that the $\mathbf{k}$-vectors are reciprocal lattice vectors. A crystal can thus be represented with two types of lattices, a real and a reciprocal lattice. In the reciprocal space, $\Delta\mathbf{k}$ can be defined as a linear combination of the reciprocal lattice vectors $\mathbf{b}_1$, $\mathbf{b}_2$, and $\mathbf{b}_3$:

$$\Delta\mathbf{k} = \xi\mathbf{b}_1 + \eta\mathbf{b}_2 + \zeta\mathbf{b}_3\,, \tag{3.14}$$

where ξ, η, and ζ can be any value and the reciprocal lattice vectors $\mathbf{b}_1$, $\mathbf{b}_2$, and $\mathbf{b}_3$ are calculated from the real space lattice vectors of the crystal, $\mathbf{a}_1$, $\mathbf{a}_2$, and $\mathbf{a}_3$

$$\mathbf{b}_1 = 2\pi\frac{\mathbf{a}_2\times\mathbf{a}_3}{\mathbf{a}_1\cdot(\mathbf{a}_2\times\mathbf{a}_3)}\,,\quad \mathbf{b}_2 = 2\pi\frac{\mathbf{a}_3\times\mathbf{a}_1}{\mathbf{a}_2\cdot(\mathbf{a}_3\times\mathbf{a}_1)}\,,\quad \mathbf{b}_3 = 2\pi\frac{\mathbf{a}_1\times\mathbf{a}_2}{\mathbf{a}_3\cdot(\mathbf{a}_1\times\mathbf{a}_2)}\,. \tag{3.15}$$

Only in the special case

$$\Delta\mathbf{k} = \mathbf{g}_{hkl} = h\mathbf{b}_1 + k\mathbf{b}_2 + l\mathbf{b}_3\,, \tag{3.16}$$

with h, k, and l as integers (the Miller indices), is the condition for diffraction fulfilled. $\mathbf{g}_{hkl}$ is normal to the plane $(h\,k\,l)$ and has the length $|\mathbf{g}_{hkl}| = 1/d_{hkl}$. This relationship can be demonstrated graphically in the Ewald sphere construction, Figure 3.10. The reciprocal lattice is a three-dimensional array of points in reciprocal space, one of these points serves as origin of the lattice. In the Ewald sphere construction, $\mathbf{k}_I$ is a vector that points towards this origin, while $\mathbf{k}_D$ is drawn tail-to-tail to $\mathbf{k}_I$. The sphere that is spanned by all possible directions of $\mathbf{k}_D$ is the Ewald sphere with radius $1/\lambda$. Only where the Ewald sphere cuts through a reciprocal lattice point, is the condition in Equation 3.16 fulfilled so that diffraction occurs. When the crystal is rotated, the reciprocal lattice is rotated around the origin. In a sufficiently large ensemble of randomly oriented crystals, the points form rings with distances to the origin that are characteristic for the crystal symmetry. Since the electrons in TEM have a very short wavelength, the Ewald sphere in TEM diffraction is much larger than in XRD for example, so that the surface of the sphere appears rather flat in the vicinity of a few reciprocal

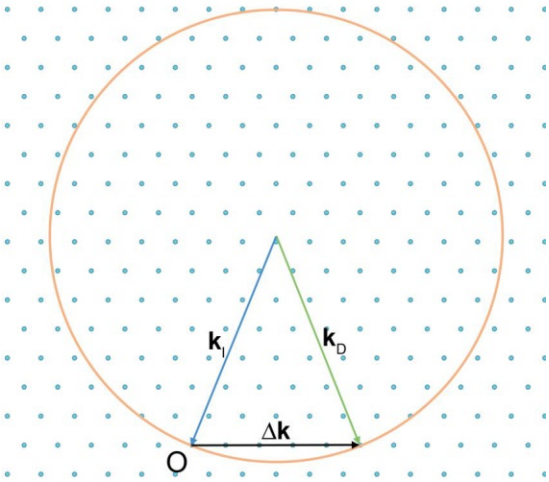

Figure 3.10: Two-dimensional representation of the Ewald sphere. O is the chosen origin of the reciprocal lattice, $\mathbf{k}_I$ and $\mathbf{k}_D$ are the incident and diffracted wave-vectors. When a reciprocal lattice point touches the Ewald sphere, the Laue condition $\Delta\mathbf{k} = \mathbf{g}_{hkl}$ is fulfilled. Adapted from [85].

lattice points. The next important difference to XRD is the shape of investigated crystal. TEM samples are typically $< 100\,\text{nm}$ thick, but much larger in the other dimensions, so that a typical sample forms a thin slab. The phenomenon of line broadening due to small crystallites in XRD also applies to electron diffraction, but here the slab-shape of the sample causes anisotropic smearing of the intensity. In reciprocal space, this manifests in elongation of the lattice points into rods. Therefore, lattice points that do not fulfill the Laue condition exactly, but are close to the Ewald sphere also show some intensity in the diffraction pattern. For this reason, TEM diffraction patterns contain many more spots than would be expected from the respective crystal symmetry.

In a polycrystalline sample with random orientation, the diffraction spots line up to create nested spheres that intersect the Ewald sphere at certain distances from the origin, resulting in ring patterns similar to powder patterns recorded in XRD. Each ring then corresponds to a set of planes, for example the (1 1 1) or (2 0 0) planes in a fcc crystal. In TEM, the rings are generally not continuous but speckled, since only a comparatively small number of crystallites contribute to the diffraction pattern, and the smaller the grains are, the broader the spots become. In a textured sample, the reciprocal lattice of each grain is rotated only

by a few degrees from a reference position, so that the individual spots become elongated into small arc segments. The appearance of an amorphous material in a diffraction pattern is similar to a polycrystalline sample, but the rings are broader and not speckled anymore.

In the image plane of the objective lens, each spot contains information of only one corresponding spot in the sample. By inserting an aperture in this plane, a diffraction pattern from this region of interest of the sample can be recorded. This very useful technique allows local analysis of the crystal structure and is called Selected Area Electron Diffraction (SAED).

In addition to parallel illumination, the electron beam can also be converged on one spot on the sample. To form an image in convergent beam mode, the beam has to be scanned across the sample, similar to SEM. This technique is therefore called Scanning TEM (STEM). STEM provides images with high contrast and enables local analysis with techniques like EDS, which functions analogous to SEM-EDS, or Electron Energy Loss Spectroscopy (EELS). On the other hand the resolution of STEM images can be worse compared to TEM. STEM mode is both capable of BF and DF recordings, but unlike in TEM mode, the direct and diffracted beams are not separated by an aperture, but by position sensitive detectors. The direct beam is collected by a detector in the optical axis, while the diffracted beams are collected by an off-axis annular detector. STEM DF images provide especially good Z-contrast, when a high-angle annular DF detector (collection angle $\theta > 50\,\text{mrads}$ off-axis) is used, which is not reached by Bragg diffracted electrons that would contribute to noise.

EELS is a complimentary technique to EDS in TEM and measures the energy loss of inelastically scattered electrons of the electron beam after passing through the sample. A typical EELS spectrum – intensity versus energy-loss ΔE – consists of a so-called zero-loss peak at $\Delta E = 0\,\text{eV}$ with very high intensity (since most electrons do not lose energy in the thin sample), a low-loss region up to $\approx 50\,\text{eV}$ in which plasmon losses lie (interaction with weakly bound conduction- and valence-band electrons from the sample), and a high-loss region, in which element-characteristic ionization edges lie. These edges can be used to quantify the chemical composition, and since EELS is not dependent on a fluorescence yield,

it is more sensitive for light elements. But EELS also requires especially thin samples to work properly, since the characteristic edges are very small and sit on a massive background of multiply scattered electrons.

TEMs are able to achieve resolutions down to atomic level, this is called High-Resolution TEM (HRTEM). However, HRTEM images are not achieved simply by increasing the magnification of a BF or DF image, which requires an aperture in the back focal plane of the objective lens to blot out either the direct or the diffracted beam. Instead, HRTEM images are interference patterns from the phase relationships of different beams and thus require a much larger aperture than is useful in normal TEM mode. The position and arrangement of periodic lattice plains of crystalline materials – and defects therein – are easily seen in HRTEM images. But since TEM images are always projections of the whole sample thickness, the absence of a periodic pattern does not necessarily indicate an amorphous material, as the crystal needs to be oriented in a certain way to show the lattice periodicity in projection. Actual atomic positions within HRTEM images depend strongly on the experimental setup and require intricate modeling of atomic positions for proper interpretation. [85, 87]

TEM investigations in this thesis were performed with a FEI TECNAI F20, equipped with a FEG, operated at 200 kV. DF, BF, STEM, and HRTEM images, as well as SAED patterns and EDS/EELS-linescans were used to analyze the coatings.

3.2.3 Chemical Analysis

Chemical analysis of thin films is a challenging task that requires special methods. Since the region of interest is only a thin layer of a few µm in thickness, the analysis method needs to be surface sensitive. This excludes the majority of quantitative analytical methods like X-Ray Fluorescence Spectroscopy, Volumetric Analysis, or Spark Emission Spectroscopy (non-exhaustive list), since they require bulk materials.

Classical elemental trace analysis methods with Inductively Coupled Plasma-Optical Emission Spectroscopy/Mass Spectrometry (ICP-OES/ICP-MS) can operate with such small sample masses, and are the preferred method for many

problems. ICP-OES or -MS is very well suited for analysis of metallic films. By selectively dissolving coatings from inert substrates, the constituents can be quantified reproducibly with very low margins of error. A solid sample introduction system with laser ablation even allows precise, surface-sensitive chemical analysis with a lateral resolution in the order of magnitude of $\sim 50\,\mu m$. But for ceramic thin films these methods are often not suited, because they operate in ambient conditions. N and O are abundant contaminants in the surrounding air, while C is ubiquitous in the plastic tubes used for sample introduction. Therefore, quantification of nitride, oxide, or carbide ceramics is only possible for the metal sublattice. While this might be sufficient in some cases, the nonmetal content is dependent on the poisoning state of the cathode during sputtering. Changes in this state affect the metal to nonmetal ratio and this influences the coating properties tremendously. The chemical composition of the nonmetal sublattice is therefore important, and its chemical analysis should not be omitted.

The problem of ambient contaminants can be circumvented with Laser Induced Breakdown Spectroscopy (LIBS), where optical emission of a local plasma, induced by laser radiation, is recorded in a pure Ar atmosphere. This technique is suited for the whole periodic system, but unfortunately the quantification of such spectra is non-trivial. In the analyzed plasma, the chemical matrix influences the response of each analyte heavily, thus well-known reference samples are always required for quantification. In explorative experimental science, and especially in young, expanding fields like high-entropy materials, such references are not available. Therefore, selected samples would have to be measured first by a different method, rendering LIBS redundant for this purpose.

A different method of quantification has been mentioned in Section 3.2.2.1, which is operated in vacuum conditions: EDS. It is a method with high spatial resolution and the ability to quantify elements of the whole periodic system from B upwards. However, the nature of high-entropy materials limits the usefulness of this method. EDS has a poor energy resolution, leading to overlapping signals for many elements. With 6 or more different elements, such coincidences are very probable, and was for example the central problem in elemental quantification of $(Al, Cr, Nb, Si, Ta, Ti)N$, since Si and Ta both have EDS signals around 1.8 keV.

Since the fluorescence yield of heavy elements like Ta is much higher, the Si content is often vastly overestimated in such compositions by EDS. In addition, while measurable, the error of measurement for light elements like C, N, or O is very high. Nonetheless, EDS is a simple method where the energy resolution is not critical, and linescans can provide useful compositional trends on a local scale. This method was therefore the first resort for chemical analysis of any new coating, and where the performance of EDS was insufficient, more sophisticated techniques were applied.

3.2.3.1 Elastic Recoil Detection Analyis

As outlined in the previous paragraphs, accurate full elemental analysis of high-entropy thin films is challenging, since so many requirements need to be satisfied: Small analysis volume, quantification of both metals and non-metals, non-availability of calibration standards, and the capability to resolve many different elements across the periodic system. These requirements are fulfilled by Elastic Recoil Detection Analysis (ERDA), which was first described in 1976 [89]. This method uses primary ions, accelerated to energies in the MeV range, to eject lighter ions from the sample, whose kinetic energies can be detected for elemental identification.

The measurement principle of ERDA is the elastic energy transfer between a primary ion with a kinetic energy in the MeV-range, and the atomic nuclei in a sample. When the mass of the impacted nucleus is lower than that of the primary ion, the nucleus is recoiled mostly in a forward direction. For measurement, the incident beam is therefore directed onto the surface at a low glancing angle. Since the transferred energies are much higher than any binding energy (which are in a magnitude of a few eV) the elastic recoiling is independent on the chemical matrix. This allows matrix-independent, surface-sensitive quantification, especially of light elements that are difficult to analyse with many other techniques.

The elastic recoil effect can be described with the kinematic factor

$$K = E_2/E_1\,, \tag{3.17}$$

where E_2 is the energy passed onto a sample atom with mass m_2 from a primary

ion with mass m_1 and energy E_1. In ERDA geometry, K can be written as

$$K = \frac{4m_1m_2}{(m_1+m_2)^2}\cos^2\phi\,, \tag{3.18}$$

where ϕ is the recoil angle. When $m_1 > m_2$, the recoiling happens mostly in the forward direction. The chosen measurement angles ϕ are therefore small. By using heavy primary ions like I^{n+}, all elements with lighter mass can be analyzed. A common detection mode is the time-of-flight (ToF) measurement, that simultaneously measures energy and velocity of recoiled atoms to identify the atomic species. The equipment for ERDA measurements is very costly, so its use has to be justified. But since the method is almost non-destructive, it allows measurement of depth-profiles for all detected elements with a depth-resolution of a few nm, and is not dependent on calibration standards for quantification. It is an ideal method for analyzing chemical compositions of thin films, especially when light elements like N or O are involved. The limit of detection lies usually between 0.1 and 1 at% for different elements. [90–92]

When EDS was not sufficiently accurate, chemical investigations in this thesis were done by ToF-ERDA with a recoil detection angle of 45° using a 36 MeV I^{8+} ion beam. The concentrations were calculated by averaging the depth profile signals below the surface oxide layer, where all concentrations remained constant.

3.2.3.2 Atom Probe Tomography

Atom probe tomography (APT) uses the principle of field evaporation to subsequently remove and detect the atoms of a fine needle-shaped sample row by row. The detector signal then allows the reconstruction of the evaporated sample to analyze local chemical compositions on the nanometer scale. APT can be viewed as a further development of the field ion microscope, in which an imaging gas is used to map the atomic arrangement on the surface of a needle-shaped sample. By applying a high positive potential to the sample tip, the imaging gas (for example He) is subsequently polarized, attracted to the surface, ionized, and electrostatically repelled towards a screen. Since the field strength increases around sharp edges of the tip (see Section 3.2.2.1), ionization occurs mostly at crystal ledges and terrace sites, from where the brightest spots on the imaging

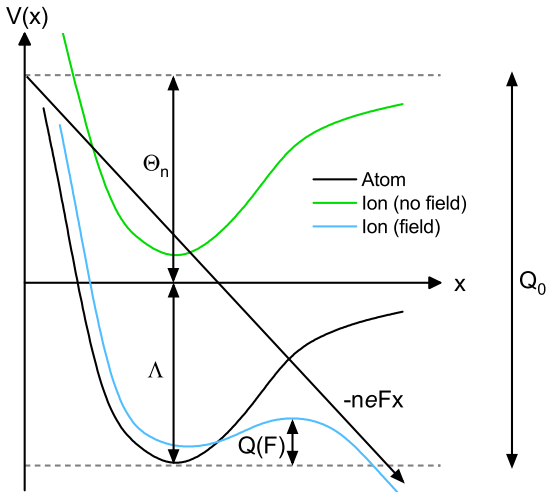

Figure 3.11: Influence of an electric field on binding potentials of a surface atom and ion. $V(x)$ is the potential depending on the distance to the surface x, Λ the sublimation energy, and Θ_n the additional energy barrier for n-fold ionization. Adapted from [93].

screen are observed. This allowed the magnification of a crystal surface with atomic resolution, requiring only a simple experimental setup. By increasing the potential applied to the specimen for a short duration, the surface atoms can also be field evaporated to reveal subsurface layers of the sample. APT focuses solely on this aspect with an adapted instrumentation.

By applying a strong electrical field to a sample, the surface atoms become polarized. When a certain threshold is met, the atoms can be desorbed from the sample while leaving an electron behind. The resulting evaporated and charged ion is then electrostatically repelled from the mirror charge at the sample surface, accelerating the ion away from the surface. The exact mechanism has not yet been clarified, but several models have been developed to understand this behavior. The first model by Müller [94], called the "image hump" model, assumes that the atoms are fully ionized before leaving the surface. The energetic transition from atomic to ionic states is depicted schematically in Figure 3.11. In its ground-state, the atom sits in its binding potential well, bonded to other atoms on the surface (black line). To remove an atom from this well and thus evaporate it from the surface without field assistance, the sublimation energy Λ has to be delivered to the atom thermally. To additionally ionize the atom n times, the energy

contribution,

$$\Theta_n = \sum_1^n I_i - n\phi_e\,, \tag{3.19}$$

needs to be overcome as well, where I_i is the ith ionization energy, and ϕ_e is the work function of the surface. Together, the energy barrier

$$Q_0 = \Lambda + \sum_1^n I_i - n\phi_e \tag{3.20}$$

is required to remove an atom from the surface and ionize it n times, which is the prerequisite to transport the atom to the detector by electric fields. In the presence of an electric field, the binding potential curve of the ionized state is affected. With increasing field strength F, the energy of the ionic states is lowered, so that the energy barrier $Q(F)$ becomes smaller and the probability of an atom escaping the surface in ionized state increases (Figure 3.11 green to blue line). Overcoming this barrier is usually thermally assisted, the evaporation rate Φ_{evap} can therefore be modeled with the Arrhenius law

$$\Phi_{evap} = \nu_0 \exp\left(\frac{-Q(F)}{k_B T}\right), \tag{3.21}$$

where ν_0 is the frequency of thermal vibrations that can lead to evaporation. The success rate is governed by the Maxwell-Boltzmann probability in the exponential function, where $Q(F)$ is the energy barrier, k_B the Boltzmann constant, and T the absolute temperature. In addition to thermal evaporation, ions can also pass the barrier by tunneling, which can become the rate determining process at low temperatures.

In APT, a very controlled evaporation is required to enable subsequent detection and thus discrimination of individual ions. The applied field strength is therefore set below the so-called "evaporation field", at which the energy barrier becomes 0. Two different mechanisms can be used to control the evaporation, short increases of the electric field at constant temperature, and vice versa, see Figure 3.12 for a schematic overview. The method of increasing the field strength is done by high voltage pulsing, while thermal energy is usually supplied by short laser pulses. The pulsed evaporation allows precise control over the departure

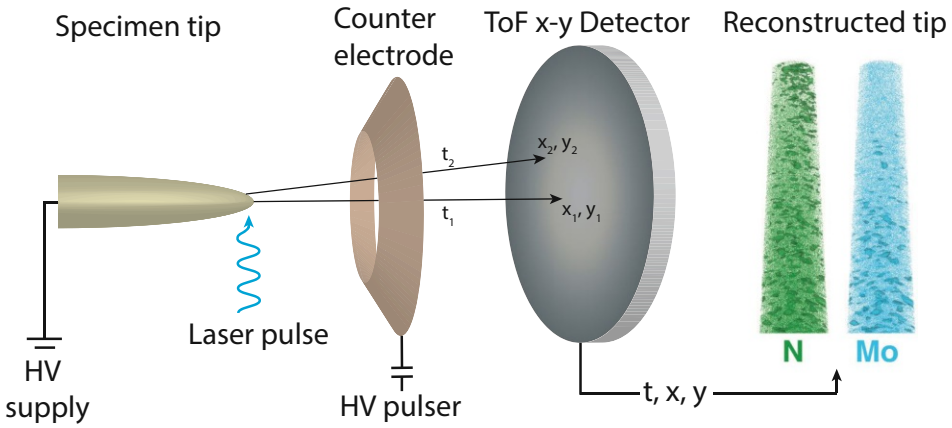

Figure 3.12: Schematic APT measurement. Both pulsing methods by laser or high voltage pulsing are depicted, but usually only one method is used. Adapted from [93] and [95].

time of the ions from the surface, since between the pulses the probability of additional ions escaping is low. The subsequently evaporated ions can therefore be separated in time, allowing time-of-flight discrimination of the ions. Assuming that the ions possess no initial velocity (measurements are typically carried out at $\sim 20\,\mathrm{K}$), all ions are accelerated by the same electrostatic field and thus gain the potential energy $E_p = neV$, with ne being the charge of the ion and V being the total voltage. This energy is then converted to kinetic energy $E_k = 1/2mv^2$, where m is the ion mass and v the velocity given by $v = L/t_{flight}$. L is the flight length between sample and detector and t_{flight} the time-of-flight. The mass/charge ratio m/n can therefore be expressed as

$$\frac{m}{n} \approx 2eV \left(\frac{t_{flight}}{L} \right)^2 , \tag{3.22}$$

so that different chemical species can be differentiated by their flight time. Since the atoms are evaporated layer by layer from the top, the combination of time-of-flight measurement with a position sensitive detector enables the reconstruction of the three-dimensional position of the ions and their chemical identity at the same time. With this information, the evaporated sample tip can then be reconstructed, giving insights to local chemical composition on the nanometer scale.

To reach the high field strengths for field evaporation, the investigated samples need to be formed into very sharp needles with a curvature radius at the sample apex of $\sim 100\,\mathrm{nm}$. Correct sample preparation is therefore of utmost importance.

The two most important methods are electropolishing and Focused Ion Beam (FIB). Since electropolishing requires conductive samples and gives little control over the investigated site, FIB-based techniques are more important for the preparation of thin films. Here, Ga^+ ions are accelerated at the sample with $\sim 5-30\,\mathrm{kV}$ to mill the sample material away. Since the ion beam can be directed at the sample with high precision, fine needle-shaped tips can be formed at a desired location of interest. [93]

3.2.4 Nanoindentation

One important aspect in the performance of protective hard coatings is the resistance to mechanical wear. Two mechanical properties that influence this resistance, hardness H and Young's modulus E, can be measured with nanoindentation. By pressing a diamond tip with a defined geometry onto a sample with a load P, the sample is deformed first elastically and then plastically. A softer material yields more and leads to a higher displacement h. After unloading, the elastic deformation is reverted, while the plastic deformation remains. Since the remaining indents after retraction of the tip are very small and difficult to analyze on hard thin films, load-displacement data is commonly used to determine H and E of such materials. A schematic load-displacement curve is shown in Figure 3.13.

The sample is loaded with the diamond tip until the maximum displacement h_{max} is reached at the peak load P_{max}. The unloading curve is different from the loading curve when plastic deformation occurs, so that a final depth $h_f > 0$ remains. Since the slope $s = \mathrm{d}P/\,\mathrm{d}h$ is usually non-linear, Oliver and Pharr [96] developed a method that considers the slope of the whole unloading curve. Since the elastic behavior of the tip influences the measurement of the E, the measured indentation modulus is actually only a so-called reduced modulus E_r and related to E by

$$\frac{1}{E_r} = \frac{(1-\nu^2)}{E} + \frac{(1-\nu_i^2)}{E_i}\,, \tag{3.23}$$

with E and ν the Young's modulus and Poisson's ratio of the sample, and E_i and ν_i Young's modulus and Poisson's ratio of the indenter. H and E_r are calculated

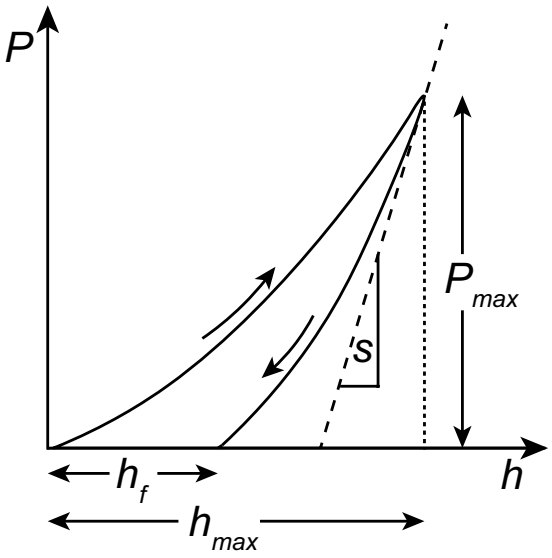

Figure 3.13: Schematic load-displacement curve of a nanoindentation measurement. Plotting load P against displacement h, the indentation hardness H and modulus E_I can be evaluated. The method by Oliver and Pharr uses the slope of the unloading curve to determine H and E_I. P_{max} is the maximal load, h_{max} the displacement under maximum load, h_f the final depth of the contact impression after unloading, and s is the initial unloading slope. Adapted from [96].

as

$$H = P_{max}/A\,, \tag{3.24}$$

and

$$E_r = \frac{\mathrm{d}P}{\mathrm{d}h}\frac{1}{2}\frac{\sqrt{\pi}}{\sqrt{A}}\,, \tag{3.25}$$

where A is the contact area. To distinguish the experimentally measured indentation modulus from the calculated Young's modulus (by DFT), the former will be abbreviated as E_I throughout this thesis.

Since the diamond tip also suffers wear, it gets blunted after prolonged use, leading to incorrect surface areas. The tip must therefore be regularly calibrated with an area function that corrects for the tip wear.

Nanoindentation measurements in this thesis were conducted with 40 indentations per sample using a Berkovich indenter with a maximum initial contact force of 30 mN, which was decreased by 0.5 mN for each following indent. This force range ensured that the displacement depth was below 10 % of the

whole coating thickness, which is necessary to exclude an influence from the substrate on the measurement. [96]

CHAPTER 4

Oxidation of Thin Films

High-performance materials usually operate under harsh conditions that lead to wear and corrosion. One particular case of corrosion is the oxidation in air at high temperatures, which leads to embrittlement, flaking, and ultimately failure of the material. Oxidation cannot be prevented, since all metals, except Au, form oxides spontaneously. The same is true for ceramics, since B, C, and N form the very stable and volatile compounds B_2O_3, CO_2, and NO_2. For simplicity, only the oxidation of metals will be described in this chapter, but the same mechanisms apply to ceramics as well. Since O_2 is ubiquitous in our atmosphere, and high temperatures are inevitable in many processes, oxidation can only be slowed down to tolerable speeds, but never stopped. One method to do so is the application of protective coatings that form a barrier on the surface. Since chemical reactions require contact of their reactants to take place, a dense coating that blocks diffusion through itself and thus separates the reactants can protect the inner material for an extended period of time. [97]

4.1 Diffusion

In a dense material, transport is determined only by diffusion, which is a kinetic process on atomic scale that leads to homogenization of the diffusing species. The driving force for all diffusion processes is the chemical potential, μ_i, which is

derived from the Gibbs free energy G at constant temperature T and pressure p

$$\mu_i = \left(\frac{\partial G}{\partial n_i}\right)_{T,p}, \tag{4.1}$$

where n_i is the number of moles of the ith component. Like the Gibbs free energy, the chemical potential strives towards a minimum for all components to reach chemical equilibrium. The chemical potential is dependent on the concentrations:

$$\mu_i = \mu_i^\circ + RT \ln a_i\,, \tag{4.2}$$

where μ_i° is the standard chemical potential (defined at a certain temperature and pressure) and a_i is the activity, which describes the deviation from a standard state for the ith component. The activity can be expressed in different ways. In diluted solutions it can be approximated with the concentration c_i of the ith component, for gases it is conveniently expressed as p_i/p_i°, where p_i is the partial pressure of the ith component and p_i° the partial pressure at which the chemical potential has its value of μ_i°. When diffusion depends only on concentration, for example within a phase, it can been mathematically described by Julius Fick's first law

$$J = -D\nabla C\,, \tag{4.3}$$

where J and C are the mass flux and the concentration of the diffusing species, respectively, and D is the diffusion constant. The transport of oxygen and metals through a coating can be considered a one-dimensional transport phenomenon, Fick's first law can therefore be formulated as

$$J = -D\left(\frac{\partial C}{\partial x}\right). \tag{4.4}$$

D is a material property, a low diffusivity means a slow transport and better resistance to oxidation. Since the flux of a reactant is difficult to observe directly, the diffusion of a species after a certain time t can be used instead to determine D. The progress of an oxidation reaction can be measured by oxidizing samples partially for certain durations, followed by immediate quenching to freeze the oxidation state in time. The relationship between time, concentration and diffusivity is governed by Fick's second law

$$\nabla^2 C = \frac{1}{D}\frac{\partial C}{\partial t}. \tag{4.5}$$

Again, this equation can be reformulated to

$$\frac{\partial^2 C}{\partial x^2} = \frac{1}{D}\frac{\partial C}{\partial t} \tag{4.6}$$

for the one-dimensional diffusion through a coating. [97, 98]

4.2 Transport Mechanisms through the Oxide Scale

After the initial oxidation at the very surface, the reactants are separated by the formed oxide scale. Prolonged oxidation requires mass transport across this oxide scale. Since oxides usually show ionic bonding, the transported species are ions and electrons as well. At the phase boundaries, metal and oxygen atoms are ionized to cations and anions, respectively

$$\mathrm{M} \rightarrow \mathrm{M}^{2+} + 2\,\mathrm{e}^{-}\,, \tag{4.7}$$

and

$$\mathrm{O} + 2\,\mathrm{e}^{-} \rightarrow \mathrm{O}^{2-}\,. \tag{4.8}$$

The cations and electrons diffuse outwards, and anions travel inwards. In most cases, either the cation or the anion transport is much faster, so that it determines the oxidation process and rate. Electroneutrality needs to be preserved locally along the whole diffusion path, which is achieved by the diffusing electrons. Since electronic mobility is usually higher than ionic mobility, electrons do not limit the reaction rate.

When cationic transport is rate determining, the oxide grows at the oxide-gas phase boundary, see Figure 4.1a)

$$\mathrm{M}^{2+} + 2\,\mathrm{e}^{-} + \frac{1}{2}\,\mathrm{O}_2 \rightarrow \mathrm{MO}\,. \tag{4.9}$$

In this case, surface cracks can be healed by overgrowing them with new oxide. When inward transport of O^{2-} is dominating, the oxide forms at the oxide-metal phase boundary, see Figure 4.1b)

$$\mathrm{M} + \mathrm{O}^{2-} \rightarrow \mathrm{MO} + 2\,\mathrm{e}^{-}\,. \tag{4.10}$$

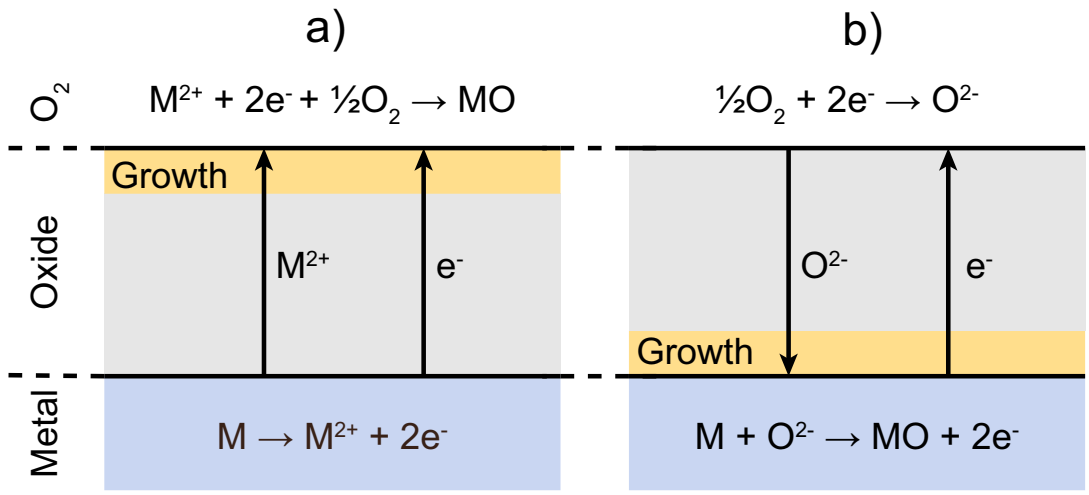

Figure 4.1: Two border cases of mass transport mechanisms through a dense oxide scale. Faster cationic a) or anionic b) transport leads to oxide formation at the oxide-gas or metal-oxide phase boundary, respectively. Adapted from [99].

Protective oxides often show predominant cationic transport, which can lead to self-healing oxide scales. [97, 99, 100]

4.3 Rate Equations

Depending on which aspect of high-temperature oxidation is limiting the reaction speed, different rate laws for the growth of oxide scale thickness x (or the mass gain Δm) with time t are used.

When the formed oxide is porous or develops cracks and voids due to large volume mismatch between metal and oxide, the transport of O_2 to the reaction front is unhindered. The oxide growth rate is then limited by the phase-boundary processes and independent of time. Since the oxide scale thickness does not influence the reaction speed, the oxide growth follows a linear relationship

$$x = k_l \cdot t\,, \tag{4.11}$$

where k_l is the linear rate constant. Linear oxidation kinetics is common in metals like Ta or Nb, which are therefore unfit as protective barriers in oxidative environments, since the metal is quickly consumed. For volatile oxides like Mo-

or W-oxides, k_l can even be negative when the formed oxide evaporates from the surface (Δm needs to be measured to observe this effect).

Where the oxide scale is compact and dense, it acts as a diffusion barrier for all species. With increasing oxidation time, the rate decreases, because the species have to diffuse through the growing oxide. A parabolic rate law describes the oxide scale growth of many materials accurately, like Fe, Al, or Si

$$x^2 = k_p \cdot t + C_p\,, \tag{4.12}$$

where k_p is the parabolic rate constant, and C_p is as an additional emperical constant. If a material forms an initial surface oxide layer very quickly, which then inhibits scale growth tremendously, a logarithmic growth model may be applicable. For pure metals it is usually only observed at low temperatures up to 400 °C

$$x = k_l \cdot \log(C_l \cdot t + B_l)\,, \tag{4.13}$$

with k_l as the logarithmic rate constant, and C_l and B_l as empirical constants. These three rate laws are presented graphically in Figure 4.2. In practice, different growth mechanisms can dominate the growth behavior as the oxide scale thickens. Especially in the early stages of oxidation the distinction is difficult. [97, 100–105]

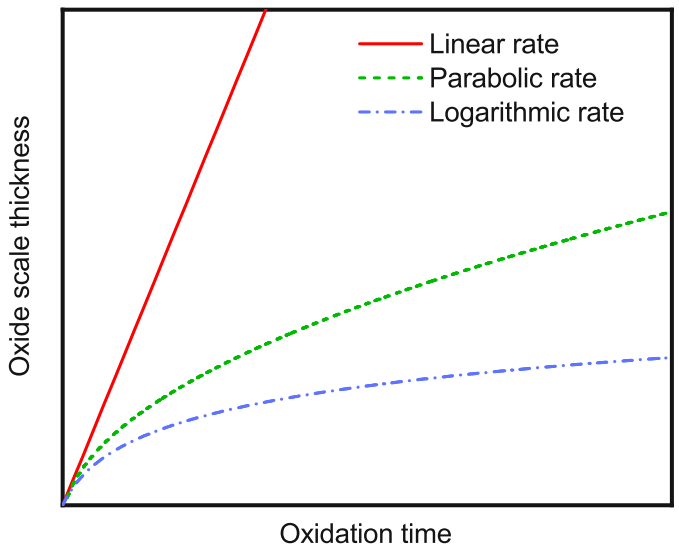

Figure 4.2: Graphical representation of three different rate laws. During the early stages of oxidation the discrimination of growth mechanisms is difficult.

CHAPTER 5

Density Functional Theory

Understanding the properties of materials on atomic scale is crucial for materials scientists. Theoretical calculations aid our understanding of materials, since they allow investigations of phenomena that are sometimes difficult or even impossible to observe experimentally. Phenomena that cannot be observed directly, or predictions over many different materials that would be to cumbersome to do experimentally, can be easily accessible by simulating the material. One of the most important – if not the most important – tools in this regard is Density Functional Theory (DFT), which is the only practical technique that gives information about the electronic structure.

5.1 The Schrödinger Equation

To predict, how a material behaves, we need to know the properties of the comprising atoms and their interactions. In a practical sense this means that we need to know the atom's energies, and how the energies react to changes of the configuration. Matter on atomic scale follows the laws of quantum mechanics that are based on the Schrödinger equation, which is a wave function of a quantum mechanical system.

Atoms consist of nuclei, which contain the protons and neutrons, and surrounding electrons. The treatment of these very different components has been simplified by the Born-Oppenheimer approximation. It states, that since electrons have much lower mass and thus also lower inertia than the nuclei, the

electrons can follow the movement of the nuclei almost instantaneously. The nuclei in contrast, are too massive to follow electronic movements and instead feel only the potential of the average electronic movement. The electronic motion can therefore be separated from the nuclear motion, and the nuclear coordinates can be considered as parameters instead of variables, which reduces the complexity of the Schrödinger equation considerably. By solving the Schrödinger equation at fixed nuclear positions, we can find the lowest energy configuration of the electrons, the so-called ground-state. This yields the so-called adiabatic potential energy surface of the atoms, which can be used to predict the behavior of the material when moving the atoms around.

The Schrödinger equation can be written in its simplest form as $\hat{\mathbb{H}}\Psi = E\Psi$, with $\hat{\mathbb{H}}$ being the Hamiltonian operator, Ψ an eigenstate of the Hamiltonian, and E the eigenvalue, which satisfies the eigenvalue equation. The detailed form of $\hat{\mathbb{H}}$ depends on the physical system that is described. A more complete, time-independent description of a system with multiple electrons interacting with multiple nuclei is

$$\left[-\frac{\hbar^2}{2m}\sum_{i=1}^{N}\nabla_i^2 + \sum_{i=1}^{N}V(\mathbf{r}_i) + \sum_{i=1}^{N}\sum_{j<i}U(\mathbf{r}_i,\mathbf{r}_j)\right]\Psi = E\Psi\,, \tag{5.1}$$

where $\hbar$ is the reduced Planck constant $h/2\pi$ ($h = 6.626\,070\,15 \cdot 10^{-34}\,\mathrm{Js}$), m the electron mass, V the interaction potential between each electron and all nuclei, and U the interaction potential between different electrons at coordinates $\mathbf{r}_i$ and $\mathbf{r}_j$. For this Hamiltonian, $\Psi = \Psi(\mathbf{r}_1, ..., \mathbf{r}_N)$ is the wave function of all N electrons, and E is the ground-state energy of the electrons. Note, that this description neglects electron spin for better clarity.

The most problematic term when solving the Schrödinger equation is the electron-electron interaction, since it poses a many-body problem. The individual wave functions $\Psi_i(\mathbf{r})$ cannot be found without simultaneously considering the individual wave functions of the other electrons. This renders analytical solutions of Schrödinger-equations with more than one electron impossible to find. However, we do not need to know the exact wave function, as it cannot be directly observed anyway. Additionally, we cannot distinguish particular electrons. The only

relevant quantity that can be measured, is the probability that a set of N electrons is located at certain coordinates, $\mathbf{r}_1, ..., \mathbf{r}_N$. What we are essentially looking for, is the electron density in space, $n(\mathbf{r})$. This density can be calculated by

$$n(\mathbf{r}) = 2 \sum_i \Psi_i^*(\mathbf{r}) \Psi_i(\mathbf{r}), \tag{5.2}$$

where the Ψ^* is the complex conjugate function of Ψ. The product inside the summation is the probability that an individual electron, denoted by the subscript "i", is located at $\mathbf{r}$. The summation over all individual wave functions then results in overall electron density $n(\mathbf{r})$. The factor of 2 accounts for the Pauli principle, since two electrons can occupy the same state, if they have different spins. Therefore, we end up with the function $n(\mathbf{r})$, that contains most of the physically observable information, and depends on only 3 coordinates, whereas the Schrödinger equation is a function of $3N$ coordinates. [106]

5.2 Arriving at Density Functionals

The field of density functional theory is based on two mathematical theorems, proved by Kohn and Hohenberg [107], and derivations of equations by Kohn and Sham [108].

The first Hohenberg-Kohn theorem states, that the ground-state energy of the Schrödinger equation is uniquely defined by a functional of the electron density. This means that the ground-state energy E can be expressed as $E[n(\mathbf{r})]$. By knowing the electron density, the ground-state energy can be acquired. This is the reason why this field is called density functional theory. Instead of finding the solution for the Schrödinger equation with $3N$ variables, we only need to find a function of 3 spatial variables, the electron density. Unfortunately, while the existence of this density functional is proven, we do not know its exact shape.

We can work around this problem with the second theorem of Hohenberg and Kohn, which states, that the electron density with the minimal energy corresponds to the full solution of the Schrödinger equation. This energy is therefore the ground-state energy. This theorem gives us a sense of direction to search for the true electron density. By varying the electron density, we arrive at the result of

the "true" functional, when the energy is minimal. This is called the variational principle.

The second important contribution is the Kohn-Sham equation,

$$\left[-\frac{\hbar^2}{2m}\nabla_i^2 + V(\mathbf{r}) + V_H(\mathbf{r}) + V_{XC}(\mathbf{r})\right]\Psi_i(\mathbf{r}) = \epsilon_i\Psi_i(\mathbf{r})\,, \tag{5.3}$$

which is a set of Schrödinger equations of non-interacting electrons that gives the same electron density as a system of interacting particles. The three potentials V, V_H, and V_{XC} are the electron-nuclei interaction, the Hartree-potential, and the exchange-correlation potential, respectively. The Hartree potential describes electrostatic interactions between an electron and the total electron density. The exchange-correlation potential is a correction term that accounts for exchange and correlation between electrons. While the other terms are well defined, the exchange-correlation potential is very difficult to solve.

Since the true form of the exchange-correlation potential is unknown, a large number of approximations have been developed, the first among them was the "Local Density Approximation" (LDA), which approximates the local exchange-correlation potential with the exchange potential of a spatially uniform electron gas with the same density. Since valence electron densities in solids usually vary only slowly, LDA provides good results in many applications of plane-waves, despite its simplicity.

The next step in approximations was the "Generalized Gradient Approximation" (GGA), which incorporates both the local electron density and the local gradient of the electron density. Since this gradient can be implemented in different ways, a number of different GGA potentials exist. Further developments have lead to so-called meta-GGA and hyper-GGA potentials, which introduce increasing amounts of input variables. Which potential performs best, depends on the investigated system. More complicated potentials perform not necessarily better, since they introduce additional constraints that can be satisfied or violated, depending on the use case. As a rule of thumb it can be stated that LDA tends to overestimate, while GGA tends to underestimate chemical binding. The development of DFT potentials is still an active field of research [109]. In this thesis, a set of GGA potentials was used for all calculations [110].

The Kohn-Sham equations are solved iteratively in a self-consistent cycle by choosing an initial electron density $n_1(\mathbf{r})$, solving the Kohn-Sham equations to obtain $\Psi_i(\mathbf{r})$, calculating the electron density $n_2(\mathbf{r}) = 2\sum_i \Psi_i^*(\mathbf{r})\Psi_i(\mathbf{r})$, and comparing $n_2(\mathbf{r})$ with $n_1(\mathbf{r})$. If the densities are equal, the ground-state has been reached, else the cycle is repeated, following the variational principle. Today, many different algorithms exist that make DFT calculations possible with very little effort. The most widespread code is the "Vienna Ab-inito Simulation Package" (VASP) [111, 112], which was also used in this thesis. [106]

5.3 Plane Waves and Reciprocal Space

Two types of functions exist to represent the solutions of the Kohn-Sham equation, localized functions and plane waves. While localized functions are ideal for atoms and molecules, periodic crystals can be represented much better by the periodic plane waves. Since crystalline solids are the subject of the investigations in this thesis, the basis of plane wave calculations will be explained in more detail here.

The Bloch theorem states, that solutions of a Schrödinger equation with periodic potential can be expressed as

$$\Psi_{\mathbf{k}}(\mathbf{r}) = \exp(i\mathbf{k}\cdot\mathbf{r})u_{\mathbf{k}}(\mathbf{r})\,, \tag{5.4}$$

where $\exp(i\mathbf{k}\cdot\mathbf{r})$ describes a plane wave, while $u_{\mathbf{k}}$ is a function with lattice periodicity. The vector $\mathbf{k}$ spans the reciprocal space (already encountered in Section 3.2.2.2), opposed to the real space vector $\mathbf{r}$. Since the reciprocal or k-space is central to DFT calculations, it will be discussed in more detail below. If we consider a periodic cell with lattice vectors $\mathbf{a}_1$, $\mathbf{a}_2$, and $\mathbf{a}_3$, then $u_{\mathbf{k}}(\mathbf{r} + n_1\mathbf{a}_1 + n_2\mathbf{a}_2 + n_3\mathbf{a}_3) = u_{\mathbf{k}}(\mathbf{r})$ for any integers n_1, n_2, and n_3. This means, that solutions for each value of $\mathbf{k}$ can be found independently. To determine $u_{\mathbf{k}}(\mathbf{r})$, it is expanded into a linear combination of basis set functions $\Psi_{j\mathbf{k}}(\mathbf{r})$

$$u_{\mathbf{k}}(\mathbf{r}) = \sum_j c_j^n(\mathbf{k})\Psi_{j\mathbf{k}}(\mathbf{r})\,. \tag{5.5}$$

In practice, the goal of a DFT calculation is the determination of the coefficients $c_j^n(\mathbf{k})$. In a typical calculation, around 100 basis functions are needed per atom.

The computational load of this calculation limits the general usefulness of DFT to systems with < 200 atoms.

Since it is mathematically much more convenient, the equations from Bloch's theorem are solved for $\mathbf{k}$ rather than $\mathbf{r}$. The reciprocal space vectors $\mathbf{b}_1$, $\mathbf{b}_2$, and $\mathbf{b}_3$ are constructed via Equation 3.15 using the real space lattice vectors $\mathbf{a}_1$, $\mathbf{a}_2$, and $\mathbf{a}_3$. In real space, a certain primitive cell can be constructed by drawing perpendicular planes at the midpoint of lines connecting a chosen lattice origin to its nearest neighboring lattice points. By connecting these planes at their intersections, a polyhedron, the Wigner-Seitz cell, is created. In reciprocal space, a primitive cell can be constructed in the same way, it is then called the Brillouin zone (BZ). This cell is important, because it is a cell with minimal volume that contains all relevant information of the crystal. All calculations can be limited to the first BZ, since the rest of the crystal follows from lattice periodicity. By accounting for symmetry in the cell, even only a fraction of the BZ can be sufficient, which is then called the irreducible BZ. Calculating an integral over the whole BZ for all possible values of $\mathbf{k}$ is computationally very demanding, therefore methods have been developed to discreetly sample the reciprocal space. The today most widespread solution was developed by Monkhorst and Pack [113], which spans a three-dimensional grid in reciprocal space of a specified number of k-points (the integration nodes) in every direction. With increasing number of k-points the accuracy, but also the computational expense increases, so that the number of k-points is kept to a minimum while seeking convergence. The required k-point density to reach convergence depends on the material and the cell size. In a supercell, fewer k-points are needed to reach the same k-point density, because the larger cell in real space corresponds to a smaller cell in reciprocal space.

The completeness of the basis set is commonly controlled by a cutoff energy, so that only plane waves with kinetic energy below the specified value are considered for each k-point. Together with the k-point spacing, the cut-off energy is the most important parameter to determine the accuracy and computational effort of a DFT calculation. [106]

5.4 Electronic structure

Since materials contain a huge number of electrons, their collective behavior is described with models and statistical functions. An early attempt to describe electrons was the Drude model, which treats electrons as "gas" particles that move between positively charged nuclei in a similar fashion to the classical kinetic theory of gasses. However, the underlying Boltzmann statistics is unable to predict properties like the thermal conductivity correctly. The Drude model was succeeded by the Sommerfeld model of the free electron, which implemented the quantum mechanical treatment of electrons. This model was introduced just one year after Bloch's theorem of periodic potentials. It considers the nature of electrons as Fermions, which implies that two electrons cannot occupy the same state (or wavefunction) due to the Pauli exclusion principle. This is reflected mathematically by the Fermi-Diraq distribution function

$$f_D(E,T) = \frac{1}{\mathrm{e}^{(E-\mu)/(k_B T)} + 1}\,, \tag{5.6}$$

where f_D is the probability of occupation of a state at energy E and temperature T. At 0 K, this probability is 1 up to μ, the chemical potential (sometimes also called Fermi-level), and 0 beyond μ. This means that the states are fully occupied by the available electrons from the lowest energy up to the threshold μ, see the graphical representation in Figure 5.1. At finite temperatures, some electrons in states at the upper end of the energy scale gain enough energy to transition into states beyond μ. The hard edge of the distribution function is therefore "softened" in a region $\approx k_B T$. The Fermi energy E_F is defined as the highest energy of an occupied state at 0 K, so that

$$E_F \equiv \mu(T = 0\,\mathrm{K})\,. \tag{5.7}$$

At finite temperatures, E_F and μ are not identical, since μ is defined as the energy at which the probability of occupation is 1/2, but in DFT calculations at 0 K these two properties are used interchangeably.

The Fermi-Diraq statistics governs the occupation of electronic states, the other important aspect are the actual states, whose energetic configuration

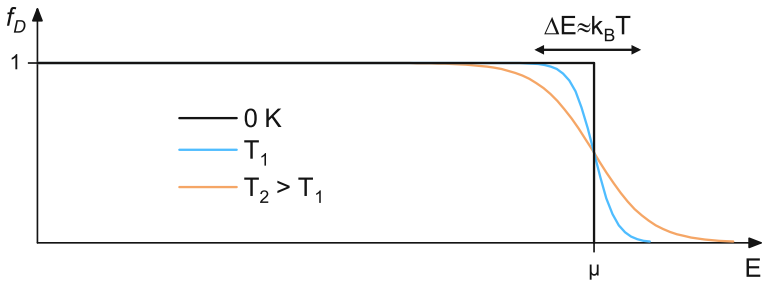

Figure 5.1: Fermi-Diraq distribution function plotted for 0 K and two temperatures T_1 and T_2 above 0 K.

depends on the element. The density of states (DOS)

$$DOS = \frac{\mathrm{d}n}{\mathrm{d}E}, \tag{5.8}$$

gives the number of electronic states n in the energy interval $(E,\ E + \mathrm{d}E)$. The presence or absence of such states around E_F determines the material's properties fundamentally. When E_F lies within a band of states, so that unoccupied states lie directly above E_F, a significant portion of the electrons near E_F can transition into higher states by thermal energy, forming partially occupied bands on both sides of E_F, in which the electrons are mobile. Mobile electrons are a key signature of metallic materials, hence such a structure in the density of states indicates metallicity. In other materials, there is a region beyond E_F without any states to occupy, so that a gap is formed between occupied and unoccupied states. Here, the electrons at or below E_F need a considerable amount of energy to transition into a higher state, so that at room temperature for example, only a very small fraction of the electrons can make this transition. Such a material is then called semiconductor, or isolator, depending on how large this band gap is.

Not only metallicity, but also covalent bonds can be made visible in the DOS. A helpful method to visualize this is the projected density of states (pDOS), where the contributions of the different s, p, and d orbitals of individual atoms to the total DOS are calculated. Two examples of ceramic materials are shown in Figure 5.2, fcc-(HfTaTiVZr)N, and rutile-(AlCrNbTaTi)O_2. In the nitride in Figure 5.2 we see that N participates only with its p electrons to the chemical bond, since the s electrons have lower energy and are closer to the nuclei. The metals contribute to the bonding a little with their p but mostly with their d

electrons. The resulting sp^3d^2 hybridization results in strong directional bonds, which are a sign of covalent bonding and responsible for the high mechanical strength of such ceramics. The region around E_F is populated by the metal d states, which results in metallic bonding characteristics as well. This reflects in mechanical behavior like ductility, but also in the appearance, as such a coating on a smooth substrate has a shiny reflective surface like a metal. Note, that the total DOS does not have to align with the pDOS contributions, since the values are given per atom and the calculation of pDOS states requires the partitioning of the k-space, the hereby resulting interstitial regions are missing in the pDOS. Hence, the absolute numbers are not as important in these considerations as the qualitative trends. [100]

While the nitride coating exhibits partial metallicity, the oxide shown in Figure 5.2b) is a semiconductor. Again, no s states are contributing to the bonding, since they are energetically too low. Instead O p states bond with the metal d and p states like in the nitride. A difference is here, that the metal p and d states are more separated in energy, with the p states contributing more in the region between -1 and -3 eV, and the d states contributing more between -4 and -6 eV. At E_F, a distinct energy gap E_g of ≈ 1.2 eV is evident, after which the states of the conduction band continue. Note, that the estimation of band gaps is very inaccurate in general DFT calculations due to the unknown exact exchange-correlation potential [114, 115], and the fact that DFT is a ground-state theory, whereas a band gap implies excitation. [106, 116]

5.5 Phase Stability

Calculating the phase stability of compounds like ceramics is done by comparing the energy of a material to the energies of its constituents. A useful quantity for this purpose is the energy of formation, E_f, which represents the driving force to form a compound out of its elements in their ground-states. It is calculated as

$$E_f = \frac{1}{\sum_i n_i} \left(E_{tot} - \sum_i \mu_i n_i \right), \tag{5.9}$$

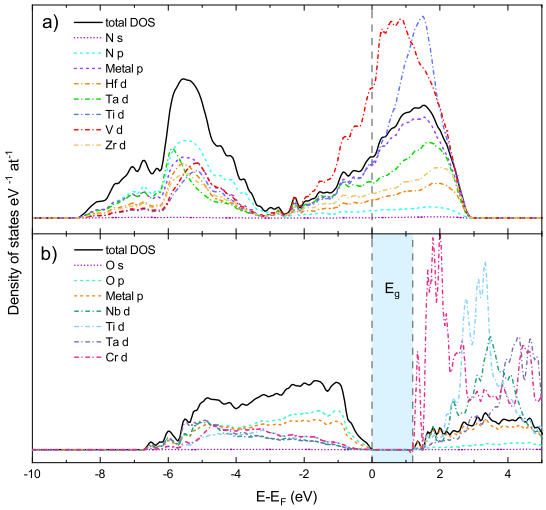

Figure 5.2: Projected density of states around E_F of a) (HfTaTiVZr)N with partial metallicity, and b) (AlCrNbTaTi)O_2 with a band gap E_g.

where E_{tot} is the total energy of the calculated cell, and μ_i and n_i are the chemical potential and number of atoms of the ith element in the cell. The chemical potential is calculated from the total energies of the respective ground-state structures

$$\mu_i = E_{tot,i}/n_i\,. \tag{5.10}$$

Here, $E_{tot,i}$ and n_i are with respect to the ground state structure of the ith element. Since the variational principle states that the lowest energy that can be found is ground-state energy, the cells are relaxed regarding a combination of cell size, shape, and atomic distances to give the configuration with the lowest energy. Caution needs to be exercised, since wrong starting conditions can lead to local minima that do not represent the ground-state. It is therefore good practice to pick known structures of similar compositions as starting conditions when investigating new systems.

For metals, the ground-state structure is their thermodynamically most stable structure, this is for instance the fcc structure for Al, the hexagonal close packed structure for Ti, or the bcc structure for W. For the gaseous nonmetals N and O, the chemical potential is calculated from their molecular dimers N_2, and O_2, respectively, for C the ground-state structure is the graphite phase, while B is calculated in its own complicated rhombohedral structure. A negative E_f

means that the compound will form spontaneously from its constituents in their ground-state structures, e.g. E_f(fcc-TiN) $= -1.9\,\mathrm{eV/at}$ means that TiN forms spontaneously out of Ti and N_2. E_f(fcc-WN) $= 0.3\,\mathrm{eV/at}$ indicates that WN is not stable in this structure and composition (but WN can form in the fcc-structure with N-vacancies or in the NbO structure with 1:1 stoichiometry [117]). The values of E_f depend on the chosen potentials, so that consistency between calculations is essential for the analysis of phase stability. The consideration of phase stability by DFT is purely thermodynamic in nature and does not take temperature or kinetics into account.

HESC, just like many lower-entropy counterparts, can be understood as mixture of their respective binary ceramics, so that (Al, Ti)N for example is composed of AlN and TiN. The properties of (Al, Ti)N in PVD coatings depend considerably on the stability of this solid solution. This solid solution is only metastable, so that wurtzite structured AlN domains form out of the (Al, Ti)N compound and soften the material tremendously during annealing [7]. Due to the contribution of configurational entropy to the free enthalpy, high-entropy materials have been presented as entropy-stabilized against such decomposition [52]. The thermodynamic driving force for mixing, ΔH_{mix}, can be predicted with DFT simply by using the E_f of the respective phases

$$\Delta H_{mix} = E_{f,product} - \sum_i \nu_i E_{f,i}\,, \tag{5.11}$$

where $E_{f,product}$ is the energy of formation of the mixing product, and ν_i and $E_{f,i}$ are the stoichiometric coefficient and energy of formation of the ith mixing educt. For the reaction between a HESN and a ternary and quaternary nitride for example, the schematic reaction can be formulated as

$$(A_{0.2}B_{0.2}C_{0.2}D_{0.2}E_{0.2})N \longleftrightarrow (A_{0.2}B_{0.2}C_{0.2})N_{0.6} + (D_{0.2}E_{0.2})N_{0.4}\,. \tag{5.12}$$

If $\Delta H_{mix} > 0$, the mixing product is unstable with respect to this reaction so that the HESN would not form, if $\Delta H_{mix} < 0$, the HESN would be stable. Equation 5.11 considers only enthalpy contributions at 0 K. For configurational entropy to act, $T > 0\,\mathrm{K}$ is required, we can therefore modify Equation 2.2 to get

$$\Delta G_{mix} = E_{f,product} - \sum_i \nu_i E_{f,i} - T\Delta S_{mix}\,. \tag{5.13}$$

Since ΔS_{mix} is the difference in configurational entropy between the product and educts, we can reformulate Equation 5.13 for equiatomic solid solutions by taking Equation 2.4 into account

$$\Delta G_{mix} = E_{f,product} - \sum_i \nu_i E_{f,i} - TR\left(\ln N_{product} - \sum_i \nu_i \ln N_i\right), \tag{5.14}$$

where $N_{product}$ and N_i are the number of elements distributed on the metal-sublattice of the product and the ith mixing educt, respectively. For the reaction in Equation 5.12, ν_i would be 0.6 and 0.4 for the quaternary and ternary nitride, respectively. This simplified description still lacks contributions to the total molar entropy by different atom sizes, atomic vibrations, magnetic moments, and electronic effects, whose investigation requires substantial computational effort.

Since high-entropy materials are highly disordered systems with randomly distributed elements, and plane waves are strictly periodic by nature, the cells have to be prepared in a special way to accommodate this property. One of most popular methods is the supercell approach with special quasi-random structures (SQS) [118]. It uses a supercell, where the atoms are distributed not completely randomly across their respective sublattices, but following the Warren-Cowley short-range order parameter. For the simple case of a mixture of 2 atomic species A and B, it can be expressed as

$$\alpha_j = 1 - \frac{N_{AB}^j}{x_A x_B N M_j}, \tag{5.15}$$

where N_{AB}^j is the number of A–B bonds between sites in the jth neighbor distance, N is the number of atoms in the supercell, x_A and x_B are the concentrations of A and B, and M_j is the number of neighbors on the jth coordination sphere. The value of α_j determines whether random alloying or an ordered phase is present. For $\alpha_j < 0$, ordering occurs, for $\alpha_j > 0$ clustering, and for $\alpha_j = 0$ a statistically random alloy is simulated. [106, 119]

5.6 Elastic Properties

DFT also allows the study of elastic properties of crystals by applying deformations to the simulation cell and mapping the corresponding changes in energy. Plastic

deformations on the other hand would require the movement of dislocations for example, which is not possible in the limited cell sizes of DFT (but ab-initio molecular dynamics is a suitable related technique, which sacrifices information on the electronic structure for larger simulation cell limits [120]).

5.6.1 Hooke's Law

When a force acts on a solid body, the applied stress causes a corresponding strain. In the case of sufficiently small deformations, these stresses and strains can be modeled within harmonic elasticity as second-rank tensors σ_{ij} and ϵ_{kl}, respectively. These properties can be visualized in a 3-dimensional coordinate system on a cubic volume element of the stressed body. The stress tensor σ_{ij}, with $(i, j = 1, 2, 3)$, contains the component of the applied force in the ith direction of the coordinate system acting on the face of the cube that faces the jth direction, the same applies also to the resulting strain with $(k, l = 1, 2, 3)$. The relationship between stress and strain in the linear elastic regime (reversible small deformations, since no bonds are broken) is governed by Hooke's law:

$$\epsilon_{ij} = S_{ijkl}\sigma_{kl} \quad (i, j, k, l = 1, 2, 3)\,, \tag{5.16}$$

or in the alternative formulation

$$\sigma_{ij} = C_{ijkl}\epsilon_{kl} \quad (i, j, k, l = 1, 2, 3)\,, \tag{5.17}$$

where S_{ijkl} and C_{ijkl} are the so-called compliance and stiffness tensors, both fourth rank tensors that characterize the material. Note, that this representation uses the Einstein summation convention, where the terms are summed up with respect to each suffix that occurs twice. Since each suffix runs from 1 to 3, Equation 5.17 represents 9 equations, each containing 9 terms on the right side. The stiffness tensor therefore consists of 81 components that characterize the material (the same and also the following relations are true for the compliance tensor as well). Due to inherent symmetry of the stress and strain tensors,

$$C_{ijkl} = C_{ijlk}, \quad C_{ijkl} = C_{jikl}\,, \tag{5.18}$$

so that only 36 of the 81 components of C_{ijkl} are independent. Additionally, $C_{ijkl} = C_{klij}$, which further reduces the number of independent components to

21. In light of this symmetry, the suffix notation can be simplified by the Voigt notation, which abbreviates two suffixes into one, running from 1 to 6 (Table 5.1).

Table 5.1: Voigt notation for symmetrical tensor suffixes.

Tensor notation	11	22	33	23,32	13,31	12,21
Voigt notation	1	2	3	4	5	6

In this notation, Equation 5.17 can be written as

$$\sigma_i = C_{ij}\epsilon_j \quad (i,j = 1,2,...,6)\,, \tag{5.19}$$

so that the stiffness tensor can be expressed as a 6×6 matrix

$$C_{ij} = \begin{pmatrix} C_{11} & C_{12} & C_{13} & C_{14} & C_{15} & C_{16} \\ C_{21} & C_{22} & C_{23} & C_{24} & C_{25} & C_{26} \\ C_{31} & C_{32} & C_{33} & C_{34} & C_{35} & C_{36} \\ C_{41} & C_{42} & C_{43} & C_{44} & C_{45} & C_{46} \\ C_{51} & C_{52} & C_{53} & C_{54} & C_{55} & C_{56} \\ C_{61} & C_{62} & C_{63} & C_{64} & C_{65} & C_{66} \end{pmatrix}. \tag{5.20}$$

Here, C_{ij} are also called the elastic constants. Due to the mentioned symmetries, $C_{ij} = C_{ji}$, so that only components on the upper or lower side of the diagonal components need to be considered, leaving 21 independent components in the most general case. By crystal symmetry, the number of independent components can be reduced even further. In the case of a cubic crystal, most relevant for nitrides, only three independent components remain, since $C_{11} = C_{22} = C_{33}$, $C_{12} = C_{13} = C_{23}$, and $C_{44} = C_{55} = C_{66}$, while all other components are 0. In this case C_{11} describes the crystals response to compression or tension, while C_{12} and C_{44} govern the response to two types of shear deformation.

When a crystal is subjected to a small strain $d\epsilon_i$, the hereby done work is

$$dW = V_0\sigma_i d\epsilon_i \quad (i = 1,2,..,6)\,, \tag{5.21}$$

with V_0 being the cell volume. When this deformation is isothermal and reversible, the work done is equal to the change in free energy dE. Using Equation 5.19, we can write

$$dE = V_0 c_{ij}\epsilon_j d\epsilon_i\,, \tag{5.22}$$

Using the relationship $C_{ij} = C_{ji}$, Equation 5.22 can be integrated to give the strain energy

$$E_{strain} = \frac{V_0}{2} C_{ij} \epsilon_i \epsilon_j \,, \tag{5.23}$$

In all symmetry classes, the elastic constants are subject to further restrictions, since the applied stress must lead to a positive strain energy. A fundamental principle of Hooke's law is that the deformation is reversible, so that the original structure is regained when removing the stress. If a deformation would lead to a negative strain energy, it would consequently lead to a new equilibrium structure with lower energy, thus the original structure would be mechanically unstable. For a cubic crystal, this condition is

$$C_{44} > 0, \quad C_{11} > |C_{12}|, \quad C_{11} + 2C_{12} > 0 \,, \tag{5.24}$$

other crystal symmetries have similar constraints. [121, 122]

5.6.2 Calculation of Elastic Properties

The basis for calculating elastic properties is always the equilibrium structure, obtained by structural relaxation of an input cell. From there, Equation 5.22 enables two methods to calculate the C_{ij} matrix, the total energy method, and the stress-strain method. The total energy method uses the variation of total energy with strain to calculate C_{ij} from Equation 5.22, while the stress-strain method uses the variation of stress with strain Equation 5.19. It was shown that the stress-strain method converges faster under the same cutoff energies and k-point densities, since the introduction of strain in the total energy method changes the lattice vectors and consequently the basis set (Equation 5.5), while the stress tensor calculation works in a fixed basis set [122]. The stress-strain method was therefore also used in this thesis, using the implementation by Yu et al. [123].

From the elastic constants, several physical properties can be derived. The exact elastic moduli are not directly accessible from C_{ij} or S_{ij}, but upper and lower polycrystalline limits have been formulated as the Voigt and Reuss estimates of the bulk modulus

$$B_V = \frac{(C_{11} + C_{22} + C_{33}) + 2(C_{12} + C_{13} + C_{23})}{9} \,, \tag{5.25}$$

$$B_R = \frac{1}{(S_{11}+S_{22}+S_{33})+2(S_{12}+S_{13}+S_{23})}, \tag{5.26}$$

and the shear modulus

$$G_V = \frac{(C_{11}+C_{22}+C_{33})-(C_{12}+C_{13}+C_{23})+3(C_{44}+C_{55}+C_{66})}{15}, \tag{5.27}$$

and

$$G_R = \frac{15}{4(S_{11}+S_{22}+S_{33})-4(S_{12}+S_{13}+S_{23})+3(S_{44}+S_{55}+S_{66})}. \tag{5.28}$$

Usually, the Hill average is used as approximate value: $B = (B_R + B_V)/2$ and $G = (G_R + R_V)/2$. Other related properties such as the Young's modulus

$$\frac{1}{E} = \frac{1}{3G} + \frac{1}{9B}, \tag{5.29}$$

and the Poisson's ratio

$$\nu = \frac{1}{2}\left(1 - \frac{3G}{3B+G}\right), \tag{5.30}$$

can be derived from B and G. The ductility/brittleness of a crystal can be estimated from the so-called Pugh-ratio via the G/B ratio [124], or the Cauchy-pressure, $C_{12} - C_{44}$ [125].

5.7 High-Throughput Computing

The objective of materials science is the exploration of new materials with improved properties to support technological advances of our society. The current state of the art in many areas is already in a very developed state with many niche technologies for certain purposes. The demand for new materials is ever growing, but experimental setups struggle to meet these demands due to high cost and time-consuming procedures. The research of new compositions has therefore been revolutionized by high-throughput computations, which allow rapid exploration of vast compositional spaces in comparatively short times, made possible by efficient theoretical tools like DFT or "CALculations of PHAse Diagram" (CALPHAD) and cheap computational hardware, realized in supercomputers with ever increasing performance, like the Vienna Scientific Cluster (VSC) that was used for the

calculations in this thesis. Combinatorial approaches have been employed in the past to reduce the amount of needed experiments needed for insights. In constrast to combinatorics, high-throughput exploration has been defined as a throughput of data that is too large to be evaluated by the researcher directly. Instead, algorithms and databases take on this workload, freeing the researcher's hands and mind for creative interpretation of the results [126].

The number of possible material combinations is especially overwhelming for high-entropy materials. As mentioned in the introductory chapter, if one designs alloys from 40 different elements with compositional steps of 1 at% between each alloy, the number of possible alloys is 10^{78}, which is far more than the number of atoms in our universe (10^{66}). This is of course overwhelming for both experimental and computational methods, but in more modest phase spaces the utility of computational tools have been proven several times [8].

Metallic HEA have attracted far more attention than their ceramic counterparts so far. This also reflects in high-throughput studies. Phase stabilities of metallic high-entropy alloys have been studied extensively by means of CALPHAD [50, 127] or DFT [128, 129], in the field of HESC on the other hand, most ab-initio studies have focused on selected carbides [31, 130–132], oxides [60, 133, 134], borides [27, 135], nitrides [66, 136], or carbonitrides [137].

One notable exception is a study on high-entropy sublattice carbides by Sarker et al. [34], who developed the so-called "entropy forming ability" (EFA) descriptor to predict the synthesizability of single-phase high-entropy sublattice carbides. The authors postulated that the energy spread of different permuted geometric configurations within small ordered cells of equal chemical composition, like (MoNbTaVW)C for example, can be used to predict the tendency to form a single-phase solid solution. If the spread in energies is small, this indicates a low barrier to form a solid solution, whereas a high spread would mean that certain configurations are energetically much more beneficial than others, which leads to ordering. The experimental validation of selected compositions proved successful, however, all of the reported compositions exhibit positive formation enthalpies and are thus metastable. A Pearsson correlation coefficient of -0.2 between the reported energies of formation and the EFA values indicates that

these properties are at best loosely connected. Also, the configurational entropy of all investigated systems is nearly the same. While entropy stabilization is claimed by the authors for compositions with high EFA, nothing in the EFA formulation (considering only energies) hints at an entropy contribution. Since the configurational entropy is similar throughout all compositions, and there is no clear relationship between EFA and formation enthalpy, the EFA cannot be used rigorously to claim entropy-stabilization, which would require a clear influence on ΔG_{mix}. Instead, it seems that the EFA descriptor represents only a kinetic barrier for phase separation, since the reported single-phase structures are only in as-cast condition (no cooling rate after synthesis at 2200 °C for 5 min was stated by the authors). The focus on as-cast microstructures has been recognized as methodical oversight in studies on metallic high-entropy alloys, so that these results should be interpreted with care [44]. In summary, this EFA descriptor is not suitable to study the impact of configurational entropy.

5.8 Limitations

All theoretical tools operate with certain limitations, for DFT this is for example the unknown exchange-correlation potential, which manifests in the poor prediction of band gaps. Another limitation is the computational effort, which strongly depends on the size of the basis set (Equation 5.5). The computation time scales with roughly the third power of the number of atoms in the cell. Despite modern supercomputers, the practical limit for calculations is soon reached, so that systems with <200 atoms are generally feasible to investigate. But for large amounts of calculations, such as in high-throughput studies, this number becomes even smaller, so that for a fcc HESN the $2 \times 2 \times 2$ supercell with 64 atoms is reasonable, whereas the next larger cubic $3 \times 3 \times 3$ supercell contains 216 atoms. The size limit produces several consequences. Due to the small number of atoms, concentrations of different elements can be adjusted only on a relatively coarse mesh. The impact of dopants, which often range in concentrations of parts per million and influence semiconductors immensely, can not be modeled at all, since the smallest quantity that can be added is a single

atom. Short-range interactions can also influence material properties significantly in a SQS setup, so that sufficiently large cells should be chosen to minimize these effects.

For these reasons the properties of perfect, infinite, surface-less DFT cells at 0 K can deviate strongly from the properties of real materials with their imperfections, grain boundaries, and surfaces at finite temperatures. The key of DFT investigations is the translation of properties in these small ideal cells onto real materials. Calculations should therefore also seek experimental validation within a reasonable scope. Combinatorial approaches of computational predictions with experimental validation of a selected subset are thus commonplace in materials science. [106, 126]

CHAPTER 6

Si-alloying of (Al,Cr,Nb,Ta,Ti)N Thin Films

The here presented results have been published in *A. Kretschmer, A. Kirnbauer, V. Moraes, D. Primetzhofer, K. Yalamanchili, H. Rudigier, P. H. Mayrhofer*, Improving phase stability, hardness, and oxidation resistance of reactively magnetron sputtered (Al,Cr,Nb,Ta,Ti)N thin films by Si-alloying, *Surface and Coatings Technology 416 (February) (2021) 127162.* doi:10.1016/j.surfcoat.2021.127162.

6.1 Introduction

A common strategy to increase the lifetime of machining tools, which need to resist wear under harsh conditions, is the use of hard protective coatings. TiN, (Ti,Al)N, (Al,Cr)N, and similar nitride based materials have been developed to protect various machining tools from abrasion and oxidation [3–6, 138–140]. Especially when synthesized by physical or chemical vapor deposition – allowing for extended solubility limits – the addition of selected alloying elements is a powerful approach to further improve their desired properties.

In 2004, Cantor et al. [9] and Yeh et al. [10] developed so-called high-entropy alloys (HEA), which consist of five or more principal elements with an equiatomic or near-equiatomic composition. Hence, this compound contains no

dominant species. High-entropy materials are commonly characterized by four core effects: high configurational entropy $\Delta S_{conf} > 1.5 \cdot R$ (R being the universal gas constant), a highly distorted crystal lattice, sluggish diffusion and the cocktail-effect [44, 127, 141]. This concept has also been expanded to high-entropy ceramics, which after a simplified notation [8, 26] consist of at least five constituting binaries. A more-precise and accurate notification was introduced recently [66] with high-entropy sublattice ceramics. As in principle only the metal-sublattice has a high entropy [26], whereas the non-metal-sublattice is formed basically by one principal element, when combining various nitrides [66, 142–144], carbides [132, 145, 146], oxides [21, 147], borides [25–27, 148], or silicides [39, 40]. Thereby, the respective non-metal occupies its own sublattice, whereas the different metal species are randomly distributed on their sublattice. Consequently, the configurational entropy essentially stems from the metal sublattice, if the non-metal sublattice is occupied by one element. By the common definition, $\Delta S_{conf} > 1.5 \cdot R$, such a material would not be considered high-entropic, but this value was intended for metallic alloys.

Ceramics are an entirely different material class, therefore when searching for the high-entropy effect in a ceramic, this criterion should be adjusted accordingly. A high-entropy material is characterized by the lack of a dominant solvent in a solid solution with many elements. For five or more components in near-equiatomic composition, such an arrangement, which is always accompanied by a high configurational entropy compared to conventional alloys, leads to a highly distorted lattice and other favorable properties of high-entropy materials. Additionally, the positions of the non-metal atoms are not independent from the metal sublattice. On the contrary, each non-metal atom is bound to a strongly varying surrounding, similar to each metal atom in an alloy. Therefore, we alter the definition of a high-entropy ceramic so that the configurational entropy is not considered per atom, but per constituting binary compound [26]. This approach is convenient, since the numerical value for classifying a high-entropy material then matches the criterion for metallic alloys ($\Delta S_{conf} > 1.5 \cdot R$) for all kinds of stoichiometric ratios in ceramics.

The high-entropy effects lead to materials that possess excellent mechanical

properties and are stable at high temperatures [143, 144, 149, 150]. Furthermore, the transport of ionic or atomic species through the lattice is significantly retarded [68, 70, 71, 151]. These key-properties advocate this material class as suitable candidates for protective coatings. However, most studies on high-entropy sublattice nitrides have been performed in vacuum conditions, whereas in real-life applications the presence of O_2 is limiting the durability of these materials. Many studies have been performed to tailor oxidation resistance in low-entropy nitrides, by adding Ta, Y, or Ce for example [139, 152–154]. We still lack such studies for high-entropy ceramics. To our knowledge, the most notable work on this problem was done by Shen et al. by developing the high-entropy sublattice nitride $(Al_{0.34}Cr_{0.22}Nb_{0.11}Si_{0.11}Ti_{0.22})_{50}N_{50}$ with exceptional oxidation resistance at high temperatures [142]. They attribute this property to the presence of dense layers of Al_2O_3 and amorphous oxide layers, which are largely composed of Si-oxides. In this work we present the impact of Si-alloying on the similar material system (Al,Cr,Nb,Ta,Ti)N and the resulting improvements to not only oxidation resistance, but also phase stability and mechanical properties.

6.2 Methods

6.2.1 Deposition Process

We used reactive magnetron sputtering with a modified Leybold Heraeus Z400 magnetron sputtering system, equipped with a powder metallurgically prepared 75-mm-diameter target of equimolar Al, Cr, Nb, Ta, and Ti composition (Plansee Composite Materials GmbH). Si was added by placing 8, 12, 16, or 24 ($2 \times 2 \times 0.38\,mm^3$) pieces evenly on the cathode racetrack. The $Al_uCr_vNb_wTa_xTi_ySi_zN$ coatings were deposited on (1 0 0)-oriented Si ($20 \times 7 \times 0.38\,mm^3$) and ($1\,\bar{1}\,0\,2$) sapphire ($10 \times 10 \times 0.53\,mm^3$) substrates, mounted face-to-face to the target at a distance of 4 cm. For all depositions the base pressure was below 0.3 mPa, the deposition temperature was 440 °C and the bias potential was -50 V DC. Before the deposition process, the substrates were Ar-ion etched at a pressure of 1.3 Pa for 15 min by applying a negative pulsed DC substrate potential of -150 V, the

pulse frequency was 150 kHz and the pulse duration 2496 ns.

The target was also cleaned by sputtering for 2 min behind the closed shutter. A 18 sccm/22 sccm gas mixture of N_2 and Ar (both 99.999 % purity) at a pressure of 0.43 mbar was used for the deposition. The cathode was operated with a constant current of 1.0 A (power density of 11.9 W/cm^2) and 0.75 A (power density of 9.1 W/cm^2) without and with Si pieces on the racetrack, respectively, for 20 min in all cases. The reduction of the sputtering-current for preparing the Si-alloyed coatings was needed to prevent breaking of the Si substrates due to increased growth stresses.

6.2.2 Sample Analysis

Cross-sections of the coatings on Si-substrates were analyzed with a FEI Quanta F200 scanning electron microscope – equipped with a field emission gun and operated at 5 kV – to investigate growth morphology and deposition rates. Chemical compositions of as-deposited coatings were analyzed by time-of-flight elastic recoil detection analysis (ToF-ERDA) with a recoil detection angle of 45° using a beam of 36 MeV I^{8+} ions. Experimental details, data analysis as well as potential systematic uncertainties are described elsewhere [155–157]. The crystal structure was investigated with X-ray-diffraction using a PANanlytical XPert Pro MPD ($\theta - \theta$ diffractometer) equipped with a Cu–Kα source ($\lambda = 0.154\,08$ nm, 45 kV and 40 mA) in Bragg-Brentano geometry. Samples on sapphire substrates were vacuum annealed in a Centorr LF22-2000 vacuum furnace at T_a = 800, 900, 1000, 1100, and 1200 °C, the heating rate was 20 K/min, the holding time 10 min, and the passive (simply turning off the heater) cooling rate at least 50 K/min down to 200 °C.

To study the oxidation resistance of the coatings, the thickness as well as chemistry of the oxide scale growing at 850 °C were studied by SEM. After an oxidation treatment within an ambient-air furnace at 850 °C for 0.5, 1, 5, 10, 30, and 100 h, the coated sapphire samples were extracted from the hot zone, cooled down to room temperature, and prepared for cross-sectional investigations. The mirror polished embedded cross sections were analyzed by energy dispersive X-ray spectroscopy-linescans across the oxide scale using a 20 kV electron beam.

Transmission electron microscopy was performed with a FEI TECNAI F20, equipped with a FEG, operated at 200 kV, on as-deposited and oxidized samples.

Mechanical properties were determined using an ultra-micro-indentation system equipped with a Berkovich tip. Indentation hardness, H, and modulus, E_I, – which, depending on materials behavior during indentation, may also be treated as Young's modulus – were obtained by evaluating the unloading segments of the indentation curves after Oliver and Pharr [96] assuming a Poisson's ratio of 0.25.

6.2.3 DFT Calculations

DFT calculations were carried out with the Vienna ab-initio simulation package (VASP) [111, 112], using projector augmented plane wave (PAW) pseudo-potentials under the generalized gradient approximation [108] to study the solid solution of $(Al, Cr, Nb, Ta, Ti)O_2$ in rutile structure, with equimolar composition, and possible decomposition products. A plane-wave cut-off energy of 600 eV, and a Γ-centered Monkhorst-Pack k-mesh [113] with $6 \times 6 \times 7$ points were used. The accuracy was set to 10^{-5} eV/at. The cells were relaxed regarding volume, shape and atomic positions. The decomposition of equiatomic $(Al, Cr, Nb, Ta, Ti)O_2$ into all possible combinations of lower-order oxides (binary, ternary, quaternary, and quintenary oxides) with equimolar composition was considered. All oxides were rutile structured (space group 136 $P4_2/mnm$), with the exception of the binaries, which were calculated both in rutile structure and their common stable structures. These are Al_2O_3 (α-structure, space group 167 $R\bar{3}c$), Cr_2O_3 (Al_2O_3-prototype, space group 167 $R\bar{3}c$), Nb_2O_5 (space group 10 $P12/m1$), Ta_2O_5 (space group 25, $Pmm2$), and TiO_2 in rutile structure. The binaries were calculated from single cells, while all multinary oxides were calculated from a $3 \times 3 \times 2$ supercell with 72 atoms in total. The metals were placed on their sublattice with the special quasi-random structure (SQS) method [118]. To reach equiatomic composition for the hexinary oxide (25 atoms on 24 positions), five permutations with different occupations, leaving one atom per metallic species out in turn, were calculated and averaged.

The thermodynamic phase stability is determined by the free enthalpy of

Table 6.1: Chemical Analysis in at% as deduced from ToF-ERDA. Since the masses of Al and Si could not be distinguished, their ratio is estimated from the Al ratio to the other metals in the sample without Si. The given uncertainties are the statistical standard errors, for Al and Si in Si-containing coatings the standard error of the sum concentration is given.ΔS_{conf} of the metal sublattice is given as multitude of R and is always $\geq 1.52 \cdot R$.

Si-pieces	Al	Cr	Nb	Si	Ta	Ti	N	$\Delta S_{conf} \cdot R$
0	9.6±0.1	11.6±0.1	7.0±0.1	0.0	7.1±0.2	9.4±0.1	55.4±0.4	1.52
8	8.1±0.1	10.9±0.1	6.2±0.1	6.4±0.1	5.4±0.1	7.7±0.2	54.9±0.3	1.68
12	7.3±0.3	9.1±0.1	5.8±0.1	9.8±0.3	4.9±0.1	6.9±0.1	55.4±0.2	1.66
16	6.8±0.1	7.5±0.1	5.4±0.1	12.0±0.1	5.0±0.1	6.6±0.1	55.9±0.2	1.63
24	6.1±0.2	7.7±0.1	4.7±0.1	15.0±0.2	4.4±0.1	5.8±0.1	55.0±0.3	1.59

mixing ΔG_{mix}, consisting of enthalpic and entropic contributions (Equation 2.2). Since the mixing entropy is only contained in the metal sublattice, which makes up 1/3 of the atoms, the weights in Equation 2.5 need to be adjusted accordingly for the MO_2 stoichiometry.

6.3 Results and Discussion

6.3.1 Chemical Composition and Growth Morphology

The results of the chemical analysis with ERDA are shown in Table 6.1. The depth profiles were all homogenous except for a thin surface oxide layer, the concentrations were therefore calculated from the bulk signals of the coatings. All coatings are overstoichiometric with a N-content of > 54.9 at%. Since the masses of Al and Si could not be distinguished, only a sum of both elements is available. However, by calculating the average elemental ratio of Al to the other metals in the Si-free sample, the Al content and thus the Si content can be estimated for the other samples. With increasing number of Si-pieces on the racetrack the concentrations of the other metals decrease, but not proportionately to each other. In the coating with the highest Si-content the Cr, Nb, Ta, and Ti concentrations decrease by 34, 33, 39, and 38 %, respectively, compared to the Si-free sample. The average decrease of up to 36 % (in the coating with the highest Si concentration) was used to estimate the Al concentration, the Si concentration was then calculated as difference to the sum signal.

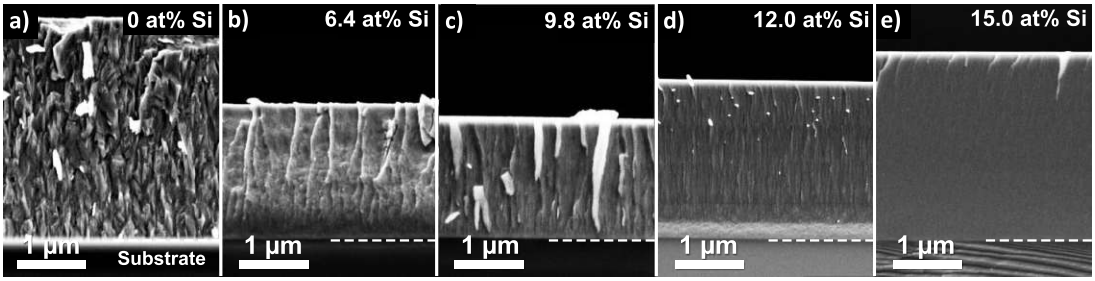

Figure 6.1: SEM fracture cross-sections of as-deposited (Al, Cr, Nb, Si, Ta, Ti)N coatings with 0 at% Si a), 6.4 at% Si b), 9.8 at% Si c), 12.0 at% Si d), and 15.0 at% Si e), deposited on (1 0 0) Si substrates. The columnar structure becomes finer with increasing Si-content, and the coating with 15.0 at% Si even shows a feature-less growth morphology.

Contrary to the metals, the N-content stays in a range between 54.9 to 55.9 at%. This overstoichiometry could be supported by metal vacancies, as was shown for TaN with ab-initio calculations [158], and the slightly different stoichiometry of Si_3N_4. All stated uncertainties are standard errors, for Al and Si in Si-containing coatings the standard error of the sum concentration is given. The configurational entropy S_{conf} is highest in the sample with 9.8 at% Si, and always $\geq 1.52 \cdot R$ (considered per formula unit). Therefore, by our definition all coatings can be considered HESN.

In Figure 6.1, the SEM-micrographs of the fracture cross-sections of as-deposited coatings reveal dense microstructures and smooth surfaces. Nevertheless, the addition of Si clearly influences the growth morphology of the individual coatings starting from a rather coarse grained and columnar structure for the Si-free sample, Figure 6.1a). Increasing the Si content to 6.4 to 9.8 to 12.0 at% results in a less-pronounced columnar growth structure, Figure 6.1b), c), and d), respectively, and even an almost featureless structure for the 15.0 at% Si-containing coating, Figure 6.1e). The deposition rates are 160 nm/min without Si at 1.0 A target current, and between 85 and 140 nm/min with Si at 0.75 A target current. The total coating thicknesses in order of increasing Si contents are 3.2, 2.0, 1.7, 2.3, and 2.7 µm, respectively. When the latter deposition rates are normalized to a current of 1 A, the growth rates lie between 113 and 186 nm/min. Thus, the differences in growth rates basically stem from the Si platelets added to the racetrack and the individual elements.

TEM analysis of our coatings on sapphire substrates support the growth morphology results obtained by SEM. Exemplarily, we show cross-sectional TEM images for the (Al, Cr, Nb, Ta, Ti)N coating without Si and with 9.8 at% Si in Figure 6.2a) and b), respectively. Although the mean column diameter decreases by the addition of 9.8 at% Si, their columnar structure is still clearly present. The corresponding selected area electron diffraction patterns (taken at positions marked by I and II in Figure 6.2a) and b), respectively) yield single-phase solid solutions with fcc rock-salt structure. The more ring-like SAED pattern for the Si-free sample hints towards a more random growth orientation. The 9.8 at% Si alloyed (Al, Cr, Nb, Ta, Ti)N coating shows more individual SAED spots suggesting a highly oriented growth. This is also because the individual columns seem to be longer for the 9.8 at% Si-containing coating. Therefore, the selected area for the SAED pattern covers basically only one column length for the 9.8 at% Si-containing coating but several ones for the Si-free HESN, see Figure 6.2b) and a), respectively. Dark field investigations nicely show that the Si-free coating in Figure 6.2c) has shorter columns than the 9.8 at% Si-containing one in Figure 6.2d). Interestingly, as suggested already by the bright field investigations, the mean column diameter decreases from around 50 to 25 nm with increasing Si content.

Spatially resolved analysis of the Si concentration is problematic due to the coincidence of the Si and Ta signals in the EDS spectrum, as well as the partial overlap of Si and Al and Si and Ta edges in the electron energy loss spectrum. But in a plan-view TEM sample of the HESN with 9.8 at% Si we could find an indication that Si is enriched in the grain boundary region, similar to TiN when alloyed with more than 4 at% Si [159, 160]. The corresponding plan-view bright field and dark field images in Figure 6.3a) and b) show that the column diameters agree well with those obtained from the cross-sectional investigations presented in Figure 6.2d). In scanning transmission electron microscopy (STEM) mode with a high angle annular dark field (HAADF) detector the contrast is generated by local sample mass and thickness. Since this sample was prepared by focused ion beam we can exclude high surface roughness to cause local intensity variations. The bright spot in Figure 6.3c) can therefore be assigned to a grain with either

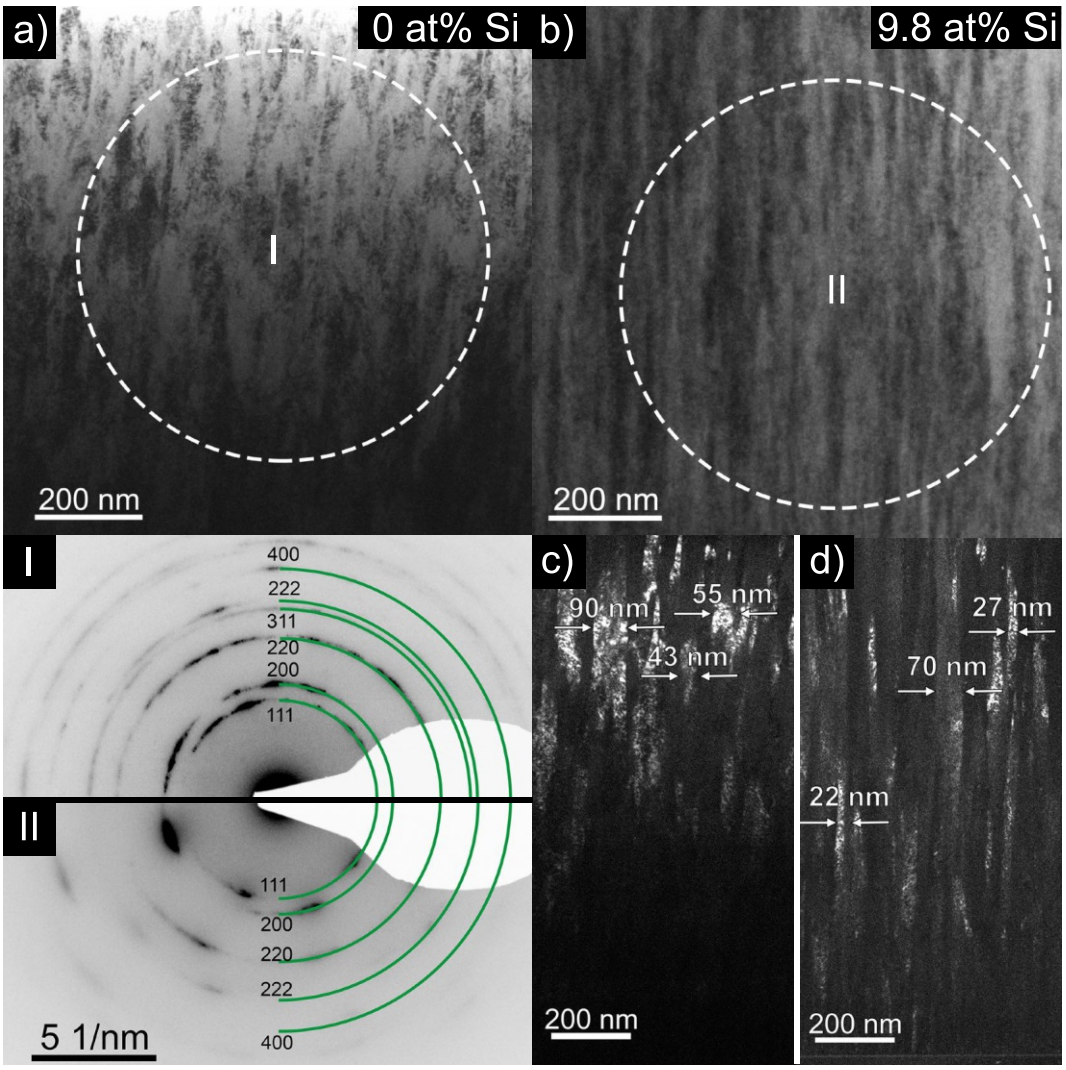

Figure 6.2: Bright field cross-sectional TEM-images of the HESN coating without Si a), and with 9.8 at% Si b). The SAED patterns taken from the region I (Si-free sample) and II (9.8 at% Si-containing sample) show single-phase solid solutions with rock-salt structure for both coatings. Dark field images of the coatings without Si c) and with 9.8 at% Si d), show that Si alloying causes thinner but longer columns.

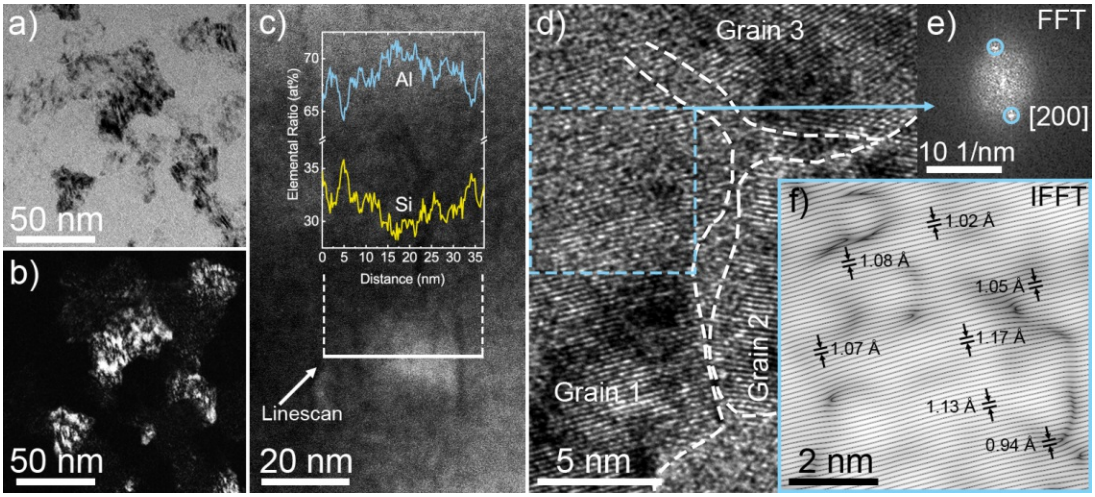

Figure 6.3: Plan-view TEM-images of the HESN coating with 9.8 at% in bright field a), dark field b), STEM-HAADF mode with an EELS linescan across one columnar grain c), and a high resolution TEM-image of the highlighted junction between three crystalline grains d). A fast fourier transformation of the blue margined area in d) reveals a single [2 0 0] oriented phase e). The inverse fast fourier transformation of the encircled spots in e) reveals the distorted lattice planes and the high defect-density in more detail f).

higher atomic mass or to closer alignment to a zone axis than its surrounding. An EELS linescan across this grain reveals a decreased Si/Al ratio in the center of the grain and an increased Si/Al ratio at the grain boundaries. Since Al is expected to be accompanying the other metals, this linescan supports the mass contrast in the STEM-HAADF image. In high-resolution mode, Figure 6.3d), the junction between three crystalline grains reveals a region with perturbed lattice plains. This could be an amorphous grain-boundary region, but careful interpretation is necessary since such a feature can also be generated by the projection of two overlapping grains.

A fast fourier transformation (FFT) of the blue margined area in Figure 6.3d) shows the diffraction spots of a single grain in [2 0 0] orientation in Figure 6.3e). The inverse fast fourier transformation (IFFT) of the two selected spots in Figure 6.3e) reveal the distorted and defected lattice plains clearly in Figure 6.3f). While this measurement is not precise enough to quantify the lattice distortion, the qualitative nature of the distorted lattice is visible. Since the line density is doubled in the IFFT and the grain is [2 0 0] oriented, the line distances are roughly a quarter of the lattice parameter. Quadrupling the average of 1.07 Å

yields a good agreement with the XRD measurement, based on which a lattice parameter of 4.30 Å was estimated for this coating. This supports the concept of severe lattice distortion not only in metallic high-entropy alloys but also in high-entropy metal-sublattice ceramics.

6.3.2 Structure and Phase Stability

The XRD measurements reveal a single-phased solid solution cubic structure for all coatings having 0 at% Si , Figure 6.4a), 6.4 at% Si, Figure 6.4b), 12.0 at% Si, Figure 6.4c), and 15.0 at% Si, Figure 6.4d) in the as-deposited state (bottom XRD pattern in black). The results confirm the SAED investigations and show that the addition of Si alters the preferred growth-orientation of the samples. Whereas the Si-free coating exhibits a more randomly oriented growth, with the [2 2 0] orientation being dominating, this changes with the addition of Si. The 6.4 at% Si-containing coating exhibits a preferred [4 2 0]-oriented growth, and for the 12.0 and 15.0 at% Si-containing coatings the [2 0 0] orientation is the preferred one. Our TEM investigations (Figure 6.3) show that a small fraction of Si can be incorporated into the lattice, whereas higher Si contents promote segregation to the grain boundaries, which was also investigated for (Ti, Si)N [159, 160]. We therefore attribute the texture changes to increased or decreased Si concentrations in the grains. The influence of Si on the peak shape is basically due to the reduction in overall grain size (as presented in Figure 6.1 as well). By increasing the Si-content, the grain size becomes smaller, as seen in the SEM and TEM micrographs. The smaller grain size leads to broader peaks, in addition, increased micro-stresses could contribute to broader peaks as well. From the SAED patterns we can conclude that only a single phase is present also in the Si-containing coatings.

The lattice parameter, simply estimated from the diffraction angle position and thus implying also contributions from stresses, increases from $a = 4.28$ to 4.34 Å with increasing Si content from 0 to 15.0 at%. The lattice parameter is similar to TiN, which is also used for reference positions. This is despite the low total Ti concentration in the coatings. The approximate lattice parameters of the constituent fcc-structured binary components are 4.05, 4.14, 4.34, 4.33, and

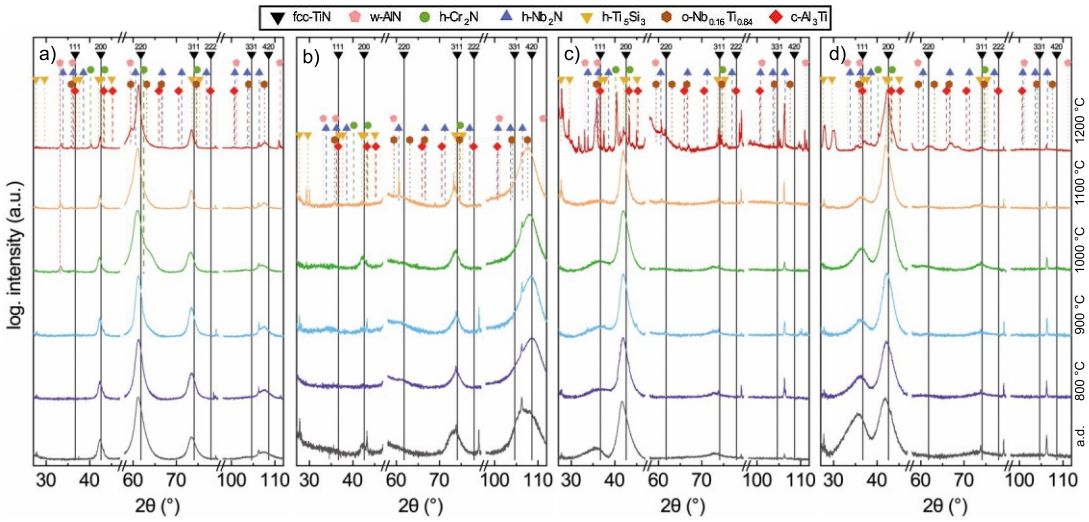

Figure 6.4: XRD-patterns of as-deposited and vacuum annealed (Al, Cr, Nb, Ta, Ti)N coatings on sapphire with 0 at% Si a), 6.4 at% Si b), 12.0 at% Si c), and 15.0 at% Si d) show first decomposition products after annealing at 1000 °C for the Si-free coating a). By Si-alloying, the decomposition onset is shifted up to 1200 °C. No XRD pattern could be recorded for the sample with 6.4 at% Si after annealing at 1200 °C, due to a complete coating-spallation. The substrate peaks around 53 and 85° are cropped for better visibility.

4.23 Å for AlN (ICDD 00-046-1200), CrN (ICDD 01-076-2494), NbN (ICDD 01-071-0162), TaN (ICDD 00-049-1283), and TiN (ICDD 00-038-1420), respectively. Even though TiN makes up only a fraction of the coating, its lattice parameter lies between the lattice parameters of the other constituent metal nitrides.

Even after annealing in vacuum up to 900 °C all coatings remain in this single-phased solid solution. When comparing the Si-free coating with its Si-containing counterparts, the decomposition upon increasing the annealing temperature to 1000 °C and further, is clearly shifted to higher temperatures. Hereby, the samples containing 12.0 at% and 15.0 at% Si, Figure 6.4c) and d), show decomposition into w-AlN, intermetallic and other N-depleted phases earliest at 1200 °C. For better visibility, only a small selection of possible peaks and phases is marked in Figure 6.4. The limiting factor for the phase stability is likely the tendency for CrN and TaN to release N and form Cr_2N above 900 °C, and Ta_2N at 1100 °C, enabling subsequent reactions to take place [161, 162]. Please note that the sample with 12.0 at% Si, Figure 6.4c), suffered from severe spallation during/after annealing to 1200 °C, so that only a careful XRD measurement but no nanoindentation test

could be performed.

6.3.3 Mechanical Properties

In Figure 6.5, the hardness H of the Si-free and Si-containing coatings depending on the annealing temperature is shown. In the as-deposited state, the addition of Si increases the hardness starting from 32.6 ± 2.0 GPa without Si to 34.3 ± 1.0 GPa and 35.4 ± 1.1 GPa for samples with 6.4 at% and 9.8 at% Si, respectively. This can be attributed to the smaller grain size, changes in bond-characteristics, and increased cohesive strength of the grain boundaries [163] due to the addition of Si (see Figure 6.2). Exceeding this Si content, the hardness drastically drops to ≈ 24 GPa (coatings with 12.0 and 15.0 at% Si). During vacuum annealing at 800 °C the hardness of all coatings increases by ≈ 2 GPa. Hereby, an exception is drawn by the coating containing 12.0 at % Si, which shows a tremendous increase from 24.5 ± 0.6 to 37.3 ± 0.9 GPa when annealed at 800 °C. Based also on previous investigations and reports, and because the XRD investigations do not show significant changes upon annealing to these temperatures, see Figure 6.4c), we attribute this to the compaction of the amorphous-like Si-rich grain boundaries, where parts may even be built into the surrounded or encapsulated grains, which increases the cohesive strength of the grain boundaries [159, 160, 164]. Note, that this is different from full crystallization of amorphous Si nitride, which happens above 1200 °C [165]. The addition of Si to transition metal nitrides is known to result in the formation of small grains and high cohesive strengths of the grain boundaries [159].

Coatings with a Si content between 6.4 and 12.0 at% retain their high hardness until $T_a = 1100$ °C. For $T_a = 1200$ °C delamination of the films impedes their investigation by nanoindentation. Only the Si-free and the 15.0 at% Si-containing thin films could be evaluated after annealing at $T_a = 1200$ °C, showing rather contrary results. Whereas the Si-free coating retains its hardness of 31.0 ± 1.6 GPa, the hardness of the coating with the highest Si content drops to ≈ 8 GPa. This coating shows a massive change in crystal structure and phase composition due to a severe loss of nitrogen, Figure 6.4d). However, the hardness retention of the lower Si-containing coatings during annealing at high temperatures is remarkable

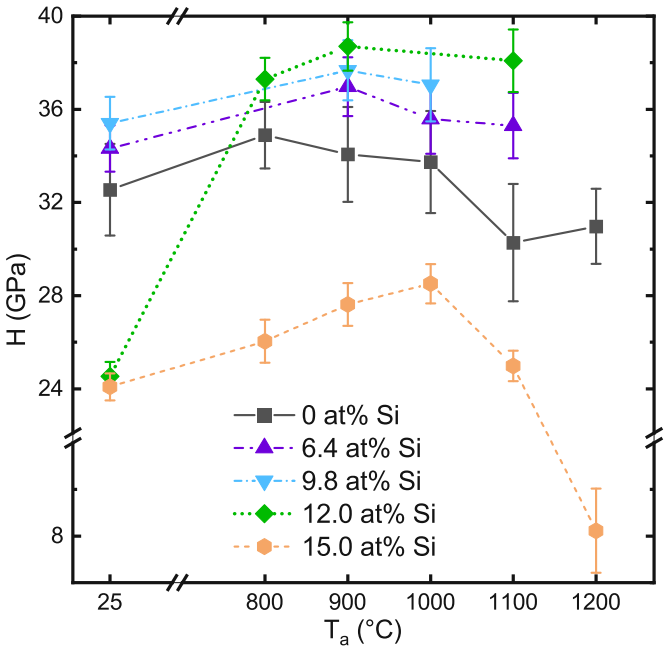

Figure 6.5: Indentation hardness, H, of the HESN coatings with and without Si-alloying in the as-deposited state and after vacuum annealing at T_a up to 1200 °C. Missing data points after annealing at 1100 and/or 1200 °C are due to complete spallation of the coating from their sapphire substrate due to the annealing treatment. The standard deviations are given as error bars.

for a single-phase coating. Unlike single-phase binaries, e.g., TiN, our high-entropy metal-sublattice nitride (Al, Cr, Nb, Ta, Ti)N with and without Si does not easily undergo recovery processes (where lattice defects arrange towards lower-energy sites), since the many elements with hugely different sizes at the metal-sublattice distort the lattice, shown in Figure 6.3d), allowing only for reduced diffusion [68]. Thus, the hardness is retained even when annealed at high temperatures due to sluggish diffusion.

For the HESN coatings without Si, the indentation modulus E_I lies in a range between 445 ± 25 and 519 ± 20 GPa for all annealing temperatures. In as-deposited state, the indentation modulus of our coatings decreases by more than 100 GPa with increasing Si-content. After annealing at 1100 °C, the coatings with 0, 6.4, 9.8, and 12.0 at% Si show similar indentation moduli of around 440 GPa. The highest Si-containing coating (with 15.0 at% Si) is again off the trend, with values below 363 ± 12 GPa. It is important to mention, with increasing Si-content

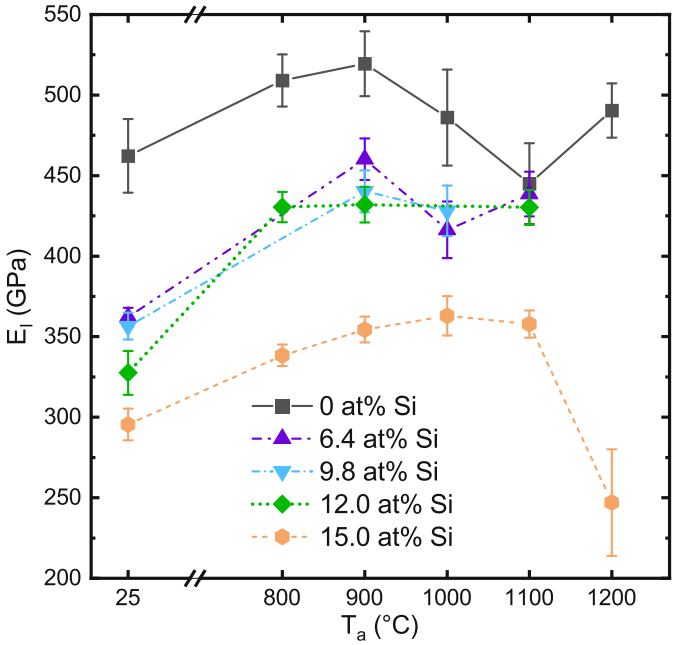

Figure 6.6: Indentation modulus, E_I, of the HESN coating with and without Si-alloying in the as-deposited state and after vacuum annealing at T_a up to 1200 °C. Missing data points after annealing at 1100 and/or 1200 °C are due to complete spallation of the coating from their sapphire substrate due to the annealing treatment. The standard deviations are given as error bars.

up to 12.0 at% the hardness increases especially if the coatings are annealed at $T_a = 800 - 1100$ °C (Figure 6.5). With Si addition the indentation modulus is lowered (Figure 6.6). Combining higher hardness with lower indentation modulus leads to higher H/E_I or H^3/E_I^2 ratios – two parameters often used to rate coatings within a series for their wear performance [166] – indicating higher elasticity behavior. Indeed, as shown by in-situ micromechanical cantilever bending tests of another high-entropy sublattice nitride, (Al, Ta, Ti, V, Zr)N, Si had nearly no impact on the fracture toughness (for the Si content tested up to 4.9 at%), but allowed for an increased area under the linear-elastic region of the stress-intensity-bending-strain curve, indicative for an increased damage tolerance [167].

6.3.4 Oxidation Resistance

In Figure 6.7 the XRD patterns of gradually oxidized samples with different Si concentrations are shown. Figure 6.7a) depicts an overview of the Si-free high-entropy metal-sublattice (Al, Cr, Nb, Ta, Ti)N coating before and after oxidation at 850 °C for 100 h. Clearly, a rutile-structured oxide is formed, but the nitride is still present in its single-phase cubic form. While in a powder the (1 1 0) peak at 27.1° possesses the highest intensity, it is only a very weak reflex in our oxide scales due to their strong texture. The highlighted (1 0 1) and (1 1 2) peaks have the highest intensities of all oxide peaks that do not overlap with a substrate or nitride signal. No other oxide phases could be detected, indicating the formation of a single-phase rutile-structured solid solution oxide from the single-phase fcc-structured high-entropy metal-sublattice $(Al_{0.20}Cr_{0.26}Nb_{0.15}Ta_{0.16}Ti_{0.23})N$ coating. Out of the metals present, Al is the only one reported to form no rutile structured oxide (there are metastable rutile-structured oxides for Cr, Nb, and Ta). Therefore, our experimental data suggest that also the Al is soluted in the structure, enabled by the many other metals forming a solid solution rutile oxide.

This could also be confirmed with DFT calculations. The free mixing enthalpy between rutile-structured solid solution $(Al, Cr, Nb, Ta, Ti)O_2$ and its stable binary metal-oxides (which are all non-rutile structured except for TiO_2) is -1.23 eV/at; clearly designating the solid solution $(Al, Cr, Nb, Ta, Ti)O_2$ energetically more preferred over the individual binary metal-oxides. Entropic effects would further support this high-entropy metal-sublattice dioxide over the individual binaries. When calculating all possible isostructural decomposition products of the $(Al, Cr, Nb, Ta, Ti)O_2$ solid solution, the most likely ones are $(Al, Ta, Ti)O_2$ and $(Cr, Nb)O_2$. But with $\Delta G_{mix} = 0.009\,84$ eV/at at 0 K (between the $(Al, Cr, Nb, Ta, Ti)O_2$ and these products), the driving force for such a decomposition is extremely small and could easily be consumed by any nucleation barrier or strain formation. Even without these retarding energies that are typically present during decomposition, already above 509 K ΔG_{mix} becomes negative due to the higher entropy of the $(Al, Cr, Nb, Ta, Ti)O_2$ solid solution than the product phases. Hence, entropy stabilization is easily reached for such an isostructural decomposition scenario. But even more important for

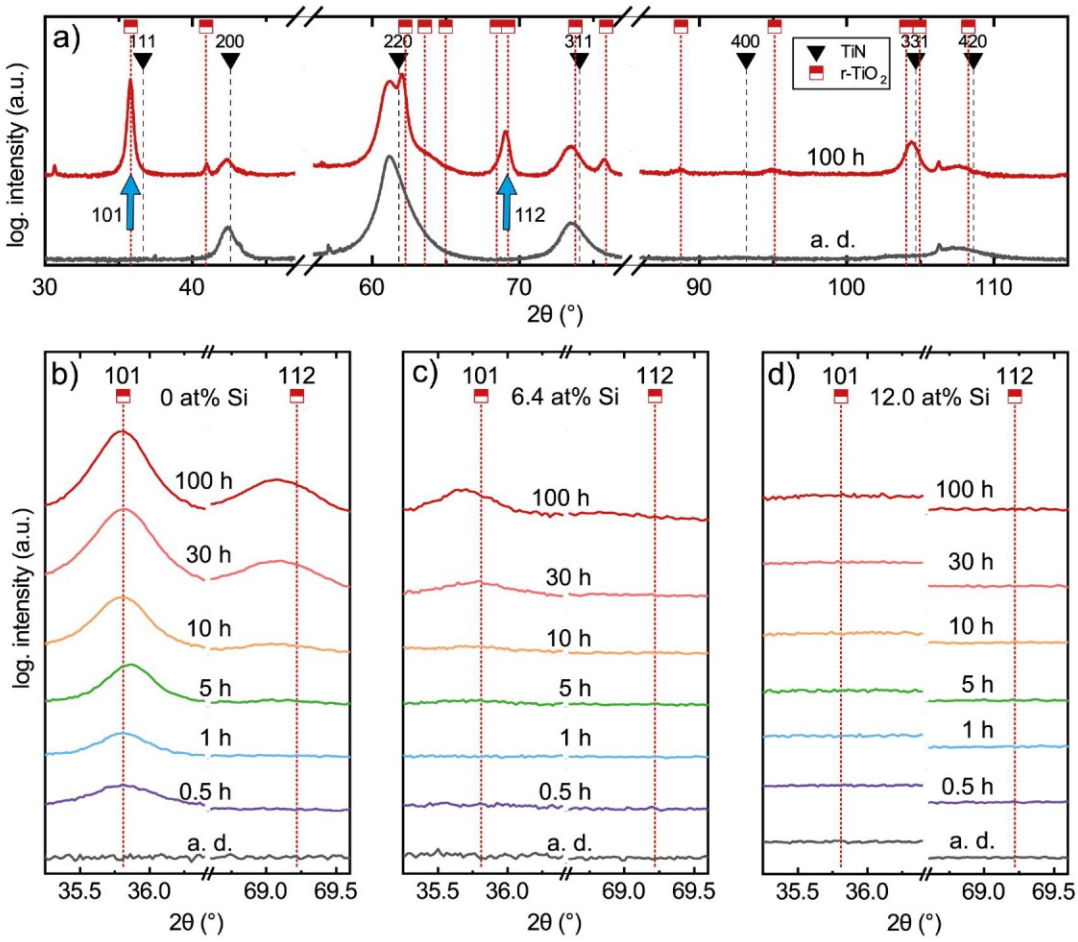

Figure 6.7: a) XRD patterns of the Si-free HESN coating in its as-deposited (a. d.) state and after exposure to ambient air at 850 °C for 100 h. The standard peak positions for TiN and rutile-structured TiO_2 (r-TiO_2) are indicated with black triangles and red squares, respectively. Details of the XRD regions around the dominating (1 0 1) and (1 1 2) peaks of r-TiO_2 (indicated by blue arrows) for the HESN coatings without Si, with 6.4 at% Si, and with 12.0 at% Si are given in b), c), and d), respectively, after the ambient-air exposure at 850 °C for 0, 0.5, 1, 5, 10, 30, and 100 h. As-deposited coatings do not show any signal (other than the background) in this range.

our oxidation scenario, the single-phased solid solution will form rather than individual oxide phases during the 850 °C oxidation experiment. Upon cooling, especially below 509 K where ΔG_{mix} would become positive, limited kinetics guarantee for the kinetic stabilization of the high-entropy metal-sublattice dioxide $(Al, Cr, Nb, Ta, Ti)O_2$.

Kirnbauer et al. [21] developed a single-phase rutile-structured high-entropy metal-sublattice dioxide of a similar composition $(Al_{0.19}Cr_{0.13}Nb_{0.19}Ta_{0.30}Ti_{0.19})O_2$ by reactive magnetron sputtering, which stayed single-phase rutile-structured even when annealed at 1200 °C. Developing a single-phase multi-elemental dioxide by PVD is taking advantage of kinetic limitations during PVD allowing to stretch the solubility-limits. But here we could show that the Al-containing solid solution rutile-structured dioxide forms by thermodynamic means during the oxidation of the HESN at 850 °C. The time-dependent development of this rutile-structured dioxide at the $(Al_{0.20}Cr_{0.26}Nb_{0.15}Ta_{0.16}Ti_{0.23})N$ is shown with the (1 0 1) and (1 1 2) XRD peaks in Figure 6.7b). The corresponding XRD patterns for the 6.4 at% Si-containing coating, Figure 6.7c), clearly show significantly lower-intensity XRD peaks. For 12.0 at% Si, Figure 6.7d), as well as for 15.0 at% Si (not shown) no crystalline oxide peaks could be detected even after 100 h exposure at 850 °C, suggesting for a significantly retarded oxidation process or the formation of an XRD-amorphous oxide.

With cross-sectional SEM investigations of the coatings after 1, 10, 30, and 100 h oxidation at 850 °C (for the Si-free coating also after 5 h), we investigated the oxide-scale thickness evolution. Exemplarily this is shown for the Si-free and 6.4 at% Si-containing sample after 100 h in Figure 6.8a) and b), respectively. While the Si-free coating exhibits a 2700 nm thick oxide scale, the Si-alloyed coatings show only a 280 nm thin oxide scale. Also, EDS-line-scans are conducted proving the relative homogeneous chemistry of the growing oxide across the scale thickness (especially for the Si-free sample). Furthermore it is important to mention that the relative metal content within the remaining nitride is very similar to that in the growing oxide. For all oxide scales investigated, the elemental distribution of metals in the oxide scale is comparable to the samples shown in the manuscript. The only inhomogeneity detectable by SEM-EDS in the oxide scale is the O content

that increases near the surface. The relatively long oxidation time of 100 h allows for an accurate determination of the oxidation kinetics derived from evaluating the time-dependent oxide-scale thickness, plotted in Figure 6.8c). The oxidation kinetic for the scale growth on the Si-free sample, $(Al_{0.20}Cr_{0.26}Nb_{0.15}Ta_{0.16}Ti_{0.23})N$, can best be described by parabolic behavior, whereas all Si-alloyed samples follow a logarithmic growth kinetic. The respective equations for the oxide thickness x as a function of time t, developed by Tammann [101, 102], are presented in Equation 4.12 and Equation 4.13, where k_p and k_l are the parabolic and logarithmic rate constants, respectively, and C_p, C_l, and B_l corresponding constants. The parabolic rate constant for the Si-free HESN at 850 °C is $k_p = (2.1 \pm 0.1) \cdot 10^{-17} m^2 s^{-1}$ with $C_p = (-1.4 \pm 2.2) \cdot 10^{-14} m^2$. As mentioned, all Si-alloyed HESN coatings follow a logarithmic oxide scale growth with a rate constant k_l of about $(7.2 \pm 0.9) \cdot 10^{-8} m$, and $C_l = (1.5 \pm 1.3) \cdot 10^{-2} s^{-1}$ and $B_l = 1.0 \pm 0.5$. Shen et al. [142], suspected already a logarithmic oxide growth behavior for their Si-containing $(Al_{0.34}Cr_{0.22}Nb_{0.11}Si_{0.11}Ti_{0.22})_{50}N_{50}$ at 900 °C. Oxidizing our Si-containing coatings (having a slightly different chemical composition, e.g., $(Al_{0.17}Cr_{0.25}Nb_{0.15}Si_{0.15}Ta_{0.12}Ti_{0.16})N$ for the 6.4 at% Si-containing case) for a much longer time (100 h) allowed us to confirm the logarithmic growth kinetic. The SEM cross sections of the oxidized Si-containing coatings show that the oxide scale thickness stays roughly the same between the different Si concentrations. Since the oxide peaks diminish with higher Si concentrations, see Figure 6.7c) and d), this is a clear indication that higher Si concentrations allow the formation of a more dense amorphous oxide scale. The results clearly show that already the 6.4 at% Si-containing coating,$(Al_{0.17}Cr_{0.25}Nb_{0.15}Si_{0.15}Ta_{0.12}Ti_{0.16})N$, shows an exceptional oxidation resistance. While the addition of more Si does not markedly improve the oxidation resistance further, it influences the mechanical properties (Figure 6.5 and Figure 6.6).

This oxidation resistance is superior to two comparable nitride coatings with lower metal-sublattice entropy, $Ti_{0.45}Al_{0.36}Ta_{0.19}N$ and $Ti_{0.41}Al_{0.56}Ta_{0.03}N$, that were oxidized for 20 h in 850 °C hot air and yielded oxide scale thicknesses of ≈ 1000 and 750 nm, respectively [139, 168]. (Ti, Al)N coatings (∼ 4 µm thick), also investigated in both studies, were fully oxidized under the same conditions.

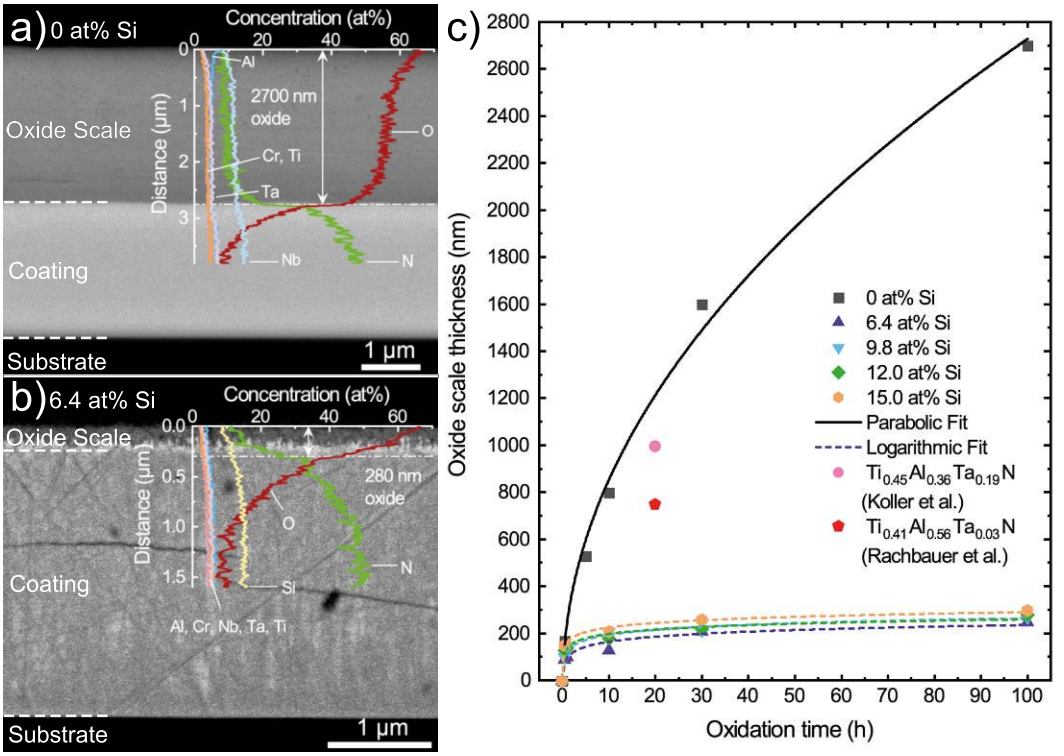

Figure 6.8: SEM cross-section of the HESN coating without Si a) and with 6.4 at% Si b) after exposure to ambient air at 850 °C for 100 h. The recorded EDS-linescans across the oxide scale are placed directly to the corresponding part. The oxide scale thickness evolution with time at 850 °C for all HESN coatings investigated (with 0, 6.4, 9.8, 12.0, and 15.0 at% Si) is presented in c). For comparison, also the oxide scale thickness of $Ti_{0.45}Al_{0.36}Ta_{0.19}N$ [139] and $Ti_{0.41}Al_{0.56}Ta_{0.03}N$ [168] coatings on sapphire after 20 h at 850 °C is added. Note that the Si content in b) is overestimated due to the interaction between Si and Ta EDS signals.

Detailed TEM investigations show that the growing oxide scale becomes significantly denser when Si is present. Bright-field and dark-field TEM cross-sections of the Si-free sample after 100 h at 850 °C in air are given in Figure 6.9a) and b), respectively. This sample shows a rather sharp interface between nitride and growing oxide scale and interestingly, the columnar grains of the nitride are neatly continued into the oxide scale, Figure 6.9b). SAED patterns taken from selected regions within the nitride and the growing oxide, indicated with (I) and (II) in Figure 6.9a), show a single-phase fcc solid solution for the remaining nitride, and a single-phase rutile-structured solid solution for the oxide. Thus, these investigations support the conclusions derived from the XRD investigations, Figure 6.7a). The rather distinct diffraction spots of the oxide

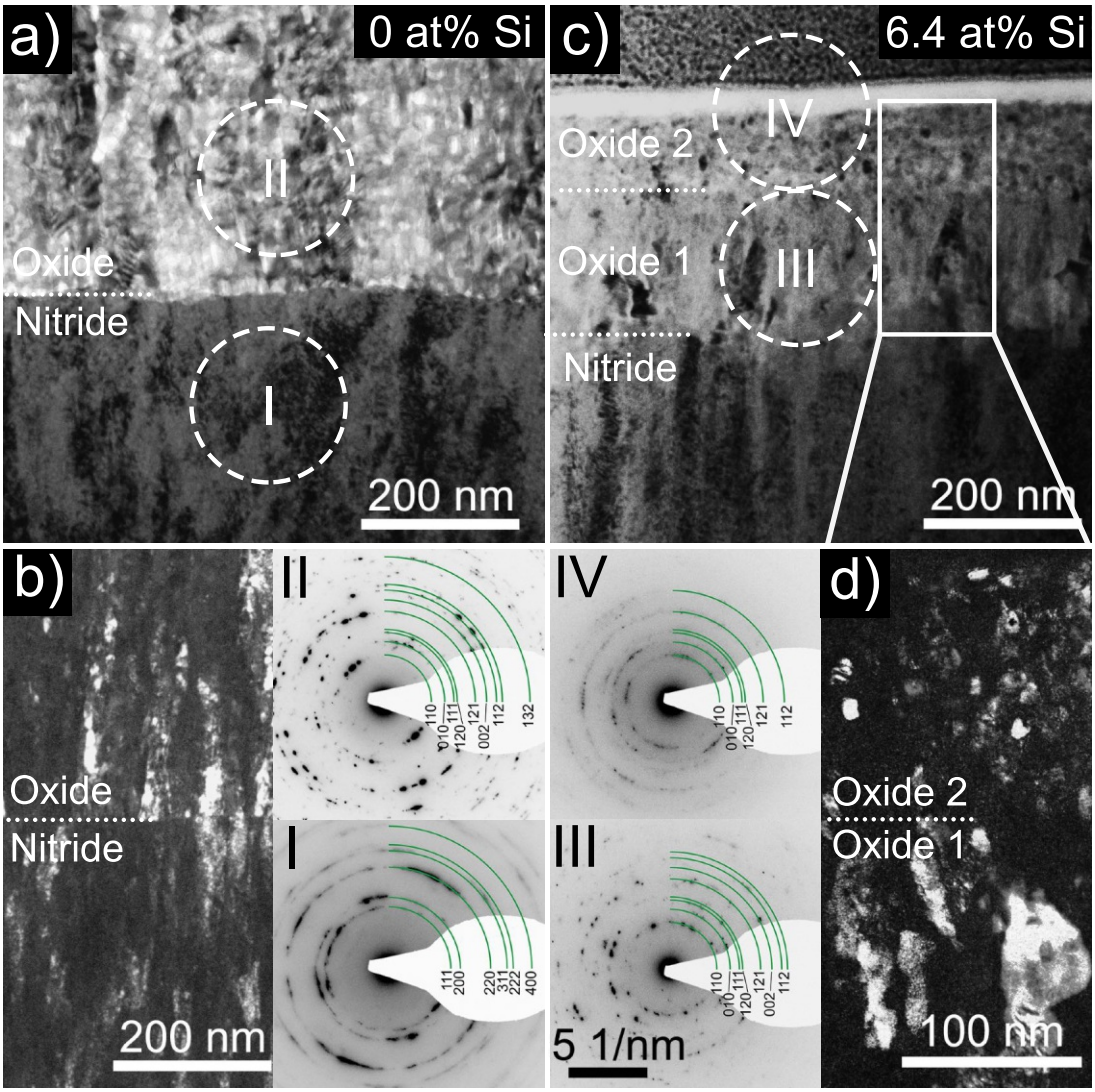

Figure 6.9: Cross-sectional TEM investigations of the HESN coating without Si a) and b), and with 6.4 at% Si c) and d) after oxidation in air at 850 °C for 100 h. a) and c) are BF, and b) and d) are DF TEM studies. The areas used for SAED are indicated in a) and c) by dashed white circles and labeled with (I), (II), (III), and (IV). The remaining nitride is still single-phase fcc rock-salt structured (SAED inset I), and all oxide regions indicate a single-phase rutile structure (SAED insets II, III, and IV).

pattern, Figure 6.9(b-II), indicate larger grains than within the nitride, which leads to a more ring-like SAED pattern, Figure 6.9(b-I).

When Si is alloyed to the HESN, the interface between nitride and growing oxide is blurred, and within the oxide two regions can be distinguished,

Figure 6.9c). The nitride-near region basically resembles the columnar grain structure of the HESN and the outer region exhibits more equiaxed grains with a much smaller average size, as proven by dark field investigations, Figure 6.9d). However, both regions are single-phase rutile structured, see the corresponding SAED patterns (III) and (IV) given in Figure 6.9d). The smaller grains of the outer oxide lead to a more ring-like SAED pattern (IV).

STEM investigations clearly show the blurred transition between Si-containing HESN and the growing oxide, Figure 6.10a). After the transition zone - which is about 100 nm thick and where the O signal increases and the N signal decreases - the O content is about 63 at%. This inner oxide shows almost no Cr, which is more concentrated in the outer oxide having also a higher O content of about 68 at%. The Si content almost gradually decreases from a high value (at the interface to the remaining nitride) to a small one at the outer surface, where the Al content is highest. Also the Si-free sample shows an Al-rich and O-rich outermost region of the growing oxide scale, compare Figure 6.8a). We could not detect any crystalline corundum in any oxidized coating neither by XRD or SAED, meaning that this Al-oxide layer is amorphous. The elements Nb and Ta are not given in the EDS line scan as their signals are essentially constant at ≈ 2 at% across the entire scan through nitride and oxide. The STEM image furthermore suggests that the outer oxide contains significantly more pores than the inner one. Thus, especially the inner oxide is able to be an effective diffusion barrier against further oxidation. The coating without Si leads to the formation of an oxide with much larger pores, Figure 6.10b), up to 30 nm in diameter. Here, no denser sub-layer oxide is present and therefore also the oxidation kinetic is faster.

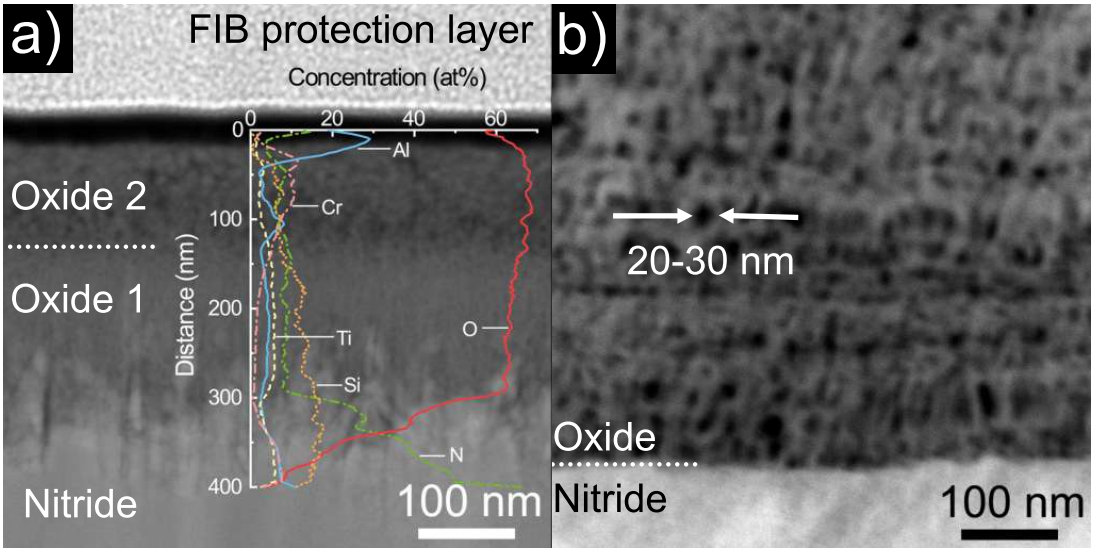

Figure 6.10: STEM investigations of the HESN coating with 6.4 at% Si a), and without Si b) after exposure to ambient air at 850 °C for 100 h. The STEM EDS line scan across the oxide scale grown on the 6.4 at% Si-containing coating is added directly to the STEM cross-section in a). For the Si-containing HESN, a gradual transition between remaining nitride and growing oxide is present a). Also, the oxide itself has gradual changes in morphology and Si as well as Cr contents. The inner Si-rich region is denser than the outer Cr-rich region, which even shows small pores. The O content increases from 63 to 68 at% towards the outer surface. Nb and Ta signals (constant at ~ 2 at%) are excluded for better visibility, and the Si content is overestimated due to interaction with the Ta EDS signal. The Si-free HESN shows a much sharper interface between remaining nitride and growing oxide and also larger pores with diameters up to 30 nm. Here, the oxide scale itself is rather homogeneous in morphology and chemistry, except for the Al-and O-rich outermost region (not shown, see Figure 6.8).

CHAPTER 7

Tuning of Microstructure and Mechanical Properties in (Al,Mo,Ta,V,W)N

7.1 Introduction

High-entropy sublattice ceramics – a subset within the high-entropy materials, discovered in 2004 [9, 10] – gain increasing recognition and attention [23]. They are characterized by disordered single-phase solid solutions of at least five elements in equiatomic or near-equiatomic composition, resulting in a high configurational entropy $S_{conf} \geq 1.5 \cdot R$, with R being the universal gas constant. High-entropy materials benefit from the four so-called core-effects: high configurational entropy, severe lattice distortion, sluggish diffusion, and the cocktail-effect [11]. To distinguish high-entropy materials from lower-entropy counterparts, two definitions have been formulated, a composition-based definition and an entropy-based definition [26]. The entropy-based definition is more concise, and has been specified more precisely for high-entropy ceramics which are composed of a metal sublattice and a non-metal sublattice. Since usually only the metal-sublattice is occupied by five or more different elements, while the non-metal sublattice is rarely modified, the entropy criterion $S_{conf} \geq 1.5 \cdot R$ is only reached for one sublattice and thus only per formula unit rather than per atom. To reflect this, the term HESC has been coined [66].

Among the different ceramic classes, physical vapor deposited transition metal

nitrides offer a combination of properties useful for protective coatings. High-entropy sublattice nitrides can be synthesized easily with reactive sputtering techniques and are reported to possess good thermal stability [66], mechanical and tribological properties [169–171], and oxidation resistance [134, 142, 172].

The microstructure and mechanical properties of reactively sputtered HESN depend strongly on the N_2 partial pressure used during deposition. For most coatings a hardness increase with rising N-content due to increased metal-N bonding is reported, which typically maxes out at ≥ 40 at% N when approaching the 1:1 stoichiometry of the fcc B1 structure (NaCl prototype) [173–175]. But in some cases, the hardness peak is reached at intermediate N contents, whereas more N incorporation leads to either no change or a slight decrease in hardness [171, 176–178]. This was explained with a saturation of covalent bonds above a certain N concentration and to different evolving microstructures, whose formation depends on the sputter conditions.

Another approach to modify the mechanical properties is the deposition of oxynitride coatings. Cr, Al, Ta, or Zr based PVD oxynitride coatings with good tribological properties have been reported, [179–183], but data on high-entropy oxynitrides is still sparse [38].

We modified and compared the microstructure, thermal, and mechanical properties of reactively magnetron sputtered (Al, Mo, Ta, V, W)N by depositing coatings with high or low N_2 partial pressure, and by depositing an oxynitride coating of the same metals. An important difference to the materials mentioned in the last paragraphs is the tendency of most of the constituting metals, Al, Ti, Zr, Hf, and Cr, to form stable fcc nitrides with a 1:1 stoichiometry at room temperature. In (Al, Mo, Ta, V, W)N on the other hand, all the constituting metals except for Al are reported to prefer N-vacancies in their fcc structure, or form N-depleted phases [66, 117, 158, 162, 184, 185]. We can therefore expect weaker metal-N bonds as a baseline that affect the thermal and mechanical properties.

7.2 Methods

7.2.1 Deposition Process

All coatings were reactively magnetron sputtered in a modified Leybold Heraeus Z400 magnetron sputtering system, using a powder metallurgically prepared equimolar $Al_{20}Mo_{20}Ta_{20}V_{20}W_{20}$ target of 75 mm in diameter (Plansee Composite Materials GmbH). The coatings were deposited on (1 0 0)-oriented Si ($20 \times 7 \times 0.38\,mm^3$), austenitic steel platelets ($20 \times 7 \times 1\,mm^3$), and $(1\,\bar{1}\,0\,2)$-oriented sapphire ($10 \times 10 \times 0.53\,mm^3$) substrates, mounted face-to-face to the target at a distance of 4 cm. The depositions were carried out after reaching a base pressure of 0.3 mPa, the deposition temperature was 440 °C and the DC bias potential was set to -50 V. Before deposition, the substrates were Ar-ion etched at a pressure of 1.3 Pa for 15 min by applying a negative pulsed DC substrate potential of -150 V with a pulse frequency of 150 kHz and a pulse duration of 2496 ns to the substrates.

After pre-sputtering behind the closed shutter for 2 min, the depositions were carried out by supplying a constant current of 0.75 A to the target for 20 min. Three different gas mixtures were used: N_2/Ar = 18/22 and 8/32 and N_2/Ar/synthetic air(20 %O_2, 80 %N_2) = 14/22/4 (in sccm). All gases were 99.999 % pure, the deposition pressure was set to 0.44 Pa. The respective power densities on the target in the different gas mixtures were 11.2, 10.3, and 11.5 W/cm^2.

7.2.2 Sample Analysis

Cross-sections of the coatings on Si and steel substrates were analyzed with a FEI Quanta 250 scanning electron microscope – equipped with a field emission gun and operated at 5 kV – to investigate growth morphology and deposition rates. Transmission electron microscopy was performed on as-deposited samples with a FEI TECNAI F20, equipped with a FEG, operated at 200 kV. Transmission Kikuchi Diffraction patterns were recorded in the FEI quanta 250 with an EDAX Hikari EBSD system on prepared TEM-samples at a working distance of 5 mm

and tilting angle of 30° with 30 kV acceleration voltage to study grain orientation. TiN in rock-salt structure (space group $Fm\bar{3}m$) was chosen as structure prototype. The TKD datasets were collected on hexagonal grids with a step size of 10 nm for the nitride samples and 15 nm for the oxynitride. The datasets were processed and analyzed with the EDAX OIM analysis software v8.0. Data clean-up was performed by using the confidence index (CI) standardization procedure, where the CI of each data point is set to the maximum value in the grain, where grains are defined with a misorientation tolerance of 5°. Secondly, one step of the neighbor orientation correlation procedure was performed, where the orientation of single data points, surrounded by at least 4 nearest neighbors belonging to the same grain, was changed to the orientation of the corresponding grain. Finally, a single iteration of grain dilation was performed to close the gaps between adjacent grains. For the data analysis, only data points with a CI ≥ 0.1 were used. The Matlab Toolbox MTEX version 6.6.1 [186] was used to calculate the orientation distribution functions and the misorientation distribution functions.

Chemical compositions of as-deposited and annealed coatings were analyzed by energy dispersive X-ray spectroscopy. Phase analysis was conducted with X-ray-diffraction using a PANanlytical XPert Pro MPD ($\theta - \theta$ diffractometer) using a Cu–Kα source ($\lambda = 0.154\,08$ nm, 45 kV and 40 mA) in Bragg-Brentano geometry. Coatings on sapphire substrates were vacuum annealed in a Centorr LF22-2000 vacuum furnace at T_a =800 °C for 30 h, the heating rate was 20 K/min, and the passive cooling rate at least 50 K/min down to 200 °C.

Indentation hardness, H, and indentation modulus, E_I, were measured on coated sapphire substrates with an UMIS II nanoindenter, following the procedure by Oliver and Pharr [96] to analyze the load-displacement curves.

7.3 Results and Discussion

7.3.1 Chemistry and Growth Morphology

Table 7.1 shows the chemical compositions of all coatings in as-deposited state and after annealing to 800 °C for 30 h. The metal ratios are very similar between

Table 7.1: Chemical Analysis in at% measured by EDS on samples in as-deposited and annealed state. The given statistical uncertainties are standard deviations of three measurements across a sample.

$f_{N_2/Ar/synth.\ air}$		Al	Mo	Ta	V	W	N	O
18/22/-	as-dep.	6±1	12±1	13±1	12±1	13±1	44±1	-
18/22/-	annealed	10±1	18±1	15±1	16±1	16±1	25±2	-
8/32/-	as-dep.	9±1	16±1	18±1	15±1	17±1	25±3	-
8/32/-	annealed	9±1	16±1	18±1	15±1	17±1	25±3	-
14/22/4	as-dep.	7±1	10±1	11±1	11±1	11±1	44±5	6±1
14/22/4	annealed	8±1	11±1	13±1	12±1	14±1	10±2	32±2

the coatings, with the exception of Al, which shows an increased concentration in the oxynitride. All coatings are understoichiometric – the degree depending on the N_2 partial pressure – due to the tendency to form N-vacancies in the nitrides of Mo [184, 187–189], Ta [158, 190, 191] (also metal-vacancies are reported), V [66, 192], and W [117, 193–195].

The coatings deposited with gas flow ratios of N_2/Ar = 18/22 and 8/32 sccm will be denoted throughout this chapter as $(Al, Mo, Ta, V, W)N_{0.79}$ and $(Al, Mo, Ta, V, W)N_{0.33}$, respectively, and the oxynitride coating as $(Al, Mo, Ta, V, W)N_{0.88}O_{0.12}$.

Figure 7.1 shows the fracture and polished cross-sections of the three deposited coatings, observed in the SEM. Since the $(Al, Mo, Ta, V, W)N_{0.33}$ coating developed cracks on the Si substrate (but not on the other substrates), no clean fracture cross-section of the whole coating thickness could be recorded. But the observed growth morphology is similar to the $(Al, Mo, Ta, V, W)N_{0.79}$ in Figure 7.1a), therefore a polished cross-section is shown in Figure 7.1b) instead to demonstrate the coating thickness. All three coatings show a dense columnar structure, but the morphology differs slightly between the nitride and the oxynitride coatings. While the $(Al, Mo, Ta, V, W)N_{0.79}$ and $(Al, Mo, Ta, V, W)N_{0.33}$ coatings consist of rather long, straight columns, the $(Al, Mo, Ta, V, W)N_{0.88}O_{0.12}$, depicted in Figure 7.1c), shows more rounded features. This becomes more apparent in the TEM studies below. The deposition rates are 171, 158, and 148 nm/min, for the $(Al, Mo, Ta, V, W)N_{0.79}$,

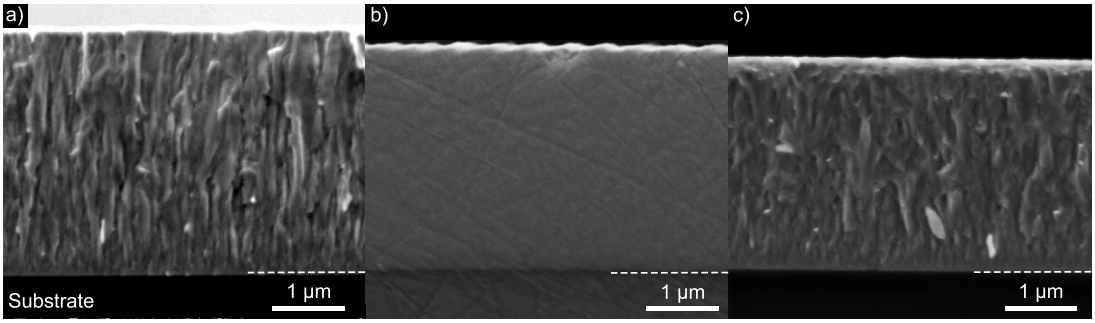

Figure 7.1: SEM fracture and polished cross-sections of coatings deposited with different gas flows: a) $(Al, Mo, Ta, V, W)N_{0.79}$, b) $(Al, Mo, Ta, V, W)N_{0.33}$, and c) $(Al, Mo, Ta, V, W)N_{0.88}O_{0.12}$. Due to cracking on the Si substrate, no whole fracture cross-section of the $(Al, Mo, Ta, V, W)N_{0.33}$ could be recorded. Since the fracture cross-section looks very similar to the $(Al, Mo, Ta, V, W)N_{0.79}$, a polished cross-section is presented instead to show the deposition rate.

$(Al, Mo, Ta, V, W)N_{0.33}$, and $(Al, Mo, Ta, V, W)N_{0.88}O_{0.12}$, respectively.

7.3.2 Microstructure and Orientation

Detailed TEM studies confirm the columnar structure of our coatings. The bright-field image, Figure 7.2a), shows the competitive growth morphology (close to the substrate) leading to dense long columns of the $(Al, Mo, Ta, V, W)N_{0.79}$ coating. The selected area electron diffraction pattern, recorded from the encircled area, shows only few spots, Figure 7.2b), although governed across several grains and columns. This indicates a highly oriented film growth. The circles show the reference positions of an fcc lattice with $a = 4.28$ Å as would be expected from a polycrystalline sample without texture. The high orientation and uniformity is also visible in the dark field image, Figure 7.2c), where the majority of the crystals are visible under the same beam conditions. The detailed BF recording, Figure 7.2d), shows the high defect density of the crystals.

The N-lean $(Al, Mo, Ta, V, W)N_{0.33}$ features a very different grain structure, see the BF-TEM image Figure 7.3a). Similar to the $(Al, Mo, Ta, V, W)N_{0.79}$, the majority of the coating consists of around 100 nm-wide columns, but here these are much shorter. In addition, two abnormally large conically shaped grains (outlined by dotted white lines) with a base width of ≈ 1.2 µm also developed from the substrate. SAED patterns collected from regions (green dashed circles)

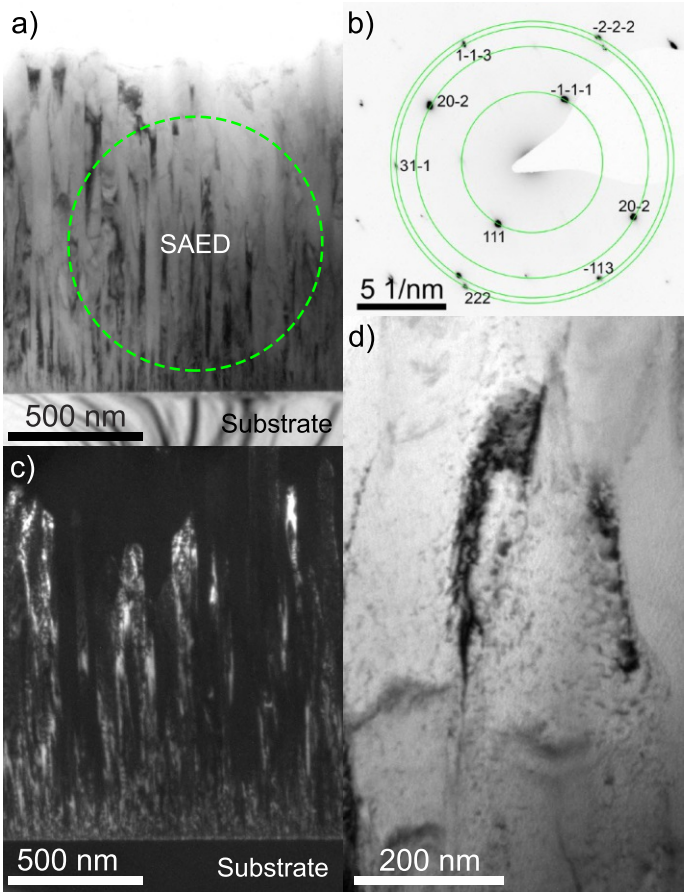

Figure 7.2: Cross-sectional TEM images of the $(Al, Mo, Ta, V, W)N_{0.79}$ coating: a) Bright field image, b) SAED pattern of the circled area in a), c) dark field image, d) bright field magnification of columns.

next to such a large grain (I), and from within the grain (II), yield fcc structures with identical lattice parameters of $\approx 4.27\,\text{Å}$ in both cases (within error of measurement). In addition, an EDS line scan across a region with smaller grains and a large grain reveals no significant difference in chemical composition, since the decrease in N-signal stems from the varying sample thickness (other metals than Al are omitted in this display for better visibility). Region (I) exhibits more individual diffraction peaks in the SAED, indicating a more random orientation when compared with Figure 7.2, but it is still a highly oriented film. Next to some diffraction spots, twin spots mark a second phase with the same symmetry but slightly different lattice parameter, which indicates a second phase with slightly

different N occupation, likely attributable to a Mo_2N type phase. A magnified view of the central large grain visible in Figure 7.3a) is presented in Figure 7.3b) with a high-resolution (HR) image outlining the grain boundary in Figure 7.3c). Due to the crystal structure examined by SAED, the chemistry measured by EDS-linescan, and the dense grain boundary region evaluated by HR-TEM we can definitely exclude these large grains to be a macro-particle or generated thereof. The DF image in Figure 7.3d) shows that the crystalline columns are distinctly shorter than in the $(Al, Mo, Ta, V, W)N_{0.79}$ coating, also local stress variations cause pronounced brightness shifts within the grains.

TEM investigations of the oxynitride coating $(Al, Mo, Ta, V, W)N_{0.88}O_{0.12}$ yield a dense coating, that features V-shaped grains at an angle of $\approx 20°$ to the growth direction instead of straight columns, Figure 7.4a). On top of the coating some Cu-redeposition from the TEM sample preparation can be seen. Overall, the growth morphology does not show the typical competitive growth close to the substrate as for $(Al, Mo, Ta, V, W)N_{0.79}$ and $(Al, Mo, Ta, V, W)N_{0.33}$. The SAED taken from the region indicated with a circle shows a single fcc phase, Figure 7.4b). The slight presence of ring patterns indicates a much less oriented growth than for the nitrides, likely facilitated by the tilted growth. The lattice parameter calculated from the fcc diffraction spots is ≈ 4.28 Å. Figure 7.4c) is the DF version of Figure 7.4a), highlighting the partly tilted growth of individual grains. The very dense growth morphology and high defect density is visible in the higher magnification investigation, Figure 7.4d), of the region marked with a dashed square in Figure 7.4a).

To analyze the influence of the deposition atmosphere during growth and the resulting film composition on the developing microstructures in more detail, the TEM samples were investigated by Transmission Kikuchi Diffraction. The inverse pole figure maps, pole figures, and misorientation angle and axis distribution plots are shown for $(Al, Mo, Ta, V, W)N_{0.79}$ in Figure 7.5a), b), and c), for $(Al, Mo, Ta, V, W)N_{0.33}$ in Figure 7.5d), e), and f), and for $(Al, Mo, Ta, V, W)N_{0.88}O_{0.12}$ in Figure 7.5g), h), and i), respectively.

The $(Al, Mo, Ta, V, W)N_{0.79}$ shows a strong orientation relationship between substrate and coating, Figure 7.5a). The grains, which in some cases stretch from

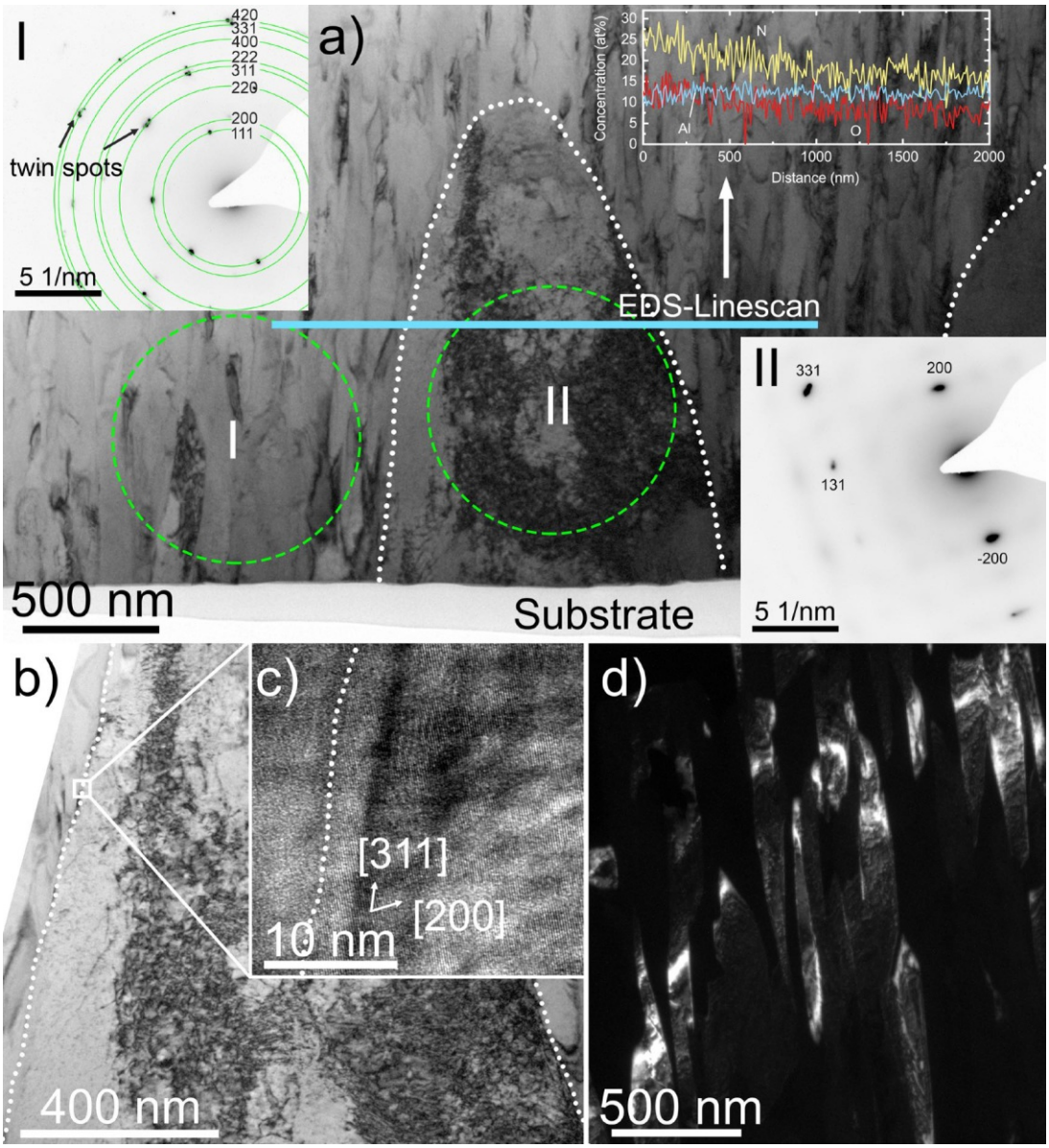

Figure 7.3: Cross-sectional TEM images of the $(Al, Mo, Ta, V, W)N_{0.33}$ coating: a) Bright field image, with two SAED patterns recorded from the circles I and II, abnormally large grains are outlined with dots. An EDS-Linescan across one such grain shows a constant chemical composition between these regions. Other elemental lines are omitted for better visibility. b) magnified view of the central large grain in a), c) high-resolution image at the border region of the large grain in b), d) dark field image of the columnar region next to the large grains.

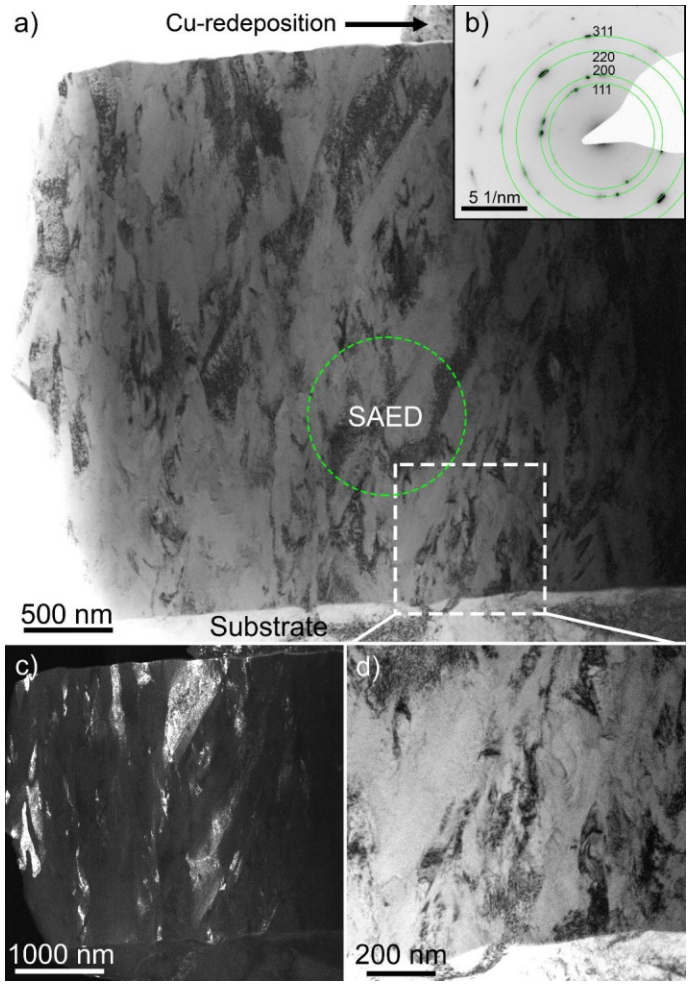

Figure 7.4: Cross-sectional TEM images of the $(Al, Mo, Ta, V, W)N_{0.88}O_{0.12}$ coating: a) bright-field image, b) SAED pattern collected from the circled region in a), c) dark field image, d) magnified bright field image of the substrate near region outlined in a).

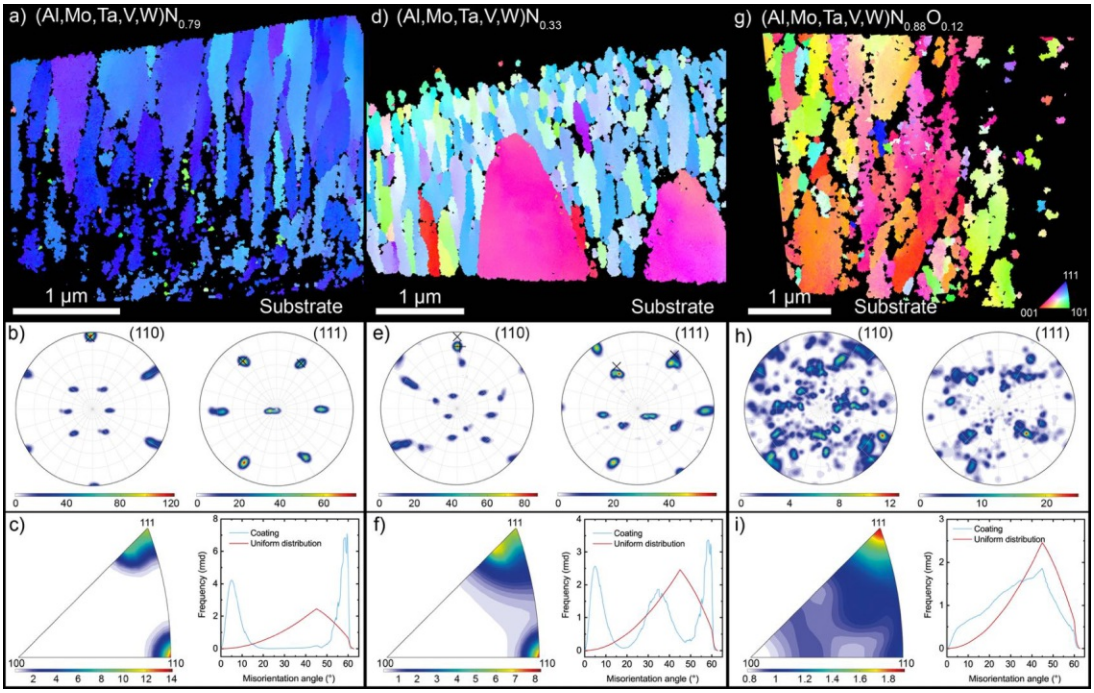

Figure 7.5: Inverse pole figures maps, pole figures, and misorientation axis distribution and misorientation angle distribution plots, measured by TKD of $(Al, Mo, Ta, V, W)N_{0.79}$ in a), b), and c), of $(Al, Mo, Ta, V, W)N_{0.33}$ in d), e), and f), and of $(Al, Mo, Ta, V, W)N_{0.88}O_{0.12}$ in g), h), and i), respectively (all coatings as-deposited). Black crosses in the pole figures mark the $[0\,1\,\bar{1}\,1]$ pole, + the $[2\,\bar{2}\,0\,1]$ pole of the substrate.

the substrate all the way through the coating, can be divided in two orientation groups. The dominant misorientation axis between the two orientations is the $[1\,1\,0]$ axis, the second axis is oriented along the $[1\,1\,1]$ direction. The $[1\,1\,0]$ pole in Figure 7.5b) is oriented close to the growth direction and aligns well with $[0\,1\,\bar{1}\,1]$ pole of the sapphire substrate (black crosses), which is therefore the dominant rotation axis since it runs through the mostly vertical grain boundaries. The misorientation angle distribution is also divided in two groups with small angles $\approx 5°$ (between the grains of one orientation group) and $\approx 60°$ between the grains of different orientation groups, Figure 7.5c). The angular distribution for a uniform cubic grain orientation is shown for comparison and highlights the strong texture once again. The misorientation axis distribution plot also exemplifies the strong $[1\,1\,0]$ and $[1\,1\,1]$ orientation.

Like in the TEM investigations, we see a distinctly different microstructure in

$(Al, Mo, Ta, V, W)N_{0.33}$ compared to the N-rich coating, see Figure 7.5d). Next to two very big grains with similar orientation many smaller and shorter columnar grains make up the coating. Within these smaller grains we see again a division into two groups like in the $(Al, Mo, Ta, V, W)N_{0.79}$. The coating features a strong [1 1 0] pole in vertical direction similar to the $(Al, Mo, Ta, V, W)N_{0.79}$, but the grain orientation is slightly twisted, compare Figure 7.5d) and Figure 7.5a), likely due to sample preparation. The orientation relationship to the substrate is also disturbed since the $[0\,1\,\bar{1}\,1]$ pole, marked by a black cross in Figure 7.5e), of the sapphire substrate does not match the column orientation as well. Instead, the crystallographically less important pole $[2\,\bar{2}\,0\,1]$, + in Figure 7.5e), lies closer to the grain orientation. The texture is therefore less dependent from the substrate, and less pronounced as for $(Al, Mo, Ta, V, W)N_{0.79}$. In the misorientation angle distribution plot, Figure 7.5f), we see a comparable distribution as in Figure 7.5c), with an additional contribution at $\approx 35°$ due to the large grains. This also results in the wider misorientation axis distribution between the [1 1 0] and [1 1 1] poles compared to the $(Al, Mo, Ta, V, W)N_{0.79}$ in Figure 7.5c).

The $(Al, Mo, Ta, V, W)N_{0.88}O_{0.12}$ shows the most randomized grain orientation, see Figure 7.5g). The grains are occasionally columnar and partly smaller equiaxed. Some of the columns are aligned in growth direction, while others are tilted by $\approx 20°$ to the growth direction. The most pronounced texture in growth direction is the [1 0 0], but the coating consists of many other randomly oriented small grains as well, so that the pole figures, Figure 7.5h), do not show a clear pattern. The misorientation angle distribution as well as the misorientation axis distribution, Figure 7.5i), follow the purely random orientation closely except for small angles, which are over represented in the coating.

7.3.3 Thermal Stability and Mechanical Properties

The XRD patterns of the coatings in as-deposited state, Figure 7.6a), and after annealing to 800 °C for 30 h, Figure 7.6b), confirm the phase analysis by SAED. The as-deposited $(Al, Mo, Ta, V, W)N_{0.79}$ coating is highly (2 0 0) oriented. After annealing, this highly preferred orientation remains, but the peak shifts to higher diffraction angles (please use the TiN standard positions as a reference). The

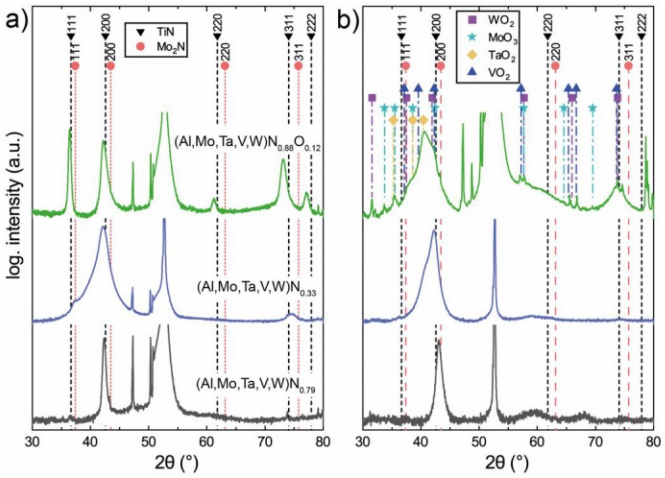

Figure 7.6: XRD patterns of coatings in as-deposited state a) and after annealing at 800 °C for 30 h b).

lattice parameter shrinks accordingly from 4.27 to 4.20 Å. At the same time the full width at half maximum of the (2 0 0) peak increases from 0.54 to 0.89°. Thus, while the macrostresses might decrease due to the annealing treatment, the microstresses remain or even increase. An additional cause for the peak shift and decreased lattice parameter can be the N-loss, as detected by EDS. After annealing, this coating (starting as a $(Al, Mo, Ta, V, W)N_{0.79}$) has approximately the same N-content of 25 at% as $(Al, Mo, Ta, V, W)N_{0.33}$ (Table 7.1), which was prepared with a N_2/Ar ratio of only 8/32. With increasing N-vacancy concentration the lattice parameters of MoN_x, TaN_x, and WN_x shrink, as suggested by DFT calculations [158, 187, 193, 195–197]. The additional XRD features at ≈ 60 and ≈ 68° indicate the formation of a hexagonal Ta_2N-based phase and are thus early signs for a decomposition. This will also contribute to the increased peak broadening.

The $(Al, Mo, Ta, V, W)N_{0.33}$ coating is also predominantly (2 0 0) oriented, but a small (3 1 1) reflex is also present. Remarkably, the relative shift of the peaks to the reference positions of TiN is different for the (2 0 0) peak (shifted to lower angles), than for the (3 1 1) peak (shifted to higher angles), indicating slightly different phases, which agrees well with the SAED analysis. When estimating the lattice parameter from the peak positions, we get $a = 4.28$ Å using the (2 0 0) peak, and $a = 4.21 \pm 0.02$ Å using the (3 1 1) peak, which is close to the lattice parameter of Mo_2N [158]. Since the total N content of this sample, as estimated by

EDS (Table 7.1), is only about 25 at%, both phases must exhibit high N-vacancy concentrations. After annealing, the (3 1 1) peak can not be detected anymore, but the (2 0 0) reflex developed a pronounced left-hand shoulder. The lattice parameter, estimated from the (2 0 0) peak position, stays at 4.28 Å, and also the chemical composition is unchanged from the as-deposited value within the error of measurement, indicating a chemical equilibrium composition for this coating.

The $(Al, Mo, Ta, V, W)N_{0.88}O_{0.12}$ coating exhibits a random growth orientation with clearly visible (1 1 1), (2 0 0), (2 2 0), (3 1 1), and (2 2 2) reflexes. But also this coating is clearly single-phased fcc-structured in its as-deposited state. This changes fundamentally during annealing, during which the N content decreases from 44 to 9 at% and the O content increases from 6 to 32 at% (Table 7.1). After the 30 h annealing at 800 °C, the XRD pattern shows the presence of W, Mo, Ta, and V oxides. A corresponding decomposition was also observed in (Co, Cr, Fe, Mn, Ni)-oxynitride films [38]. Since the specific volumes of the oxides are much larger than of the oxynitride phase (12.3, 11.3, 9.9, and 11.1 Å^3/at for MoO_3, TaO_2, VO_2, and WO_2, respectively [198–201], versus 9.8 Å^3/at in the $(Al, Mo, Ta, V, W)N_{0.88}O_{0.12}$ coating) this phase separation causes the coating to crack open, as proven by SEM top-view investigations, Figure 7.7. The as-deposited and annealed state of the $(Al, Mo, Ta, V, W)N_{0.79}$, $(Al, Mo, Ta, V, W)N_{0.33}$, and $(Al, Mo, Ta, V, W)N_{0.88}O_{0.12}$ are compared in Figure 7.7a) and b), c) and d), e) and f), respectively. All three coatings feature comparably smooth surfaces in as-deposited state. After annealing, coarse features in the order of ≈ 1 µm appear on the $(Al, Mo, Ta, V, W)N_{0.79}$, which could be a sign of the ongoing decomposition. On the $(Al, Mo, Ta, V, W)N_{0.33}$, the surface appears to be even smoother after annealing, no other change is visible after annealing. On the $(Al, Mo, Ta, V, W)N_{0.88}O_{0.12}$, cracks spanning several µm in length are drawn through the surface with only few µm between the cracks. Thus, the exposed surface area increases greatly, this allows N to leave and O to enter the coating more easily, leading to the complete change in chemistry compared with the as-deposited state.

The indentation hardness, H, and indentation modulus, E_I, Figure 7.8, of the coatings in their as-deposited state and after the 30 h annealing at

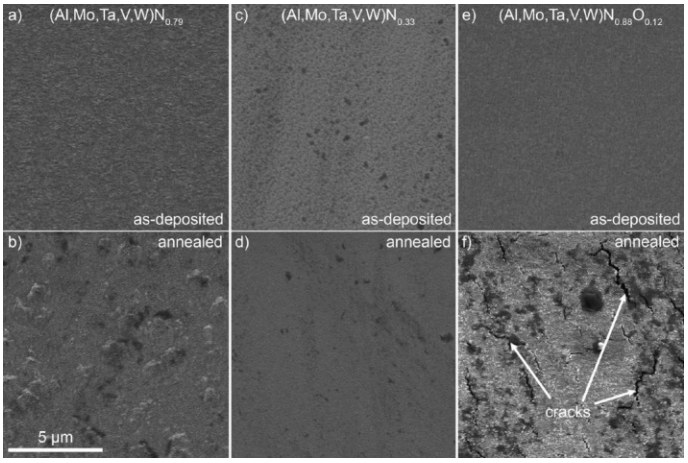

Figure 7.7: SEM top-view micrographs show that the surface of the $(Al, Mo, Ta, V, W)N_{0.79}$ coating stays smooth after annealing at 800 °C for 30 h, except for some island formation a)-b). No change is visible in the surface of the $(Al, Mo, Ta, V, W)N_{0.33}$ c)-d), while the $(Al, Mo, Ta, V, W)N_{0.88}O_{0.12}$ develops cracks due to separation into oxide phases with larger specific volumes e)-f).

800 °C nicely reflect the microstructural and morphological changes. In the as-deposited state, the $(Al, Mo, Ta, V, W)N_{0.79}$ coating exhibits a hardness of 32.3 ± 1.6 GPa, which is exceeded by both the $(Al, Mo, Ta, V, W)N_{0.88}O_{0.12}$ and $(Al, Mo, Ta, V, W)N_{0.33}$ coatings with 34.6 ± 1.5 GPa and 39.7 ± 1.4 GPa, respectively. The latter is even touching the domain of superhard materials (for which the hardness would need to be above 40 GPa [160]). After the annealing treatment, the $(Al, Mo, Ta, V, W)N_{0.79}$ reaches even 35.2 ± 1.4 GPa, while the hardness of $(Al, Mo, Ta, V, W)N_{0.33}$ decreased slightly to 38.1 ± 2.0 GPa. Only the $(Al, Mo, Ta, V, W)N_{0.88}O_{0.12}$ suffers a severe hardness loss down to 14.1 ± 2.7 GPa, which can be explained by the almost entire transformation towards individual oxides and the concomitant formation of cracks. But interestingly, the $(Al, Mo, Ta, V, W)N_{0.79}$ and $(Al, Mo, Ta, V, W)N_{0.33}$ coatings, which are separated in their hardness by 8 GPa in as-deposited state, exhibit only a difference of ≈ 3 GPa after the annealing treatment. The latter caused also an alignment in their chemical composition, which became almost identical especially with respect to their N-content, although they started with 44 respectively 25 at% (Table 7.1). The significantly higher hardness of the N-lean $(Al, Mo, Ta, V, W)N_{0.33}$, already in its as-deposited state, combined with the annealing-induced hardness

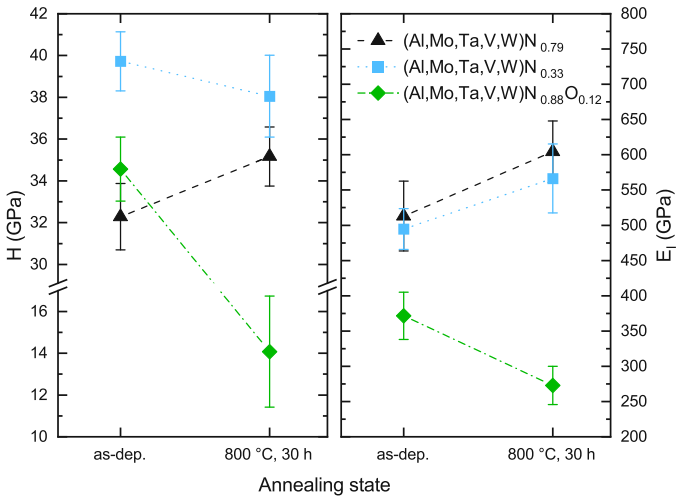

Figure 7.8: Hardness H and Indentation modulus E_I measured on coatings in as-deposited state and after annealing at 800 °C for 30 h.

increase of the originally N-richer $(Al, Mo, Ta, V, W)N_{0.79}$, suggests that for this material system – $(Al, Mo, Ta, V, W)N$ – a N/metal ratio of 1/2 to 1/3 is beneficial in terms of hardness and phase stability. The observed hardness trend nicely follows the decreasing valence electron concentration from 9.2 e^-/f.u. in the as-deposited $(Al, Mo, Ta, V, W)N_{0.79}$ to 6.9 e^-/f.u. in both the annealed $(Al, Mo, Ta, V, W)N_{0.79}$ and the $(Al, Mo, Ta, V, W)N_{0.33}$ (as-deposited and annealed) due to the N-vacancies in the fcc structure [187, 202, 203].

Interestingly, the indentation moduli of $(Al, Mo, Ta, V, W)N_{0.79}$ and $(Al, Mo, Ta, V, W)N_{0.33}$ are very similar with 513 ± 50 GPa and 495 ± 28 GPa in their as-deposited state as well as after annealing, during which E_I increased to 604 ± 44 GPa and 566 ± 49 GPa, respectively. The $(Al, Mo, Ta, V, W)N_{0.88}O_{0.12}$ coating, although only containing 6 at% O exhibits a much lower indentation modulus of only 372 ± 33 GPa in the as-deposited state, which further decreased to 273 ± 27 GPa during annealing, as a consequence of the massive structural and chemical changes.

CHAPTER 8

Development of Compositionally Complex Superhard (Hf,Ta,Ti,V,Zr)-B-N Coatings

8.1 Introduction

By leaving the paradigm of having a major constituent or solvent, which dominates the properties, high-entropy materials have opened up a vast field of interesting properties to material scientists [9, 10]. The basic premise of high-entropy materials is the distribution of five or more atoms on a crystal lattice in equiatomic or near-equiatomic concentration to form a distorted random solid solution. This condition leads to a high configurational entropy $S_{conf} \geq 1.5 \cdot R$, with R being the gas constant, that stabilizes the solid solution thermodynamically. High-entropy materials are commonly characterized by 4 core-effects: High configurational entropy, severe lattice distortion, sluggish diffusion, and the so-called cocktail effect [11]. Invented for metallic alloys, the high-entropy concept has also been applied to ceramic materials with great success. Instead of constituent metals, these ceramics are composed of at least 5 binary ceramics such as nitrides, oxides, carbides, or borides [26]. Since usually only the metal-sublattice of these phases is disordered, the threshold $S_{conf} \geq 1.5 \cdot R$ is usually only reached per formula unit and not per atom as was intended for metallic alloys. To reflect this in their notation, such materials have also been named high-entropy metal-sublattice ceramics [66].

In the pursuit of high-entropy materials, the formal criteria of such a definition are often not met in real materials. Still, interesting properties do not adhere strictly to arbitrary definitions such as $S_{conf} \geq 1.5 \cdot R$. To reflect a broader horizon of materials, terms such as compositionally complex alloys or complex concentrated alloys (CCA) have been coined [44]. There is no consensus yet for a definition of CCAs, but commonly named attributes (as demarcation to high-entropy materials) are: possible multi-phase structures, lower requirements for the number of composing elements (even down to 3) [45], or that no component represents a base element (all concentrations $< 35\,\text{at}\%$) [48]. Sometimes a precise definition is even omitted, instead multi-principal element compositions with "significant concentrations" of the components are deemed sufficiently accurate [46, 47]. CCAs represent hence not a rigorous classification, but can be understood from the perspective of material development. The common trait of CCAs is a significant disorder on the atomic level (to what magnitude is not always defined), while not fulfilling the strict criteria of a high-entropy material. In any case, these classifications should serve only as a guide for materials design and not obstruct our advances.

Despite the comparably low entropy, multi-principal element ceramics possess compelling properties for protective thin films, usually synthesized by PVD. Easy to deposit in a fcc solid solution with reactive magnetron sputtering, nitrides have received the most attention so far among the different ceramic classes [23]. Nitride thin films with good thermal stability [66], mechanical properties [169, 170], low diffusivity [15, 71], and high oxidation resistance [134, 142, 172] have been reported. But among thin films, only two high-entropy sublattice borides with excellent high-temperature stability have been investigated so far, that outperform their lower-entropy counterparts [26, 27]. These investigations all focus on the metal-sublattice, whereas the non-metal sublattice is often neglected. Although deliberate introduction of disorder on the non-metal sublattice could open the door to outstanding material properties, so far, such investigations of mixed ceramic classes are rare.

Since S_{conf} increases logarithmically with the number of elements [11], the first additional elements in a random solid solution offer the largest returns.

Changing the non-metal sublattice from a perfectly ordered nitride into an equimolar boronnitride would increase the configurational entropy of the non-metal sublattice from 0 to $0.69 \cdot R$, which is a much larger gain than could be obtained by tweaking a metal-sublattice that contains high S_{conf} already. So far, high-entropy metal sublattice carbonitride [36, 37] and oxynitride [38] thin films have been reported, but no high-entropy metal sublattice boronnitrides, even though Ti-B-N prototypes have been investigated in the past [164]. A possible reason for this lack of attention could be the incongruence of the fcc nitride and the hexagonal diboride structures that leads to nanocomposite structures in Ti-B-N instead of single-phase solid solutions, which are the prerequisite of high-entropy materials.

In this work we explore the alloying possibilities and mechanical properties of equi-metal-atomic (Hf, Ta, Ti, V, Zr)-B-N – having a high-entropy metal-sublattice – with density functional theory calculations. Based on these results we deposited (Hf, Ta, Ti, V, Zr)-B-N films with reactive and non-reactive magnetron sputtering (recently we showed that using reactive or non-reactive sputtering has a large influence on the coating properties in Ti-B-N [204]) possessing excellent mechanical properties and thermal stability.

8.2 Methods

8.2.1 Density Functional Theory

Ab-initio investigations were conducted using the Vienna Ab-initio Simulation Package (VASP) [111, 112] with projector augmented plane wave (PAW) pseudo-potentials under the generalized gradient approximation [110]. This approach allows the study of electronic, thermodynamic, and mechanical properties of (Hf, Ta, Ti, V, Zr)-B-N with equiatomic metal-sublattice and different B:N occupations on the non-metal sublattice in four different structures: the fcc NaCl-type structure, vacancy-free and with 50 % non-metal vacancies (equally distributed between B and N), the hexagonal AlB_2-type structure (abbreviated with α, according to the suggestion by Euchner et al. [205] to

Table 8.1: DFT parameters.

Structure	prototype	space group	SQS supercell size	k-points
fcc 1:1	TiN	225	$2 \times 2 \times 2$	$6 \times 6 \times 6$
fcc 2:1	TiN	225	$2 \times 2 \times 2$	$6 \times 6 \times 6$
α	AlB_2	191	$3 \times 3 \times 3$	$6 \times 6 \times 5$
FeB	FeB	62	$2 \times 2 \times 3$	$4 \times 5 \times 5$

differentiate this structure from the other typical structure for diborides - the WB_2-structure, which is abbreviated with ω), and the orthorhombic FeB-type structure. Representative visualizations of the unrelaxed cells of each structure type with B:N = 50:50 ratios are shown in Appendix A. The cutoff energy was set to 500 eV and the stopping criterion for ionic relaxation to $\approx 10^{-4}$ eV/at, using a Γ-centered Monkhorst-Pack k-mesh [113]. To simulate the random distribution of elements on their respective sublattices, special quasi-random structure (SQS) supercells were constructed [118], in which the metals were distributed on the metal-sublattice and B and N on the non-metal sublattice, see Table 8.1 for the respective supercell sizes and k-meshes. Since for the chosen cubic and hexagonal supercells the number of metal sites is not divisible by 5, the equiatomic occupation of the metal-sublattice was realized by averaging over 10 cells, in which the metal occupations were permuted on the 6+6+6+7+7 or 5+5+5+6+6 sites for the fcc and α structures, respectively. The cells were then relaxed regarding size, shape, and atomic positions towards equilibrium. The phase stability of the different structures was calculated with their formation energies E_f [195], using the total energy per atom of the metals and B in their ground state structures, and of the N_2 molecule as chemical potentials.

Mechanical properties were calculated from the relaxed cells with the stress-strain method [123]. The resulting elastic constants were projected onto cubic or hexagonal symmetry with the method of Moakher and Norris [206]. The bulk and shear moduli B and G are averaged from the Reuss and Voigt estimates described in [207]. The directional Young's moduli of certain crystallographic orientations [121] were calculated in addition to the polycrystalline Young's modulus E and the effective Cauchy pressure Cp, as described in [195].

The projected density of states was calculated with an energy resolution of $0.05\,\mathrm{eV}^{-1}$ in the region between -10 and 5 eV around the Fermi-level to discuss individual bonding contributions of the constituents.

8.2.2 Depositions

All coatings were deposited on mirror-polished substrates, (1 0 0)-oriented Si ($20\times7\times0.38\,\mathrm{mm}^3$), austenitic steel platelets ($20\times7\times1\,\mathrm{mm}^3$), and (1 $\bar{1}$ 0 2)-oriented sapphire ($10\times10\times0.53\,\mathrm{mm}^3$), at 440 °C by magnetron sputtering in a modified Leybold Heraeus Z400 deposition facility. Reactive depositions were performed in mixed Ar+N_2 discharges (with an Ar/N_2 flow rate ratio of 18/22 sccm at 0.44 Pa) using an equiatomic, metallic, 3"-diameter $Hf_{0.2}Ta_{0.2}Ti_{0.2}V_{0.2}Zr_{0.2}$ target (Plansee Composite Materials GmbH). Placing an increasing number of the combined set of HfB_2, TaB_2, TiB_2, VB_2, and ZrB_2 pieces (all from Plansee Composite Materials GmbH, roughly 4 mm in diameter) on the target racetrack allowed us to prepare (Hf, Ta, Ti, V, Zr)-B-N coatings in addition to the (Hf, Ta, Ti, V, Zr)N. Details on the preparation of the latter can also be found in [66]. The non-reactive depositions were performed in Ar discharges (with an Ar flow of 30 sccm at 0.36 Pa) using a 3"-diameter Zr(N,C) target (Plansee Composite Materials GmbH, the C content in the target is 10 at%). Also here, we added an increasing number of the combined set of HfB_2, TaB_2, TiB_2, and VB_2 pieces, each, on the target racetrack to prepare not just ZrN but also (Hf, Ta, Ti, V, Zr)-B-N coatings with different metal and B:N ratios.

The substrates were ultra-sonically cleaned with Acetone and Ethanol for 10 minutes and mounted face-to-face at a distance of 4 cm to the target. After waiting for a base pressure of 0.3 mPa the substrates were heated to a temperature of 440 °C and Ar-ion etched at a pressure of 1.3 Pa for 15 min, applying a negative pulsed DC bias of -150 V to the substrates with a pulse frequency of 150 kHz and pulse duration of 2496 ns. During all depositions a DC bias voltage of -50 V was applied. The depositions were performed supplying a constant current of 0.5 A to the ZrN target, and 1.0 A to the metallic target. The deposition time was adjusted between 30 and 50 min to ensure that the coatings are between 2 and 3 µm thick.

8.2.3 Sample Analysis

Cross-sections of the coatings on Si substrates were analyzed with a FEI Quanta 250 scanning electron microscope – equipped with a field emission gun and operated at 5 kV – to investigate growth morphology and deposition rates. Since the Si substrates in the non-reactive depositions broke during or after depositions, coatings on steel substrates were cut, embedded and polished to determine the growth rates from the polished cross-sections. Transmission electron microscopy was performed with a FEI TECNAI F20, equipped with a FEG, operated at 200 kV, on as-deposited samples.

Chemical compositions of reactively deposited coatings were analyzed by energy dispersive X-ray spectroscopy, non-reactively deposited samples were analyzed by time-of-flight elastic recoil detection analysis with a recoil detection angle of 45° using a primary beam of 36 MeV I^{8+} ions. Experimental details, data analysis as well as potential systematic uncertainties are described in [155–157]. Phase analysis was conducted with X-ray-diffraction using a PANanlytical XPert Pro MPD ($\theta-\theta$ diffractometer) equipped with a Cu–Kα source ($\lambda = 0.154\,08$ nm, 45 kV and 40 mA) in Bragg-Brentano geometry. Coatings on sapphire substrates were vacuum annealed in a Centorr LF22-2000 vacuum furnace at T_a = 800, 900, 1000, 1100, and 1200 °C for 10 min, the heating rate was 20 K/min, and the passive cooling rate at least 50 K/min down to 200 °C. Indentation hardness, H, and modulus, E_I, were measured on polished coated sapphire substrates with an UMIS II nanoindenter, equipped with a Berkovich tip, following the procedure by Oliver and Pharr [96], assuming a Poisson's ratio of 0.25 to analyze the load-displacement curves.

8.3 Results and Discussion

8.3.1 Density Functional Theory

The energies of formation of the different structures presented in Figure 8.1 for different B:N ratios show a clear preference of the vacancy-free fcc structure over a wide composition range from the pure nitride up to ≈ 78 at% of B on the

non-metal sublattice (all values are listed in Appendix B). In this structure, E_f increases linearly from ≈-1.7 eV/at to ≈ −0.7 eV/at at 90 at% N on the non-metal sublattice. The fcc structure with 50 % non-metal vacancies (equally distributed between B and N) shows a constant offset of ≈ 0.4 eV/at in comparison. The FeB structure features slightly less-negative E_f values than the fcc structure. At 25 at% B on the non-metal sublattice, the E_f is very close to the vacancy-free fcc structure, a detailed inspection of the corresponding relaxed cell reveals that the original atomic coordination transforms from the layered arrangement of the FeB structure into a more cubic coordination (6 nearest neighbors with ≈90° angles) upon relaxation. Only in a narrow window between 78 and 91 at% B this structure is preferred energetically, but since the difference to the higher-symmetry fcc and α phases is very small, this structure might not be observable in PVD experiments. It is therefore excluded from further considerations together with the fcc structure with vacancies. The α structure follows a non-linear trend as well and is preferred only in the pure boride phase and down to a B content of 90 or 84 at% on the non-metal sublattice, depending on which competing phase is considered. A similar behavior is also visible in the constituting binary phases (see Appendix A).

The compatibility of B and N incorporation in the fcc and α structure is also noticeable in the lattice parameters. In Figure 8.2a) the average and standard deviation of the lattice distances and angles of the 10 individual calculated cells are shown for the fcc and α structures. In all cubic structures, the angle of 90° is adhered to with only little deviation (due to random occupation of differently sized metal atoms). At the same time the lattice spacing increases linearly with increasing B content from 4.42 to 4.62 Å at 90 at% B (on the non-metal sublattice). Contrary, in the α structured cells with increasing N content, large deviations between individual cells are evident for both lattice angles α and γ, as well as the lattice parameters a and c. At high N concentrations the a/c ratio is even reversed. The deviation of lattice parameters and angles means that while the B incorporation on the non-metal sublattice of the fcc structure poses no problem, the N incorporation in the hexagonal phase perturbs the structure strongly. This property is also showcased in Figure 8.2b) and c), which depict representative

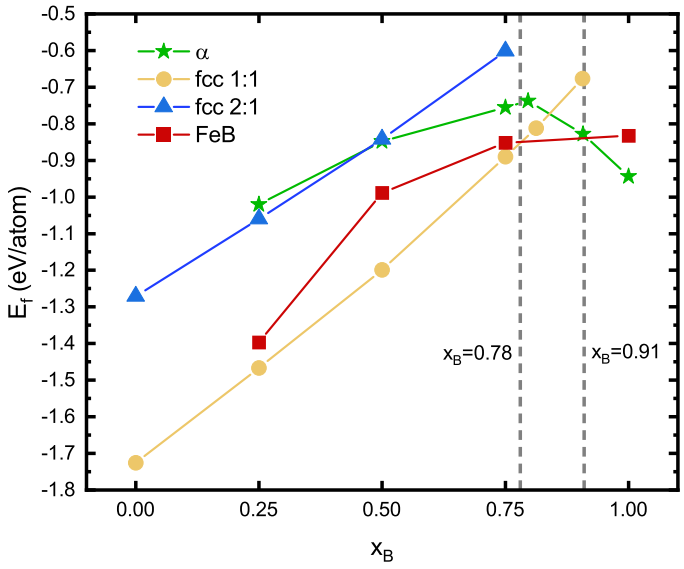

Figure 8.1: Phase stabilities of the investigated structures as function of the B concentration on the non-metal sublattice x_B shows that a fully occupied fcc structure is preferred up to ≈78 at%. The α-structure is preferred in the pure boride and down to ≈91 at% B. Between x_B=78 and 91 at% the FeB-structure has the lowest energy. Since the energy difference to the higher-symmetry structures is small, this structure may not form in PVD experiments.

fcc and hexagonal cells with 50:50 B:N ratio in [0 0 1] direction after structural relaxation. Clearly, the cubic symmetry is basically unaffected by the B, while the non-metal hexagon network of the α structure is broken by the N incorporation.

The polycrystalline bulk, shear, and Young's modulus, B, G, and E, change only slightly for the fcc structure with B incorporation (Figure 8.3). From 0 to 90 at% B (on the non-metal sublattice), B, G, and E decrease by 24, 18, and 19 %, respectively. In the α structure, going from 0 to 75 at% N on the non-metal sublattice, B, G, and E decline by 45, 85, and 82 %, respectively in contrast, showing a massive deterioration of mechanical properties by the N incorporation. Since the used formula for the Young's modulus is only strictly valid for isotropic systems, this representation could skew the comparison between the cubic and hexagonal cell, but different directional Young's moduli calculated for both phases yield the same trends.

The G/B ratio and C_p are useful criteria to study the inherent lattice ductility of materials. In Figure 8.4, all the fcc structured cells are grouped around the ductile/brittle threshold, while the pure α structured boride is very brittle. This

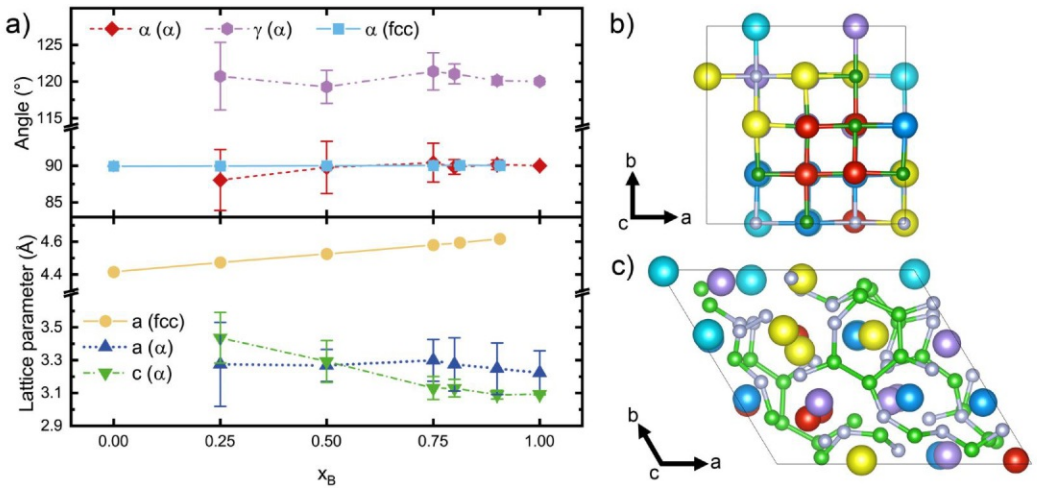

Figure 8.2: a) The averages and standard deviations of the lattice parameters calculated from 10 respective cells of the 1:1 fcc and the α structure. In the cubic structure, B incorporation causes no perturbation of the cell angle, the lattice distance increases linearly with rising B-content on the non-metal sublattice x_B from 4.43 to 4.62 Å. In the α-structure the strong fluctuations in lattice angles and spacing with increasing N-content indicate less compatibility of N with the α-structure. b) and c) show two representative 50:50 B:N populated cells in fcc and α structure after structural relaxation. The cubic structure remains almost unchanged, while the layered BN-hexagons in the α structure are broken.

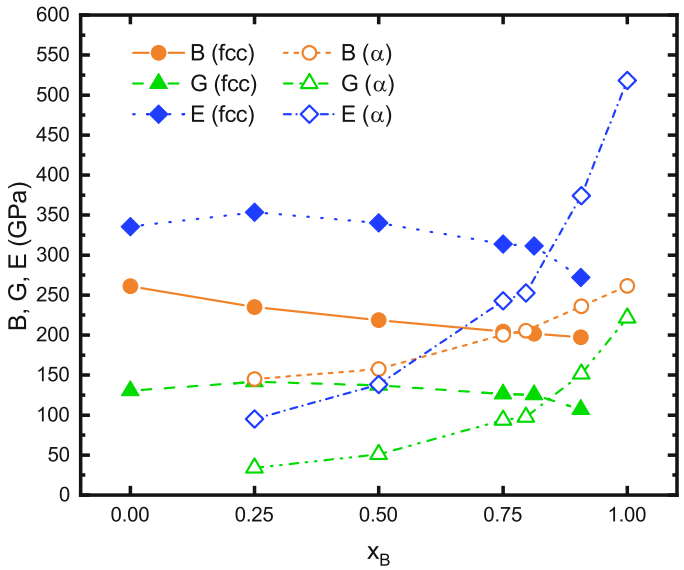

Figure 8.3: The bulk, shear, and Young's modulus, B, G, and E, respectively, of the fcc and α structures show comparatively little variation in dependence of the B concentration on the non-metal sublattice x_B. In the α structure on the other hand high values of B, G, and E decline sharply, when N is introduced to the non-metal-sublattice.

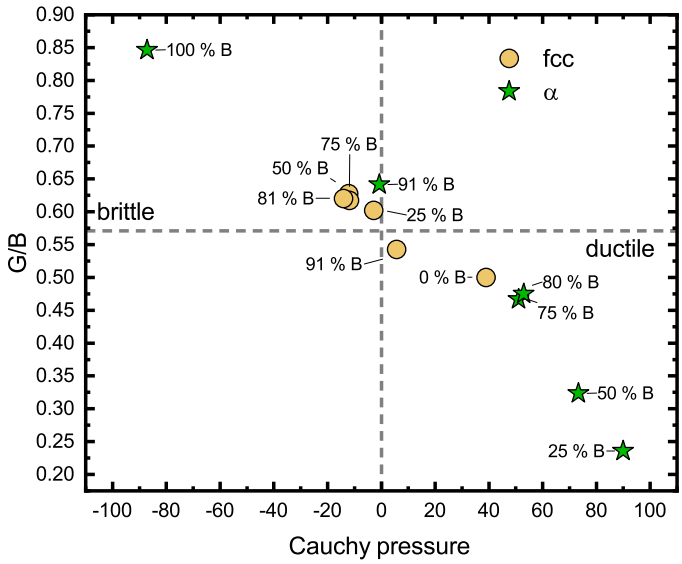

Figure 8.4: The ductility map with the G/B ratio and the Cauchy pressure shows that the pure boride in α structure is the most brittle composition. Adding N in this structure quickly transforms the material to ductile behavior. The fcc cells are positioned around the brittle-ductile thresholds, with higher B contents on the non-metal sublattice leading to more brittle behavior, except for the highest B-containing composition (which is unstable with respect to the α phase).

is expected since borides are known to form strong covalent bonds that lend a brittle fracture behavior [208]. The α structured cells quickly change to ductile behavior when N is added to the non-metal sublattice, this can be explained with the broken chemical bond network, Figure 8.2c), and thereby resulting low values of G (Figure 8.3).

To further understand this behavior, the projected density of states – summing up all metal contributions as well as summing up over all individual atoms and averaged over the 10 individual structures – was mapped for the different compositions in fcc and α structure, which can be seen in Figure 8.5. In the pure cubic nitride, a strong interaction of N p and metal d states at around -5 eV is evident, which indicates sp^3d^2 hybridization and thus strong covalent bonds [100], while the core-near N s states do not contribute to bonding in any of the considered cases. In all investigated compositions the region close below the Fermi-level is populated - mostly by metal d, but also by B p states – indicating additional metallic bonding character in all compositions. When

gradually replacing N with B in the fcc structure, the B p and metal d states hybridize, form a peak at -2.5 eV, and thus supplant the N. At the same time, B s states also hybridize with the metal d states around -6 to -7 eV.

In the N-free α structured boride (bottom row of Figure 8.5), the interaction between B p and metal d states around -4 eV is visible. When N is added to this structure, the N p states gather around -6 eV, while the metal d states shift towards the Fermi level, indicating less intense bonding between the metals and non-metals. Unlike in the fcc structure, the N and B states overlap partially on the energy scale, which is due to the bonding to each other within the hexagon planes. At the same time, the N and B states are spread over a large range on the energy scale, indicating also a wider spread of the electronic states in real space and thus less pronounced covalent character. This delocalization explains the drastically worse mechanical properties of the N-alloyed α structure. Please note that the total DOS does not have to align with the summed pDOS contributions, which themselves lack the contributions from the interstitial regions. Also, the presented pDOS are given per atom, so that low concentrations of an element lead to high contribution in the pDOS but only minor contributions in the total DOS.

8.3.2 Chemical Analysis

The chemical compositions of the reactively deposited coatings measured by EDS are listed in Table 8.2. In all coatings, the heavier elements Hf and Ta are more abundant, which is common in sputtered coatings due to different poisoning states of the individual target grains [209] or preferential resputtering of the lighter elements [210, 211]. This effect is even more pronounced in the boronnitride coatings, since the HfB_2 and TaB_2 pieces show a higher sputter rate compared to the lighter elements. The B content increases from 0 up to ~18 at% with increasing number of metal diboride pieces on the target. The N concentration is largest in the B-free coating with 48 at% N, with B addition, the N-content decreases at first, but then increases together with the B content, which is a sign of BN formation. The maximum B:N ratio obtained is 0.44.

The chemical compositions of the non-reactively sputtered coatings, analyzed

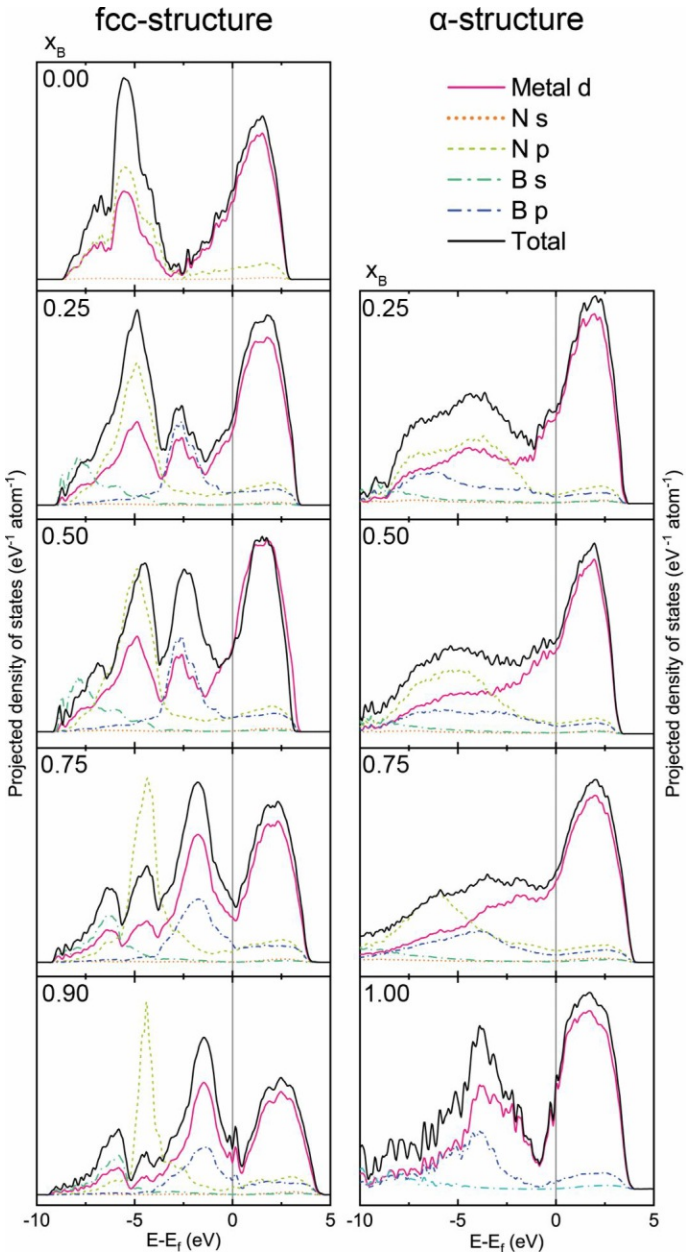

Figure 8.5: The projected density of states of N, B, and the summarized metals of the relaxed fcc and α structured cells show the trend of bonding partners at different B concentrations on the non-metal sublattice x_B. In the pure nitride (top row), the chemical bonds are formed by interaction of N p with metal d states, while the core-near N s states do not participate in any case. With increasing B content the bonding N p states are gradually replaced by B p and s states. The overlapping states shift from -5 eV to -2.5 eV. In the α structure with only B (bottom row) the chemical bonds are formed between the B p and Metal d. With the introduction of N, the peak at -4 eV is flattened into a broad feature, and only at 75 at% N peaks emerge again, now with contributions of the N p, B p, and B s states.

Table 8.2: Chemical compositions of the reactively sputtered coatings on Si substrates were analyzed with EDS. Standard errors of 3 respective measurements are 1 at% for all coatings and elements. Chemical compositions of the non-reactively sputtered coatings on sapphire substrates were obtained with ERDA. The signal from 1000 to 2000 $\times 10^{15}$ at/cm^2 was averaged for all samples, the standard error from this region is given as statistical uncertainty. Configurational entropies have been calculated with the sublattice model [44] and are shown for the metal sublattice M, the non-metal sublattice NM, and their combination Σ.

	Chemical composition (at%)									S_{conf}/R		
	B	N	O	Hf	Ta	Ti	V	Zr	B:N	M	NM	Σ
Reactive	0	48	0	12	12	10	9	9	0	1.62	0.03	0.83
	12	38	2	16	10	8	8	6	0.32	1.52	0.68	1.10
	14	37	2	13	12	8	8	6	0.38	1.53	0.71	1.12
	18	41	1	11	11	7	5	6	0.44	1.43	0.61	1.02
	B	N	O	C	Hf+Ta	Ti	V	Zr	B:N	M	NM	Σ
Non-reactive	0	37.7±0.3	2.4±0.1	15.0±0.4	0	0	0	44.9±0.4	0	0.13	0.71	0.42
	20.0±1.0	26.2±0.7	2.9±0.4	9.3±0.7	4.6±0.3	2.5±0.3	2.5±0.5	32.0±0.9	0.76	0.81	1.18	0.99
	21.8±0.4	26.2±0.4	1.4±0.1	8.5±0.3	4.6±0.1	2.6±0.1	3.6±0.2	31.2±0.4	0.83	0.85	1.30	1.08
	23.6±0.7	22.9±0.5	7.1±0.3	9.1±0.3	4.1±0.1	2.9±0.2	2.6±0.2	27.7±0.4	1.03	0.86	1.10	0.98
	24.1±0.5	24.5±0.6	1.5±0.1	7.4±0.2	4.7±0.2	2.5±0.1	3.4±0.2	31.9±0.4	0.98	0.84	1.09	0.97
	25.5±0.6	22.8±0.5	2.1±0.2	7.9±0.4	4.5±0.1	2.9±0.2	4.2±0.2	30.1±0.6	1.12	0.89	1.13	1.01

by ERDA, are presented in Table 8.2. The depth profiling with ERDA yielded constant concentrations across the scanned depth, see the exemplary depth profile of the coating with the highest B content in Figure 8.6. The only exception is a changed B:C ratio at larger depths, which is due to the inability of the technique to distinguish B and C at larger depths [212]. To also avoid influence of surface contamination, the depth between 1000 and 2000 $\times 10^{15}$ at/cm^2 was therefore averaged for quantification in all samples, and the given uncertainties are the statistical errors of measurement from averaging over this region. The coatings prepared from the Zr(N, C) target contain 15.0 at% C, which decreases to 7-9 at% when placing additional diboride pieces (that contain no measureable C content) on the racetrack. All non-reactively sputtered multi-element boronnitride coatings contain around 30 at% Zr, while the sum of the other metals increases from 9.3 to 11.8 at% with increasing number of diboride pieces on the racetrack. The oxygen content stays around 2 at%, except in the coating with 23.6 at% B, where 7.1 at% of oxygen have amassed. Since we used broken diboride pieces with irregular shapes, the surface contamination with oxygen on these pieces could be significant. This contamination was taken care of by pre-sputtering behind the closed shutter, but for this sample the procedure was apparently insufficient. The B and N

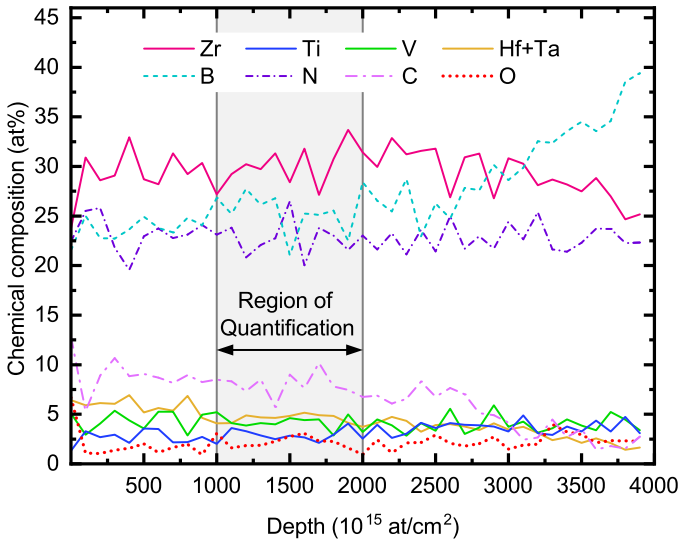

Figure 8.6: ERDA depth profile of the non-reactively sputtered coating with the highest B content. The element ratios are constant across the measured depth, with the exception of B and C, which become indistinguishable at high depths [212]. The depth between 1000 and 2000×10^{15} at/cm^2 was used for quantification in all samples.

contents are both close to 25 at%, so that their sum is between 48 and 50 at% in all coatings. The B:N ratio changes from 0.76 to 1.12 with increasing B content of the (Hf, Ta, Ti, V, Zr)-B-N coatings, see Table 8.2.

The configurational entropy S_{conf}, calculated with the sublattice model [44], for the reactively sputtered nitride is $1.62 \cdot R$ on the metal sublattice, while the small number of N-vacancies on the non-metal sublattice contribute only a negligible amount of configurational entropy, see Table 8.2. This coating is therefore a high-entropy sublattice nitride. The combined S_{conf} across both sublattices amounts to $0.83 \cdot R$ (per atom), which is expected of a typical fcc high-entropy sublattice nitride. In the reactively sputtered boronnitride coatings, the metal sublattice contributes between 1.43 and $1.52 \cdot R$ to S_{conf}, while the contribution from the non-metal sublattice lies between 0.61 and $0.71 \cdot R$. In combination (considering both sublattices), these coatings exhibit S_{conf} values between 1.02 and $1.12 \cdot R$ (per atom). But these values are overestimated and provide only a rough guideline, since the reactively sputtered coatings all exhibited an additional BN phase to varying degrees, as will be shown by XRD data in Section 8.3.3. The individual configurational entropy data for these reactively

prepared coatings indicate that only (Hf, Ta, Ti, V, Zr)N fulfills the condition of $S_{conf} \geq 1.5 \cdot R$ for one sublattice and single-phase solid solution and can thus be named high-entropy sublattice nitride, see Table 8.2. The reactively sputtered (Hf, Ta, Ti, V, Zr)-B-N coatings on the other hand are multi-phase coatings and can therefore be called compositionally complex boronnitrides (CCBN).

For the non-reactively sputtered coatings, the calculation of S_{conf} is complicated by the carbon content, but using different assumptions, we estimated a value. Due to the high Zr content in all these non-reactively prepared coatings, the threshold of $S_{conf} \geq 1.5 \cdot R$ is missed even for the metal sublattice, which provides a maximum of only $0.89 \cdot R$, Table 8.2. But with the addition of B, C, and O, the configurational entropy of the non-metal sublattice could be massively increased in the non-reactively prepared coatings. If C and O reside on the non-metal sublattice, which is reasonable when considering studies about Ti-C-N [213, 214] and Ti-O-N [215], then S_{conf} of the non-metal sublattice increases from 0.71 (when considering only B and N) to $1.30 \cdot R$. Together with the contribution of the metal sublattice this amounts to a maximum of $1.08 \cdot R$ (per atom), a higher value than in the reactively sputtered high-entropy sublattice nitride. Still, no sublattice reaches the criterion for a HESC, so that these coatings should be called single-phase CCBNs.

The compositions of our calculated and deposited systems are outlined in the ternary metal-B-N phase diagram in Figure 8.7, also here we considered C (as well as O) to substitute for N in the non-reactively prepared coatings. Our calculations traced out the phase field between the compositions MeN, MeB, and MeB_2 as most likely for beneficial properties. The reactively deposited coatings start in this region, but at the highest B concentration (and B:N ratio) take a turn towards the BN phase. In Ti-B-N, it was shown that reactive depositions follow the MeN-BN line even at very low B concentrations [204], while our reactively sputtered coatings show this trend only at higher B concentrations, which can be due to different sputtering conditions and N_2 partial pressure. The non-reactively deposited coatings on the other hand sustain much higher B concentrations (and B:N ratios) and would still lie in the MeN-MeB-MeB_2 triangle, if we discount the shift by the additional C and O. The one non-reactively sputtered sample that

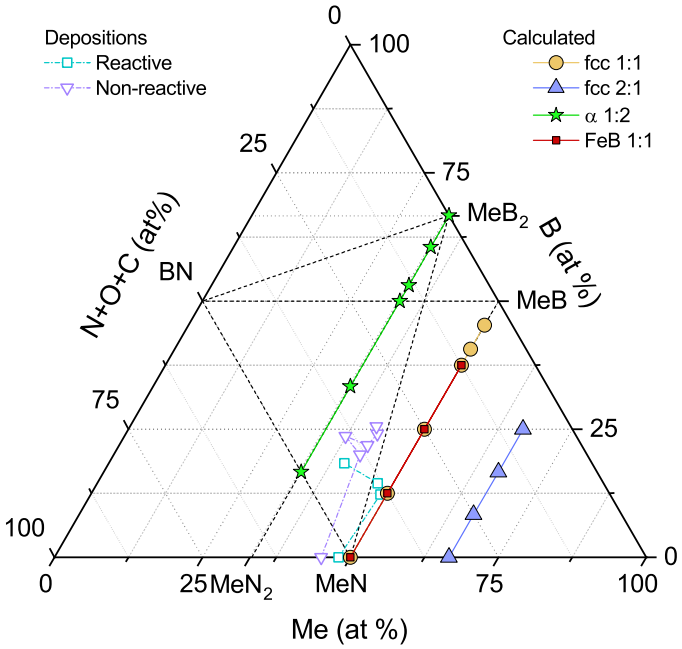

Figure 8.7: The ternary phase diagram of B, N, and summed metals (Me) shows the relative positions of the calculated and deposited compositions. The non-reactively sputtered coatings lie along the MeN-MeB_2 line, while reactive sputtering clearly leads to BN formation at higher B contents. For simplicity reasons, we counted possible O and C incorporation as N.

sticks out towards the BN phase does so because of its high O content.

8.3.3 Structure and Mechanical Properties

The difference between the reactively and non-reactively sputtered coatings manifests even more in the XRD patterns, see the non-reactively as-deposited coatings on Si in Figure 8.8a). The reactively prepared HESN shows a single phase fcc structure, but with B addition the contribution of an amorphous structure clearly increases, see the increased background between 25 and ≈35°. Furthermore, the crystalline (1 1 1), (2 0 0), and (2 2 0) peaks widen with increasing B content (and B:N ratio) tremendously.

A similar behavior could not be identified for the non-reactively sputtered coatings, which essentially only exhibit XRD features that point towards a single crystalline phase in as-deposited state, independent of the B content (and B:N ratio), see Figure 8.8b). The B content in the single-phase fcc-structured non-

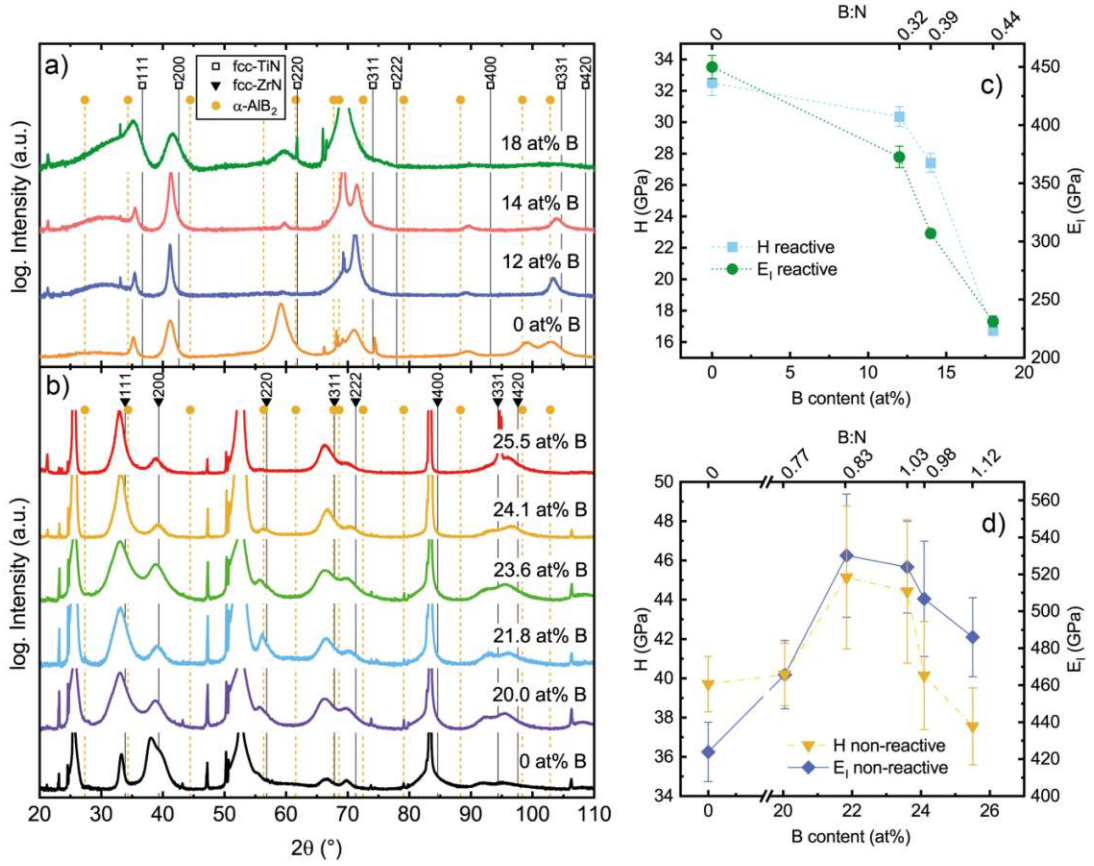

Figure 8.8: a) XRD patterns of as-deposited reactively sputtered coatings on Si substrates reveal crystalline fcc reflexes, but also amorphous features with increasing B content, stemming from excess BN. b) XRD patterns of as-deposited non-reactively sputtered coatings on sapphire substrates reveal broad crystalline fcc peaks without amorphous phase fractions in all coatings. c) Nanoindentation of as-deposited reactively sputtered coatings shows a drastic decline in hardness H and indentation modulus E_I with increasing B content, due to the increasing amorphous phase fraction. d) The as-deposited non-reactively sputtered coatings are superhard, peaking at 46.3 GPa in the coating with 23.6 at% B. Note the much higher B:N ratio in the non-reactively prepared coatings.

reactively prepared coatings is also significantly higher (maximum of 25.5 at%) than the maximum reported for a single-phase fcc-structured Ti-B-N of 17.4 at% [216]. This suggests that the higher elemental complexity allows to solute more B into the fcc transition-metal-nitride-based lattice. Contrary to the reactively prepared coatings, the XRDs for the non-reactively prepared coatings are obtained from coated sapphire substrates, since the Si substrates always broke during or after deposition. Generally, the peak positions of the Zr(N, C) coating are shifted significantly towards lower diffraction angles (pointing towards a higher lattice parameter of 4.65 Å). This is likely due to the high compressive stresses and the high C content, ZrC is also fcc structured with a larger lattice constant of 4.69 Å (ICDD 00-035-0784) compared to ZrN with 4.58 Å (ICDD 00-035-0753). With the addition of B the preferred orientation changes from a (2 0 0) towards a (1 1 1)-oriented growth. All of our coatings have lattice parameters varying between 4.62 and 4.67 Å without a clear trend, which is considerably more than the reference value for ZrN, and also more than the predicted lattice parameter of 4.53 Å for the 50:50 B:N system (see Figure 8.2). For the latter case this is due to the very high Zr content in our coatings, whereas the calculations use equimolar distribution of the metals. In addition, our coatings are highly stressed, which can cause a shift of the XRD positions (macro-stresses) and also significant peak broadening (micro-stresses). In none of our samples could we detect any sign of an α phase, in good agreement with calculations.

The phase composition influences the mechanical properties heavily, see Figure 8.8c) for the indentation hardness H and modulus E_I of the as-deposited reactively sputtered coatings. The HESN has a H and E_I of 32.5 and 450 GPa, respectively, with B addition, both these values decrease immediately. The decline is pronounced, especially for E_I when increasing the B content beyond 12 at%, which is a clear proof for the formation of amorphous BN, as suggested by XRD (Figure 8.8). The deterioration of the mechanical properties by BN formation was studied in reactively sputtered Ti-B-N films, where too high N partial pressures quickly lead to reduced hardness due to the formation of an amorphous BN phase [217–221]. Therefore, all reactively sputtered boronnitride coatings in this study perform much worse than the HESN and established nitride coatings [7], let

alone borides for which superhardness (H above 40 GPa [222]) is often reported [26, 27, 223, 224]. Whether depositions at lower N_2 partial pressures would lead to favorable properties remains to be seen. Due to the reduced mechanical properties in the reactively sputtered coatings, only the non-reactively sputtered coatings were studied further for their thermal stability (the HESN coating is presented in [66]).

The non-reactively sputtered coatings can clearly be classified as superhard, see Figure 8.8d) for their H and E_I values in the as-deposited state. The Zr(N, C) coating features a hardness of 36.3 GPa and an indentation modulus of 460 GPa. Both values peak with the addition of B, where highest H values of 46.3 and 45.7 GPa and highest E_I values of 518 and 511 GPa are obtained for 21.8 at% B (B:N=0.83) and 23.6 at% B (B:N=1.03), respectively. This is especially remarkable for the coating with 23.6 at% B, which also contains ≈7 at% oxygen, where we would expect significant softening due to the increasingly ionic bonding character caused by the electronegative oxygen.

The cross-section TEM micrograph of the coating with 23.6 at% B shows a dense micro-columnar coating, see the bright-field image in Figure 8.9a) but especially its dark-field variation in Figure 8.9b). No amorphous-like structure could be identified at the column or grain boundaries, not even for this coating despite having the highest oxygen content. Therefore, our previous made assumption seems plausible, that also oxygen is incorporated in the lattice. SAED patterns recorded from regions I (close to the substrate) and II (close to the surface) in Figure 8.9 confirm the single-phase fcc structure throughout the whole thin film. The lattice parameter calculated from the SAEDs is 4.73±0.05 Å for region I and 4.77±0.06 Å for region II, in reasonable agreement with XRD measurements. The grain morphology of this coating is vastly different from non-reactively prepared Ti-B-N coatings with similar B contents and B:N ratios, that are usually nanocomposites of TiN and TiB_2 with a disordered encapsulation phase [164, 225]. The coating with the highest B content (25.5 at%) and also highest B:N ratio of 1.12 shows identical cross-section TEM images and SAED patterns as this one presented in Figure 8.9 (therefore, not shown here).

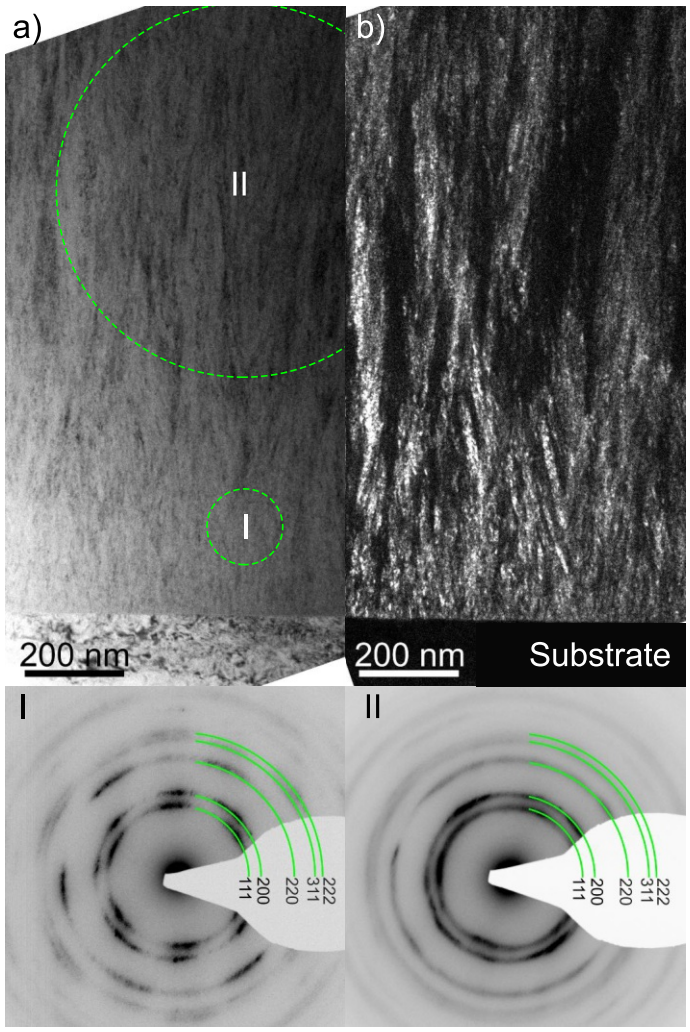

Figure 8.9: Cross-sectional TEM micrographs of the as-deposited non-reactively prepared coating with 23.6 at% B. Bright-field a) and dark-field b) investigations show a very fine-grained micro-structure. Selected Area Electron Diffraction patterns from regions I and II confirm the single-phase fcc structure (reference circles shown for a =4.75 Å) and a strong texture near the substrate, that decreases further into the coating.

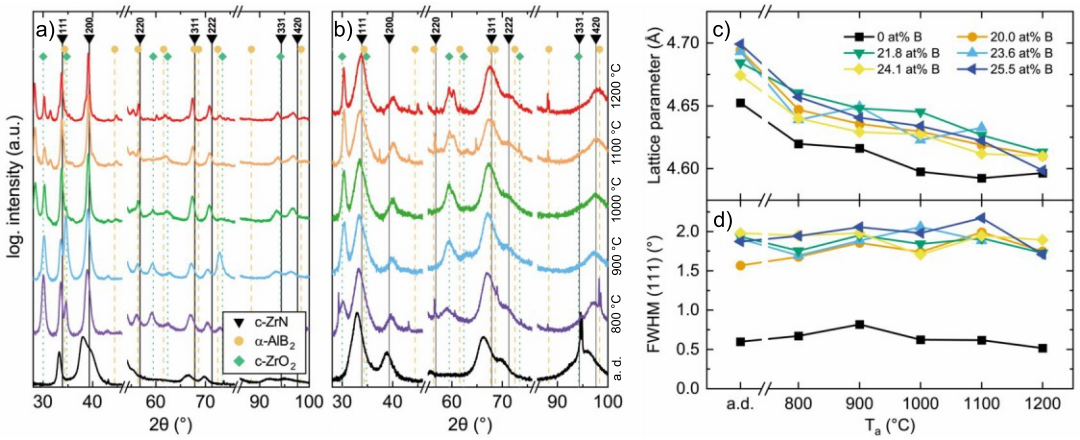

Figure 8.10: XRD patterns of non-reactively sputtered Zr(N, C) a) and the multi-element boronnitride with 25.5 at% B b), in as-deposited state and after vacuum annealing at up to 1200 °C for 10 min. The multi-element coating retains its single-phase fcc structure even after annealing to 1200 °C. Only the formation of surface oxides by residual O_2 are visible (reference positions for c-ZrO_2 are shown). The only other notable change is a slight decrease of the lattice parameter, shown in c), calculated from the shift of the (1 1 1) reflex. The B-alloying leads to highly strained lattices and broad peaks, visible from the FWHM of the (1 1 1) reflex in d). The peak width is basically independent of the thermal treatment.

8.3.4 Thermal Stability

XRD investigations indicate that the non-reactively sputtered coatings experience only a marginal change of their structure upon vacuum annealing up to 1200 °C. Exemplarily, Figure 8.10a) and b) show the XRD patterns of Zr(N, C) and the non-reactively prepared multi-element boronnitride coating having 25.5 at% B. To minimize any substrate interference, the annealing studies were conducted with coatings grown on sapphire. All coatings still exhibit a single-crystalline fcc structure even when annealed to 1200 °C. The most notable change upon the annealing is the rather strong formation of ZrO_2 even when annealed only at 800 °C, due to the high oxygen affinity of Zr for which even the relatively small amount of residual O_2 in the vacuum furnace is sufficient. Basically, several Zr-oxide phases are present, but we have exemplarily marked only the positions of cubic ZrO_2 (ICDD 00-049-1642). Before the nanoindentation tests the coatings were polished to remove these oxides.

The other noticeable change is the shift of the peak positions to higher diffraction angles, corresponding to smaller lattice parameters. This is nicely

presented by the evolution of the lattice parameter with the annealing temperature T_a, Figure 8.10c). All non-reactively prepared coatings show the same behavior. For Zr(N, C) for example, the lattice parameter decreases from 4.66 to 4.60 Å upon increasing T_a to 1200 °C. The reference value for stress-free ZrN powder is 4.57 Å (ICDD 00-031-1493). The single-phase fcc-CCBN coatings follow the same pattern, starting at up to 4.70 Å.

All CCBN coatings exhibit much broader peaks than Zr(N, C), which is also nicely shown by the evolution of the full width at half maximum (FWHM) of the (1 1 1) peak with annealing temperature in Figure 8.10d). Although the lattice parameters are steadily decreased with increasing annealing temperature – indicative for reduced macrostresses – the FWHM does essentially not change even when annealed at 1200 °C. This observation indicates that the microstresses basically remain, pointing towards reduced recovery rates (during which crystal defects would arrange to lower energy sites).

The slow recovery rate in further consequence explains their much better thermal stability of mechanical properties, where even after vacuum annealing to 1200 °C, Figure 8.11a), the hardness does not change too much. The Zr(N, C) possesses a H of 36.3 GPa in its as-deposited state and still 35.1 GPa when annealed at $T_a = 900$ °C. After annealing to $T_a = 1200$ °C the hardness decreases to 30.2 GPa. Since this coating contains some C, its hardness decreases much slower than in a typical binary nitride (compare for example the softening in TiN to < 30 GPa when annealed at $T_a = 600$ °C [7]). Since ZrC itself is rather hard [226] the hardness of our Zr(N, C) coating is also significantly higher than what has been reported for ZrN thin films so far [227–229].

Even after annealing to 1200 °C, the CCBN coating with 23.6 at% B (B:N=1.03) loses only ≈2 GPa in hardness, while the coating with 25.5 at% B (B:N=1.12) does not lose any hardness within the error of measurement. This performance is similar to high-entropy sublattice diboride coatings [26, 27], but vastly superior to Ti-B-N coatings, which lose hardness above annealing temperatures of 900 °C due to evaporation of B from the disordered encapsulation region [164]. We attribute the hardness retention of our coatings to the stable crystalline fcc solid solution up to 1200 °C, which is mirrored also by the rather

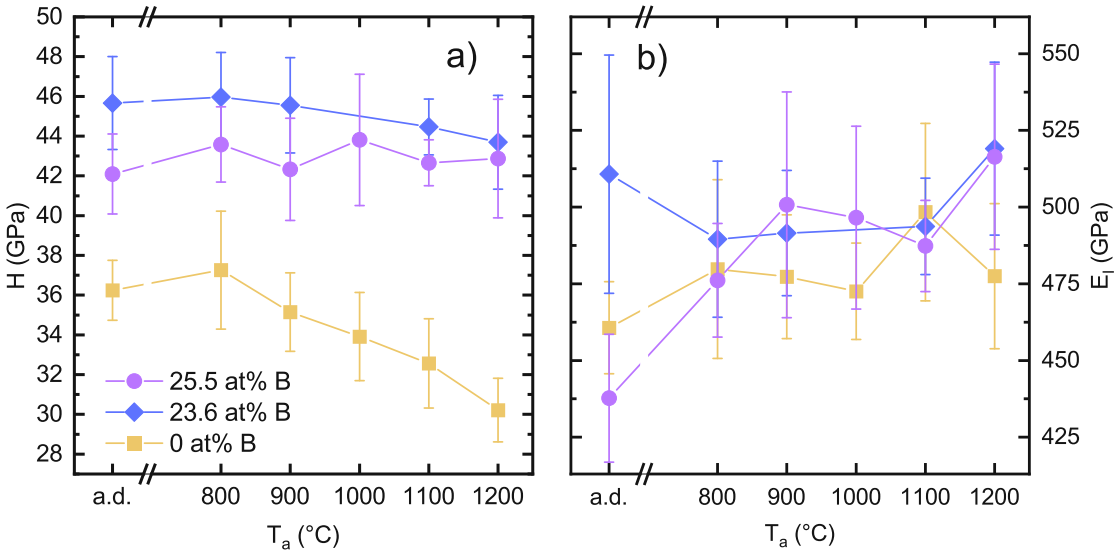

Figure 8.11: Nanoindentation performed on polished vacuum-annealed non-reactively sputtered coatings with 0, 23.6, and 25.5 at% B reveals great hardness retention in these multi-element boronnitride coatings a). Even after vacuum annealing to 1200 °C, a hardness of 42.9 and 43.7 GPa is retained in both multi-element coatings, respectively. The Zr(N, C) coating on the other hand gradually loses 6 GPa. The indentation modulus E_I is very similar in all coatings b).

stable FWHM values up to this temperature.

Also, the indentation modulus, E_I, shows little dependence (within the error of measurement) on the annealing temperature, see Figure 8.11b), but here also Zr(N, C) provides rather stable values.

CHAPTER 9

Strain-Stabilized Al-Containing High-Entropy Sublattice Nitrides

9.1 Introduction

Since their discovery, high-entropy materials have increasingly caught attention of material scientists [9, 10]. The basic principle is the random distribution of five or more elements in equiatomic or near-equiatomic composition on the same crystal lattice, leading to a locally distorted lattice with high configurational entropy $S_{conf} \geq 1.5 \cdot R$, R being the gas constant. Four core effects have been postulated that characterize these materials, although the importance of these effects has recently been questioned [230]: high configurational entropy, distorted lattice, sluggish diffusion, and cocktail effects. Originally defined for metallic alloys, the high-entropy principle has since been expanded to ceramic materials too [23]. Since only one sublattice, which contains a fraction of all atoms, is usually occupied with chemically different species, the configurational entropy of such phases reaches $\geq 1.5 \cdot R$ only per formula unit [8]. Therefore, the name high-entropy sublattice ceramics has been coined for such materials [66].

Rost et al. [52] demonstrated the high-entropy effect in oxides, where only the metal-sublattice is occupied by five or more metal species in equiatomic or near-equiatomic composition. The authors consequently claimed that configurational entropy dominates the thermodynamic landscape. However, studies on metallic

alloys indicated that the impact of configurational entropy on phase stability may have been overestimated in some cases [231, 231, 232]. The controversy about whether S_{conf} [10, 52], H_{mix} [56, 127], or a descriptor termed "entropy forming ability" [34] defines the stability of high-entropy ceramics has not yet been addressed systematically and quantitatively.

Among the different ceramic classes, physical vapor deposited nitrides are of great relevance in machining industries as protective thin films against wear and corrosion. PVD also represents an important synthesis route for HESC [23]. Common industry standards include (Al, Ti)N or (Al, Cr)N [7, 233], which are metastable and only form solid solutions within certain chemical composition limits, which depend on various parameters [100]. The supersaturated lattices formed by PVD tend to decompose towards their thermodynamically stable phases upon thermal treatments. Typically, the mechanical properties and oxidation resistance, but also the mixing enthalpy (driving force for decomposition) of such coatings increase with the Al content in the cubic regime, whereas the formation of wurtzite-structured domains initiates the decline in the mechanical properties [234–236]. Stabilizing AlN in the cubic structure is therefore beneficial for many applications. Since high-entropy materials should benefit from sluggish diffusion and enhanced phase stability due to S_{conf}, they are prime candidates to improve the thermal stability of Al-containing nitride coatings. Additionally, lattice strains in (Ti, Al)N have been proven to influence the decomposition behavior substantially [237–239]. The stabilizing potential of this effect has been proposed [127], but not yet investigated for high-entropy materials.

The discovery of new materials is aided greatly by high-throughput computations [126], since they allow efficient scanning of phase spaces that are inaccessible to experiments due to the sheer number of possible compositions. This is especially true for the field of high-entropy materials. While phase stabilities of metallic high-entropy alloys have been studied extensively by means of CALPHAD [127, 240] or density functional theory (DFT) [128, 129], we still lack high-throughput studies for HESC or intermetallics, which have attracted comparatively little attention so far. Ab-initio studies have been performed on selected carbide [31, 130–132], oxide [60, 133, 134], boride [135], nitride [66, 136],

and even carbonitride systems [137], but with the exception of carbides [34, 132], no high-throughput studies have been published so far on HESC.

Since the exploration of the vast phase space is a daunting task, different methods - including data science approaches - have been developed to screen for possible entropy-stabilized candidates more efficiently within the framework of computational investigations [34, 128, 241]. While these "entropy forming ability" or "small set of ordered structures" based methods provide an efficient direction for experimental validation, they are often unable to uncover the underlying materials science. Especially the contribution of configurational entropy, claimed to dominate the thermodynamic landscape in HESC [52], remains questionable.

We have therefore investigated all equimolar Al-containing high-entropy sublattice nitrides within the phase space of the group IVb, Vb, and VIb transition metal nitrides with ab-initio simulations, to critically assess the roles of enthalpy, configurational entropy, and strain energy on phase stability. To this end, we calculated the decomposition driving forces of these solid solutions, and also of all possible decomposition products of the different multinary levels. We use the following terminology in this article: hexinary nitrides = $(M_1M_2M_3M_4M_5)N$, quintenary nitrides = $(M_1M_2M_3M_4)N$, quaternary nitrides = $(M_1M_2M_3)N$, ternary nitrides = $(M_1M_2)N$, and binary nitrides = MN. The phase space was constrained to only Al-containing HESN, since Al is paramount for resistance against oxidation, which is often limiting the performance of PVD coatings, and also for its beneficial impact on hardness. The predictions were critically evaluated with experimental thermal stability data.

9.2 Methods

9.2.1 Density Functional Theory

DFT calculations were performed with the Vienna Ab-initio Simulation Package (VASP) [111, 112], using projector augmented plane wave (PAW) pseudo-potentials under the generalized gradient approximation [110], to study the decomposition of equimolar $(AlM_2M_3M_4M_5)N$ into all possible combinations

Table 9.1: Calculated decomposition scenarios for the 126 hexinary nitrides $(M_1M_2M_3M_4M_5)N$ considered here. These nitrides are all possible hexinary combinations of AlN with IVb, Vb, and VIb transition metal nitrides. For example, there are 5 possible combinations of the decomposition products for the reaction $(M_1M_2M_3M_4M_5)N \longrightarrow (M_1M_2M_3M_4)N + M_5N$, etc.

Combinations	Product 1	Product 2	Product 3	Product 4	Product 5
5	$(M_1M_2M_3M_4)N$	$+M_5N$			
10	$(M_1M_2M_3)N$	$+(M_4M_5)N$			
15	$(M_1M_2M_3)N$	$+M_4N$	$+M_5N$		
15	$(M_1M_2)N$	$+(M_3M_4)N$	$+M_5N$		
5	$(M_1M_2)N$	$+M_3N$	$+M_4N$	$+M_5N$	
1	M_1N	$+M_2N$	$+M_3N$	$+M_4N$	$+M_5N$

of equimolar multinary or binary nitrides. Table 9.1 gives a summary of all 51 possible combinations of decomposition products. For brevity, we refer to all calculated compositions, which always contain equimolar metal ratios, throughout the thesis with a shortened notation: $(M_1M_2M_3M_4M_5)N$ or $M_1M_2M_3M_4M_5N$ always stand for 20 at% of each metal on the metal-sublattice, and a non-metal sublattice with full N-occupation. The same principle applies to the other multinary level nitrides.

The binary nitrides were calculated in the fcc rock-salt structure with 1:1 stoichiometries. This represents the most stable structure at room temperature for CrN, HfN, TiN, VN, and ZrN. For the other metal nitrides their currently known most stable structures in 1:1 stoichiometry were calculated in addition. AlN was calculated in wurtzite structure (space group=SG 186) [239], MoN in NiAs-structure (SG 194) [184, 187], NbN in WC-structure (SG 187) [242], TaN in hexagonal structure (SG 189) [243], and WN in NbO structure (SG 221) [117]. For the investigations of phase stability only the most stable structures were used. The structure files of all binary nitrides used, can be found in Appendix A. All multinary level nitrides were calculated in B1 structure in $2 \times 2 \times 2$ supercells with 64 atoms (32 metals, 32 N atoms). The metals were distributed on the metal sublattice by the special quasi-random structure method to simulate random solid solutions [118]. Since 32 metallic sites do not allow for equimolar 3 or 5 component alloys, the properties of interest were obtained by averaging over 3 or 10 cells, respectively, in which the metals were permuted over the 11+11+10 or

7+7+6+6+6 sites.

The reciprocal space was sampled with a Γ-centered Monkhorst-Pack mesh [113] with $6 \times 6 \times 6$ k-points for all multinary nitrides. The structures, space groups, and corresponding k-meshes for the binary nitrides are listed in Table B.3. The k-mesh was chosen to give the same k-point density across all cells and dimensions. The energy-cutoff was set to 500 eV, the stopping criterion for ionic relaxation to $\approx 10^{-4}$ eV. The cells were relaxed regarding size, shape, and atomic positions. We did not consider magnetism in CrN (important in CrN [63]), defects, or other structures like intermetallic compounds between the constituting metals (other than the Hägg phase to which these nitrides typically belong).

9.2.1.1 Phase Stability

The driving force ΔG_{mix} of a mixing reaction $\mathrm{A} + \mathrm{B} \rightleftarrows \mathrm{AB}$, is composed of enthalpy and entropy contributions (Equation 2.2), where a negative value of ΔG_{mix} indicates a stable mixture AB and a positive value decomposition into the constituting phases A and B. ΔH_{mix} is calculated from the E_f of educt and product phases (Equation 5.11), with E_f calculated by Equation 5.9.

The mixing entropy, ΔS_{mix}, is calculated as the difference in configurational entropies of the reactants (Equation 2.3), other entropy contributions such as vibrational, magnetic, and electronic entropy are not considered here. Since the non-metal sublattice is perfectly ordered, the nitrogen-atoms do not contribute to configurational entropy. Only the metal-sublattice is randomly occupied, so that the configurational entropy (per atom) for our 1:1 metal-nitrides is calculated by

$$S_{conf} = -k_B \frac{1}{2} \sum_i X_i \ln X_i \,, \tag{9.1}$$

with k_B being the Boltzmann constant, and X_i being the mole fraction of the ith component in the solid solution. Since all compositions are equimolar, a simplified formula can be applied

$$S_{conf} = \frac{1}{2} k_B \ln N \,, \tag{9.2}$$

where N is the number of elements on the metal-sublattice. The entropy contribution was calculated for 0 and 1073 K. The volume change during

decomposition of our hexinary nitrides was calculated by

$$\Delta V = \frac{\sum_i \nu_i V_i - V_{product}}{V_{product}}, \tag{9.3}$$

with V_i and $V_{product}$ being the volumes of the ith educt and the product, respectively. The elastic properties of predicted stable decomposition products were calculated with the stress-strain method [123] from their structurally relaxed cells. The elastic constants were projected onto cubic symmetry with the method of Moakher and Norris [206]. The bulk modulus was calculated as average of the Reuss and Voigt estimates [207]. With the bulk modulus, the strain energy for the isostructural decomposition was calculated with the Birch-Murnaghan equation of states (applied to the total energy, instead of E_f) [244]

$$E_{BM} = E_0 + 9V_0B_0/16\{[(V_0/V)^{2/3} - 1]^3 B_0' + [(V_0/V)^{2/3} - 1]^2[6 - 4(V_0/V)^{2/3}]\}, \tag{9.4}$$

where V_0 is the equilibrium volume, B_0 is the bulk modulus at V_0, E_0 is the equilibrium energy at V_0, B_0' is the derivative of the bulk modulus with respect to pressure. Since the equilibrium structures were calculated by automatic full structural optimizations, relaxing atomic positions, cell shape, and volume, we did not calculate explicit values of energies at different volumes. We therefore do not know the exact value of B_0' in our compositions, and instead assumed $B_0' = 4$ in all cases [245–247]. E_{BM} is the total energy at the desired volume V.

9.2.1.2 Structure Analysis

The variation of bond lengths in the relaxed structures was analyzed by a radial distribution function, $rdf(r)$, representing a density of atoms at a spherical ring with radius r and thickness dr from an atom. Thereby, its peaks correspond to coordination shell radii, which were fitted with Gauss distributions:

$$rdf(r) = a_i \cdot e^{-\frac{(r-r_{0,i})^2}{2\sigma_i^2}}, \tag{9.5}$$

with $r_{0,i}$ being the mean bond length (for the ith peak), a_i being a fitting parameter, and σ_i^2 the variance in atomic bond lengths. The values of σ_1 were

plotted against the average nominal bond length difference between the metal and non-metal sublattice δ, calculated as

$$\delta = \sqrt{\sum_{i=1}^{N} X_i \left(\frac{1 - r_i}{\overline{r}}\right)^2}, \tag{9.6}$$

with X_i being the mole fraction of the ith component, r_i the nearest neighbor N-metal bond length of the ith metal, and $\overline{r}$ the average nearest neighbor N-metal bond length of all metals present [62]. The bond lengths were calculated from the relaxed fcc-structured binary nitrides, the relevant values are listed in Table B.4.

9.2.2 Deposition

Coatings of the material systems (Al, Cr, Nb, Ta, Ti)N, (Al, Hf, Ti, V, Zr)N, (Al, Hf, Mo, V, Zr)N, and (Al, Mo, Ta, V, W)N were deposited by reactive magnetron sputtering in a modified Leybold Heraeus Z400 facility from powder-metallurgically prepared equimolar 75 mm-diameter targets of the corresponding metals (Plansee Composite Materials GmbH). (1 0 0)-oriented Si ($20 \times 7 \times 0.38\,\mathrm{mm}^3$) and (1 $\overline{1}$ 0 2) sapphire ($10 \times 10 \times 0.53\,\mathrm{mm}^3$) substrates were coated, mounted face-to-face to the target at a distance of 4 cm, with a bias potential of -50 V DC and at a deposition temperature of 440 °C.

After reaching a base pressure of 0.3 mPa, the substrates were Ar-ion etched at a pressure of 1.3 Pa for 15 min by applying a negative pulsed DC substrate potential of -150 V with a pulse frequency of 150 kHz and a pulse duration of 2496 ns. The targets were cleaned prior to deposition by sputtering for 2 min behind the closed shutter. A 18 sccm/22 sccm gas mixture of N_2/Ar (both 99.999 % purity) at a pressure of 0.43 Pa was used for all depositions. The cathode was operated with a constant current of 0.75 A.

9.2.3 Sample Characterization

Chemical compositions were obtained from coatings on Si substrates by energy dispersive X-ray spectroscopy using a FEI Philips XL30 scanning electron microscope equipped with an EDAX EDS detector, operated with 20 kV. Samples

on sapphire substrates were vacuum annealed in a Centorr LF20-2000 vacuum furnace at T_a =800 °C, the heating rate was 20 K/min, the hold time 30 h, and the passive (simply turning off the heater) cooling rate at least 50 K/min down to 200 °C. The phase evolution was then investigated with X-ray-diffraction using a PANanlytical XPert Pro MPD ($\theta - \theta$ diffractometer) equipped with a Cu–Kα source ($\lambda = 0.154\,08$ nm, 45 kV and 40 mA) in Bragg-Brentano geometry. Indentation hardness, H, and indentation modulus, E_I, of the coatings were measured before and after the annealing process on coated sapphire substrates using an UMIS II nanoindenter. The procedure by Oliver and Pharr [96] was used to analyze the load-displacement curves.

The nanometer-scale composition of thin films in as-deposited state and after annealing treatment at 800 °C for 30 h was characterized by atom probe tomography. A CAMECA local electrode atom probe 4000X HR was employed and field evaporation was assisted by laser pulses at 125 kHz frequency, 60 K base temperature and 1.0 % average detection rate. Based on the electric field strength-dependent measurement accuracy of laser-assisted APT for (Al, Ti)N, the laser pulse energy of 10 pJ was used [248]. 30 million ions were collected in each measurement, data analysis was carried out with IVAS 3.8.6 and the shank angle protocol was used for the reconstructions. Needle-like specimens were prepared in a FEI Helios Nanolab 660 dual-beam microscope by focused ion beam techniques using a standard protocol [249]. Low voltage specimen cleaning was done at 5 kV and 40 pA for 30 s.

9.3 Results and Discussion

9.3.1 Density Functional Theory

9.3.1.1 Phase Stability

Figure 9.1 shows a stability landscape of all here investigated 126 HESN (rows) into their most stable decomposition products (columns) at 0 K, considering only enthalpic effects since $T\Delta S_{mix} = 0$. Only the reaction with the highest driving force (maximum ΔH_{mix}) out of the possible 51 combinations (see Table 9.1) is

displayed for each hexinary nitride. The colored squares indicate which phases are predicted to form out of the respective HESN, the color indicates the driving force ΔG_{mix} (here only ΔH_{mix}) of the reaction in eV/at. Additionally, the experimentally tested compositions are highlighted in red. The parent phases are sorted by increasing driving force from bottom to top, while the decomposition products are grouped by their multinary levels (MN to $(M_1M_2M_3M_4)N$) and then alphabetically. White squares mean that either a different decomposition reaction is more likely (higher ΔG_{mix}), or that one or more occurring elements do not match the parent phase. The box on the left marks the elements present in each corresponding row (except Al and N). For example, in the topmost row (AlMoNbTaW)N is predicted to decompose into each binary nitride, the driving force for this reaction is $\approx 0.27\,\mathrm{eV/at}$. Other reactions, such as the decomposition into a combination of some binary and ternary nitrides, possess a lower driving force and are therefore not shown.

From a purely energetic point of view, decomposition is expected to take place in all compositions. The main cause for this is the separation of AlN, which is predicted to form in all cases (colored squares in the leftmost column for all rows). The lowest driving force for decomposition (equal to ΔG_{mix}) with 0.1 eV/at shows (AlCrHfTiV)N, the highest ΔG_{mix} with 0.27 eV/at shows (AlMoNbTaW)N. The occurrence of the different elements sorted by driving force (left box) shows interesting patterns for Cr and W, while the other elements are more randomly dispersed across the range of the energy landscape. While Cr is present only in compositions that exhibit $\Delta G_{mix} < 0.215\,\mathrm{eV/at}$, meaning it is not present in compositions with the highest driving forces, W shows the opposite behavior. The consideration of the magnetic ground-state of CrN would shift the ΔG_{mix} values up. All W-containing compositions show a $\Delta G_{mix} > 0.151\,\mathrm{eV/at}$. This is an indication that especially W is not compatible in solid solutions with a 1:1 stoichiometry without vacancies (as considered here). This can be explained with the mechanical and thermodynamic instability of WN in fcc structure [117] (positive E_f in 1:1 fcc structure, and $\approx$-0.4 eV/at in the stable NbO-structure). Interestingly, MoN does not show this trend even though its stability is comparable to WN (E_f very close to 0 and $\approx$-0.4 eV/at for the 1:1 fcc and the stable hexagonal

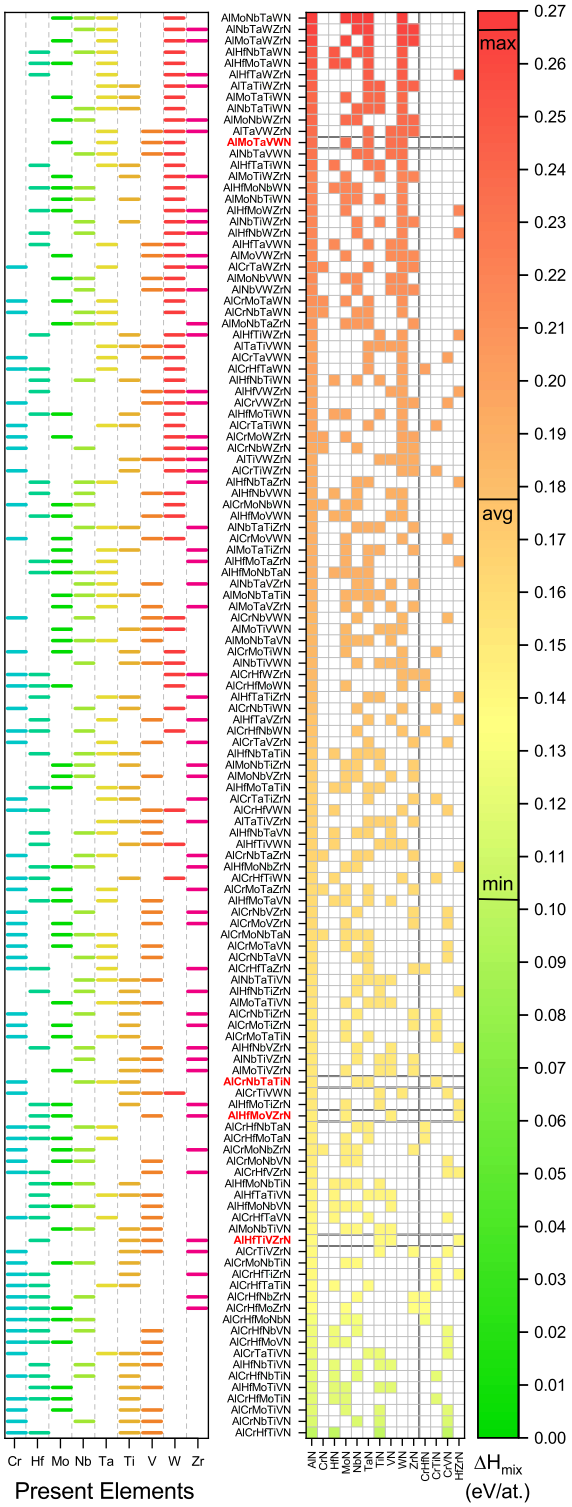

Figure 9.1: Stability landscape of the most likely decomposition products at 0 K (no entropy contribution). The 126 hexinary nitrides are sorted by the driving force $\Delta G_{mix} = \Delta H_{mix}$. Only 4 ternary nitrides, (CrHf)N, (CrTi)N, (CrV)N, and (HfZr)N, are predicted to form next to the binary nitrides. No composition is predicted to be stable against decomposition, and w-AlN is always predicted to form together with other phases. The left box indicates the metals present in each educt. The maximum, minimum, and average ΔH_{mix} of all compositions are marked on the scale. The four highlighted compositions (marked in red) were tested experimentally.

structure, respectively, compare [158]). This could be due to the comparatively lower volume mismatch between the fcc and hexagonal MoN phases.

The mixing enthalpy of (AlCrNbTiV)N was calculated in [136] to be 0.06 eV/at, which is significantly lower than the 0.12 eV/at calculated here. Among other reasons such as different calculation settings and treatment of magnetic disorder, this is due to the choice of decomposition products. While AlN was correctly treated in its wurtzite structure in [136], the E_f of NbN in the fcc structure is also significantly higher than in its thermodynamically more stable hexagonal WC-structure (being considered here). Also, even at 0 K, the ternary compound (CrV)N is predicted to be favored over CrN+VN, leading to a comparatively higher driving force for decomposition towards their most stable products, which includes also possible ternaries or other multinaries and not the binaries alone. From the ΔH_{mix} of 0.06 eV/at the authors estimated that the entropic-benefit at temperatures above 727 °C stabilizes (AlCrNbTiV)N against decomposition. However, the experimental validation [136] showed that this material did indeed decompose, meaning that the postulated decomposition path was too optimistic.

So far only enthalpic effects were considered. By including $T\Delta S_{mix}$ to the phase stability, the overall picture changes slightly. The maximum entropy stabilization for a decomposition into binary nitrides is $6.9 \cdot 10^{-5}$ eV/(at · K). Figure 9.2 shows the same kind of stability landscape as Figure 9.1 but with an entropy contribution at 1073 K. While in theory we can use any higher temperature to reach entropy stabilization eventually, the thermal stability of nitrides imposes practical limits. For example, Cr, Ta, and V are reported to lose nitrogen at temperatures above 900 °C [66, 161, 162, 250], while binary MoN and WN are unstable in their 1:1 stoichiometry [117, 158, 184, 185]. Hence, as N-loss is not implemented in the computational strategy employed here, 800 °C=1073 K was selected for the calculations as well as for the annealing experiments.

Even with the contribution of configurational entropy, all compositions are predicted to decompose into AlN and other phases. On average, the driving force decreases by 0.065±0.007 eV/at, a minimum driving force of $\Delta G_{mix} \approx 0.053$ eV/at is now calculated for (AlCrHfTiV)N, while (AlMoNbTaW)N shows – like at 0 K –

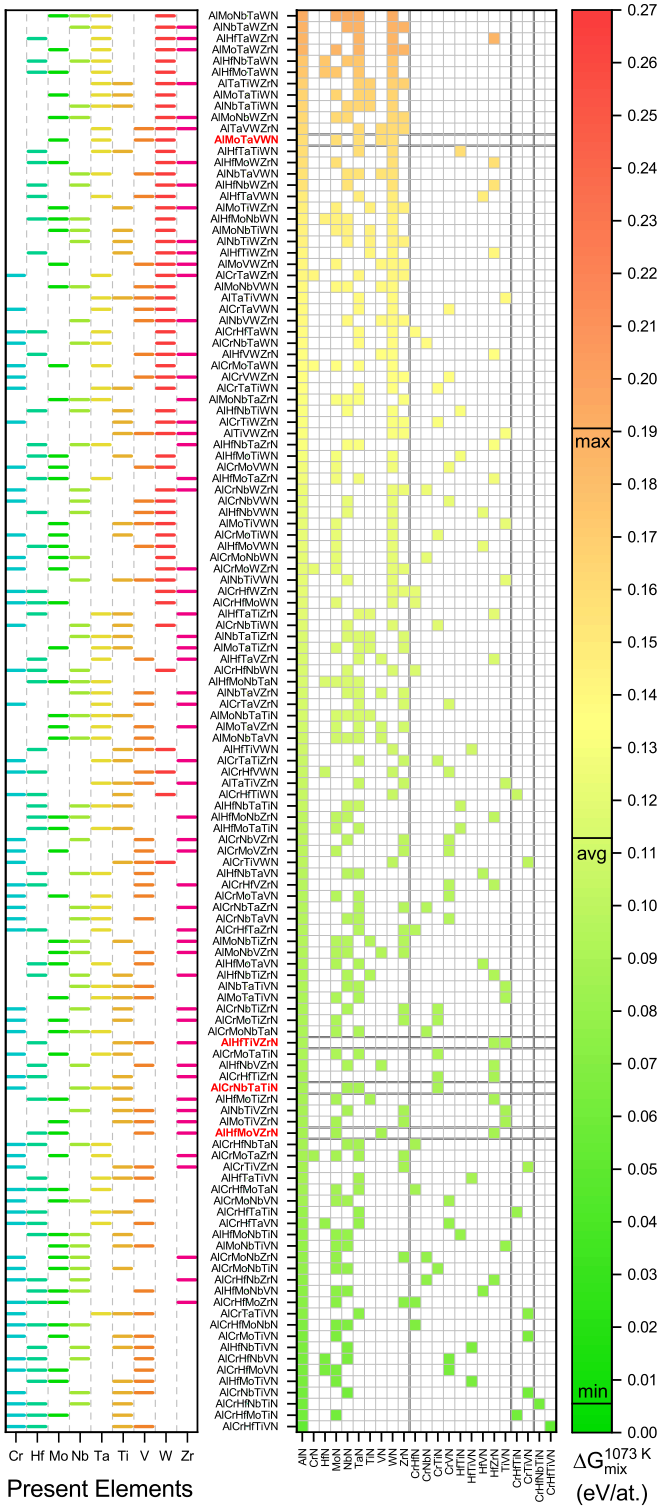

Figure 9.2: Stability landscape of the most stable decomposition products at 1073 K. The added contribution by $1073\,\mathrm{K} \cdot \Delta S_{mix}$ changes the stability landscape at 0 K Figure 9.1 only little, indicating that the configurational entropy has only a small impact on ΔG_{mix} for these ceramic materials with their typically high enthalpy. Compared to 0 K, the number of favorable products increases to include 9 ternary, 2 quaternary, and 2 quintenary nitrides, which become entropy stabilized against their binary nitrides. The left box shows clustering of the metals along the ΔG_{mix} axis. The maximum, minimum, and average ΔG_{mix} of all compositions are marked on the scale. The four highlighted compositions (marked in red) were tested experimentally.

the highest driving force of now $\approx 0.192\,\mathrm{eV/at}$. The distribution of elements along the sequence of ΔG_{mix} changes very little with the added entropy contribution. W leads to the highest driving forces for decomposition, while Cr tends to lead to lower ΔG_{mix}. Although configurational entropy does not prevent nucleation and growth of AlN, it does change the nature of the most likely decomposition products to include nitrides with more configurational entropy. For example at 0 K the (AlCrHfTiV)N is predicted to decompose into AlN+HfN+TiN+(CrV)N, while at 1073 K the formation of AlN+(CrHfTiV)N is preferred. Since this quintenary nitride also contains considerable configurational entropy, $1.39 \cdot R$ on the equimolar metal-sublattice, it profits from the $T\Delta S_{mix}$ and therefore becomes more favored as decomposition product at higher temperatures. The same is true to a lesser extent for ternary and quaternary nitrides. At 0 K, only four ternary nitrides are predicted to form: (CrHf)N, (CrTi)N, (CrV)N, and (HfZr)N. At 1073 K, 9 ternary, 2 quaternary, and 2 quintenary nitrides are among the most stable decomposition products, so while we cannot attest entropy stabilization to any of the investigated HESN, we see this stabilization in a few lower-entropy nitrides without Al at temperatures where decomposition reactions are kinetically able to take place. The entropy stabilization causes some of the compositions to change place in the ΔG_{mix}-sequence. Those educts, which are predicted to form products with more entropy, are found in the lower part of Figure 9.2 (low driving force), while the compositions at the upper end of ΔG_{mix} form mostly binaries and occasionally a ternary nitride.

9.3.1.2 Strain Stabilization

In addition to energetic and entropic effects, volume mismatch of the decomposition products can also influence the decomposition process significantly [237–239]. In all cases considered here, the decomposition products have between 1.3 % ((AlCrNbVZr)N) and 8.1 % ((AlCrMoTaW)N) larger volumes than their parent phases, see Figure A.3 for a detailed overview. This is partly due to the much larger volumes of some binaries in their thermodynamically more stable structure, like AlN. The distribution of elements in the compositions in the ΔV-sequence is different to the ordering by ΔG_{mix}, mostly due to the different

structure types in the binary nitrides. Ta and especially W are concentrated in compositions with large mismatch. This is because of their much larger volumes in their most stable structures compared to their fcc cells: TaN has a 6.3 % larger volume in its hexagonal structure, and WN a 12.3 % larger volume in its NbO-structure compared to the respective fcc cells. For comparison, the fcc volumes of MoN and NbN are 1.0 and 3.0 % larger than in their stable structures, respectively, while for AlN the wurtzite structure has a 20.1 % larger volume than the fcc phase, causing a large activation energy barrier in Al-containing transition metal nitrides [7]. This means that while from an energetic point of view the driving force for decomposition is high in all investigated compositions, the volume mismatch can hinder the decomposition. Additionally, what is not considered here is that decompositions would also require the formation of interfaces, which further consumes energy [237].

Figure 9.3 depicts the stability landscape of most likely decomposition reactions at 0 K with added strain stabilization, calculated from the volume mismatch and the bulk modulus of all decomposition products. 22 compositions show a negative ΔG_{mix}, indicating potential for sufficient strain stabilization against decomposition. Among the stable compositions Cr and V are common, which are absent in the upper part of the stability landscape (representing a high driving force for decomposition). This results from a combination of comparatively lower driving force in such compositions without stabilizing effects, and high bulk moduli (see Table 9.2). Although we only considered non-magnetic CrN, which leads to an overestimation of the strain energy due to a much larger B than reported for paramagnetic CrN [251, 252], we can conclude from repeated calculations with $B_{Cr} = 250$ GPa that there is only a negligible influence (≈ 0.001 eV/at difference on average) by this parameter. Mo and Nb are present in only 3 and 2 strain stabilized compositions, respectively, and are common in many compositions with high ΔG_{mix}.

9.3.1.3 Distribution of Bond Lengths

Atomic radii represent size trends poorly in ceramics, as shown in [25] for borides, where the lattice constants of metal diborides were used instead. Since ceramics

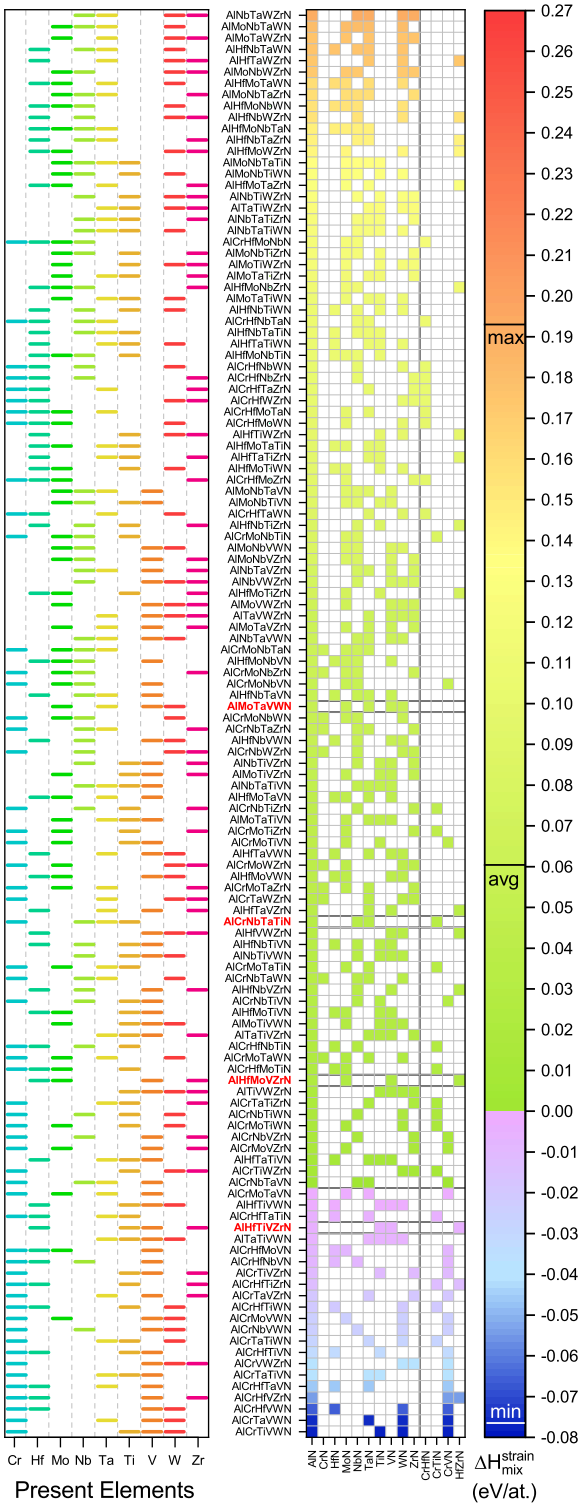

Figure 9.3: Stability landscape at 0 K like in Figure 9.1, but with strain energies considered. These evolve upon decomposition due to the different specific volumes between decomposition products and their parent phases. The strain energies obtained by the Birch-Murnaghan equation of states show a more pronounced influence on the stability landscape than the configurational entropy, compare Figure 9.1 and Figure 9.2. 22 compositions are predicted to be stabilized by strain energy (being in the range 0.01-0.28 eV/at). The average decrease of ΔG_{mix} by strain is $\approx$ 0.12 eV/at. The left box shows the clustering of metals along the ΔG_{mix} axis and provides insights on stability trends. The maximum, minimum, and average ΔH_{mix} of all compositions are marked on the scale. In the strain stabilized materials, Cr and V are the most common elements, they are also absent in the compositions with the highest driving forces for decomposition. The four highlighted compositions (marked in red) were tested experimentally. They were selected based on the criteria of being stabilized by strain alone, in the case of (Al, Hf, Ti, V, Zr)N, and being potentially stabilized when considering also entropic contributions ((Al, Cr, Nb, Ta, Ti)N, (Al, Hf, Mo, V, Zr)N, and (Al, Mo, Ta, V, W)N).

Table 9.2: Bulk moduli and lattice constants of the predicted decomposition products at 0 K in their stable structures. The fcc binaries follow the trend of increasing B with rising valence electron concentration, while the corresponding ternary nitrides deviate strongly from the average of the binaries [203]. The NbO structure of WN is abbreviated with c.

Material	B (GPa)	a (Å)	c (Å)
w-AlN	186	3.13	5.02
fcc-CrN	340	4.14	
fcc-HfN	256	4.54	
h-MoN	332	5.78	5.69
h-NbN	368	2.92	2.85
h-TaN	304	5.24	2.92
fcc-TiN	278	4.26	
fcc-VN	329	4.11	
c-WN	354	4.13	
fcc-ZrN	248	4.13	
fcc-(CrHf)N	214	4.35	
fcc-(CrTi)N	272	4.16	
fcc-CrVN	284	4.09	
fcc-(HfZr)N	258	4.58	

have different chemical behavior than metals, the size trends between metals do not generally agree with the size trends between the ceramics formed by these metals. Therefore, we use the nearest neighbor metal-nitride bond lengths (from fcc binary nitrides) to evaluate the size differences δ between individual nitrides.

Figure 9.4 shows the relationship between δ and σ_1, the parameter from the radial distribution function for the first coordination sphere, indicating the spread of nearest neighbor bond lengths. In all binary nitrides, σ_1 and δ are 0. In nitrides with differently sized metals, a correlation between σ_1 and δ can be seen. A linear fitting function is displayed as guide, but the calculated R^2 score of 0.65 indicates only a moderate correlation. The multinary level of the nitride plays no significant role in this relationship, so that the highest bond length differences of 5-6 % in (AlZr)N or (CrZr)N lead to the highest values of σ_1. This means that the high lattice distortion, which is supposed to be a characteristic core effect in high-entropy materials, is directly achieved by the differently sized metals rather than by the number of different species alone.

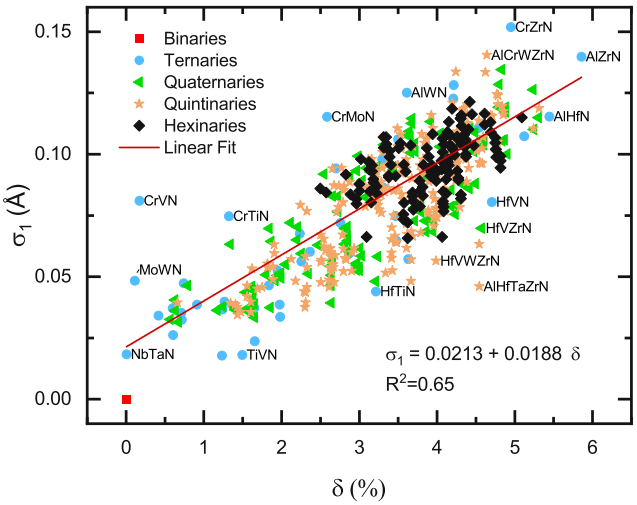

Figure 9.4: Radial distribution function for the first coordination sphere, σ_1. σ_1 indicates the spread of nearest neighbor bond lengths in relation to the nearest neighbor metal-nitride bond lengths δ, for the individual binary, ternary, quaternary, quintenary, and Al-containing hexinary nitrides considered here. With increasing number of different metals sharing the same metal-sublattice, the individual values concentrate and shift to the upper right side. Hence, with increasing multinary level the lattice distortions may increase on average, but there are also some specific ternary, quaternary, and quintenary nitrides with even larger distortions. A linear fit is shown as guide, but the correlation is only moderate.

The HESN do form a cluster at the upper part of the plot, but this is in part due to the constraint of always having Al present in these nitrides, which is the element with the smallest metal-N bond length of the here considered fcc nitrides. VN and CrN have slightly longer bonds, while the other metal nitrides show significantly larger bond lengths (see Table B.4). When expanding the phase space to Al-free hexinary nitrides, the smallest δ of 1.4 % would be reached in (HfMoNbTaW)N, presumably accompanied by a correspondingly low σ_1.

Since lattice distortion and the corresponding sluggish diffusion have been reported to be central to the high-temperature properties of high-entropy materials numerous times [27, 66–68], we postulate that the lattice distortion should not be taken for granted in HESC. The material selection should also encompass the size of the constituents in the respective chemical setting. This is further supported by Ref. [65], reporting that the diffusion in several medium- and high-entropy alloys depends strongly on the presence of Mn.

9.3.1.4 Limitations

By accounting for strain stabilization, the driving force for decomposition decreases on average by $0.118 \pm 0.051\,\mathrm{eV/at}$, which is much higher than the $\sim 0.06\,\mathrm{eV/at}$ entropy contribution at 1073 K, shown in Figure 9.2. By combining both effects, a larger list of stabilized compositions could be obtained, but a clear threshold value cannot be given here, since the strain stabilization is only known at 0 K, while the entropy contribution comes into play at high temperatures like 1073 K. The temperature-dependence of lattice parameters and elastic constants can be calculated with ab-initio methods [253–255], but this is prohibitively expensive on such a large number of compositions. Also, other entropy contributions like vibrational, magnetic, and electronic entropy can influence the properties significantly. In the so-called "Cantor-alloy", CoCrFeMnNi, these contributions can amount to 50 % of the configurational entropy [53]. Such effects could not be considered here, because there is currently no method accessible for high-throughput calculations.

The here considered non-magnetic fcc-CrN and fcc-VN are both dynamically unstable [63, 256], but our data are in agreement with calculations on (Al, Cr)N and (Al, V)N (considering the correct magnetic situation and reference state), which show considerably smaller mixing enthalpies than (Al, Ti)N [257, 258]. We therefore expect only a small uncertainty in our calculations that would not change the overall picture when using a different reference state. Since this study considers only fully relaxed solid solutions, whereas in PVD coating microstructures compressive stresses are common due to growth defects, the results need to be treated with care when interpreting experiments.

Based on our calculations, four compositions were chosen for experimental validation: (Al, Hf, Ti, V, Zr)N, predicted to be already stabilized by strain alone (ΔG_{mix} = -0.005 eV/at), as well as (Al, Hf, Mo, V, Zr)N ($\Delta G_{mix} = 0.023\,\mathrm{eV/at}$), (Al, Cr, Nb, Ta, Ti)N ($\Delta G_{mix} = 0.036\,\mathrm{eV/at}$), and (Al, Mo, Ta, V, W)N) ($\Delta G_{mix} = 0.055\,\mathrm{eV/at}$), which are predicted to decompose.

Table 9.3: Chemical compositions in at% analyzed with EDS. Standard deviations are ±3 at% for N, ±2 at% for W, and ±1 at% for all other metals.

Material	Al	Cr	Hf	Mo	Nb	Ta	Ti	V	W	Zr	N
(Al, Cr, Nb, Ta, Ti)N	8	12			9	15	9				47
(Al, Hf, Ti, V, Zr)N	8		11				12	10		10	49
(Al, Hf, Mo, V, Zr)N	8		10	13				13		9	46
(Al, Mo, Ta, V, W)N	7			13		13		12	14		42

9.3.2 Experimental Validation

9.3.2.1 Chemistry and Phase Formation

The chemical compositions of our as-deposited coatings on Si substrates, analyzed with EDS, are shown in Table 9.3. All coatings are understoichiometric to some extent, which is most pronounced in (Al, Mo, Ta, V, W)N. This can be explained with the tendency of all the comprising metals except for Al to form N-vacancies in their cubic structures [66, 117, 158, 162, 184, 185]. Using equimolar targets, higher concentrations of the heavier elements and a lower Al content are obtained, which is typical for sputtered materials due to different poisoning states of the individual target grains [209, 259] or due to preferential gas-scattering and resputtering of AlN [210, 211]. Additionally, the quantification of light elements in EDS is uncertain due to absorption of X-rays in the sample and the spectrometer [86]. Since Al is the largest contributor in driving force for decomposition, but also for strain stabilization, we need to consider this deviation from equimolarity when interpreting the results.

Figure 9.5a) and b) show the XRD patterns of our coatings as-deposited and after annealing at 800 °C for 30 h, respectively. This temperature was chosen to match the 1073 K used in our simulations, and also because we have to balance the thermal stability of the nitrides with the slow kinetics in high-entropy materials. Since N-loss occurs in nitrides at high temperatures, this would lead to the formation of additional phases, which complicates the comparison with our DFT data. In addition, the adhesion of (Al, Mo, Ta, V, W)N on sapphire was insufficient at 850 °C and above. The long annealing time of 30 h ($\leq$ 1 h is common for thin

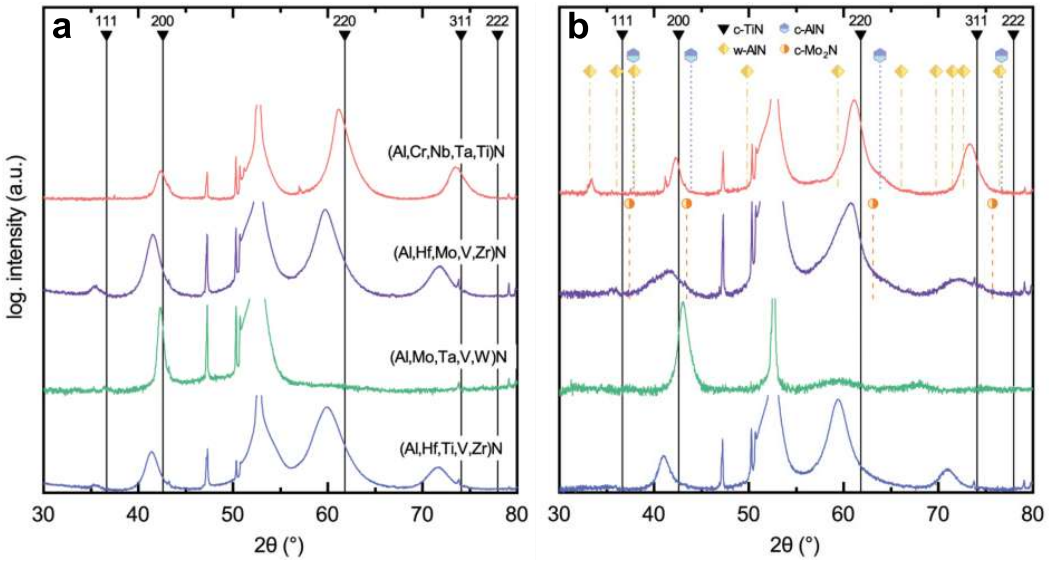

Figure 9.5: XRD analysis of the 4 experimentally investigated coatings deposited on sapphire before a), and after 30 h vacuum-annealing at 800 °C b). In the as-deposited state all coatings show a single phase fcc structure. After annealing, only (Al, Cr, Nb, Ta, Ti)N shows the formation of w-AlN and possibly fcc-AlN. (Al, Hf, Mo, V, Zr)N and (Al, Mo, Ta, V, W)N exhibit N-loss, hence, only (Al, Hf, Ti, V, Zr)N seems to be unaffected by this annealing treatment.

films) was chosen to account for the slow diffusion processes in high-entropy materials (one of the four core-effects [11, 15, 66, 134]).

All coatings show single-phase fcc rock-salt structures in their as-deposited state. The (Al, Cr, Nb, Ta, Ti)N, (Al, Hf, Ti, V, Zr)N, and (Al, Hf, Mo, V, Zr)N exhibit a similar pronounced (2 2 0) growth orientation, with smaller (2 0 0) and (3 1 1) reflexes, and very small (1 1 1) peaks in the case of (Al, Hf, Ti, V, Zr)N and (Al, Hf, Mo, V, Zr)N. (Al, Mo, Ta, V, W)N on the other hand exhibits a pronounced (2 0 0) growth orientation. These preferred growth orientations remain unchanged by the thermal treatment for all coatings studied. The only notable change for (Al, Hf, Ti, V, Zr)N (Figure 9.5, bottom pattern) is a slight narrowing of the individual peaks, indicative for structural recovery effects, where lattice-defects rearrange towards lower energy sites. No N-loss, or formation of a secondary phase could be detected. This corresponds well to the predicted strain stabilization of this material.

The (Al, Mo, Ta, V, W)N is still highly (2 0 0) oriented (Figure 9.5, second pattern from bottom) after annealing, but the peak shifts from 42.33 to 43.07°.

This reduction in lattice plane distances is typically indicative for reduced stresses (macro-stresses), but would go hand-in-hand with a reduction of peak broadening (micro-stresses) as well. However, the FWHM of the (2 0 0) peak increases from 0.54 to 0.89°. Therefore, in combination with DFT (MoN, TaN, and WN are prone for N-loss [158, 193, 195]), this pronounced peak-shift suggests a reduced lattice size due to N-loss of the fcc structure. At diffraction angles of around 59° and 68° two additional very broad and small features can be detected after the annealing treatment, but no crystalline phase could be unambiguously assigned. We do not see formation of w-AlN, which can be due to the comparably low Al concentration. Of all the coatings investigated, this (Al, Mo, Ta, V, W)N deviates most from the equimolar composition that was used for DFT. Additionally, the N-loss could also stabilize the nitride in its fcc structure. While these features are hints for decomposition reactions, XRD remains inconclusive in this case.

For the (Al, Hf, Mo, V, Zr)N coating (Figure 9.5, third pattern from bottom), the (2 2 0) XRD peak becomes asymmetric upon annealing due to a possible formation of a N-depleted phase similar to cubic Mo_2N. Other than that, no additional phase formation (like w-AlN) or decomposition could be detected.

Contrary to these three coatings – where no w-AlN formation could be detected or any other binary phase (ternary or quaternary fcc phases could still be hidden behind the major XRD peaks of the parent phase) – the (Al, Cr, Nb, Ta, Ti)N coating (Figure 9.5, topmost pattern) exhibits a distinct formation of w-AlN (peak at ≈33°). Here, also the formation of fcc-AlN seems to be plausible, see the right-hand shoulder of the (2 2 0) reflex, indicating a spinodal decomposition process. Other phases like NbN or TaN, which were predicted to form, cannot be detected due to the sluggish kinetics. The driving force for AlN formation is the highest among the constituents and we still see some fcc-AlN, therefore we can deduce that our annealing process is too mild to finish the decomposition reaction. Thus, the NbN and TaN formation would take an even more severe heat treatment to be initiated or completed. A plausible explanation is also, that the generated strains (due to the formation of w-AlN) lead to the stagnation of the decomposition process [237]. Since this material contains no Mo or W, which are prone to lose N, the observed decomposition behavior matches the predicted

one best of the investigated coatings. The results prove that the configurational entropy alone is not sufficient to fully stabilize AlN thermodynamically in an fcc lattice.

To complement the phase evolution with chemical analysis at the nanometer scale, APT was performed and a brief comparison of the two coatings (Al, Cr, Nb, Ta, Ti)N and (Al, Hf, Ti, V, Zr)N is presented in Figure 9.6 (a complete analysis of all samples is provided in Figures A.4, A.5, A.6, and A.7). In Figure 9.6a) and b), the reconstructed Al, Ti, and N positions of as-deposited (Al, Cr, Nb, Ta, Ti)N and (Al, Hf, Ti, V, Zr)N, respectively, are shown. The composition profiles from the cylindrical regions marked in Figure 9.6a) and b) are shown in Figure 9.6c) and d), respectively, and support the formation of a random solid solution. After annealing, the (Al, Cr, Nb, Ta, Ti)N exhibits Al-rich regions, Figure 9.6e), highlighted by ≥ 45 at% isoconcentration surfaces. The annealed (Al, Hf, Ti, V, Zr)N, Figure 9.6f), also shows such clustering, but to a much smaller extent. Here, isoconcentration surfaces of ≥ 20 at% Al show comparatively small and less enriched clusters. The composition profiles from the cylindrical regions marked in Figure 9.6e) and f), shown in Figure 9.6g) and h), respectively, illustrate this even more.

The APT studies of annealed (Al, Cr, Nb, Ta, Ti)N clearly show that AlN regions are formed (in agreement with XRD), whereas any Al-enriched domains detected in annealed (Al, Hf, Ti, V, Zr)N are too small to be identified by XRD. The apparent reduction of N in the Al-rich region can be understood by the electric field strength dependent accuracy of N quantification [248]. Since the required electric field strength for evaporation of Al is significantly lower than for transition metals such a Ti [260], underestimation of N in Al-rich regions is caused by the formation of neutral fragments upon dissociation of molecular ions [261]. This effect is visible in all investigated coatings. The other two coatings also show pronounced AlN formation, though not as much as for (Al, Cr, Nb, Ta, Ti)N, as well as segregation of Mo and W. However, (Al, Hf, Ti, V, Zr)N does show signs of Al enrichment on the nanometer scale, caused by endothermic mixing, which is also consistent with the predictions. Hence, we show that while the mixing enthalpy drives the decomposition of all the Al-containing HESN studied

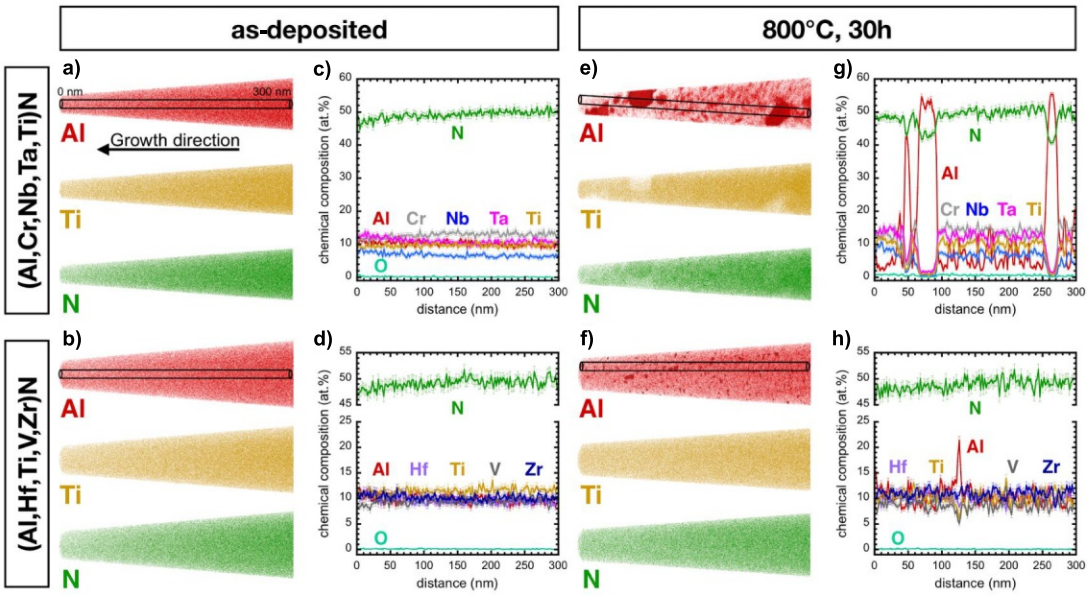

Figure 9.6: Local chemical composition of (Al, Cr, Nb, Ta, Ti)N and (Al, Hf, Ti, V, Zr)N in as-deposited and annealed state. The reconstruction of Al, Ti, and N atomic positions of as-deposited (Al, Cr, Nb, Ta, Ti)N and (Al, Hf, Ti, V, Zr)N are shown in a) and b), respectively. Composition profiles from the cylindrical regions in a) and b) are provided in c) and d). The reconstruction of Al, Ti and N atomic positions after annealing are presented in e) and f). In addition, Al-rich regions with ≥ 45 at% and ≥ 20 at% are shown for (Al, Cr, Nb, Ta, Ti)N and (Al, Hf, Ti, V, Zr)N, respectively. Composition profiles from the cylindrical regions in e) and f) are provided in g) and h), respectively.

here, the predicted strain stabilization clearly prevents the formation of w-AlN in (Al, Hf, Ti, V, Zr)N after 30 h of vacuum annealing. With insufficient strain stabilization, for example in (Al, Cr, Nb, Ta, Ti)N, decomposition and formation of w-AlN is observed, consistent with our predictions.

9.3.2.2 Mechanical Properties

All coatings investigated show a hardness H between 32 and 36 GPa and an indentation modulus E_I between 430 and 520 GPa in their as-deposited state (see Table B.5 for details). The mechanical properties are only slightly influenced by the vacuum annealing treatment for 30 h at 800 °C. Essentially, H and E_I remain within the error of measurement, with two exceptions: (Al, Hf, Mo, V, Zr)N experiences a reduction in H from $\sim$ 34 to $\sim$ 26 GPa, while for (Al, Mo, Ta, V, W)N the indentation modulus increases from $\sim$ 514 to

$\sim$ 595 GPa. The increased indentation modulus for the latter could be within the error of measurement, but the hardness reduction for (Al, Hf, Mo, V, Zr)N is statistically significant and can be explained by the more pronounced structural change of this coating (see Figure 9.5) involving N-loss, and surface oxidation (see Figure A.6). Although the formation of w-AlN could be detected in (Al, Cr, Nb, Ta, Ti)N, its fraction is too small to cause negative impact on the mechanical properties, while the additionally present fcc-AlN is even beneficial in terms of age hardening effects [7].

CHAPTER 10

Summary and Conclusions

10.1 Si-Alloying of (Al, Cr, Nb, Ta, Ti)N Thin Films

Alloying the reactively magnetron sputtered high-entropy sublattice nitride (Al, Cr, Nb, Ta, Ti)N with different Si concentrations improves the performance under thermal and mechanical loading, and protects against oxidative attack. All coatings exhibit single-phase solid solutions in fcc rock-salt structure, with lattice parameters increasing from 4.28 to 4.34 Å with increasing Si content, the corresponding coating morphology changes to finer and longer columns. Upon vacuum annealing, this crystal structure is maintained until decomposition reactions set in at 1000 °C for the Si-free material. By Si-alloying the decomposition is shifted to higher temperatures and starts at about 1200 °C for the coating with 12.0 at% Si. Si-enrichment at the grain boundaries, as well as the severe lattice distortion (one of the core-effects of high-entropy materials) are determined by TEM-studies.

With increasing Si content to 9.8 at% the hardness of as-deposited coatings increases from 32.6 to 35.4 GPa. A further increase in Si causes a hardness drop to 24.1 GPa, which for the 12.0 at% Si-containing coating can be reversed into a hardness increase to 37.3 GPa upon a subsequent vacuum annealing to 800 °C. Also, the other coatings (except for the highest Si-containing one with 15.0 at% Si) experience a hardness increase (to a smaller extent) upon annealing. The

indentation modulus decreases with increasing Si content from ≈470 to ≈350 GPa.

Upon exposure to ambient air at 850 °C for 100 h, a single-phase rutile-structured oxide grows on the Si-free (Al, Cr, Nb, Ta, Ti)N coating with a parabolic growth rate k_p of $2.1 \cdot 10^{-17} m^2/s$. The formation of a single-phase multielemental dioxide is supported by DFT calculations of an equimolar $(Al, Cr, Nb, Ta, Ti)O_2$, which is energetically more stable than the formation of the respective binary oxides (in the thermodynamically most stable configuration). Only the formation of a rutile-structured mixture of $(Al, Ta, Ti)O_2$ and $(Cr, Nb)O_2$ would be more favorable than the single-phase solid solution. But the higher entropy of the solid solution $(Al, Cr, Nb, Ta, Ti)O_2$ ensures that already above 509 K its formation is preferred over these mixtures.

The Si-containing HESN coatings exhibit a significantly reduced oxide scale growth kinetic, which at 850 °C can best be described with a logarithmic function of $k_l = 7.2 \cdot 10^{-8} m$, independent on the Si content investigated (between 6.4 and 15.0 at%). Although, also here no different crystalline oxide phases could be identified, the oxide scale morphology is divided into a denser Si-rich inner oxide and a slightly more porous Cr-rich outer scale. Without Si, the oxide scale morphology is more uniform throughout the entire thickness but also more porous with pore diameters up to 30 nm. Our results suggest that especially the inner Si-rich but Cr-lean oxide scale, which is rather dense and well adherent without a sharp transition to the underlying nitride, guarantees for the excellent oxidation resistance of the Si-containing HESN (in addition to the thin, dense outermost Al-rich oxide).

10.2 Tuning of Microstructure and Mechanical Properties in (Al,Mo,Ta,V,W)N

The microstructure, mechanical properties, and thermal stability of (Al, Mo, Ta, V, W)-nitrides can be easily modified by the sputter gas composition. Both deposited nitrides, $(Al, Mo, Ta, V, W)N_{0.79}$ and $(Al, Mo, Ta, V, W)N_{0.33}$, exhibit significant N-vacancy concentrations, while in the as-deposited oxynitride with 6 at% oxygen the metal/nonmetal ratio is roughly 1. Structurally,

the $(Al, Mo, Ta, V, W)N_{0.79}$ consists of long, highly oriented columns. The $(Al, Mo, Ta, V, W)N_{0.33}$ is also textured to a slightly lesser extent, but the columns are much shorter. In addition, very large grains can be found throughout the coating. The $(Al, Mo, Ta, V, W)N_{0.88}O_{0.12}$ consists of randomly oriented columns, of which some are tilted 20° to the growth direction, and smaller equiaxed grains with random growth orientation.

The hardness of the $(Al, Mo, Ta, V, W)N_{0.79}$ is 32.3 GPa in as-deposited state, which increases to 35.2 GPa when vacuum annealed at 800 °C for 30 h. This hardness increase is due to the decreasing N-content from ≈44 to ≈25 at% with a corresponding decrease in valence electron concentration. The $(Al, Mo, Ta, V, W)N_{0.33}$, deposited with a lower N_2 partial pressure, does not change its chemistry significantly during annealing and is thus in chemical equilibrium. The hardness also changes only little from 39.7 to 38.1 GPa during annealing. The indentation moduli of both nitride coatings are very similar around 510 and 580 GPa before and after annealing.

In as-deposited state, the $(Al, Mo, Ta, V, W)N_{0.88}O_{0.12}$ surpasses the hardness of $(Al, Mo, Ta, V, W)N_{0.79}$ with 34.6 GPa, which is essentially related to the different microstructure with smaller grains. However, the same annealing treatment as for the nitrides resulted in a severe hardness reduction down to 14.1 GPa due to the transformation towards individual Mo-, Ta-, V-, and W-oxides. Their much higher specific volumes with respect to the starting oxynitride phase causes the coating to crack open.

10.3 Compositionally Complex Superhard (Hf,Ta,Ti,V,Zr)-B-N Coatings

Ab-initio calculations have shown that the system (Hf, Ta, Ti, V, Zr)-B-N strongly prefers the fcc structure in a wide compositional range, supporting up to 78 at% B on the non-metal sublattice. The B is well incorporated into the cubic structure, as seen by the small variation of the lattice parameters of individual cells and the projected density of states. The elastic properties of such a boronnitride are also stable in a wide compositional range, with only slowly varying bulk, shear,

and Young's moduli. The ductility criteria G/B and Cauchy pressure indicate that such boronnitride coatings should be significantly less brittle than an α structured boride.

The α-structure on the other hand is only preferred for very high B contents, and the hexagonal lattice does not tolerate N incorporation well. The local atomic symmetry is perturbed gravely, leading to rapidly decreasing elastic properties with increasing N content. We therefore expected the formation of fcc structured high-entropy sublattice boronnitride thin films in our experiments.

Reactive sputtering from a $Hf_{0.2}Ta_{0.2}Ti_{0.2}V_{0.2}Zr_{0.2}$ target with corresponding metal-diboride pieces on the racetrack leads to formation of amorphous BN next to the cubic multimetal-boronnitride, which is accompanied by a significant hardness drop from 32.5 GPa (no B) to 16.7 GPa at 18 at% B (B:N=0.44). This is similar to the behavior in reactively sputtered Ti-B-N.

The non-reactively sputtered coatings on the other hand, deposited from a Zr(N,C) target with metal-diboride pieces on the racetrack, lead to single phase fcc structures with no amorphous phase and can be assigned as single-phase compositionally complex boronnitride (CCBN) coatings. These coatings with B contents between 20.0 and 25.5 at% (B:N ratios between 0.76 and 1.12) are superhard ($H \geq 40$ GPa) and possess excellent thermal stability. Our results suggest that the compositional complexity allows to incorporate much more B in the fcc structure than Ti-B-N for example. With increasing B:N ratio the hardness peaks between 46.3 and 45.7 GPa at B:N ratios between 0.83 and 1.03, respectively. Even after vacuum annealing to 1200 °C, a hardness of 43.7 GPa is retained, which makes the hardness retention of these coatings comparable to high-entropy metal sublattice diborides. But the CCBNs studied here are all single-phase fcc structured and ab-initio calculations suggest them to be less brittle than in the AlB_2-type structure.

Based on our results we can conclude that by increasing the compositional complexity of both sublattices in ceramic-like materials (like these transition-metal-boronnitrides) the solubility limits especially of fcc structures can be stretched leading to superior mechanical properties and thermal stabilities.

10.4 Strain-Stabilized Al-Containing High-Entropy Sublattice Nitrides

Based on the theoretical and experimental data presented here, it is evident that the impact of the entropy stabilization, often mentioned as major advantage of high-entropy ceramics over lower-entropy counterparts, has been overestimated in the past. For the here studied nitrides, $T\Delta S_{mix}$ for reasonable temperatures is still below enthalpy contributions, which are often much larger in ceramics than for metallic alloys.

Caused mostly by the formation of w-AlN, the enthalpic driving forces for decomposition dominate the thermodynamic landscape in the investigated Al-containing nitrides. While ΔH_{mix} ranges from 0.10 to 0.27 eV/at, the average entropic benefit at 1073 K amounts to only ≈-0.06 eV/at, too small to compensate the ΔH_{mix}-governed decomposition driving force. This predicted formation of AlN is also confirmed by our XRD and APT investigations. Future attempts at finding thermodynamically stable ceramic compounds, without taking enthalpic interactions between the elements into account, are thus incomplete.

In the case of Al-containing nitrides, the strain stabilization, caused by the larger volumes of the thermodynamically stable binary phases, can have a much larger impact (-0.01 to -0.28 eV/at) on the decomposition behavior than $T\Delta S_{mix}$. Among the investigated compositions, 22 were predicted to be strain stabilized against decomposition and good agreement between predictions and experimental data was obtained for (Al, Hf, Ti, V, Zr)N. Hence, it is reasonable to assume that this principle of strain stabilization can also be applied to other material classes. While also considering enthalpy changes [258], screening for large volume mismatches between materials and their expected decomposition products can provide an efficient path to discover potentially strain stabilized compositions.

The expectations should also be adjusted for the lattice distortion, another core-effect of high-entropy materials. Our analysis of the radial distribution function shows that a large number of alloyed elements alone does not guarantee a highly distorted lattice. While more elements increase the probability of resulting in a moderate to large lattice distortion, the system (HfMoNbTaW)N for example

is predicted to result in a lower lattice distortion than commonly observed for many ternary or quaternary compounds. Clearly, the size mismatch has to be tailored to maximize the lattice distortions.

Bibliography

[1] J. E. Greene, Tracing the 5000-year recorded history of inorganic thin films from ∼3000 BC to the early 1900s AD, Applied Physics Reviews 1 (4) (2014) 041302. doi:10.1063/1.4902760.

[2] P. M. Martin, Deposition technologies for films and coatings, Elsevier, 2005.

[3] P. C. Jindal, A. T. Santhanam, U. Schleinkofer, A. F. Shuster, Performance of PVD TiN, TiCN, and TiAlN coated cemented carbide tools in turning, International Journal of Refractory Metals and Hard Materials 17 (1) (1999) 163–170. doi:10.1016/S0263-4368(99)00008-6.

[4] J. L. Mo, M. H. Zhu, B. Lei, Y. X. Leng, N. Huang, Comparison of tribological behaviours of AlCrN and TiAlN coatings-Deposited by physical vapor deposition, Wear 263 (7-12 SPEC. ISS.) (2007) 1423–1429. doi:10.1016/j.wear.2007.01.051.

[5] J. L. Mo, M. H. Zhu, A. Leyland, A. Matthews, Impact wear and abrasion resistance of CrN, AlCrN and AlTiN PVD coatings, Surface and Coatings Technology 215 (2013) 170–177. doi:10.1016/j.surfcoat.2012.08.077.

[6] M. Kawate, A. K. Hashimoto, T. Suzuki, Oxidation resistance of $Cr_{1-x}Al_xN$ and $Ti_{1-x}Al_xN$ films, Surface and Coatings Technology 165 (2) (2003) 163–167. doi:10.1016/S0257-8972(02)00473-5.

[7] P. H. Mayrhofer, A. Hörling, L. Karlsson, J. Sjölén, T. Larsson, C. Mitterer, L. Hultman, Self-organized nanostructures in the Ti-Al-N system, Applied Physics Letters 83 (10) (2003) 2049–2051. doi:10.1063/1.1608464.

[8] B. Murty, J. W. Yeh, S. Ranganathan, High Entropy Alloys, 1st Edition, Elsevier, 2014. doi:10.1016/C2013-0-14235-3.

[9] B. Cantor, I. T. Chang, P. Knight, A. J. Vincent, Microstructural development in equiatomic multicomponent alloys, Materials Science and Engineering A 375-377 (1-2 SPEC. ISS.) (2004) 213–218. doi:10.1016/j.msea.2003.10.257.

[10] J.-W. Yeh, S.-K. Chen, S.-J. Lin, J.-Y. Gan, T.-S. Chin, T.-T. Shun, C.-H. Tsau, S.-Y. Chang, Nanostructured High-Entropy Alloys with Multiple Principal Elements: Novel Alloy Design Concepts and Outcomes, Advanced Engineering Materials 6 (5) (2004) 299–303. doi:10.1002/adem.200300567.

[11] J.-W. Yeh, Recent Progress in High-entropy Alloys, Annales De Chimie – Science des Materiaux 31 (2006) 633–648.

[12] Scopus, accessed: July 2021.
URL https://www.scopus.com/

[13] T. Chen, T. Shun, J. Yeh, M. Wong, Nanostructured nitride films of multi-element high-entropy alloys by reactive DC sputtering, Surface and Coatings Technology 188-189 (5-6) (2004) 193–200. doi:10.1016/j.surfcoat.2004.08.023.

[14] T.-K. Chen, M.-S. Wong, T.-T. Shun, J.-W. Yeh, Nanostructured nitride films of multi-element high-entropy alloys by reactive DC sputtering, Surface and Coatings Technology 200 (5-6) (2005) 1361–1365. doi:10.1016/j.surfcoat.2005.08.081.

[15] M. H. Tsai, C. W. Wang, C. H. Lai, J. W. Yeh, J. Y. Gan, Thermally stable amorphous $(AlMoNbSiTaTiVZr)_{50}N_{50}$ nitride film as diffusion barrier in copper metallization, Applied Physics Letters 92 (5) (2008) 90–93. doi:10.1063/1.2841810.

[16] T. K. Chen, M. S. Wong, Structure and properties of reactively-sputtered Al_xCoCrCuFeNi oxide films, Thin Solid Films 516 (2-4) (2007) 141–146. doi:10.1016/j.tsf.2007.06.142.

[17] M. I. Lin, M. H. Tsai, W. J. Shen, J. W. Yeh, Evolution of structure and properties of multi-component (AlCrTaTiZr)O_x films, Thin Solid Films 518 (10) (2010) 2732–2737. doi:10.1016/j.tsf.2009.10.142.

[18] H. Chen, J. Fu, P. Zhang, H. Peng, C. W. Abney, K. Jie, X. Liu, M. Chi, S. Dai, Entropy-stabilized metal oxide solid solutions as CO oxidation catalysts with high-temperature stability, Journal of Materials Chemistry A 6 (24) (2018) 11129–11133. doi:10.1039/c8ta01772g.

[19] J. Dąbrowa, M. Stygar, A. Mikuła, A. Knapik, K. Mroczka, W. Tejchman, M. Danielewski, M. Martin, Synthesis and microstructure of the $(Co, Cr, Fe, Mn, Ni)_3O_4$ high entropy oxide characterized by spinel structure, Materials Letters 216 (2018) 32–36. doi:10.1016/j.matlet.2017.12.148.

[20] J. Gild, M. Samiee, J. L. Braun, T. Harrington, H. Vega, P. E. Hopkins, K. Vecchio, J. Luo, High-entropy fluorite oxides, Journal of the European Ceramic Society 38 (10) (2018) 3578–3584. doi:10.1016/j.jeurceramsoc.2018.04.010.

[21] A. Kirnbauer, C. Spadt, C. M. Koller, S. Kolozsvári, P. H. Mayrhofer, High-entropy oxide thin films based on Al–Cr–Nb–Ta–Ti, Vacuum 168 (July) (2019) 108850. doi:10.1016/j.vacuum.2019.108850.

[22] A. Sarkar, R. Djenadic, D. Wang, C. Hein, R. Kautenburger, O. Clemens, H. Hahn, Rare earth and transition metal based entropy stabilised perovskite type oxides, Journal of the European Ceramic Society 38 (5) (2018) 2318–2327. doi:10.1016/j.jeurceramsoc.2017.12.058.

[23] C. Oses, C. Toher, S. Curtarolo, High-entropy ceramics, Nature Reviews Materials 5 (4) (2020) 295–309. doi:10.1038/s41578-019-0170-8.

[24] C. P. Lee, Y. Y. Chen, C. Y. Hsu, J. W. Yeh, H. C. Shih, The Effect of Boron on the Corrosion Resistance of the High Entropy Alloys $Al_{0.5}$CoCrCuFeNiB_x,

Journal of The Electrochemical Society 154 (8) (2007) C424. doi:10.1149/1.2744133.

[25] J. Gild, Y. Zhang, T. Harrington, S. Jiang, T. Hu, M. C. Quinn, W. M. Mellor, N. Zhou, K. Vecchio, J. Luo, High-Entropy Metal Diborides: A New Class of High-Entropy Materials and a New Type of Ultrahigh Temperature Ceramics, Scientific Reports 6 (October) (2016) 2–11. doi:10.1038/srep37946.

[26] P. H. Mayrhofer, A. Kirnbauer, P. Ertelthaler, C. M. Koller, High-entropy ceramic thin films; A case study on transition metal diborides, Scripta Materialia 149 (2018) 93–97. doi:10.1016/j.scriptamat.2018.02.008.

[27] A. Kirnbauer, A. Wagner, V. Moraes, D. Primetzhofer, M. Hans, J. Schneider, P. Polcik, P. Mayrhofer, Thermal stability and mechanical properties of sputtered (Hf,Ta,V,W,Zr)-diborides, Acta Materialia (sep 2020). doi:10.1016/j.actamat.2020.09.018.

[28] T. T. Shun, Y. C. Du, Age hardening of the $Al_{0.3}CoCrFeNiC_{0.1}$ high entropy alloy, Journal of Alloys and Compounds 478 (1-2) (2009) 269–272. doi:10.1016/j.jallcom.2008.12.014.

[29] V. Braic, M. Balaceanu, M. Braic, A. Vladescu, S. Panseri, A. Russo, Characterization of multi-principal-element (TiZrNbHfTa)N and (TiZrNbHfTa)C coatings for biomedical applications, Journal of the Mechanical Behavior of Biomedical Materials 10 (2012) 197–205. doi:10.1016/j.jmbbm.2012.02.020.

[30] P. Malinovskis, S. Fritze, L. Riekehr, L. von Fieandt, J. Cedervall, D. Rehnlund, L. Nyholm, E. Lewin, U. Jansson, Synthesis and characterization of multicomponent (CrNbTaTiW)C films for increased hardness and corrosion resistance, Materials and Design 149 (2018) 51–62. doi:10.1016/j.matdes.2018.03.068.

[31] Y. Yang, W. Wang, G. Y. Gan, X. F. Shi, B. Y. Tang, Structural, mechanical and electronic properties of (TaNbHfTiZr)C high entropy carbide

under pressure: Ab initio investigation, Physica B: Condensed Matter 550 (September) (2018) 163–170. doi:10.1016/j.physb.2018.09.014.

[32] J. Dusza, P. Švec, V. Girman, R. Sedlák, E. G. Castle, T. Csanádi, A. Kovalčíková, M. J. Reece, Microstructure of (Hf-Ta-Zr-Nb)C high-entropy carbide at micro and nano/atomic level, Journal of the European Ceramic Society 38 (12) (2018) 4303–4307. doi:10.1016/j.jeurceramsoc.2018.05.006.

[33] X. Yan, L. Constantin, Y. Lu, J. F. Silvain, M. Nastasi, B. Cui, $(Hf_{0.2}Zr_{0.2}Ta_{0.2}Nb_{0.2}Ti_{0.2})C$ high-entropy ceramics with low thermal conductivity, Journal of the American Ceramic Society 101 (10) (2018) 4486–4491. doi:10.1111/jace.15779.

[34] P. Sarker, T. Harrington, C. Toher, C. Oses, M. Samiee, J. P. Maria, D. W. Brenner, K. S. Vecchio, S. Curtarolo, High-entropy high-hardness metal carbides discovered by entropy descriptors, Nature Communications 9 (1) (2018) 1–10. arXiv:1811.07730, doi:10.1038/s41467-018-07160-7.

[35] V. F. Gorban', A. A. Andreyev, G. N. Kartmazov, A. M. Chikryzhov, M. V. Karpets, A. V. Dolomanov, A. A. Ostroverkh, E. V. Kantsyr, Production and mechanical properties of high-entropic carbide based on the TiZrHfVNbTa multicomponent alloy, Journal of Superhard Materials 39 (3) (2017) 166–171. doi:10.3103/S1063457617030030.

[36] S. Y. Chang, S. Y. Lin, Y. C. Huang, Microstructures and mechanical properties of multi-component $(AlCrTaTiZr)N_xC_y$ nanocomposite coatings, Thin Solid Films 519 (15) (2011) 4865–4869. doi:10.1016/j.tsf.2011.01.043.

[37] S. Y. Lin, S. Y. Chang, Y. C. Huang, F. S. Shieu, J. W. Yeh, Mechanical performance and nanoindenting deformation of $(AlCrTaTiZr)NC_y$ multi-component coatings co-sputtered with bias, Surface and Coatings Technology 206 (24) (2012) 5096–5102. doi:10.1016/j.surfcoat.2012.06.035.

[38] D. D. Le, S. K. Hong, T. S. Ngo, J. Lee, Y. C. Park, S. I. Hong, Y. S. Na, Microstructural Investigation of CoCrFeMnNi High Entropy Alloy Oxynitride Films Prepared by Sputtering Using an Air Gas, Metals and Materials International 24 (6) (2018) 1285–1292. doi:10.1007/s12540-018-0143-2.

[39] Y. Qin, J. C. Wang, J. X. Liu, X. F. Wei, F. Li, G. J. Zhang, C. Jing, J. Zhao, H. Wu, High-entropy silicide ceramics developed from (TiZrNbMoW)Si_2 formulation doped with aluminum, Journal of the European Ceramic Society 40 (8) (2020) 2752–2759. doi:10.1016/j.jeurceramsoc.2020.02.059.

[40] L. Liu, L. Zhang, D. Liu, Complete elimination of pest oxidation by high entropy refractory metallic silicide $(Mo_{0.2}W_{0.2}Cr_{0.2}Ta_{0.2}Nb_{0.2})Si_2$, Scripta Materialia 189 (2020) 25–29. doi:10.1016/j.scriptamat.2020.07.059.

[41] S. Roychowdhury, T. Ghosh, R. Arora, U. V. Waghmare, K. Biswas, Stabilizing n-Type Cubic GeSe by Entropy-Driven Alloying of $AgBiSe_2$: Ultralow Thermal Conductivity and Promising Thermoelectric Performance, Angewandte Chemie 130 (46) (2018) 15387–15391. doi:10.1002/ange.201809841.

[42] R. Z. Zhang, F. Gucci, H. Zhu, K. Chen, M. J. Reece, Data-Driven Design of Ecofriendly Thermoelectric High-Entropy Sulfides, Inorganic Chemistry 57 (20) (2018) 13027–13033. doi:10.1021/acs.inorgchem.8b02379.

[43] H. M. Daoud, A. M. Manzoni, R. Völkl, N. Wanderka, U. Glatzel, Oxidation Behavior of $Al_8Co_{17}Cr_{17}Cu_8Fe_{17}Ni_{33}$, $Al_{23}Co_{15}Cr_{23}Cu_8Fe_{15}Ni_{15}$, and $Al_{17}Co_{17}Cr_{17}Cu_{17}Fe_{17}Ni_{17}$ Compositionally Complex Alloys (High-Entropy Alloys) at Elevated Temperatures in Air, Advanced Engineering Materials 17 (8) (2015) 1134–1141. doi:10.1002/adem.201500179.

[44] D. B. Miracle, O. N. Senkov, A critical review of high entropy alloys and related concepts, Acta Materialia 122 (2017) 448–511. doi:10.1016/j.actamat.2016.08.081.

[45] D. B. Miracle, High entropy alloys as a bold step forward in alloy development, Nature Communications 10 (1) (2019) 1–3. doi:10.1038/s41467-019-09700-1.

[46] H. S. Oh, S. J. Kim, K. Odbadrakh, W. H. Ryu, K. N. Yoon, S. Mu, F. Körmann, Y. Ikeda, C. C. Tasan, D. Raabe, T. Egami, E. S. Park, Engineering atomic-level complexity in high-entropy and complex concentrated alloys, Nature Communications 10 (1) (2019) 1–8. doi:10.1038/s41467-019-10012-7.

[47] S. Gorsse, D. B. Miracle, O. N. Senkov, Mapping the world of complex concentrated alloys, Acta Materialia 135 (2017) 177–187. doi:10.1016/j.actamat.2017.06.027.

[48] A. M. Manzoni, U. Glatzel, New multiphase compositionally complex alloys driven by the high entropy alloy approach, Materials Characterization 147 (2019) 512–532. doi:10.1016/j.matchar.2018.06.036.

[49] P. H. Mayrhofer, D. Music, J. M. Schneider, Erratum: Ab initio calculated binodal and spinodal of cubic $Ti_{1-x}Al_xN$ (Applied Physics Letters (2006) 88 (071922)), Applied Physics Letters 90 (2) (2007) 2006–2007. doi:10.1063/1.2409364.

[50] Y. Zhang, T. T. Zuo, Z. Tang, M. C. Gao, K. A. Dahmen, P. K. Liaw, Z. P. Lu, Microstructures and properties of high-entropy alloys, Progress in Materials Science 61 (2014) 1–93. doi:10.1016/j.pmatsci.2013.10.001.

[51] B. Fultz, Vibrational thermodynamics of materials, Progress in Materials Science 55 (4) (2010) 247–352. doi:10.1016/j.pmatsci.2009.05.002.

[52] C. M. Rost, E. Sachet, T. Borman, A. Moballegh, E. C. Dickey, D. Hou, J. L. Jones, S. Curtarolo, J. P. Maria, Entropy-stabilized oxides, Nature Communications 6 (2015) 1–8. doi:10.1038/ncomms9485.

[53] D. Ma, B. Grabowski, F. Körmann, J. Neugebauer, D. Raabe, Ab initio thermodynamics of the CoCrFeMnNi high entropy alloy: Importance of

entropy contributions beyond the configurational one, Acta Materialia 100 (2015) 90–97. doi:10.1016/j.actamat.2015.08.050.

[54] L. Anthony, L. J. Nagel, J. K. Okamoto, B. Fultz, Magnitude and Origin of the Difference in Vibrational Entropy between Ordered and Disordered Fe_3Al, Physical Review Letters 73 (22) (1994) 3034–3037. doi:10.1103/PhysRevLett.73.3034.

[55] T. L. Swan-Wood, O. Delaire, B. Fultz, Vibrational entropy of spinodal decomposition in FeCr, Physical Review B - Condensed Matter and Materials Physics 72 (2) (2005) 1–7. doi:10.1103/PhysRevB.72.024305.

[56] F. Otto, Y. Yang, H. Bei, E. P. George, Relative effects of enthalpy and entropy on the phase stability of equiatomic high-entropy alloys, Acta Materialia 61 (7) (2013) 2628–2638. doi:10.1016/j.actamat.2013.01.042.

[57] A. Sarkar, Q. Wang, A. Schiele, M. R. Chellali, S. S. Bhattacharya, D. Wang, T. Brezesinski, H. Hahn, L. Velasco, B. Breitung, High-Entropy Oxides: Fundamental Aspects and Electrochemical Properties, Advanced Materials 31 (26) (2019) 1806236. doi:10.1002/adma.201806236.

[58] Z. Grzesik, G. Smoła, M. Stygar, J. Dąbrowa, M. Zajusz, K. Mroczka, M. Danielewski, Defect structure and transport properties in (Co,Cu,Mg,Ni,Zn)O high entropy oxide, Journal of the European Ceramic Society 39 (14) (2019) 4292–4298. doi:10.1016/j.jeurceramsoc.2019.06.018.

[59] M. R. Chellali, A. Sarkar, S. H. Nandam, S. S. Bhattacharya, B. Breitung, H. Hahn, L. Velasco, On the homogeneity of high entropy oxides: An investigation at the atomic scale, Scripta Materialia 166 (2019) 58–63. doi:10.1016/j.scriptamat.2019.02.039.

[60] G. Anand, A. P. Wynn, C. M. Handley, C. L. Freeman, Phase stability and distortion in high-entropy oxides, Acta Materialia 146 (2018) 119–125. doi:10.1016/j.actamat.2017.12.037.

[61] J. W. Yeh, S. Y. Chang, Y. D. Hong, S. K. Chen, S. J. Lin, Anomalous decrease in X-ray diffraction intensities of Cu-Ni-Al-Co-Cr-Fe-Si alloy systems with multi-principal elements, Materials Chemistry and Physics 103 (1) (2007) 41–46. doi:10.1016/j.matchemphys.2007.01.003.

[62] Y. Zhang, Y. J. Zhou, J. P. Lin, G. L. Chen, P. K. Liaw, Solid-solution phase formation rules for multi-component alloys, Advanced Engineering Materials 10 (6) (2008) 534–538. doi:10.1002/adem.200700240.

[63] L. Zhou, F. Körmann, D. Holec, M. Bartosik, B. Grabowski, J. Neugebauer, P. H. Mayrhofer, Structural stability and thermodynamics of CrN magnetic phases from ab initio calculations and experiment, Physical Review B - Condensed Matter and Materials Physics 90 (18) (2014) 1–12. doi:10.1103/PhysRevB.90.184102.

[64] K. Y. Tsai, M. H. Tsai, J. W. Yeh, Sluggish diffusion in Co-Cr-Fe-Mn-Ni high-entropy alloys, Acta Materialia 61 (13) (2013) 4887–4897. doi:10.1016/j.actamat.2013.04.058.

[65] J. Dąbrowa, M. Zajusz, W. Kucza, G. Cieślak, K. Berent, T. Czeppe, T. Kulik, M. Danielewski, Demystifying the sluggish diffusion effect in high entropy alloys, Journal of Alloys and Compounds 783 (2019) 193–207. doi:10.1016/j.jallcom.2018.12.300.

[66] A. Kirnbauer, A. Kretschmer, C. M. Koller, T. Wojcik, V. Paneta, M. Hans, J. M. Schneider, P. Polcik, P. H. Mayrhofer, Mechanical properties and thermal stability of reactively sputtered multi-principal-metal Hf-Ta-Ti-V-Zr nitrides, Surface and Coatings Technology 389 (2020) 125674. doi:10.1016/j.surfcoat.2020.125674.

[67] S.-Y. Chang, M.-K. Chen, D.-S. Chen, Multiprincipal-Element AlCrTaTiZr-Nitride Nanocomposite Film of Extremely High Thermal Stability as Diffusion Barrier for Cu Metallization, Journal of The Electrochemical Society 156 (5) (2009) G37. doi:10.1149/1.3097186.

[68] S. Y. Chang, Y. C. Huang, C. E. Li, H. F. Hsu, J. W. Yeh, S. J. Lin, Improved diffusion-resistant ability of multicomponent nitrides: From unitary TiN to senary high-entropy (TiTaCrZrAlRu)N, Jom 65 (12) (2013) 1790–1796. doi:10.1007/s11837-013-0676-2.

[69] W. H. Liu, Y. Wu, J. Y. He, T. G. Nieh, Z. P. Lu, Grain growth and the Hall-Petch relationship in a high-entropy FeCrNiCoMn alloy, Scripta Materialia 68 (7) (2013) 526–529. doi:10.1016/j.scriptamat.2012.12.002.

[70] R. Li, B. Qiao, H. Shang, J. Zhang, C. Jiang, W. Zhang, Multi-component AlCrTaTiZrMo-nitride film with high diffusion resistance in copper metallization, Journal of Alloys and Compounds 748 (2018) 258–264. doi:10.1016/j.jallcom.2018.03.084.

[71] P. Kumar, S. Avasthi, Diffusion barrier with 30-fold improved performance using AlCrTaTiZrN high-entropy alloy, Journal of Alloys and Compounds 814 (2020) 151755. doi:10.1016/j.jallcom.2019.151755.

[72] S. Ranganathan, Alloyed pleasures: Multimetallic cocktails, Current Science 85 (10) (2003) 1404–1406.
URL http://eprints.iisc.ac.in/id/eprint/6189

[73] P. H. Mayrhofer, Lecture Notes Surface Technology, TU Wien (2021).

[74] R. Bosco, J. V. Van Den Beucken, S. Leeuwenburgh, J. Jansen, Surface engineering for bone implants: A trend from passive to active surfaces, Coatings 2 (3) (2012) 95–119. doi:10.3390/coatings2030095.

[75] S. Berg, T. Nyberg, Fundamental understanding and modeling of reactive sputtering processes, Thin Solid Films 476 (2) (2005) 215–230. doi:10.1016/j.tsf.2004.10.051.

[76] D. Depla, S. Heirwegh, S. Mahieu, J. Haemers, R. De Gryse, Understanding the discharge voltage behavior during reactive sputtering of oxides, Journal of Applied Physics 101 (1) (2007) 013301. doi:10.1063/1.2404583.

[77] D. Depla, S. Heirwegh, S. Mahieu, R. De Gryse, Towards a more complete model for reactive magnetron sputtering, Journal of Physics D: Applied Physics 40 (7) (2007) 1957–1965. doi:10.1088/0022-3727/40/7/019.

[78] E. Bauer, Phänomenologische Theorie Der Kristallabscheidung An Oberflächen. II, Zeitschrift fur Kristallographie - New Crystal Structures 110 (1-6) (1958) 395–431. doi:10.1524/zkri.1958.110.1-6.395.

[79] B. A. Movchan, A. V. Demchishin, Structure and Properties of Thick Condensates of Nickel, Titanium, Tungsten, Aluminium Oxides, and Zirconium Dioxide in Vacuum, Phys. Metals Metallogr. 28 (4) (1969).

[80] P. B. Barna, M. Adamik, Fundamental structure forming phenomena of polycrystalline films and the structure zone models, Thin Solid Films 317 (1-2) (1998) 27–33. doi:10.1016/S0040-6090(97)00503-8.

[81] J. A. Thornton, Influence of Apparatus Geometry and Deposition Conditions on the Structure and Topography of Thick Sputtered Coatings., J Vac Sci Technol 11 (4) (1974) 666–670. doi:10.1116/1.1312732.

[82] R. Messier, A. P. Giri, R. A. Roy, Revised structure zone model for thin film physical structure, Journal of Vacuum Science & Technology A: Vacuum, Surfaces, and Films 2 (2) (1984) 500–503. doi:10.1116/1.572604.

[83] A. Anders, A structure zone diagram including plasma-based deposition and ion etching, Thin Solid Films 518 (15) (2010) 4087–4090. doi:10.1016/j.tsf.2009.10.145.

[84] L. Spieß, G. Teichert, R. Schwarzer, H. Behnken, C. Genzel, Moderne Röntgenbeugung, Springer Fachmedien Wiesbaden, Wiesbaden, 2019. doi:10.1007/978-3-8348-8232-5.

[85] D. B. Williams, C. B. Carter, Transmission Electron Microscopy - A Textbook for Materials Science, second edi Edition, Springer, New York, 2009.

[86] J. I. Goldstein, D. E. Newbury, J. R. Michael, N. W. Ritchie, J. H. J. Scott, D. C. Joy, Scanning Electron Microscopy and X-Ray Microanalysis, fourth edi Edition, Springer New York, New York, NY, 2018. doi:10.1007/978-1-4939-6676-9.

[87] B. Fultz, J. M. Howe, Transmission Electron Microscopy and Diffractometry of Materials, first edit Edition, Springer, 2001.

[88] B. L. Adams, S. R. Kalidindi, D. T. Fullwood, Electron Backscatter Diffraction Microscopy and Basic Stereology, in: Microstructure Sensitive Design for Performance Optimization, Elsevier, 2013, pp. 341–371. doi:10.1016/B978-0-12-396989-7.00016-2.

[89] J. L'Ecuyer, C. Brassard, C. Cardinal, J. Chabbal, L. Deschênes, J. P. Labrie, B. Terreault, J. G. Martel, R. St.-Jacques, An accurate and sensitive method for the determination of the depth distribution of light elements in heavy materials, Journal of Applied Physics 47 (1) (1976) 381–382. doi:10.1063/1.322288.

[90] D. Jalabert, I. Vickridge, A. Chabli, Swift Ion Beam Analysis in Nanosciences, first edit Edition, John Wiley & Sons, Inc., Hoboken, NJ, 2017. doi:10.1002/9781119005063.

[91] A. Macková, A. Pratt, Ion/Neutral Probe Techniques, in: Handbook of Spectroscopy, second edi Edition, Wiley-VCH Verlag GmbH & Co. KGaA, Weinheim, 2014, pp. 741–778. doi:10.1002/9783527654703.ch19.

[92] A. Vértes, S. Nagy, Z. Klencsár, R. G. Lovas, F. Rösch (Eds.), Handbook of Nuclear Chemistry, second edi Edition, Springer US, Boston, MA, 2011. doi:10.1007/978-1-4419-0720-2.

[93] B. Gault, M. P. Moody, J. M. Cairney, S. P. Ringer, Atom Probe Microscopy, Springer Series in Materials Science, Springer New York, 2012. doi:10.1007/978-1-4614-3436-8.

[94] E. W. Müller, Field desorption, Physical Review 102 (3) (1956) 618–624. doi:10.1103/PhysRev.102.618.

[95] A. Kirnbauer, Dissertation The High-Entropy Concept for Ceramic Thin Films, Ph.D. thesis, TU Wien (2020).

[96] W. Oliver, G. Pharr, An improved technique for determining hardness and elastic modulus using load and displacement sensing indentation experiments, Journal of Materials Research 7 (6) (1992) 1564–1583. doi:10.1557/jmr.1992.1564.

[97] N. Birks, G. H. Meier, F. S. Pettit, Introduction to the High-Temperature Oxidation of Metals, Vol. 40, Cambridge University Press, Cambridge, 2006. doi:10.1017/CBO9781139163903.

[98] M. E. Glicksman, Diffusion in Solids: field theory, solid-state principles, and applications, first edit Edition, John Wiley & Sons, Inc., New York, NY, 2000.

[99] C. Leyens, Oxidation and Protection of Titanium Alloys and Titanium Aluminides, in: Titanium and Titanium Alloys, Wiley-VCH Verlag GmbH & Co. KGaA, Weinheim, FRG, 2005, pp. 187–230. doi:10.1002/3527602119.ch6.

[100] P. H. Mayrhofer, R. Rachbauer, D. Holec, F. Rovere, J. M. Schneider, Protective Transition Metal Nitride Coatings, Vol. 4, Elsevier, 2014. doi:10.1016/B978-0-08-096532-1.00423-4.

[101] G. Tammann, Über Anlauffarben von Metallen, Zeitschrift für anorganische und allgemeine Chemie 111 (1) (1920) 78–89. doi:10.1002/zaac.19201110107.

[102] G. Tammann, W. Köster, Die Geschwindigkeit der Einwirkung von Sauerstoff, Schwefelwasserstoff und Halogenen auf Metalle, Zeitschrift für anorganische und allgemeine Chemie 123 (1) (1922) 196–224. doi:10.1002/zaac.19221230115.

[103] D. J. Young, The Nature of High Temperature Oxidation, in: High Temperature Oxidation and Corrosion of Metals, Elsevier, 2016, pp. 1–30. doi:10.1016/B978-0-08-100101-1.00001-7.

[104] M. F. Ashby, D. R. Jones, Engineering Materials 1, Third edition, first edit Edition, Elsevier Inc., 2005.

[105] R. J. Borg, G. Dienes, An Introduction to Solid State Diffusion, first edit Edition, Academic Press, Inc., 1988.

[106] D. S. Sholl, J. A. Steckel, Density Functional Theory, first edit Edition, John Wiley & Sons, Inc., Hoboken, New Jersey, 2009. doi:10.1002/9780470447710.

[107] P. Hohenberg, W. Kohn, Inhomogeneous Electron Gas, Physical Review 136 (3B) (1964) B864–B871. doi:10.1103/PhysRev.136.B864.

[108] W. Kohn, L. J. Sham, Self-Consistent Equations Including Exchange and Correlation Effects, Physical Review 140 (4A) (1965) A1133–A1138. doi:10.1103/PhysRev.140.A1133.

[109] J. Hafner, Ab-initio simulations of materials using VASP: Density-functional theory and beyond, Journal of Computational Chemistry 29 (13) (2008) 2044–2078. doi:10.1002/jcc.21057.

[110] J. P. Perdew, K. Burke, Y. Wang, Generalized gradient approximation for the exchange-correlation hole of a many-electron system, Physical Review B 54 (23) (1996) 16533–16539. doi:10.1103/PhysRevB.54.16533.

[111] G. Kresse, J. Furthmüller, Efficient iterative schemes for ab initio total-energy calculations using a plane-wave basis set, Physical Review B - Condensed Matter and Materials Physics 54 (16) (1996) 11169–11186. doi:10.1103/PhysRevB.54.11169.

[112] G. Kresse, D. Joubert, From ultrasoft pseudopotentials to the projector augmented-wave method, Physical Review B 59 (3) (1999) 1758–1775. doi:10.1103/PhysRevB.59.1758.

[113] J. D. Pack, H. J. Monkhorst, Special points for Brillouin-zone integrations, Physical Review B 16 (4) (1977) 1748–1749. doi:10.1103/PhysRevB.16.1748.

[114] J. P. Perdew, M. Levy, Physical content of the exact kohn-sham orbital energies: Band gaps and derivative discontinuities, Physical Review Letters 51 (20) (1983) 1884–1887. doi:10.1103/PhysRevLett.51.1884.

[115] L. J. Sham, M. Schlüter, Density-functional theory of the energy gap, Physical Review Letters 51 (20) (1983) 1888–1891. doi:10.1103/PhysRevLett.51.1888.

[116] J. Singleton, Band Theory and Electronic Properties of Solids, first edit Edition, Oxford University Press, New York, NY, 2001.

[117] K. Balasubramanian, S. Khare, D. Gall, Vacancy-induced mechanical stabilization of cubic tungsten nitride, Physical Review B 94 (17) (2016) 36–38. doi:10.1103/PhysRevB.94.174111.

[118] S. H. Wei, L. G. Ferreira, J. E. Bernard, A. Zunger, Electronic properties of random alloys: Special quasirandom structures, Physical Review B 42 (15) (1990) 9622–9649. doi:10.1103/PhysRevB.42.9622.

[119] D. Holec, Lecture Notes Atomistic Materials Modeling, TU Wien (2018).

[120] D. G. Sangiovanni, Inherent toughness and fracture mechanisms of refractory transition-metal nitrides via density-functional molecular dynamics, Acta Materialia 151 (2018) 11–20. doi:10.1016/j.actamat.2018.03.038.

[121] J. F. Nye, Physical Properties of Crystals: Their Representation by Tensors and Matrices, first edit Edition, Oxford University Press, Bury St Edmunds, Suffolk, 1985.

[122] M. A. Caro, S. Schulz, E. P. O'Reilly, Comparison of stress and total energy methods for calculation of elastic properties of semiconductors, Journal of Physics: Condensed Matter 25 (2) (2013) 025803. doi:10.1088/0953-8984/25/2/025803.

[123] R. Yu, J. Zhu, H. Q. Ye, Calculations of single-crystal elastic constants made simple, Computer Physics Communications 181 (3) (2010) 671–675. doi:10.1016/j.cpc.2009.11.017.

[124] S. Pugh, XCII. Relations between the elastic moduli and the plastic properties of polycrystalline pure metals, The London, Edinburgh, and Dublin Philosophical Magazine and Journal of Science 45 (367) (1954) 823–843. doi:10.1080/14786440808520496.

[125] D. G. Pettifor, Theoretical predictions of structure and related properties of intermetallics, Materials Science and Technology 8 (4) (1992) 345–349. doi:10.1179/mst.1992.8.4.345.

[126] S. Curtarolo, G. L. Hart, M. B. Nardelli, N. Mingo, S. Sanvito, O. Levy, The high-throughput highway to computational materials design, Nature Materials 12 (3) (2013) 191–201. doi:10.1038/nmat3568.

[127] D. B. Miracle, J. D. Miller, O. N. Senkov, C. Woodward, M. D. Uchic, J. Tiley, Exploration and development of high entropy alloys for structural applications, Entropy 16 (1) (2014) 494–525. doi:10.3390/e16010494.

[128] C. Jiang, B. P. Uberuaga, Efficient Ab initio Modeling of Random Multicomponent Alloys, Physical Review Letters 116 (10) (2016) 1–5. doi:10.1103/PhysRevLett.116.105501.

[129] D. J. King, S. C. Middleburgh, A. G. McGregor, M. B. Cortie, Predicting the formation and stability of single phase high-entropy alloys, Acta Materialia 104 (2016) 172–179. doi:10.1016/j.actamat.2015.11.040.

[130] Q. Zhang, J. Zhang, N. Li, W. Chen, Understanding the electronic structure, mechanical properties, and thermodynamic stability of (TiZrHfNbTa)C combined experiments and first-principles simulation, Journal of Applied Physics 126 (2) (2019). doi:10.1063/1.5094580.

[131] B. Ye, T. Wen, M. C. Nguyen, L. Hao, C. Z. Wang, Y. Chu, First-principles study, fabrication and characterization of $(Zr_{0.25}Nb_{0.25}Ti_{0.25}V_{0.25})C$ high-entropy ceramics, Acta Materialia 170 (2019) 15–23. doi:10.1016/j.actamat.2019.03.021.

[132] T. J. Harrington, J. Gild, P. Sarker, C. Toher, C. M. Rost, O. F. Dippo, C. McElfresh, K. Kaufmann, E. Marin, L. Borowski, P. E. Hopkins, J. Luo,

S. Curtarolo, D. W. Brenner, K. S. Vecchio, Phase stability and mechanical properties of novel high entropy transition metal carbides, Acta Materialia 166 (2019) 271–280. doi:10.1016/j.actamat.2018.12.054.

[133] Y. Zhong, H. Sabarou, X. Yan, M. Yang, M. C. Gao, X. Liu, R. D. Sisson, Exploration of high entropy ceramics (HECs) with computational thermodynamics - A case study with $LaMnO_{3\pm\delta}$, Materials and Design 182 (2019) 108060. doi:10.1016/j.matdes.2019.108060.

[134] A. Kretschmer, A. Kirnbauer, V. Moraes, D. Primetzhofer, K. Yalamanchili, H. Rudigier, P. H. Mayrhofer, Improving phase stability, hardness, and oxidation resistance of reactively magnetron sputtered (Al,Cr,Nb,Ta,Ti)N thin films by Si-alloying, Surface and Coatings Technology 416 (February) (2021) 127162. doi:10.1016/j.surfcoat.2021.127162.

[135] Y. P. Wang, G. Y. Gan, W. Wang, Y. Yang, B. Y. Tang, Ab Initio Prediction of Mechanical and Electronic Properties of Ultrahigh Temperature High-Entropy Ceramics $(Hf_{0.2}Zr_{0.2}Ta_{0.2}M_{0.2}Ti_{0.2})B_2$ (M = Nb, Mo, Cr), Physica Status Solidi (B) Basic Research 255 (8) (2018) 1–7. doi:10.1002/pssb.201800011.

[136] K. Yalamanchili, F. Wang, I. C. Schramm, J. M. Andersson, M. P. Johansson Jöesaar, F. Tasnádi, F. Mücklich, N. Ghafoor, M. Odén, Exploring the high entropy alloy concept in (AlTiVNbCr)N, Thin Solid Films 636 (2017) 346–352. doi:10.1016/j.tsf.2017.06.029.

[137] T. Wen, B. Ye, M. C. Nguyen, M. Ma, Y. Chu, Thermophysical and mechanical properties of novel high-entropy metal nitride-carbides, Journal of the American Ceramic Society 103 (11) (2020) 6475–6489. doi:10.1111/jace.17333.

[138] M. Wittmer, J. Noser, H. Melchior, Oxidation kinetics of TiN thin films, Journal of Applied Physics 52 (11) (1981) 6659–6664. doi:10.1063/1.328659.

[139] C. M. Koller, R. Hollerweger, C. Sabitzer, R. Rachbauer, S. Kolozsvári, J. Paulitsch, P. H. Mayrhofer, Thermal stability and oxidation resistance of arc evaporated TiAlN, TaAlN, TiAlTaN, and TiAlN/TaAlN coatings, Surface and Coatings Technology 259 (PC) (2014) 599–607. doi:10.1016/j.surfcoat.2014.10.024.

[140] J. L. Endrino, V. Derflinger, The influence of alloying elements on the phase stability and mechanical properties of AlCrN coatings, Surface and Coatings Technology 200 (1-4 SPEC. ISS.) (2005) 988–992. doi:10.1016/j.surfcoat.2005.02.196.

[141] J. W. Yeh, Alloy design strategies and future trends in high-entropy alloys, Jom 65 (12) (2013) 1759–1771. doi:10.1007/s11837-013-0761-6.

[142] W. J. Shen, M. H. Tsai, K. Y. Tsai, C. C. Juan, C. W. Tsai, J. W. Yeh, Y. S. Chang, Superior oxidation resistance of $(Al_{0.34}Cr_{0.22}Nb_{0.11}Si_{0.11}Ti_{0.22})_{50}N_{50}$ high−entropy nitride, Journal of the Electrochemical Society 160 (11) (2013) 531–535. doi:10.1149/2.028311jes.

[143] Q. W. Xing, S. Q. Xia, X. H. Yan, Y. Zhang, Mechanical properties and thermal stability of (NbTiAlSiZr)N_x high-entropy ceramic films at high temperatures, Journal of Materials Research 33 (19) (2018) 3347–3354. doi:10.1557/jmr.2018.337.

[144] T. H. Hsieh, C. H. Hsu, C. Y. Wu, J. Y. Kao, C. Y. Hsu, Effects of deposition parameters on the structure and mechanical properties of high-entropy alloy nitride films, Current Applied Physics 18 (5) (2018) 512–518. doi:10.1016/j.cap.2018.02.015.

[145] E. Chicardi, C. García-Garrido, F. J. Gotor, Low temperature synthesis of an equiatomic (TiZrHfVNb)C_5 high entropy carbide by a mechanically-induced carbon diffusion route, Ceramics International 45 (17) (2019) 21858–21863. doi:10.1016/j.ceramint.2019.07.195.

[146] J. K. Xiao, H. Tan, J. Chen, A. Martini, C. Zhang, Effect of carbon content on microstructure, hardness and wear resistance of $CoCrFeMnNiC_x$ high-entropy alloys, Journal of Alloys and Compounds 847 (2020) 156533. doi:10.1016/j.jallcom.2020.156533.

[147] D. Wang, S. Jiang, C. Duan, J. Mao, Y. Dong, K. Dong, Z. Wang, S. Luo, Y. Liu, X. Qi, Spinel-structured high entropy oxide $(FeCoNiCrMn)_3O_4$ as anode towards superior lithium storage performance, Journal of Alloys and Compounds 844 (2020) 156158. doi:10.1016/j.jallcom.2020.156158.

[148] X. Q. Shen, J. X. Liu, F. Li, G. J. Zhang, Preparation and characterization of diboride-based high entropy $(Ti_{0.2}Zr_{0.2}Hf_{0.2}Nb_{0.2}Ta_{0.2})B_2$–SiC particulate composites, Ceramics International 45 (18) (2019) 24508–24514. doi:10.1016/j.ceramint.2019.08.178.

[149] P. K. Huang, J. W. Yeh, Effects of substrate temperature and post-annealing on microstructure and properties of (AlCrNbSiTiV)N coatings, Thin Solid Films 518 (1) (2009) 180–184. doi:10.1016/j.tsf.2009.06.020.

[150] P. K. Huang, J. W. Yeh, Inhibition of grain coarsening up to 1000 °C in (AlCrNbSiTiV)N superhard coatings, Scripta Materialia 62 (2) (2010) 105–108. doi:10.1016/j.scriptamat.2009.09.015.

[151] R. Li, M. Li, C. Jiang, B. Qiao, W. Zhang, J. Xu, Thermal stability of AlCrTaTiZrMo-nitride high entropy film as a diffusion barrier for Cu metallization, Journal of Alloys and Compounds 773 (2019) 482–489. doi:10.1016/j.jallcom.2018.09.283.

[152] R. Hollerweger, H. Riedl, M. Arndt, S. Kolozsvari, S. Primig, P. Mayrhofer, Guidelines for increasing the oxidation resistance of Ti-Al-N based coatings, Thin Solid Films 688 (May) (2019) 137290. doi:10.1016/j.tsf.2019.05.009.

[153] H. Asanuma, P. Polcik, S. Kolozsvari, F. F. Klimashin, H. Riedl, P. H. Mayrhofer, Cerium doping of Ti-Al-N coatings for excellent thermal stability

and oxidation resistance, Surface and Coatings Technology 326 (2017) 165–172. doi:10.1016/j.surfcoat.2017.07.037.

[154] M. Pfeiler, C. Scheu, H. Hutter, J. Schnöller, C. Michotte, C. Mitterer, M. Kathrein, On the effect of Ta on improved oxidation resistance of Ti–Al–Ta–N coatings, Journal of Vacuum Science & Technology A: Vacuum, Surfaces, and Films 27 (3) (2009) 554–560. doi:10.1116/1.3119671.

[155] P. Ström, P. Petersson, M. Rubel, G. Possnert, A combined segmented anode gas ionization chamber and time-of-flight detector for heavy ion elastic recoil detection analysis, Review of Scientific Instruments 87 (10) (2016) 103303. doi:10.1063/1.4963709.

[156] M. V. Moro, R. Holeňák, L. Zendejas Medina, U. Jansson, D. Primetzhofer, Accurate high-resolution depth profiling of magnetron sputtered transition metal alloy films containing light species: A multi-method approach, Thin Solid Films 686 (July) (2019). doi:10.1016/j.tsf.2019.137416.

[157] H. Y. Qu, D. Primetzhofer, M. A. Arvizu, Z. Qiu, U. Cindemir, C. G. Granqvist, G. A. Niklasson, Electrochemical Rejuvenation of Anodically Coloring Electrochromic Nickel Oxide Thin Films, ACS Applied Materials and Interfaces 9 (49) (2017) 42420–42424. doi:10.1021/acsami.7b13815.

[158] N. Koutná, D. Holec, O. Svoboda, F. F. Klimashin, P. H. Mayrhofer, Point defects stabilise cubic Mo-N and Ta-N, Journal of Physics D: Applied Physics 49 (37) (2016) 375303. doi:10.1088/0022-3727/49/37/375303.

[159] J. Patscheider, T. Zehnder, M. Diserens, Structure-performance relations in nanocomposite coatings, Surface and Coatings Technology 146-147 (2001) 201–208. doi:10.1016/S0257-8972(01)01389-5.

[160] S. Vepřek, S. Reiprich, A concept for the design of novel superhard coatings, Thin Solid Films 268 (1-2) (1995) 64–71. doi:10.1016/0040-6090(95)06695-0.

[161] W. Ernst, J. Neidhardt, H. Willmann, B. Sartory, P. H. Mayrhofer, C. Mitterer, Thermal decomposition routes of CrN hard coatings synthesized

by reactive arc evaporation and magnetron sputtering, Thin Solid Films 517 (2) (2008) 568–574. doi:10.1016/j.tsf.2008.06.086.

[162] C. M. Koller, A. Kirnbauer, R. Rachbauer, S. Kolozsvári, P. H. Mayrhofer, Thermally-induced phase transformation sequence of arc evaporated Ta-Al-N coatings, Scripta Materialia 113 (2016) 75–78. doi:10.1016/j.scriptamat.2015.09.040.

[163] L. Hultman, J. Bareño, A. Flink, H. Söderberg, K. Larsson, V. Petrova, M. Odén, J. E. Greene, I. Petrov, Interface structure in superhard TiN-SiN nanolaminates and nanocomposites: Film growth experiments and ab initio calculations, Physical Review B - Condensed Matter and Materials Physics 75 (15) (2007) 1–6. doi:10.1103/PhysRevB.75.155437.

[164] P. H. Mayrhofer, C. Mitterer, J. G. Wen, I. Petrov, J. E. Greene, Thermally induced self-hardening of nanocrystalline Ti–B–N thin films, Journal of Applied Physics 100 (4) (2006) 044301. doi:10.1063/1.2222406.

[165] R. Riedel, M. Seher, Crystallization behaviour of amorphous silicon nitride, Journal of the European Ceramic Society 7 (1) (1991) 21–25. doi:10.1016/0955-2219(91)90049-6.

[166] A. Leyland, A. Matthews, On the significance of the H/E ratio in wear control: A nanocomposite coating approach to optimised tribological behaviour, Wear 246 (1-2) (2000) 1–11. doi:10.1016/S0043-1648(00)00488-9.

[167] R. Hahn, A. Kirnbauer, M. Bartosik, S. Kolozsvári, P. H. Mayrhofer, Toughness of Si alloyed high-entropy nitride coatings, Materials Letters 251 (2019) 238–240. doi:10.1016/j.matlet.2019.05.074.

[168] R. Rachbauer, D. Holec, P. H. Mayrhofer, Increased thermal stability of Ti-Al-N thin films by Ta alloying, Surface and Coatings Technology 211 (2012) 98–103. doi:10.1016/j.surfcoat.2011.07.009.

[169] W.-J. Shen, M.-H. Tsai, J.-W. Yeh, Machining Performance of Sputter-Deposited $(Al_{0.34}Cr_{0.22}Nb_{0.11}Si_{0.11}Ti_{0.22})_{50}N_{50}$ High-Entropy

Nitride Coatings, Coatings 5 (3) (2015) 312–325. doi:10.3390/coatings5030312.

[170] Y. C. Lin, S. Y. Hsu, R. W. Song, W. L. Lo, Y. T. Lai, S. Y. Tsai, J. G. Duh, Improving the hardness of high entropy nitride $(Cr_{0.35}Al_{0.25}Nb_{0.12}Si_{0.08}V_{0.20})N$ coatings via tuning substrate temperature and bias for anti-wear applications, Surface and Coatings Technology 403 (101) (2020) 126417. doi:10.1016/j.surfcoat.2020.126417.

[171] X. Feng, K. Zhang, Y. Zheng, H. Zhou, Z. Wan, Chemical state, structure and mechanical properties of multi-element (CrTaNbMoV)Nx films by reactive magnetron sputtering, Materials Chemistry and Physics 239 (May 2019) (2020) 121991. doi:10.1016/j.matchemphys.2019.121991.

[172] J.-J. Wang, F.-Y. Ouyang, Oxidation behavior of Al-Cr-Nb-Si-Zr high entropy nitride thin films at 850 ℃, Corrosion Science 187 (October 2020) (2021) 109467. doi:10.1016/j.corsci.2021.109467.

[173] K. H. Cheng, C. H. Lai, S. J. Lin, J. W. Yeh, Structural and mechanical properties of multi-element $(AlCrMoTaTiZr)N_x$ coatings by reactive magnetron sputtering, Thin Solid Films 519 (10) (2011) 3185–3190. doi:10.1016/j.tsf.2010.11.034.

[174] R. Chen, Z. Cai, J. Pu, Z. Lu, S. Chen, S. Zheng, C. Zeng, Effects of nitriding on the microstructure and properties of VAlTiCrMo high-entropy alloy coatings by sputtering technique, Journal of Alloys and Compounds 827 (2020) 153836. doi:10.1016/j.jallcom.2020.153836.

[175] P. Cui, W. Li, P. Liu, K. Zhang, F. Ma, X. Chen, R. Feng, P. K. Liaw, Effects of nitrogen content on microstructures and mechanical properties of (AlCrTiZrHf)N high-entropy alloy nitride films, Journal of Alloys and Compounds 834 (2020) 155063. doi:10.1016/j.jallcom.2020.155063.

[176] X. Lu, C. Zhang, C. Wang, X. Cao, R. Ma, X. Sui, J. Hao, W. Liu, Investigation of $(CrAlTiNbV)N_x$ high-entropy nitride coatings via tailoring nitrogen flow rate for anti-wear applications in aviation lubricant, Applied

Surface Science 557 (March) (2021) 149813. doi:10.1016/j.apsusc.2021.149813.

[177] H. T. Hsueh, W. J. Shen, M. H. Tsai, J. W. Yeh, Effect of nitrogen content and substrate bias on mechanical and corrosion properties of high-entropy films $(AlCrSiTiZr)_{100-x}N_x$, Surface and Coatings Technology 206 (19-20) (2012) 4106–4112. doi:10.1016/j.surfcoat.2012.03.096.

[178] K. von Fieandt, L. Riekehr, B. Osinger, S. Fritze, E. Lewin, Influence of N content on structure and mechanical properties of multi-component Al-Cr-Nb-Y-Zr based thin films by reactive magnetron sputtering, Surface and Coatings Technology 389 (March) (2020) 125614. doi:10.1016/j.surfcoat.2020.125614.

[179] J. Nohava, P. Dessarzin, P. Karvankova, M. Morstein, Characterization of tribological behavior and wear mechanisms of novel oxynitride PVD coatings designed for applications at high temperatures, Tribology International 81 (2015) 231–239. doi:10.1016/j.triboint.2014.08.016.

[180] K. Bobzin, T. Brögelmann, C. Kalscheuer, M. Naderi, Hybrid dcMS/HPPMS PVD nitride and oxynitride hard coatings for adhesion and abrasion reduction in plastics processing, Surface and Coatings Technology 308 (2016) 349–359. doi:10.1016/j.surfcoat.2016.07.103.

[181] B. Warcholinski, A. Gilewicz, A. S. Kuprin, G. N. Tolmachova, V. D. Ovcharenko, T. A. Kuznetsova, V. A. Lapitskaya, S. A. Chizhik, Comparison of Mechanical and Tribological Properties of Nitride and Oxynitride Coatings Based on Chrome and Zirconium Obtained by Cathodic Arc Evaporation, Journal of Friction and Wear 40 (2) (2019) 163–170. doi:10.3103/S1068366619020156.

[182] D. Cristea, D. Constantin, A. Crisan, C. S. Abreu, J. R. Gomes, N. P. Barradas, E. Alves, C. Moura, F. Vaz, L. Cunha, Properties of tantalum oxynitride thin films produced by magnetron sputtering: The influence of processing parameters, Vacuum 98 (2013) 63–69. doi:10.1016/j.vacuum.2013.03.017.

[183] F. Ahmad, L. Zhang, J. Zheng, I. Sidra, F. Cai, S. Zhang, Structural evolution and high-temperature tribological properties of AlCrON coatings deposited by multi-arc ion plating, Ceramics International 46 (15) (2020) 24281–24289. doi:10.1016/j.ceramint.2020.06.208.

[184] K. Balasubramanian, L. Huang, D. Gall, Phase stability and mechanical properties of $Mo_{1-x}N_x$ with $0 \leq \times \leq 1$, Journal of Applied Physics 122 (19) (2017) 0–12. doi:10.1063/1.4998686.

[185] M. J. Mehl, D. Finkenstadt, C. Dane, G. L. Hart, S. Curtarolo, Finding the stable structures of $N_{1-x}W_x$ with an ab initio high-throughput approach, Physical Review B - Condensed Matter and Materials Physics 91 (18) (2015) 1–19. doi:10.1103/PhysRevB.91.184110.

[186] F. Bachmann, R. Hielscher, H. Schaeben, Texture analysis with MTEX-Free and open source software toolbox, Solid State Phenomena 160 (2010) 63–68. doi:10.4028/www.scientific.net/SSP.160.63.

[187] F. F. Klimashin, N. Koutná, H. Euchner, D. Holec, P. H. Mayrhofer, The impact of nitrogen content and vacancies on structure and mechanical properties of Mo–N thin films, Journal of Applied Physics 120 (18) (2016) 185301. doi:10.1063/1.4966664.

[188] L. Stöber, J. P. Konrath, V. Haberl, F. Patocka, M. Schneider, U. Schmid, Nitrogen incorporation in sputter deposited molybdenum nitride thin films, Journal of Vacuum Science & Technology A: Vacuum, Surfaces, and Films 34 (2) (2016) 021513. doi:10.1116/1.4941141.

[189] A. A. Bagdasaryan, A. V. Pshyk, L. E. Coy, P. Konarski, M. Misnik, V. I. Ivashchenko, M. Kempiński, N. R. Mediukh, A. D. Pogrebnjak, V. M. Beresnev, S. Jurga, A new type of (TiZrNbTaHf)N/MoN nanocomposite coating: Microstructure and properties depending on energy of incident ions, Composites Part B: Engineering 146 (March) (2018) 132–144. doi:10.1016/j.compositesb.2018.04.015.

[190] C. Stampfl, A. J. Freeman, Metallic to insulating nature of (formula presented) Role of Ta and N vacancies, Physical Review B - Condensed Matter and Materials Physics 67 (6) (2003) 1–7. doi:10.1103/PhysRevB.67.064108.

[191] H. Yusa, F. Kawamura, T. Taniguchi, N. Hirao, Y. Ohishi, T. Kikegawa, High-pressure synthesis and compressive behavior of tantalum nitrides, Journal of Applied Physics 115 (10) (2014) 103520. doi:10.1063/1.4867986.

[192] L. Skala, P. Capkova, Nitrogen vacancy and chemical bonding in substoichiometric vanadium nitride, Journal of Physics: Condensed Matter 2 (42) (1990) 8293–8301. doi:10.1088/0953-8984/2/42/007.

[193] B. Ozsdolay, C. Mulligan, K. Balasubramanian, L. Huang, S. Khare, D. Gall, Cubic β-WN_x layers: Growth and properties vs N-to-W ratio, Surface and Coatings Technology 304 (2016) 98–107. doi:10.1016/j.surfcoat.2016.06.079.

[194] A. A. Bagdasaryan, A. V. Pshyk, L. E. Coy, M. Kempiński, A. D. Pogrebnjak, V. M. Beresnev, S. Jurga, Structural and mechanical characterization of (TiZrNbHfTa)N/WN multilayered nitride coatings, Materials Letters 229 (2018) 364–367. doi:10.1016/j.matlet.2018.07.048.

[195] J. Buchinger, N. Koutná, Z. Chen, Z. Zhang, P. H. Mayrhofer, D. Holec, M. Bartosik, Toughness enhancement in TiN/WN superlattice thin films, Acta Materialia 172 (2019) 18–29. doi:10.1016/j.actamat.2019.04.028.

[196] J. E. Lowther, Lattice model for the properties of non-stoichiometric cubic and hexagonal molybdenum nitride, Journal of Alloys and Compounds 364 (1-2) (2004) 13–16. doi:10.1016/S0925-8388(03)00537-1.

[197] M. Grumski, P. P. Dholabhai, J. B. Adams, Ab initio study of the stable phases of 1:1 tantalum nitride, Acta Materialia 61 (10) (2013) 3799–3807. doi:10.1016/j.actamat.2013.03.018.

[198] S. Åsbrink, L. Kihlborg, M. Malinowski, High-pressure single-crystal X-ray diffraction studies of MoO_3. I. Lattice parameters up to 7·4 GPa, Journal of Applied Crystallography 21 (6) (1988) 960–962. doi:10.1107/S0021889888008271.

[199] Y. Syono, M. Kikuchi, T. Goto, K. Fukuoka, Formation of rutile-type Ta(IV)O_2 by shock reduction and cation-deficient $Ta_{0.8}O_2$ by subsequent oxidation, Journal of Solid State Chemistry 50 (2) (1983) 133–137. doi:10.1016/0022-4596(83)90180-9.

[200] K. D. Rogers, An X-ray diffraction study of semiconductor and metallic vanadium dioxide, Powder Diffraction 8 (4) (1993) 240–244. doi:10.1017/S0885715600019448.

[201] D. J. Palmer, P. G. Dickens, Tungsten dioxide: structure refinement by powder neutron diffraction, Acta Crystallographica Section B Structural Crystallography and Crystal Chemistry 35 (9) (1979) 2199–2201. doi:10.1107/s0567740879008785.

[202] R. Chen, G. Qin, H. Zheng, L. Wang, Y. Su, Y. L. Chiu, H. Ding, J. Guo, H. Fu, Composition design of high entropy alloys using the valence electron concentration to balance strength and ductility, Acta Materialia 144 (2018) 129–137. doi:10.1016/j.actamat.2017.10.058.

[203] K. Balasubramanian, S. V. Khare, D. Gall, Valence electron concentration as an indicator for mechanical properties in rocksalt structure nitrides, carbides and carbonitrides, Acta Materialia 152 (2018) 175–185. doi:10.1016/j.actamat.2018.04.033.

[204] R. Hahn, A. Tymoszuk, T. Wojcik, A. Kirnbauer, T. Kozák, J. Capek, M. Sauer, A. Foelske, O. Hunold, P. Polcik, P. Mayrhofer, H. Riedl, Phase formation and mechanical properties of reactively and non-reactively sputtered Ti-B-N hard coatings, Surface and Coatings Technology 420 (March) (2021) 127327. doi:10.1016/j.surfcoat.2021.127327.

[205] H. Euchner, P. H. Mayrhofer, Designing thin film materials-Ternary borides from first principles, Thin Solid Films 583 (1) (2015) 46–49. doi:10.1016/j.tsf.2015.03.035.

[206] M. Moakher, A. N. Norris, The closest elastic tensor of arbitrary symmetry to an elasticity tensor of lower symmetry, Journal of Elasticity 85 (3) (2006) 215–263. arXiv:0608311, doi:10.1007/s10659-006-9082-0.

[207] R. Hill, The elastic behaviour of a crystalline aggregate, Proceedings of the Physical Society. Section A 65 (5) (1952) 349–354. doi:10.1088/0370-1298/65/5/307.

[208] V. Moraes, H. Riedl, C. Fuger, P. Polcik, H. Bolvardi, D. Holec, P. H. Mayrhofer, Ab initio inspired design of ternary boride thin films, Scientific Reports 8 (1) (2018) 1–9. doi:10.1038/s41598-018-27426-w.

[209] K. Strijckmans, R. Schelfhout, D. Depla, Tutorial: Hysteresis during the reactive magnetron sputtering process, Journal of Applied Physics 124 (24) (2018) 241101. doi:10.1063/1.5042084.

[210] B. G. Priydarshini, N. Esakkiraja, S. Aich, M. Chakraborty, Resputtering Effect on Nanocrystalline Ni-Ti Alloy Films, Metallurgical and Materials Transactions A: Physical Metallurgy and Materials Science 47 (4) (2016) 1751–1760. doi:10.1007/s11661-015-3319-0.

[211] M. Ougier, A. Michau, F. Schuster, H. Maskrot, M. L. Schlegel, Effects of HiPIMS discharges and annealing on Cr-Al-C thin films, Surface and Coatings Technology 399 (July) (2020) 126141. doi:10.1016/j.surfcoat.2020.126141.

[212] E. Pitthan, M. Moro, S. Corrêa, D. Primetzhofer, Assessing boron quantification and depth profiling of different boride materials using ion beams, Surface and Coatings Technology 417 (April) (2021) 127188. doi:10.1016/j.surfcoat.2021.127188.

[213] T. Miller, J. M. Lin, L. Pirolli, L. Coquilleau, R. Luharuka, A. V. Teplyakov, Investigation of thin titanium carbonitride coatings deposited onto stainless

steel, Thin Solid Films 522 (2012) 193–198. doi:10.1016/j.tsf.2012.08.012.

[214] Y. Y. Guu, J. F. Lin, C. F. Ai, The tribological characteristics of titanium nitride, titanium carbonitride and titanium carbide coatings, Thin Solid Films 302 (1-2) (1997) 193–200. doi:10.1016/S0040-6090(96)09546-6.

[215] J.-M. Chappé, N. Martin, G. Terwagne, J. Lintymer, J. Gavoille, J. Takadoum, Water as reactive gas to prepare titanium oxynitride thin films by reactive sputtering, Thin Solid Films 440 (1-2) (2003) 66–73. doi:10.1016/S0040-6090(03)00832-0.

[216] P. H. Mayrhofer, M. Stoiber, Thermal stability of superhard Ti-B-N coatings, Surface and Coatings Technology 201 (13) (2007) 6148–6153. doi:10.1016/j.surfcoat.2006.08.132.

[217] C. Mitterer, M. Rauter, P. Rödhammer, Sputter deposition of ultrahard coatings within the system Ti-B-C-N, Surface and Coatings Technology 41 (3) (1990) 351–363. doi:10.1016/0257-8972(90)90146-4.

[218] O. Knotek, F. Jungblut, R. Breidenbach, Magnetron-sputtered superhard coatings within the system TiBCN, Vacuum 41 (7-9) (1990) 2184–2186. doi:10.1016/0042-207X(90)94220-K.

[219] C. Héau, J. Terrat, Ultrahard Ti–B–N coatings obtained by reactive magnetron sputtering of a Ti–B target, Surface and Coatings Technology 108-109 (1998) 332–339. doi:10.1016/S0257-8972(98)00621-5.

[220] J. Neidhardt, M. O'Sullivan, A. E. Reiter, W. Rechberger, W. Grogger, C. Mitterer, Structure-property-performance relations of high-rate reactive arc-evaporated Ti-B-N nanocomposite coatings, Surface and Coatings Technology 201 (6) (2006) 2553–2559. doi:10.1016/j.surfcoat.2006.04.031.

[221] L. García-González, J. Hernández-Torres, P. J. García-Ramírez, J. Martínez-Castillo, Á. Sauceda, A. L. Herrera-May, F. J. Espinoza-Beltrán, Structure

and mechanical properties of TiBN coatings fabricated by dc reactive sputtering technique, Journal of Materials Processing Technology 186 (1-3) (2007) 362–366. doi:10.1016/j.jmatprotec.2007.01.002.

[222] S. Vepřek, P. Nesládek, A. Niederhofer, F. Glatz, M. Jílek, M. Šíma, Recent progress in the superhard nanocrystalline composites: Towards their industrialization and understanding of the origin of the superhardness, Surface and Coatings Technology 108-109 (1998) 138–147. doi:10.1016/S0257-8972(98)00618-5.

[223] K. J. Martin, A. Madan, D. Hoffman, J. Ji, S. A. Barnett, Mechanical properties and thermal stability of TiN/TiB_2 nanolayered thin films, Journal of Vacuum Science & Technology A: Vacuum, Surfaces, and Films 23 (1) (2005) 90–98. doi:10.1116/1.1827628.

[224] C. Fuger, V. Moraes, R. Hahn, H. Bolvardi, P. Polcik, H. Riedl, P. H. Mayrhofer, Influence of Tantalum on phase stability and mechanical properties of WB_2, MRS Communications 9 (1) (2019) 375–380. doi:10.1557/mrc.2019.5.

[225] C. X. Tian, Z. S. Wang, C. W. Zou, X. S. Tang, X. Xie, S. Q. Li, F. Liang, Z. J. Li, Y. F. Liu, F. H. Su, Ternary and quarternary TiBN and TiBCN nanocomposite coatings deposited by arc ion plating, Surface and Coatings Technology 359 (December 2018) (2019) 445–450. doi:10.1016/j.surfcoat.2018.12.081.

[226] A. Gilewicz, K. Mydłowska, J. Ratajski, Ł. Szparaga, P. Bartosik, P. Kochmański, R. Jędrzejewski, Structural, mechanical and tribological properties of ZrC thin films deposited by magnetron sputtering, Vacuum 169 (August) (2019) 108909. doi:10.1016/j.vacuum.2019.108909.

[227] Z. T. Wu, Z. B. Qi, D. F. Zhang, Z. C. Wang, Nanoindentation induced plastic deformation in nanocrystalline ZrN coating, Materials Letters 164 (2016) 120–123. doi:10.1016/j.matlet.2015.10.091.

[228] Z. B. Qi, P. Sun, F. P. Zhu, Z. C. Wang, D. L. Peng, C. H. Wu, The inverse Hall-Petch effect in nanocrystalline ZrN coatings, Surface and Coatings Technology 205 (12) (2011) 3692–3697. doi:10.1016/j.surfcoat.2011.01.021.

[229] Y. Y. Chang, C. J. Wu, Mechanical properties and impact resistance of multilayered TiAlN/ZrN coatings, Surface and Coatings Technology 231 (2013) 62–66. doi:10.1016/j.surfcoat.2012.03.013.

[230] D. B. Miracle, High-Entropy Alloys: A Current Evaluation of Founding Ideas and Core Effects and Exploring "Nonlinear Alloys", Jom 69 (11) (2017) 2130–2136. doi:10.1007/s11837-017-2527-z.

[231] O. N. Senkov, J. D. Miller, D. B. Miracle, C. Woodward, Accelerated exploration of multi-principal element alloys with solid solution phases, Nature Communications 6 (2015) 1–10. doi:10.1038/ncomms7529.

[232] M. C. Troparevsky, J. R. Morris, P. R. Kent, A. R. Lupini, G. M. Stocks, Criteria for predicting the formation of single-phase high-entropy alloys, Physical Review X 5 (1) (2015) 1–6. doi:10.1103/PhysRevX.5.011041.

[233] O. Knotek, F. Löffler, H. J. Scholl, Properties of arc-evaporated CrN and (Cr, Al)N coatings, Surface and Coatings Technology 45 (1-3) (1991) 53–58. doi:10.1016/0257-8972(91)90205-B.

[234] P. H. Mayrhofer, D. Music, J. M. Schneider, Ab initio calculated binodal and spinodal of cubic $Ti_{1-x}Al_xN$, Applied Physics Letters 88 (7) (2006) 10–13. doi:10.1063/1.2177630.

[235] B. Alling, M. Odn, L. Hultman, I. A. Abrikosov, Pressure enhancement of the isostructural cubic decomposition in Ti1-x Alx N, Applied Physics Letters 95 (18) (2009) 0–3. doi:10.1063/1.3256196.

[236] S. PalDey, S. C. Deevi, Single layer and multilayer wear resistant coatings of (Ti,Al)N: A review, Materials Science and Engineering A 342 (1-2) (2003) 58–79. doi:10.1016/S0921-5093(02)00259-9.

[237] P. H. Mayrhofer, F. D. Fischer, H. J. Böhm, C. Mitterer, J. M. Schneider, Energetic balance and kinetics for the decomposition of supersaturated $Ti_{1-x}Al_xN$, Acta Materialia 55 (4) (2007) 1441–1446. doi:10.1016/j.actamat.2006.09.045.

[238] C. Höglund, B. Alling, J. Birch, M. Beckers, P. O. Persson, C. Baehtz, Z. Czigány, J. Jensen, L. Hultman, Effects of volume mismatch and electronic structure on the decomposition of ScAlN and TiAlN solid solutions, Physical Review B - Condensed Matter and Materials Physics 81 (22) (2010) 1–7. doi:10.1103/PhysRevB.81.224101.

[239] D. Holec, R. Rachbauer, L. Chen, L. Wang, D. Luef, P. H. Mayrhofer, Phase stability and alloy-related trends in Ti-Al-N, Zr-Al-N and Hf-Al-N systems from first principles, Surface and Coatings Technology 206 (7) (2011) 1698–1704. doi:10.1016/j.surfcoat.2011.09.019.

[240] F. Zhang, C. Zhang, S. L. Chen, J. Zhu, W. S. Cao, U. R. Kattner, An understanding of high entropy alloys from phase diagram calculations, Calphad: Computer Coupling of Phase Diagrams and Thermochemistry 45 (2014) 1–10. doi:10.1016/j.calphad.2013.10.006.

[241] K. Kaufmann, D. Maryanovsky, W. M. Mellor, C. Zhu, A. S. Rosengarten, T. J. Harrington, C. Oses, C. Toher, S. Curtarolo, K. S. Vecchio, Discovery of high-entropy ceramics via machine learning, npj Computational Materials 6 (1) (2020) 1–9. doi:10.1038/s41524-020-0317-6.

[242] V. I. Ivashchenko, P. E. Turchi, E. I. Olifan, Phase stability and mechanical properties of niobium nitrides, Physical Review B - Condensed Matter and Materials Physics 82 (5) (2010) 1–9. doi:10.1103/PhysRevB.82.054109.

[243] N. Koutná, D. Holec, M. Friák, P. H. Mayrhofer, M. Šob, Stability and elasticity of metastable solid solutions and superlattices in the MoN–TaN system: First-principles calculations, Materials and Design 144 (2018) 310–322. doi:10.1016/j.matdes.2018.02.033.

[244] F. Birch, Finite elastic strain of cubic crystals, Physical Review 71 (11) (1947) 809–824. doi:10.1103/PhysRev.71.809.

[245] C. L. Cao, Z. F. Hou, G. Yuan, First-principles study of the structural stability and electronic structures of TaN, Physica Status Solidi (B) Basic Research 245 (8) (2008) 1580–1585. doi:10.1002/pssb.200844065.

[246] D. Holec, R. Franz, P. H. Mayrhofer, C. Mitterer, Structure and stability of phases within the NbN-AlN system, Journal of Physics D: Applied Physics 43 (14) (2010). doi:10.1088/0022-3727/43/14/145403.

[247] A. Srivastava, B. D. Diwan, Structural and elastic properties of ZrN and HfN: Ab initio study, Canadian Journal of Physics 92 (9) (2014) 1058–1061. doi:10.1139/cjp-2013-0377.

[248] M. Hans, J. M. Schneider, Electric field strength-dependent accuracy of TiAlN thin film composition measurements by laser-assisted atom probe tomography, New Journal of Physics 22 (3) (2020). doi:10.1088/1367-2630/ab7770.

[249] K. Thompson, D. Lawrence, D. J. Larson, J. D. Olson, T. F. Kelly, B. Gorman, In situ site-specific specimen preparation for atom probe tomography, Ultramicroscopy 107 (2-3) (2007) 131–139. doi:10.1016/j.ultramic.2006.06.008.

[250] M. Hans, H. Rueß, Z. Czigány, J. Krause, P. Ondračka, D. Music, S. Evertz, D. M. Holzapfel, D. Primetzhofer, J. M. Schneider, Spinodal decomposition of reactively sputtered $(V_{0.64}Al_{0.36})_{0.49}N_{0.51}$ thin films, Surface and Coatings Technology 389 (March) (2020) 125641. doi:10.1016/j.surfcoat.2020.125641.

[251] B. Alling, T. Marten, I. A. Abrikosov, Questionable collapse of the bulk modulus in CrN, Nature Materials 9 (4) (2010) 283–284. doi:10.1038/nmat2722.

[252] L. Zhou, D. Holec, P. H. Mayrhofer, First-principles study of elastic properties of cubic $Cr_{1-x}Al_xN$ alloys, Journal of Applied Physics 113 (4) (2013) 043511. doi:10.1063/1.4789378.

[253] H. H. Pham, M. E. Williams, P. Mahaffey, M. Radovic, R. Arroyave, T. Cagin, Finite-temperature elasticity of fcc Al: Atomistic simulations and ultrasonic measurements, Physical Review B - Condensed Matter and Materials Physics 84 (6) (2011) 1–10. doi:10.1103/PhysRevB.84.064101.

[254] L. Liu, X. Wu, R. Wang, W. Li, Q. Liu, First principle study on the temperature dependent elastic constants, anisotropy, generalized stacking fault energy and dislocation core of NiAl and FeAl, Computational Materials Science 103 (2015) 116–125. doi:10.1016/j.commatsci.2015.03.024.

[255] N. Shulumba, O. Hellman, L. Rogström, Z. Raza, F. Tasnádi, I. A. Abrikosov, M. Odén, Temperature-dependent elastic properties of $Ti_{1-x}Al_xN$ alloys, Applied Physics Letters 107 (23) (2015) 231901. doi:10.1063/1.4936896.
URL http://aip.scitation.org/doi/10.1063/1.4936896

[256] A. B. Mei, O. Hellman, N. Wireklint, C. M. Schlepütz, D. G. Sangiovanni, B. Alling, A. Rockett, L. Hultman, I. Petrov, J. E. Greene, Dynamic and structural stability of cubic vanadium nitride, Physical Review B - Condensed Matter and Materials Physics 91 (5) (2015) 1–11. doi:10.1103/PhysRevB.91.054101.

[257] B. Alling, T. Marten, I. A. Abrikosov, A. Karimi, Comparison of thermodynamic properties of cubic $Cr_{1-x}Al_xN$ and $Ti_{1-x}Al_xN$ from first-principles calculations, Journal of Applied Physics 102 (4) (2007) 044314. doi:10.1063/1.2773625.

[258] F. Rovere, D. Music, S. Ershov, M. T. Baben, H.-G. Fuss, P. H. Mayrhofer, J. M. Schneider, Experimental and computational study on the phase stability of Al-containing cubic transition metal nitrides, Journal of Physics D: Applied Physics 43 (3) (2010) 035302. doi:10.1088/0022-3727/43/3/035302.

[259] L. Chen, M. Moser, Y. Du, P. H. Mayrhofer, Compositional and structural evolution of sputtered Ti-Al-N, Thin Solid Films 517 (24) (2009) 6635–6641. doi:10.1016/j.tsf.2009.04.056.

[260] M. Hans, J. M. Schneider, On the chemical composition of TiAlN thin films - Comparison of ion beam analysis and laser-assisted atom probe tomography with varying laser pulse energy, Thin Solid Films 688 (May) (2019) 137251. doi:10.1016/j.tsf.2019.04.026.

[261] B. Gault, D. W. Saxey, M. W. Ashton, S. B. Sinnott, A. N. Chiaramonti, M. P. Moody, D. K. Schreiber, Behavior of molecules and molecular ions near a field emitter, New Journal of Physics 18 (3) (2016) 033031. arXiv:1511.09029, doi:10.1088/1367-2630/18/3/033031.

CHAPTER 11

Contributions to the field

11.1 Publication I

A. Kretschmer, A. Kirnbauer, V. Moraes, D. Primetzhofer, K. Yalamanchili, H. Rudigier, P. H. Mayrhofer, Improving phase stability, hardness, and oxidation resistance of reactively magnetron sputtered (Al,Cr,Nb,Ta,Ti)N thin films by Si-alloying, Surface and Coatings Technology, 416 (February):127162, 2021. https://doi.org/10.1016/j.surfcoat.2021.127162

My contribution: I designed the experiments together with A.K. and P.H.M. I performed the depositions, the DFT calculations, the annealing and oxidation experiments, the sample analysis (except for ERDA measurement), evaluated the results, and wrote the manuscript.

11.2 Publication II

A. Kirnbauer, **A. Kretschmer**, C. M. Koller, T. Wojcik, V. Paneta, M. Hans, J. M. Schneider, P. Polcik, P. H. Mayrhofer, Mechanical properties and thermal stability of reactively sputtered multi-principal-metal Hf-Ta-Ti-V-Zr nitrides, Surface and Coatings Technology, 389 (March):125674, 2020. https://doi.org/10.1016/j.surfcoat.2020.125674

My contribution: I performed and evaluated the DFT calculations, discussed the results with the main author, and revised the manuscript.

11.3 Future Publications

The results from chapters 7, 8, and 9 have been sent to peer-reviewed journals and are at the time of writing this thesis in the submission process.

CHAPTER 12

Scientific supervision

I supervised two master students,

- Luca Lezuo
- Bálint Hajas

who worked on experimental validation of mechanical properties and thermal stability of my DFT calculations. I also supervised and corrected exams for the undergraduate courses

- Materials Science of Metallic Materials
- Surface and Coatings Technology

at TU Wien.

APPENDICES

APPENDIX A Figures

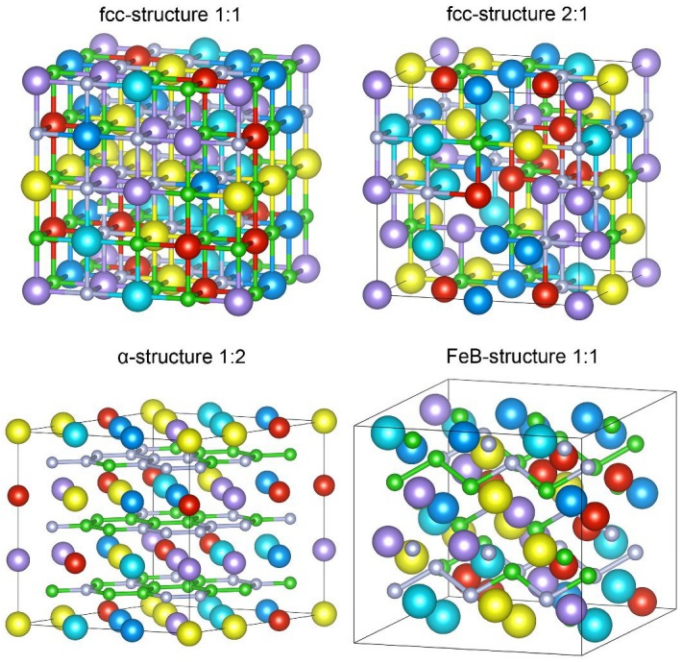

Figure A.1: Unrelaxed SQS supercells of the four investigated structures with equal B and N occupation: fcc structure (TiN prototype) without and with 50 % nonmetal-vacancies (equally distributed between B and N), the hexagonal α-structure (AlB_2 prototype), and the orthorhombic FeB-structure. The equimolar metal content is achieved by averaging 10 cells with permuted metal contents in the fcc and α structures. The small grey and green atoms represent N and B, respectively, the other colored atoms represent Hf, Ta, Ti, V, and Zr.

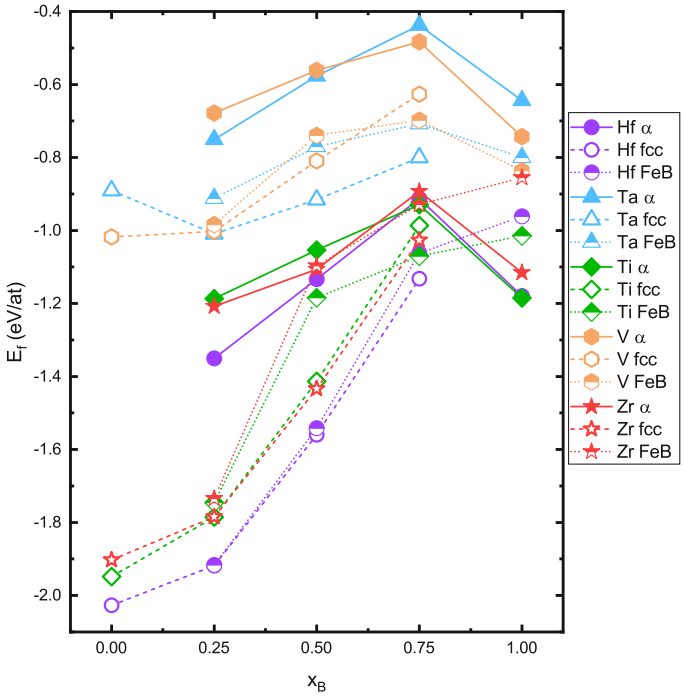

Figure A.2: Energies of formation E_f, of the binary metal-boronnitride phases in α, fcc (without vacancies), and FeB structures.

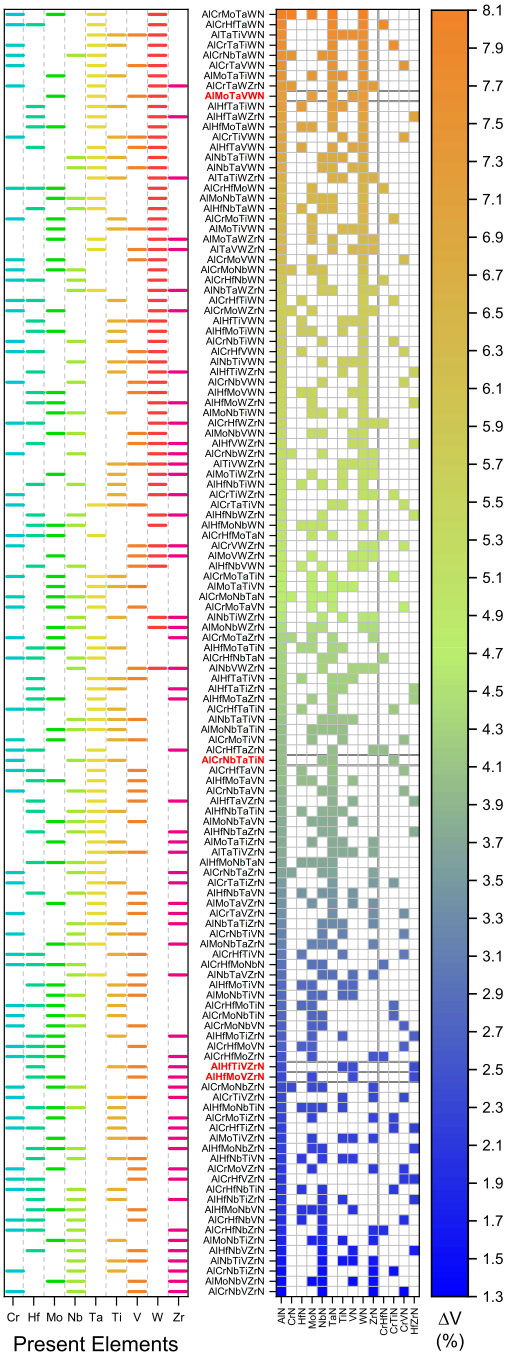

Figure A.3: Overview of the volume change ΔV by the decomposition into the predicted decomposition products at 0 K (Figure 9.1). The left box shows the elements present in each row (except Al and N). All decompositions exhibit a positive ΔV, partly due to the larger volumes of the thermodynamically stable non-cubic binary phases. The sorting by ΔV reveals a strong clustering of Ta and especially W in compositions with a high volume mismatch to their products. This is due to the large volume mismatches of 6.3 and 12.3 % for TaN and WN, respectively, between their stable and their fcc structures (for AlN 20.1 %). The four highlighted compositions (marked in red) were tested experimentally.

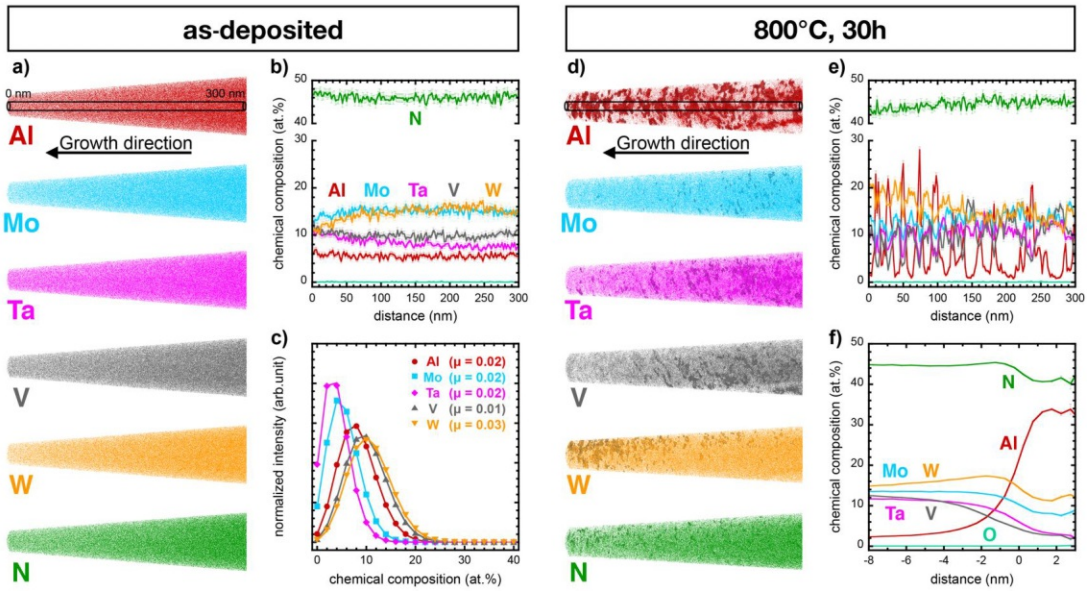

Figure A.4: Local chemical composition analysis of $(Al, Mo, Ta, V, W)N$ in as-deposited and annealed state by atom probe tomography. a) Reconstruction of Al, Mo, Ta, V, W, and N atomic positions in as-deposited state. b) Composition profile from the cylindrical region indicated in a). The frequency distribution analysis in c) is shown together with Pearson correlation coefficients, which are based on the comparison of the measured distribution with a random, binomial distribution. The Pearson correlation coefficients close to 0 emphasize the formation of a random solid solution. d) Reconstruction of Al, Mo, Ta, V, W, and N atomic positions after annealing together with chemically enriched regions represented by isoconcentration surfaces ≥ 20 at% Al, 20 at% Mo, 15 at% Ta, 20 at% V, and 25 at% W, as well as ≤ 39 at% N. e) The composition profile from the cylindrical region indicated in d) reveals a chemical modulation with alternations between Al-rich and (Mo, Ta, V, W)-rich regions. f) Proximity histogram of regions with ≥ 20 at% Al. The Al content increases from 2 to 34 at%, while especially Ta and V are reduced. From Ta and V proximity histograms (not shown) it is evident that these species co-segregate, indicating an early stage $(Ta, V)_2N$ segregation which has been observed in decomposed $(Hf, Ta, Ti, V, Zr)N$ [66].

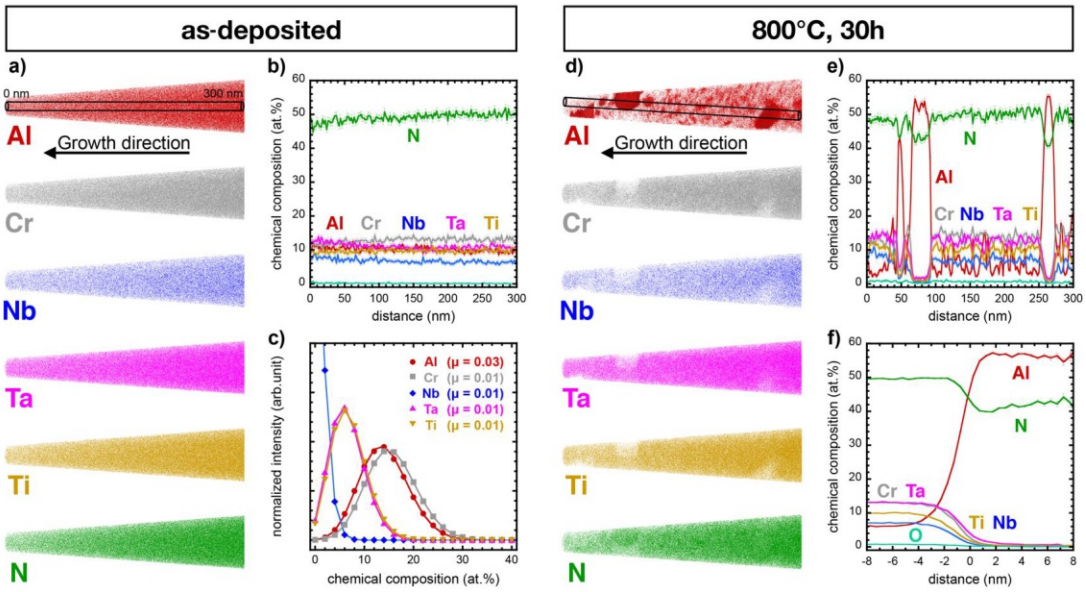

Figure A.5: Local chemical composition analysis of (Al, Cr, Nb, Ta, Ti)N in as-deposited and annealed state by APT. a) Reconstruction of Al, Cr, Nb, Ta, Ti, and N atomic positions in as-deposited state. b) Composition profile from the cylindrical region indicated in a). The frequency distribution analysis shown in c) with Pearson correlation coefficients close to 0 emphasize the formation of a random solid solution. d) Reconstruction of Al, Cr, Nb, Ta, Ti, and N atomic positions after annealing and Al-rich regions are represented by isoconcentration surfaces with ≥ 45 at%. e) The composition profile from the cylindrical region indicated in d) as well as the proximity histogram of regions with ≥ 45 at% Al in f) provide evidence for the local formation of AlN in agreement with XRD data.
Based on DFT predictions the formation of TaN and NbN was expected as well. As discussed in the main article, the driving force for AlN formation is dominant in all coatings and since still some remaining c-AlN is visible in the XRD data, it can be concluded that the decomposition reaction is still in an early stage and other decomposition products have not formed yet.

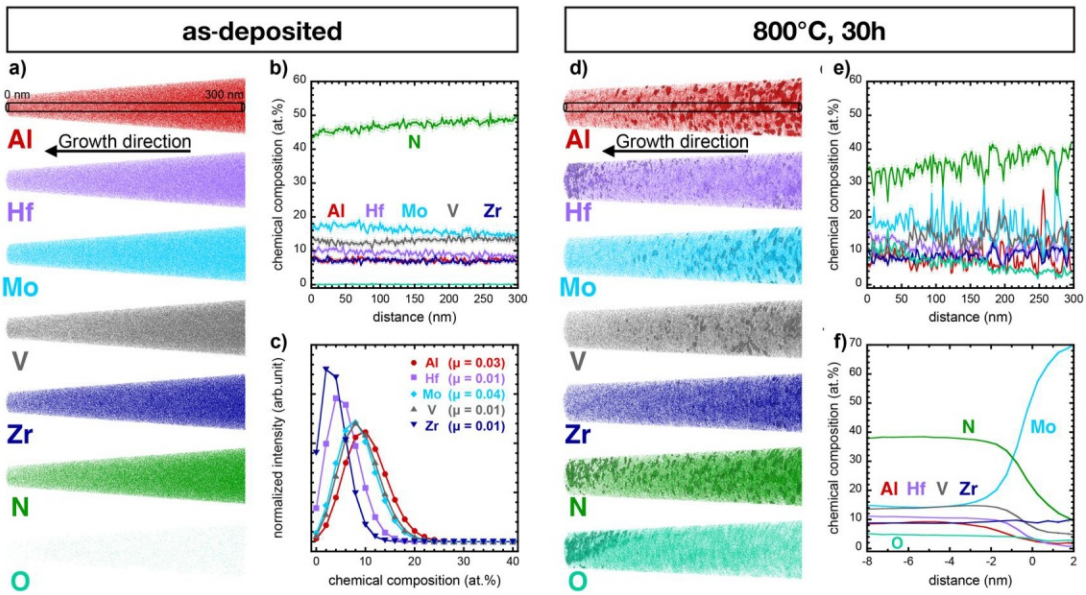

Figure A.6: Local chemical composition analysis of (Al, Hf, Mo, V, Zr)N in as-deposited and annealed state by APT. a) Reconstruction of Al, Hf, Mo, V, Zr, N, and O atomic positions in as-deposited state. b) Composition profile from the cylindrical region indicated in a). The frequency distribution analysis shown in c) with Pearson correlation coefficients close to 0 emphasize the formation of a random solid solution. d) Reconstruction of Al, Hf, Mo, V, Zr, N, and O atomic positions after annealing together with chemically enriched regions represented by isoconcentration surfaces $\geq$ 20 at% Al, 16 at% Hf, 40 at% Mo, 25 at% V, 15 at% Zr, and 13 at% O, as well as $\leq$ 28 at% N. e) The composition profile from the cylindrical region indicated in d) reveals that the surface-near region contains up to 10 at% O, which is reduced to 4 at% at a distance range of 250 to 300 nm. The proximity histogram of regions with $\geq$ 40 at% Mo in f) reveals that the Mo content increases locally up to 70 at% and emphasizes the instability of the Mo-N bond. While the Mo segregations appear to be more pronounced than Al, it has to be considered that in the as-deposited state the amount of Al is with $\sim$ 8 at% significantly lower than Mo with $\sim$13 at% (concentrations based on EDS analysis).

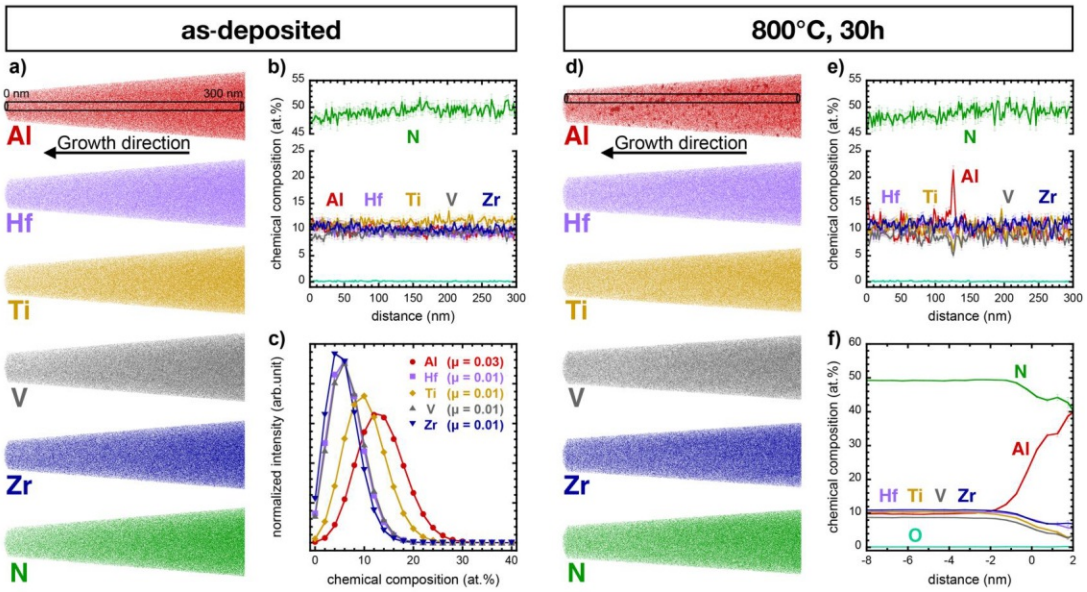

Figure A.7: Local chemical composition analysis of (Al, Hf, Ti, V, Zr)N in as-deposited and annealed state by APT. a) Reconstruction of Al, Hf, Ti, V, Zr, and N atomic positions in as-deposited state. The composition profile in b) is from the cylindrical region indicated in a) and demonstrates that this coating is closest to equimolarity in comparison to the other systems. The frequency distribution analysis shown in c) with Pearson correlation coefficients close to 0 emphasize the formation of a random solid solution. d) Reconstruction of Al, Hf, Ti, V, Zr, and N atomic positions after annealing and Al-rich regions are represented by isoconcentration surfaces with $\geq$20 at%. e) The composition profile from the cylindrical region indicated in d) as well as the proximity histogram of regions with $\geq$ 20 at% Al in f) provide evidence for the onset of local AlN formation. The content of transition metals becomes gradually depleted, but the segregation into AlN is not complete as there are still between 3 and 8 at% of the other metals present inside the Al-rich regions. So, while the (Al, Hf, Ti, V, Zr)N decomposes, the decomposition speed is much slower than e.g. in (Al, Cr, Nb, Ta, Ti)N.

APPENDIX B Tables

Table B.1: Energies of formation E_f, in eV/at, lattice parameters a, b, and c, in Å, and angles α, β, and γ, in degrees of the calculated (HfTaTiVZr)-B-N cells with different B concentrations in the non-metal sublattice x_B in the α, fcc (without and with vacancies) and FeB structures. Where multiple cells were calculated per composition, the average parameter and the corresponding standard deviation, denoted with s, are given.

	x_B	E_f	a	s(a)	c	s(c)	α	s(α)	γ	s(γ)	a/c
α structure	0.25	-1.02	3.27	0.26	3.44	0.15	88.05	4.14	120.72	4.62	0.95
	0.50	-0.85	3.27	0.10	3.29	0.13	89.77	3.55	119.28	2.26	0.99
	0.75	-0.76	3.30	0.13	3.13	0.07	90.42	2.64	121.37	2.55	1.05
	0.80	-0.74	3.27	0.16	3.13	0.05	89.84	1.00	121.04	1.36	1.05
	0.91	-0.83	3.25	0.16	3.09	0.03	90.15	0.67	120.12	0.55	1.05
	1.00	-0.94	3.22	0.13	3.09	0.00	90.00	0.03	120.01	0.01	1.04
	x_B	E_f	a	s(a)	α	s(α)					
fcc 1:1	0.00	-1.73	4.42	0.01	89.94	0.09					
	0.25	-1.47	4.47	0.02	89.98	0.09					
	0.50	-1.20	4.53	0.02	90.01	0.10					
	0.75	-0.89	4.58	0.01	90.04	0.12					
	0.81	-0.81	4.59	0.01	90.05	0.10					
	0.91	-0.68	4.62	0.01	90.02	0.09					
	x_B	E_f	a	s(a)	α	s(α)					
fcc 2:1	0.00	-1.27	4.36	0.01	89.94	0.09					
	0.25	-1.06	4.40	0.02	89.98	0.09					
	0.50	-0.84	4.44	0.02	90.01	0.10					
	0.75	-0.60	4.48	0.01	90.04	0.12					
	x_B	E_f	a	b	c	α	β	γ			
FeB	0.25	-1.40	6.36	3.15	4.51	89.08	90.53	90.27			
	0.50	-0.99	6.17	3.23	4.72	91.68	88.71	90.67			
	0.75	-0.85	6.00	3.19	4.84	89.53	89.01	89.27			
	1.00	-0.83	6.26	3.12	4.74	90.00	89.95	89.96			

Table B.2: Calculated elastic properties of the α- and fcc-structured (without vacancies) boronnitrides with different B concentrations in the non-metal sublattice x_B. Elastic constants C_{ij} as well as the expressed bulk B, shear G, and Young's moduli E, and the Poisson's ratio ν and the effective Cauchy pressure C_p are given. All values are given in GPa, except for the dimensionless G/B and ν.

	x_B	C_{11}	C_{12}	C_{13}	C_{33}	C_{44}	C_{66}	B	G	E	E_{100}	E_{110}	E_{111}	G/B	ν	C_p
α	0.25	215	117	110	202	20	49	145	34	95	134	134	70	0.24	0.39	90
	0.50	245	127	115	220	41	59	158	51	138	160	160	125	0.32	0.35	73
	0.75	359	141	136	278	85	109	200	94	243	273	273	238	0.47	0.30	51
	0.80	366	136	146	274	93	115	205	98	253	277	277	257	0.47	0.30	53
	0.91	478	124	148	345	149	177	236	151	374	405	405	385	0.64	0.24	-1
	1.00	597	90	146	413	234	253	262	221	518	542	542	550	0.85	0.17	-87
	x_B	C_{11}	C_{12}			C_{44}		B	G	E	E_{100}	E_{110}	E_{111}	G/B	ν	C_p
fcc 1:1	0.00	485	149			110		261	130	336	416	313	289	0.50	0.29	39
	0.25	456	124			127		235	141	353	402	340	323	0.60	0.25	-3
	0.50	435	110			122		219	137	340	391	327	310	0.63	0.24	-12
	0.75	429	92			104		204	126	314	397	290	266	0.62	0.24	-12
	0.81	432	87			101		202	125	311	404	284	259	0.62	0.24	-14
	0.91	426	83			77		197	107	272	399	233	205	0.54	0.27	6

Table B.3: Structures and k-point mesh of calculated binary nitrides.

Material	Structure prototype	Space group	k-point mesh
AlN	β-ZnS	$P6_3mc$	$22 \times 22 \times 12$
CrN	NaCl	$Fm\bar{3}m$	$14 \times 14 \times 14$
HfN	NaCl	$Fm\bar{3}m$	$13 \times 13 \times 13$
MoN	NiAs	$P6_3/mmc$	$12 \times 12 \times 11$
NbN	WC	$P\bar{6}m2$	$24 \times 24 \times 21$
TaN	TaN	$P\bar{6}2m$	$13 \times 13 \times 21$
TiN	NaCl	$Fm\bar{3}m$	$14 \times 14 \times 14$
VN	NaCl	$Fm\bar{3}m$	$15 \times 15 \times 15$
WN	NbO	$Pm\bar{3}m$	$15 \times 15 \times 15$
ZrN	NaCl	$Fm\bar{3}m$	$13 \times 13 \times 13$

Table B.4: Nearest neighbor N-metal bond lengths of the relaxed fcc binary nitrides.

Metal	bond length (Å)
Al	2.035
Cr	2.072
Hf	2.269
Mo	2.182
Nb	2.213
Ta	2.214
Ti	2.128
V	2.065
W	2.187
Zr	2.288

Table B.5: Indentation hardness H and modulus E_I measured by nanoindentation on the nitride coatings used in the thermal stability study in as-deposited state and after annealing to 800 °C for 30 h. All values are given in GPa with standard deviations as error of measurement.

	H		E_I	
Coating	as-dep.	annealed	as-dep.	annealed
(Al, Cr, Nb, Ta, Ti)N	35.6±2.6	35.5±3.5	515±44	532±57
(Al, Hf, Mo, V, Zr)N	33.8±1.6	26.3±1.5	473±46	435±41
(Al, Mo, Ta, V, W)N	36.2±4.3	35.5±3.5	514±68	595±69
(Al, Hf, Ti, V, Zr)N	32.7±1.5	32.3±2.7	437±20	457±30

APPENDIX C Structure files

The structure files of the investigated binary ceramic phases are presented in the VASP POSCAR format. The first line contains the name and chemistry of the structure. The universal scaling factor of the lattice size and atomic positions in the second line is always 1 in the here presented files. Lines 3 to 5 contain the three lattice vectors of the unit cell. The sixth line states the present elements, followed by the quantitiy of each element in the seventh line, in the same sequence. The eight line is a flag that sets the atomic coordinates in the next lines to fractional coordinates (as opposed to Cartesian coordinates). The ninth and following lines contain the atomic coordinates of the species by the same sequence as line 6 (first all N, then all metal atoms). For more information, please visit the vasp wiki. Supercell structures of higher multinary order were created from the TiN file, using a special quasi-random structure generator by Dominik Nöger (Montanuniversität Leoben) to replace Ti and N with the appropriate elements to achieve random distributions. The same procedure was applied to the boride phases.

```
fcc AlN
1.00000000000000
4.0689997673000002     0.0000000000000000     0.0000000000000000
0.0000000000000000     4.0689997673000002     0.0000000000000000
0.0000000000000000     0.0000000000000000     4.0689997673000002
N    Al
4     4
Direct
0.5000000000000000  0.0000000000000000  0.0000000000000000
0.0000000000000000  0.5000000000000000  0.0000000000000000
0.0000000000000000  0.0000000000000000  0.5000000000000000
0.5000000000000000  0.5000000000000000  0.5000000000000000
0.0000000000000000  0.0000000000000000  0.0000000000000000
0.0000000000000000  0.5000000000000000  0.5000000000000000
0.5000000000000000  0.0000000000000000  0.5000000000000000
0.5000000000000000  0.5000000000000000  0.0000000000000000
```

```
wurtzite AlN
1.00000000000000
3.1274478961319829    -0.0000000000000000     0.0000000000000000
-1.5637239480659915     2.7084493270771755     0.0000000000000000
-0.0000000000000000     0.0000000000000000     5.0150649303214863
N    Al
2     2
Direct
0.3333333429999996  0.6666666870000029 -0.0002415131438318
0.6666666269999979  0.3333333129999971  0.4997584868561682
0.3333333429999996  0.6666666870000029  0.3812415251438330
0.6666666269999979  0.3333333129999971  0.8812415551438282
```

```
fcc CrN
1.00000000000000
4.1440000534000001    0.0000000000000000    0.0000000000000000
0.0000000000000000    4.1440000534000001    0.0000000000000000
0.0000000000000000    0.0000000000000000    4.1440000534000001
N    Cr
4     4
Direct
0.5000000000000000  0.0000000000000000  0.0000000000000000
0.0000000000000000  0.5000000000000000  0.0000000000000000
0.0000000000000000  0.0000000000000000  0.5000000000000000
0.5000000000000000  0.5000000000000000  0.5000000000000000
0.0000000000000000  0.0000000000000000  0.0000000000000000
0.0000000000000000  0.5000000000000000  0.5000000000000000
0.5000000000000000  0.0000000000000000  0.5000000000000000
0.5000000000000000  0.5000000000000000  0.0000000000000000
```

```
fcc HfN
1.00000000000000
4.5374999999999996    0.0000000000000000    0.0000000000000000
0.0000000000000000    4.5374999999999996    0.0000000000000000
0.0000000000000000    0.0000000000000000    4.5374999999999996
N    Hf
4     4
Direct
0.5000000000000000  0.0000000000000000  0.0000000000000000
0.0000000000000000  0.5000000000000000  0.0000000000000000
0.0000000000000000  0.0000000000000000  0.5000000000000000
0.5000000000000000  0.5000000000000000  0.5000000000000000
0.0000000000000000  0.0000000000000000  0.0000000000000000
0.0000000000000000  0.5000000000000000  0.5000000000000000
0.5000000000000000  0.0000000000000000  0.5000000000000000
0.5000000000000000  0.5000000000000000  0.0000000000000000
```

```
fcc MoN
1.00000000000000
4.3639998436000003     0.0000000000000000     0.0000000000000000
0.0000000000000000     4.3639998436000003     0.0000000000000000
0.0000000000000000     0.0000000000000000     4.3639998436000003
N    Mo
4     4
Direct
0.5000000000000000  0.0000000000000000  0.0000000000000000
0.0000000000000000  0.5000000000000000  0.0000000000000000
0.0000000000000000  0.0000000000000000  0.5000000000000000
0.5000000000000000  0.5000000000000000  0.5000000000000000
0.0000000000000000  0.0000000000000000  0.0000000000000000
0.0000000000000000  0.5000000000000000  0.5000000000000000
0.5000000000000000  0.0000000000000000  0.5000000000000000
0.5000000000000000  0.5000000000000000  0.0000000000000000

hex_NiAs MoN
1.0
5.7806696892          0.0000000000          0.0000000000
-2.8903356037          5.0062019586          0.0000000000
0.0000037859          0.0000004372          5.6863126755
N   Mo
8    8
Direct
0.333325624          0.666667104          0.520046234
0.666659117          0.333333194          0.020045893
0.166501522          0.833492339          0.993049800
0.333009154          0.166507304          0.493049979
0.166498899          0.333013505          0.993048906
0.833486438          0.166504905          0.493050992
0.666981101          0.833495378          0.993049860
0.833485425          0.666984797          0.493050039
0.999995887          0.999999225          0.257107198
0.999996305          0.999999046          0.757107079
0.488337308          0.511656284          0.247898802
0.976682127          0.488345265          0.747898579
0.488338858          0.976690829          0.247899488
0.511648953          0.488344312          0.747899532
0.023304876          0.511655748          0.247898445
0.511648417          0.023310775          0.747899175
```

```
fcc NbN
1.00000000000000
4.4264999999999999     0.0000000000000000     0.0000000000000000
0.0000000000000000     4.4264999999999999     0.0000000000000000
0.0000000000000000     0.0000000000000000     4.4264999999999999
N    Nb
4     4
Direct
0.5000000000000000  0.0000000000000000  0.0000000000000000
0.0000000000000000  0.5000000000000000  0.0000000000000000
0.0000000000000000  0.0000000000000000  0.5000000000000000
0.5000000000000000  0.5000000000000000  0.5000000000000000
0.0000000000000000  0.0000000000000000  0.0000000000000000
0.0000000000000000  0.5000000000000000  0.5000000000000000
0.5000000000000000  0.0000000000000000  0.5000000000000000
0.5000000000000000  0.5000000000000000  0.0000000000000000
```

```
hex_WC NbN
1.00000000000000
2.9203719474902390     0.0000000000009841     0.0000000000000000
-1.4601859736949032     2.5291162950222574    -0.0000000000000000
0.0000000000000000    -0.0000000000000000     2.8510743348718872
N    Nb
1     1
Direct
0.6666666779999986  0.3333333550000006  0.5000000000000000
0.0000000000000000  0.0000000000000000 -0.0000000000000000
```

```
fcc TaN
1.00000000000000
4.4269999999999996     0.0000000000000000     0.0000000000000000
0.0000000000000000     4.4269999999999996     0.0000000000000000
0.0000000000000000     0.0000000000000000     4.4269999999999996
N    Ta
4     4
Direct
0.5000000000000000  0.0000000000000000  0.0000000000000000
0.0000000000000000  0.5000000000000000  0.0000000000000000
0.0000000000000000  0.0000000000000000  0.5000000000000000
0.5000000000000000  0.5000000000000000  0.5000000000000000
0.0000000000000000  0.0000000000000000  0.0000000000000000
0.0000000000000000  0.5000000000000000  0.5000000000000000
0.5000000000000000  0.0000000000000000  0.5000000000000000
0.5000000000000000  0.5000000000000000  0.0000000000000000
```

```
hex TaN SG 189
1.0
5.2370800972          0.0000000000          0.0000000000
-2.6184632778          4.5353114349          0.0000000000
0.0000000000          0.0000000000          2.9239878654
N   Ta
3    3
Direct
0.375503242          0.008341336          0.000000000
0.983321965          0.400471359          0.000000000
0.591172278          0.616196156          0.000000000
0.983317077          0.008340931          0.000000000
0.649986565          0.341661245          0.500000000
0.316632152          0.674988985          0.500000000
```

```
fcc TiN
1.00000000000000
4.2549999999999999     0.0000000000000000     0.0000000000000000
0.0000000000000000     4.2549999999999999     0.0000000000000000
0.0000000000000000     0.0000000000000000     4.2549999999999999
N    Ti
4     4
Direct
0.5000000000000000  0.0000000000000000  0.0000000000000000
0.0000000000000000  0.5000000000000000  0.0000000000000000
0.0000000000000000  0.0000000000000000  0.5000000000000000
0.5000000000000000  0.5000000000000000  0.5000000000000000
0.0000000000000000  0.0000000000000000  0.0000000000000000
0.0000000000000000  0.5000000000000000  0.5000000000000000
0.5000000000000000  0.0000000000000000  0.5000000000000000
0.5000000000000000  0.5000000000000000  0.0000000000000000
```

```
fcc VN
1.00000000000000
4.1297870000000003     0.0000000000000000     0.0000000000000000
0.0000000000000000     4.1297870000000003     0.0000000000000000
0.0000000000000000     0.0000000000000000     4.1297870000000003
N    V
4     4
Direct
0.5000000000000000  0.0000000000000000  0.0000000000000000
0.0000000000000000  0.5000000000000000  0.0000000000000000
0.0000000000000000  0.0000000000000000  0.5000000000000000
0.5000000000000000  0.5000000000000000  0.5000000000000000
0.0000000000000000  0.0000000000000000  0.0000000000000000
0.0000000000000000  0.5000000000000000  0.5000000000000000
0.5000000000000000  0.0000000000000000  0.5000000000000000
0.5000000000000000  0.5000000000000000  0.0000000000000000
```

```
cub_NbO WN
1.00000000000000
4.1300001143999996     0.0000000000000000     0.0000000000000000
0.0000000000000000     4.1300001143999996     0.0000000000000000
0.0000000000000000     0.0000000000000000     4.1300001143999996
N    W
3     3
Direct
0.5000000000000000  0.0000000000000000  0.0000000000000000
0.0000000000000000  0.5000000000000000  0.0000000000000000
0.0000000000000000  0.0000000000000000  0.5000000000000000
0.0000000000000000  0.5000000000000000  0.5000000000000000
0.5000000000000000  0.0000000000000000  0.5000000000000000
0.5000000000000000  0.5000000000000000  0.0000000000000000
```

```
fcc WN
1.00000000000000
4.3738000000000001    0.0000000000000000    0.0000000000000000
0.0000000000000000    4.3738000000000001    0.0000000000000000
0.0000000000000000    0.0000000000000000    4.3738000000000001
N    W
4     4
Direct
0.5000000000000000  0.0000000000000000  0.0000000000000000
0.0000000000000000  0.5000000000000000  0.0000000000000000
0.0000000000000000  0.0000000000000000  0.5000000000000000
0.5000000000000000  0.5000000000000000  0.5000000000000000
0.0000000000000000  0.0000000000000000  0.0000000000000000
0.0000000000000000  0.5000000000000000  0.5000000000000000
0.5000000000000000  0.0000000000000000  0.5000000000000000
0.5000000000000000  0.5000000000000000  0.0000000000000000
```

```
fcc ZrN
1.00000000000000
4.5755000114000000    0.0000000000000000    0.0000000000000000
0.0000000000000000    4.5755000114000000    0.0000000000000000
0.0000000000000000    0.0000000000000000    4.5755000114000000
N    Zr
4     4
Direct
0.5000000000000000  0.0000000000000000  0.0000000000000000
0.0000000000000000  0.5000000000000000  0.0000000000000000
0.0000000000000000  0.0000000000000000  0.5000000000000000
0.5000000000000000  0.5000000000000000  0.5000000000000000
0.0000000000000000  0.0000000000000000  0.0000000000000000
0.0000000000000000  0.5000000000000000  0.5000000000000000
0.5000000000000000  0.0000000000000000  0.5000000000000000
0.5000000000000000  0.5000000000000000  0.0000000000000000
```

```
alpha-TiB2
1.00000000000000
3.0314433906553471     0.0000000000000000     0.0000000000000000
-1.5157216953276735     2.6253069864978542    -0.0000000000000000
0.0000000000000000     0.0000000000000000     3.2526162955817912
B    Ti
2     1
Direct
0.3333333420000031  0.6666666830000025  0.5000000000000000
0.6666666590000005  0.3333333189999976  0.5000000000000000
-0.0000000000000000 -0.0000000000000000  0.0000000000000000



FeB-structured TiB
1.00000000000000
6.1255714876230494     0.0000000000000000     0.0000000000000000
0.0000000000000000     3.0561619522706813     0.0000000000000000
0.0000000000000000     0.0000000000000000     4.5700467512493530
B    Ti
4     4
Direct
0.0299012875559607  0.2500000000000000  0.0992950886668852
0.9700987174440433  0.7500000200000017  0.9007048813331195
0.4700987174440433  0.7500000200000017  0.5992951186668805
0.5299012825559567  0.2500000000000000  0.4007049113331148
0.1775656566808828  0.2500000000000000  0.6224196502556728
0.8224343003191172  0.7500000200000017  0.3775803787443260
0.3224343433191172  0.7500000200000017  0.1224196212556740
0.6775656566808828  0.2500000000000000  0.8775803497443272
```

Andreas Kretschmer

Computational and experimental materials scientist,
unraveling the secrets of high-entropy materials.

Education

2018–2021 **TU Wien**, *1040 Wien*, PhD candidate at the faculty of Mechanical and Industrial Engineering, Topic: *Computationally Guided Optimization of High-Entropy Sublattice Ceramic Thin Films.*

2016–2018 **TU Wien**, *1040 Wien*, Msc. in Applied Physical and Analytical Chemistry, Master thesis: *Selective Stripping of AlCrN-hard coatings from WC-Co cemented carbides.*
Passed with Distinction

2011–2016 **TU Wien**, *1040 Wien*, Bsc. in Technical Chemistry, Bachelor thesis: *Analyse anorganischer Werkstoffe mit Laser Induced Breakdown Spectroscopy.*

2002–2010 **Bundesgymnasium und Bundesrealgymnasium**, *1120 Wien.*
Passed with Distinction

Experience

10/2017–02/2018
10/2016–02/2017 **TU Wien**, *1040 Wien*, Tutor for gravimetry, volumetric analysis, UV/Vis spectroscopy, F-OES.

07/2017–08/2017 **voestalpine**, *4020 Linz*, Intern, Sample extraction, water analysis with gravimetry, UV/Vis spectroscopy and ion chromatography.

03/2016–07/2016 **TU Wien**, *1040 Wien*, Tutor for instrumental FTIR-spectroscopy and ion chromatography.

01/2011–09/2011 **Arbeiter-Samariterbund**, *1150 Wien*, Civil Service as Paramedic.

Languages

German Mother tongue
English Fluent
Norwegian Basic

+43 1 58801-308108 • andreas.kretschmer@tuwien.ac.at

Computer skills

Excellent	MS Office, Origin
Proficient	Photoshop, VASP, LaTeX
Intermediate	Linux/shell scripting, Illustrator, Indesign
Basic	Python, R

Interests

Reading

Classical Music

Ballroom Dancing

References

Prof. Dr. Paul Heinz Mayrhofer
PhD supervisor, paul.mayrhofer@tuwien.ac.at

Ass.Prof. Dr. Andreas Limbeck
Master thesis supervisor, andreas.limbeck@tuwien.ac.at

Dr. David Holec
Scientific collaborator, david.holec@unileoben.ac.at

Publications

1. A. Kretschmer, A. Kirnbauer, V. Moraes, D. Primetzhofer, K. Yalamanchili, H. Rudigier, P. H. Mayrhofer, Improving phase stability, hardness, and oxidation resistance of reactively magnetron sputtered (Al,Cr,Nb,Ta,Ti)N thin films by Si-alloying, Surface and Coatings Technology 416 (February) (2021) 127162. doi:10.1016/j.surfcoat.2021.127162.

2. A. Kirnbauer, A. Kretschmer, C. M. Koller, T. Wojcik, V. Paneta, M. Hans, J. M. Schneider, P. Polcik, P. H. Mayrhofer, Mechanical properties and thermal stability of reactively sputtered multi-principal-metal Hf-Ta-Ti-V-Zr nitrides, Surface and Coatings Technology 389 (March) (2020) 125674. doi:10.1016/j.surfcoat.2020.125674.

Conferences

THERMEC 2021, *Wien, Austria/Online*, Oral presentation.

ICMCTF 2021, *San Diego, USA/Online*, Oral and poster presentation.

PSE 2020, *Erfurt, Germany*, Oral presentation.

Supervision

Luca Lezuo, *Msc. student.*

Bálint Hajas, *Msc. student.*